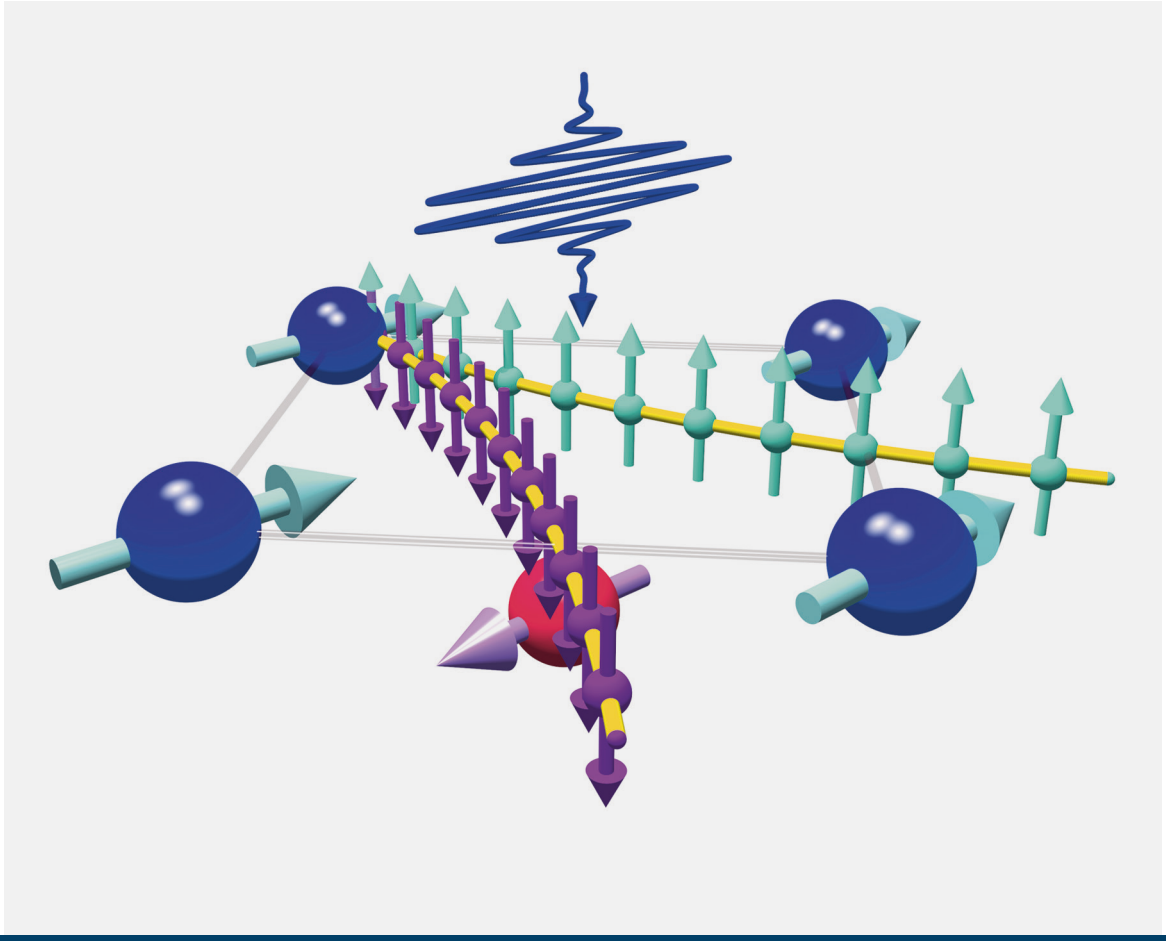

# Light-matter interaction from ab-initio Keldysh formalism

Maximilian Daniel Merte

Information
Band / Volume 126
ISBN 978-3-95806-906-0

Mitglied der Helmholtz-Gemeinschaft

JÜLICH
Forschungszentrum

Schriften des Forschungszentrums Jülich
Reihe Information / Information Band / Volume 126

Forschungszentrum Jülich GmbH
Peter Grünberg Institut (PGI)
Quanten-Theorie der Materialien (PGI-1)

# Light-matter interaction from ab-initio Keldysh formalism

Maximilian Daniel Merte

Schriften des Forschungszentrums Jülich
Reihe Information / Information Band / Volume 126

ISSN 1866-1777 ISBN 978-3-95806-906-0

Bibliografische Information der Deutschen Nationalbibliothek.
Die Deutsche Nationalbibliothek verzeichnet diese Publikation in der
Deutschen Nationalbibliografie; detaillierte Bibliografische Daten
sind im Internet über http://dnb.d-nb.de abrufbar.

| | |
|---|---|
| Herausgeber und Vertrieb: | Forschungszentrum Jülich GmbH<br>Zentralbibliothek, Verlag<br>52425 Jülich<br>Tel.: +49 2461 61-5368<br>Fax: +49 2461 61-6103<br>zb-publikation@fz-juelich.de<br>www.fz-juelich.de/zb |
| Umschlaggestaltung: | Grafische Medien, Forschungszentrum Jülich GmbH |
| Druck: | Grafische Medien, Forschungszentrum Jülich GmbH |
| Copyright: | Forschungszentrum Jülich 2026 |

Schriften des Forschungszentrums Jülich
Reihe Information / Information, Band / Volume 126

D 82 (Diss. RWTH Aachen University, 2025)

ISSN 1866-1777
ISBN 978-3-95806-906-0

Vollständig frei verfügbar über das Publikationsportal des Forschungszentrums Jülich (JuSER)
unter www.fz-juelich.de/zb/openaccess.

# Light-matter interaction from ab-initio Keldysh formalism

Von der Fakultät für Mathematik und Naturwissenschaften der RWTH Aachen University zur Erlangung des akademischen Grades eines Doktors der Naturwissenschaften genehmigte Dissertation

von

Maximilian Daniel Merte,
M.Sc. Simulation Sciences

aus
Marburg

Berichter: Univ.-Prof. Dr. rer. nat. Stefan Blügel
Jun.-Prof. Dr. Yuriy Mokrousov
Univ.-Prof. Dr. rer. nat. Dante M. Kennes

Tag der mündlichen Prüfung: 25.11.2025

# *Acknowledgements*

I am very thankful for the opportunity given by Prof. Dr. Yuriy Mokrousov and Prof. Dr. Stefan Blügel to work in the Peter Grünberg Institute and their guidance. I thank Dr. Frank Freimuth for various discussions, the in-depth insights he shared and his helping hand with many practical matters. Furthermore I would like to express my appreciation towards all colleagues at the Peter Grünberg Institute who created an environment of genuine enthusiasm for learning. In particular, Dr. Dongwook Go exemplified this spirit with his dedication to exploring new ideas and sharing insights. I thank Fabian Lux for many discussion on and off topic, inside and outside the office.

Finally I thank my parents for their continuous support, which enabled me to fabricate this thesis.

# *Abstract*

The ever-increasing demand for data and computing power ignited by data driven technology raises the desire for a new generation of faster and more efficient computing devices. Furthermore, the sheer amount of data generated requires storage devices to pack information as dense as possible. Emerging data processing techniques, such as machine learning, call for a new generation of computing devices. The field of ultrafast spintronics has emerged as a viable candidate to address these challenges. Within spintronics the electric charge is superseded by the electrons spin degree of freedom as information carrier. Antiferromagnetic materials are of special interest in this context, due to their fast internal dynamics in the THz regime and their robustness with respect to stray fields, which allows for dense packaging of individual memory domains. To overcome conventional electronics and leverage the potential THz speeds of antiferromagnetic spintronic devices an all optical control of these devices is paramount. One key challenge is to identify viable material candidates and this thesis aims to support this task by providing the computational tools to calculate second order responses to femtosecond laser pulses. In this thesis a highly parallelized Wannier interpolation code was developed capable of calculating second order response tensors by means of the Keldysh non-equilibrium formalism. With the developed method second order effects such as photocurrents of charge and spin as well as the inverse Faraday effect can be calculated. Furthermore, the orbital equivalents of the aforementioned spin effects can be calculated. The developed methods were applied to study second order laser responses in various magnetic materials and the analysis demonstrated that charge photocurrents act as a good proxy to measure the orientation of the magnetic moments. The emergence of chiral photocurrents in canted antiferromagnets suggests that photocurrents can also be used to track the switching process of the Néel vector. A large staggered inverse Faraday effect was found on the Mn sublattices of $Mn_2Au$ suggesting that efficient direct switching of the order parameter is possible in this material. Further, a non-linear optical equivalent to the spin Hall effect, dubbed the *photospin Hall effect*, was discovered in collinear antiferromagnet $Mn_2Au$. Finally, canted $Mn_2Au$ was found to host gigantic spin photocurrents, making the material a good candidate for practical spintronic device applications.

# *Zusammenfassung*

Die ständig steigende Nachfrage nach Daten und Rechenleistung, vorangetrieben durch datengesteuerte Technologie, weckt den Wunsch nach einer neuen Generation schnellerer und effizienterer Computer. Außerdem erfordert die schiere Menge der erzeugten Daten, dass zukünftige Speichergeräte die Informationen so dicht wie möglich packen. Aufkommende Datenverarbeitungstechniken wie das maschinelle Lernen erfordern eine neue Generation von Rechengeräten. Der Bereich der ultraschnellen Spintronik hat sich als ein geeigneter Kandidat für die Bewältigung dieser Herausforderungen erwiesen. In der Spintronik wird die elektrische Ladung der Elektronen durch deren Spinfreiheitsgrad als Informationsträger abgelöst. Eine zentrale Herausforderung besteht darin, geeignete Materialkandidaten zu identifizieren. Die vorliegende Arbeit soll diese Aufgabe unterstützen, indem sie ein Programm zur Berechnung von Effekten zweiter Ordnung in Reaktion auf einen Femtosekunden-Laserpuls bereitstellt. Dafür wurde ein hochparallelisiertes Wannier-Interpolationsprogramm entwickelt, das in der Lage ist, Laser-Reaktionstensoren zweiter Ordnung mit Hilfe des Keldysh-Formalismus zu berechnen. Mit der entwickelten Methode können bekannte Effekte wie spin-polarisierte oder rein elektrische Photoströme sowie der inverse Faraday-Effekt berechnet werden. Desweiteren können orbitale Äquivalente der oben genannten Spineffekte berechnet werden. Die entwickelten Methoden wurden angewandt, um Photoeffekte zweiter Ordnung in verschiedenen magnetischen Materialien zu untersuchen. Die Analyse zeigte, dass Ladungsphotoströme ein guter Proxy für die Messung der Ausrichtung der magnetischen Momente sind. Das Auftreten chiraler Photoströme in Antiferromagneten mit verkippten magnetischen Momenten deutet darauf hin, dass Photoströme auch verwendet werden können, um den Schaltprozess des Néel -Vektors zu verfolgen. Ein großer entgegengesetzter inverser Faraday-Effekt wurde in den Mn-Untergittern des kollinearen Antiferromagneten $Mn_2Au$ festgestellt, was darauf hindeutet, dass in diesem Material eine effiziente direkte Schaltung des Ordnungsparameters möglich ist. Darüber hinaus wurde im kollinearen Antiferromagneten $Mn_2Au$ ein nichtlineares optisches Äquivalent zum Spin-Hall-Effekt, benannt als Photospin Hall Effekt (englisch: *photospin Hall effect*), entdeckt. Abschließend wurde festgestellt, dass nicht kollineares $Mn_2Au$ gigantische Spin-Photoströme beherbergt und daher ein guter Kandidat für praktische spintronische Anwendungen ist.

# *Quotes*

"Science itself, no matter whether it is the search for truth or merely the need to gain control over the external world, to alleviate suffering, or to prolong life, is ultimately a matter of feeling, or rather, of desire-the desire to know or the desire to realize."

— Louis de Broglie, Nouvelles perspectives en microphysique

"Moral, das ist, wenn man moralisch ist"

- Georg Büchner, Woyzeck

"Can you please help me find my friend
I'll give you anything you need multiplied by ten
I heard he moved to a place where the time don't end
You don't need money, all you got is time to spend"

- Mac Miller

# *Eidesstattliche Erklärung*

**Eidesstattliche Erklärung**

Ich, Maximilian Daniel Merte, erkläre hiermit, dass diese Dissertation und die darin dargelegten Inhalte die eigenen sind und selbstständig, als Ergebnis der eigenen originären Forschung, generiert wurden. Hiermit erkläre ich an Eides statt

1. Diese Arbeit wurde vollständig oder größtenteils in der Phase als Doktorand dieser Fakultät und Universität angefertigt;
2. Sofern irgendein Bestandteil dieser Dissertation zuvor für einen akademischen Abschluss oder eine andere Qualifikation an dieser oder einer anderen Institution verwendet wurde, wurde dies klar angezeigt;
3. Wenn immer andere eigene- oder Veröffentlichungen Dritter herangezogen wurden, wurden diese klar benannt;
4. Wenn aus anderen eigenen- oder Veröffentlichungen Dritter zitiert wurde, wurde stets die Quelle hierfür angegeben. Diese Dissertation ist vollständig meine eigene Arbeit, mit der Ausnahme solcher Zitate;
5. Alle wesentlichen Quellen von Unterstützung wurden benannt;
6. Wenn immer ein Teil dieser Dissertation auf der Zusammenarbeit mit anderen basiert, wurde von mir klar gekennzeichnet, was von anderen und was von mir selbst erarbeitet wurde;
7. Teile dieser Arbeit wurden zuvor veröffentlicht, und zwar in Ref. [1], Ref. [2] sowie Ref. [3] und Ref. [4].

Ort, Datum

Unterschrift

# Contents

# Part I

# Motivation

# Chapter 1

# *Introduction to Photospintronics*

## 1.1 Moore's Law is dying

Since the late 1980s the amount of internet traffic to and from data centers has increased at an exponential rate, by 2030 data centers and networks are predicted to take up 20% of the worlds electricity demands[5]. A trend which has been further accelerated by the Corona pandemic[6]. At the same time, the advancement of computing speed and efficiency of microprocessors has seen a significant slowdown in recent years, silicon based CPUs have hit a wall in terms of frequency[7] and although transistor density is still increasing at an exponential rate, and, thus, upholding Gordon Moore's law in its original formulation[8], progress in single threaded performance has slowed down since the late 2000's[9]. In recent years even the strategy to increase logical cores to further drive progress has hit a limit due to Amdahl's law[9–11]. These trends can also be seen in Figure 1.1, motivating some to claim that Moore's law is coming to an end or at least has to be reformulated[12] or shifted towards GPU based computing[13,14]. Another problem of modern computing devices is the so-called "Memory gap", which refers to the fact that the information processing of CPUs is often much faster than the speed at which new data can be loaded from memory, which leads to a stalling of CPU cores[15].

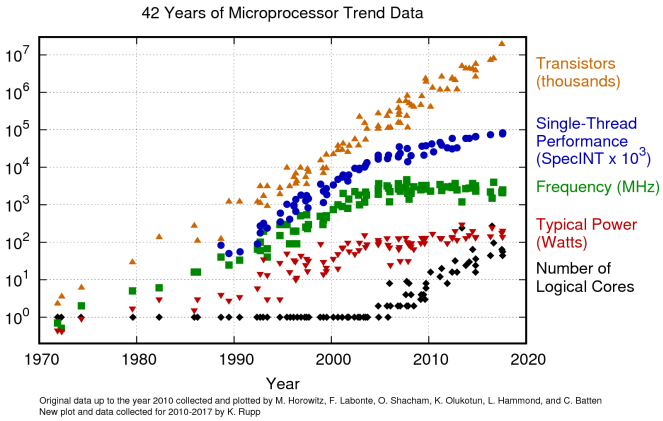


**FIGURE 1.1.** Evolution of microprocessors adapted from Ref. [9]. ©ACM Computing Surveys.

Indeed, it was predicted that so-called domain specific architectures, where hardware is specialized to perform only a narrow set of tasks, will be required in the next years to further drive advancements in computing [16]. Another current development is an increasing popularity in crowd sourced hardware development, highlighting the need for new innovations in the field [17]. Although increased efficiency alone might not solve the energy demand problem [18–20], these trends call for a new generation of computing hardware which operates at higher speeds while being more efficient at the same time.

According to Lloyd the theoretical maximum of operations (op) per second of an ultimate "black hole" laptop of mass $m = 1$ kg is given as [21]

$$R_{\text{peak}}(\text{ultimate laptop}) = 5.4258 \cdot 10^{50} \frac{\text{op}}{s} \approx 5 \times 10^{50} \frac{\text{Flop}}{s}. \tag{1.1}$$

Eq. (1.1) can be seen as the ultimate physical limit of computation. In 2022 the first supercomputer achieving exascale performance for floating point operations (Flop) was released [22], with a peak of

$$R_{\text{peak}}(2022\ \text{supercomputer}) \approx 1.0 \times 10^{18} \frac{\text{Flop}}{s}. \tag{1.2}$$

Arguably the fastest contemporary silicon-based supercomputers are still $\sim 10^{32}$ orders of magnitude slower than the most fundamental theoretical limit on computation, again highlighting the potential a technology change might unlock. One candidate to replace electronic based computing devices is the field of spintronics [23]. Here the spin degree of freedom is leveraged as information carrier, either alongside the electronic degree of freedom, or in some scenarios replacing it completely.

## 1.2 Ultrafast spintronics & photospintronics

The discovery of ultrafast demagnetization induced by femtosecond laser pulses [24] can be seen as the starting point of the field of ultrafast spintronics. The goal of spintronics research in general is to replace the electric charge with the spin degree of freedom as information carrier to overcome the speed limitations of current electronic devices, boost their efficiency and increase the packing density of individual memory units. To unlock the full potential of novel spintronic devices they would have to be operated at THz (or faster) speed. Operation at such speeds is often referred to as ultrafast spintronics and can only be achieved by optical control [25,26]. Thus, the optical manipulation and readout of spin configuration is a fundamental challenge in spintronics and remains subject of ongoing research [27]. In this work a highly parallelized code was developed which can calculate various responses induced by femtosecond laser pulses in a unified framework by means of the Keldysh nonequilibrium formalism [28,29].

In recent years antiferromagnets have picked up great attention in the context of spintronics, due to their unique properties, such as THz dynamics of the Néel vector, which acts as an order parameter in AFM-spintronics [30] and close packaging densities, due to their robustness with respect to stray fields [31,32]. Indeed, several antiferromagnetic applications have been proposed and AFM based random access memory chips have been demonstrated already for von-Neumann architectures [33,34]. Further AFMs have been proposed as a good platform for beyond von-Neumann Logic-in memory computing devices, which are of special interest in the realm of machine learning [35,36]. The urge for such devices is highlighted by the recent proposed framework to run Logic-in memory hardware with the open RISC-V instruction set architecture [37]. To utilize AFMs for spintronic devices the switching of the Néel vector has to be achieved, however, due to the opposing magnetization on the antitferromagnetic sublattices and the corresponding robustness with respect to external fields, switching of AFMs has been challenging but can be overcome for example by electrically induced spin transfer torques [33,38,39]. To leverage the advantages of THz switching, optical control of AFMs is crucial. The optical switching of the AFM order parameter and its optical readout are often referred to as all optical switching and remain a hot topic of research in the field of spintronics [40–43]. The ultrafast switching of ferromagnetic devices via optical spin transfer torques created by femtosecond laser pulses was proposed [28] and reported recently [44]. These optically induced torques in ferromagnets are expected to be closely related to the inverse Faraday effect [45,46]. In the context of antiferromagnets the direct switching of the Néel vector via a staggered version of the inverse Faraday effect, which induces

quenching of the magnetization on AFM sublattices was proposed theoretically[43]. This concept will be further explored in this work and scenarios will be presented were a large staggered nonequilibrium spin density, as shown in Figure 1.2, can be induced in $\mathcal{PT}$-symmetric antiferromagnet $Mn_2Au$. The induced staggered spin density directly quenches the magnetization on the manganese sublattices and is sensitive not only to circularly but also to the more accessible linearly polarized light. For the class of $\mathcal{PT}$-symmetric AFMs staggered spin orbit torques have been suggested as possible driver of switching processes[47].

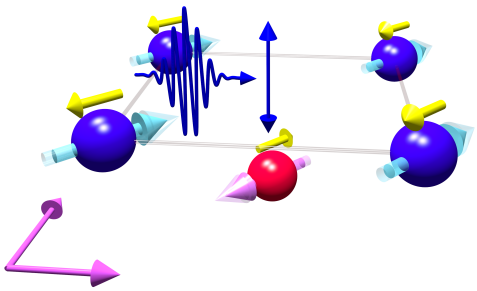

**Figure 1.2.** Staggered nonequilibrium spin density (yellow arrows) on the Mn sublattices (blue and red spheres with arrows indicating the orientation of the magnetization of the sublattice) of collinear antiferromagnet $Mn_2Au$, induced by a THz laser pulse (reprinted from[2], ©2023 CC BY 4.0).

Besides the switching of the order parameter its readout in an ultrafast manner is also crucial for spintronic applications. Photocurrents have emerged as a viable candidate acting as a proxy to read out the state of the order parameter[48–50] and are currently heavily investigated[44,51–54]. In this work it will be demonstrated that magnetic photocurrents can act as proxy to detect the orientation of the magnetization in ferromagnetic and the Néel vector in antiferromagnetic materials alike. Further the notion of *chiral*-flavored photocurrents will be introduced. *Chiral* photocurrents only emerge in case of canted magnetic moments and could thus act as an experimentally easily accessible proxy to track the switching trajectory during torque based switching in antiferromagnetic materials.

Spin polarized currents, or spin currents, play another crucial role in spintronic applications[55], often acting as information carrier. The generation of spin currents can be achieved by the spin Hall effect[56], where a spin polarized current flows perpendicular to the charge current. The effect is caused by spin orbit coupling, which deflects the spin up and spin down components of a charge current in opposing directions. Electrically induced nonlinear spin current generation in noncentrosymmetric materials has been proposed[57]

and was extended to the realm of photoresponses[29]. In this thesis, second order spin photocurrents will be analyzed in detail. It will be demonstrated that charge photocurrents in magnetic materials are often accompanied by spin polarized photocurrents. It will be shown that two-dimensional (2D) van-der-Waals magnet $Fe_3GeTe_2$ host sizable spin photocurrents. Magnetic 2D van-der-Waals materials have emerged in recent years[58–61] as rich platform to realize new device concepts. Due to the weak van-der-Waals bond between individual layers, coupling different functional layers becomes relatively easy and can even be achieved for larger lattice mismatches between individual layers. $Fe_3GeTe_2$ has proven as prominent candidate material for such 2D magnets. While in $Fe_3GeTe_2$ the spin photocurrents will be shown to flow along the direction of the charge photocurrents, in the antiferromagnet $Mn_2Au$ spin photocurrents flowing perpendicular to the charge photocurrents were found, thus obeying the geometry of spin Hall effects. Based on the findings the concept of a *photospin Hall effect* will be introduced and characterized by an introduced *photospin Hall angle*. Figure 8.18 shows the geometry of the photospin Hall effect, by measuring the charge photocurrent flowing perpendicular to the spin photocurrent in conjunction with photospin Hall angle the amplitude of the induced spin photocurrent can be determined.

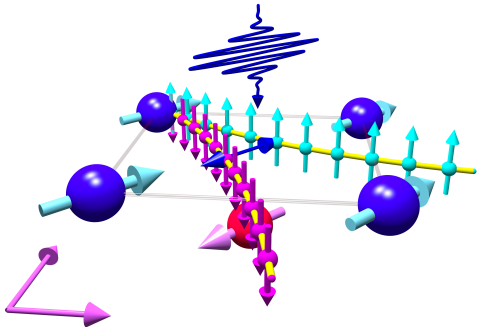

**Figure 1.3.** Sketch of the photospin Hall effect in $Mn_2Au$ (reprinted from[2], ©2023 CC BY 4.0). A linearly polarized femtosecond laser pulse induces a charge photocurrent flowing perpendicular to the Néel vector. At the same time a fully spin polarized photocurrent flows parallel to the Néel vector.

By considering spin photocurrents in the canted scenario, the notion of *chiral* spin photocurrents will be introduced. These where found to be of large amplitude in $Mn_2Au$, making the material a good candidate as a strong spin current source for spintronic applications, which can operate at THz speeds.

## 1.3 Structure of thesis

The thesis is structured in six parts, each consisting of one or more chapters. The first part contains the current motivational chapter. The second part of the thesis describes the theory of photogalvanic effects in two chapters. Chapter 2 gives an overview over various existing photogalvanic effects in a phenomenological manner. In Chapter 3 expressions for such photogalvanic effects, for example photocurrents of spin and charge, are derived by means of the Keldysh nonequilibrium formalism. The third part of the thesis is concerned with the applied methods used to obtain photogalvanic responses from first principles. Chapter 4 describes fundamentals of density functional theory, with an emphasis on the FLAPW method and the Fleur code. In Chapter 5 Maximally Localized Wannier functions are introduced and the Wannier interpolation technique is described. Chapter 6 describes in detail the Wannier interpolation code developed to calculate the photoresponse tensors derived with the Keldysh formalism. Development of this code was the central part of this work and thus the code is described in great detail with further information provided in the last part containing Chapter VI. In the fourth part results obtained with the developed methods are presented. Photoresponses in various magnetic materials which are prominent candidates in the context of ultrafast spintronics were considered. Chapter 7 discusses photocurrents in 2D van-der-Waals ferromagnet $Fe_3GeTe_2$. In Chapter 8 an in depth analysis of photoeffects in collinear antiferromagnetic $Mn_2Au$ is performed. Further Chapter 8 introduces the *photospin Hall effect*. In the final results Chapter 9, the effect of canting the magnetic moments of antiferromagnetic materials in considered, which leads to *chiral* magneto-optical effects. Results presented have, in part, been published in several publications. This work is centered around results published by the author in Ref. [1,2], which are embedded into a broader context supported by previously unpublished results in this work. Optical conductivity calculations performed by the author and published in Ref. [3,4], where the author of this work acted as a coauthor, are reproduced in this work to motivate higher order effects. Whenever results in this work were adopted from previous publications it is indicated at the beginning of the according chapter and the role of the author in the publication is clarified. In the fifth part an outlook towards future research is presented in Chapter 10. The sixth and final part can be considered as appendix. Here details on how to run and compile the developed Wannier interpolation code are provided.

Part II

# Theory

# Chapter 2

## *Photogalvanic effects*

Photocurrents can be understood as the result of nonlinear optical effects which rectify an oscillating electric field, *i.e.* the alternating current (AC) field of a laser, into a direct current (DC) in materials with reduced symmetry[62]. Phenomenologically the AC field induces an oscillating current in the material, in case of a perfectly inversion-symmetric crystal the oscillating current will average to zero. However, if the crystal symmetry is lowered and the laser induced current oscillates along the direction of symmetry lowering, the average of the induced current might not be zero anymore, which effectively generates a net DC current known as the photocurrent. In this chapter fundamentals and modern developments of the theoretical description of photocurrents are outlined. In the next chapter a detailed derivation of photoresponse tensors with the nonequilibrium Keldysh formalism will be provided. Photocurrents, also referred to as the photogalvanic effect, have already been heavily studied theoretically in noncentrosymmetric semiconductors in the 80s[63,64] and realized as a key ingredient in the design of efficient solar cells[65–68]. More recently photocurrents have attracted increased scientific interest again as a powerful tool in the context of optical characterization of materials[53]. Especially the detection of the order parameter is of great importance in the context of ultrafast spintronics. Various theoretical efforts have been made recently to extend the existing formalism and allow for an accurate computational calculation of photocurrents[50,69–72].

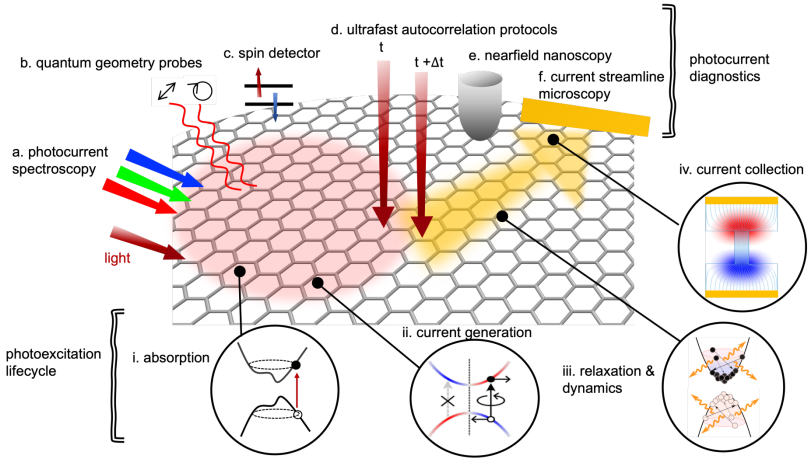


**FIGURE 2.1.** Photocurrent as a multi-physics diagnostic of quantum materials (adapted from Qiong *et al.* Ref. [53], ©2023 Springer Nature Limited).

Purely magnetic photocurrents were predicted to be present in collinear antiferromagnets[50], which directly depend on the orientation of the Néel vector and could thus be used as experimental proxy to determine the orientation of the Néel vector[50,73]. Besides that in recent years photocurrents were proposed as probes for the dipole moments of the derivatives of the quantum geometric tensor[74,75], namely the dipole moment of the quantum metric and the Berry curvature dipole[76–79], highlighting the rich field of physics accessible by photocurrents[53]. Figure 2.1 was adopted from a publication by Qiong *et al.* published in Ref. [53] to illustrate the various quantum effects which can be probed by means of photocurrents. In this work the current generation, spectroscopy, spin detection and quantum geometry probing via photocurrents listed in Figure 2.1, will be explored in great detail.

## 2.1 THE BULK PHOTOGALVANIC EFFECT

The bulk photogalvanic effect (BPGE) describes a rectified DC-current $J_i$ induced by an AC electric field, often named the photocurrent, which is of second order in the applied field[63,64]

$$J_i^{\mathrm{BPGE}} = \rho_{ijk}(\omega) E_j E_k^* \tag{2.1}$$

where $\rho_{ijk}$ is the rank 3 photogalvanic tensor, or photoconductivity tensor, and $E_i$ are the components of the electric field oscillating at frequency $\omega$. Since the BPGE is of second order in the electric field and field and current switch

sign under a spatial inversion $\mathcal{I}$, the tensor $\rho_{ijk}$ is also required to switch sign under spatial inversion and, thus, only allowed in noncentrosymmetric materials[63].

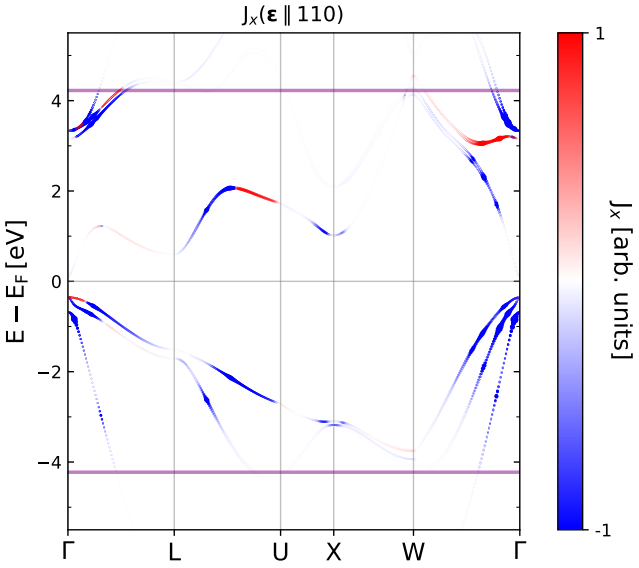


**FIGURE 2.2.** Example of the photogalvanic effect in bulk semiconductor GaAs. The $x$-component of the photocurrent in response to light linearly polarized along the [110]-direction is presented band resolved along a representative high symmetry path in the first Brillouin zone. The color coding indicates the sign of the photocurrent and the thickness of the bands the amplitude of the transition rate at a given $k$-point. For a given laser frequency $\hbar\omega$, here $\hbar\omega = 4.2$ eV, transitions between bands around the selected Fermi energy within the energy window $E_F \pm \hbar\omega$ will be induced by the laser. The energy window is indicated by the horizontal purple lines. Note that some bands outside the given Laser frequency appear to be activated, however this is just a shortcoming of the visualization.

### 2.1.1 *Linear and circular photogalvanic effect*

Photocurrents are observable quantities and as such must be real valued. The conductivity tensor in Eq. (2.1) must thus obey $\rho_{ijk} = \rho^*_{ikj}$, namely the real part of the tensor is even under reversal of the last two indices, while the imaginary part of the tensor is odd. Therefore, the response tensor can be split into an even, or symmetric, and an odd, antisymmetric, part. For Eq. (2.1) it follows[63]

$$J_i^{\mathrm{BPGE}} = \rho^s_{ijk}(\omega) E_j E^*_k + i\rho^a_{il}(\omega)[\mathbf{E}\mathbf{E}^*]_l, \tag{2.2}$$

where the symmetric part $\rho^s_{ijk} = \mathrm{Re}\,\rho_{ijk}$ is the real part of the conductivity tensor and $\rho^a_{ijk} = \mathrm{Im}\,\rho_{ijk}$ the antisymmetric part given by the imaginary part.

The antisymmetric part is only present in case of circularly, or elliptically, polarized fields and dubbed the circular photogalvanic effect (CPGE). The symmetric contribution can be present for arbitrary polarization but is maximized in case of linearly polarized light and named the linear photogalvanic effect (LPGE)[63]. LPGE effects and CPGE effects are allowed by symmetry in different material classes respectively, with LPGE present in materials from the piezoelectric class and CPGE effects allowed in gytropic materials[63]. A band resolved example of the LPGE effect in semiconductor GaAs is given in Figure 2.2. In this thesis various magnetic materials will be studied in which both effects coexist.

### 2.1.2 *Magnetic photogalvanic effect*

If an external magnetic field is applied to a noncentrosymmetric crystal a circular magnetophotocurrent sensitive to the applied magnetic field might be induced[80]. This raises the question what effect the magnetization in magnetic materials lacking inversion symmetry have on the photocurrents, and if it is possible to identify these magnetic contributions. In general third rank tensors describing dissipative processes, such as the photogalvanic tensor in Eq. (2.1), can be split into a magnetization dependent and a magnetization independent contribution[81]

$$\rho_{ijk} = \rho_{ijk}^{(\mathrm{NM})} + \rho_{ijk}^{(\mathrm{M})} \tag{2.3}$$

where $\rho_{ijk}^{(\mathrm{NM})}$ is the nonmagnetic contribution independent of the magnetic moments and $\rho_{ijk}^{(\mathrm{M})}$ is the magnetic contribution which switches sign under magnetization reversal. The two contributions behave as even and odd respectively when a time-reversal operation $\mathcal{T}$ (flipping the magnetization) is applied[81]

$$\begin{aligned} \mathcal{T}\rho_{ijk}^{(\mathrm{NM})} &= \rho_{ijk}^{(\mathrm{NM})} \\ \mathcal{T}\rho_{ijk}^{(\mathrm{M})} &= -\rho_{ijk}^{(\mathrm{M})}. \end{aligned} \tag{2.4}$$

In the context of the photogalvanic effect this suggests that besides the LPGE and CPGE, which are already present in nonmagnetic noncentrosymmetric semiconductors[65], magnetic versions of these two effects are present in noncentrosymmetric magnetic materials which will be dubbed the magnetic linear/circular photogalvanic effect (MLPGE/MCPGE). These magnetic photogalvanic effects (MPGE) are characterized by their behavior under a time reversal operation. The MLPGE is expected to be odd with respect to a time-reversal operation since the response tensor $\rho_{ijk}^{(\mathrm{M})}$ is flipped by the time

reversal operation, while the linear field polarization (see Eq. (2.4)) is even under time reversal. In case of the MCPGE the behavior is reversed, since the sense of rotation of the electric field is flipped by the time-reversal operation as well as the response tensor. Thus, effectively, the resulting current undergoes two sign flips under a single time reversal operation such that effectively no sign change occurs.

In the context of DFT calculations of magnetic materials, a time reversal operation could be modeled by performing a second DFT calculation with reversed magnetization, however this approach is rather cumbersome and time-consuming. An alternative approach to quickly check how a time reversal operation effects the photoconductivity tensor is to reverse the sign of the broadening parameter applied in the calculation of the response tensor.

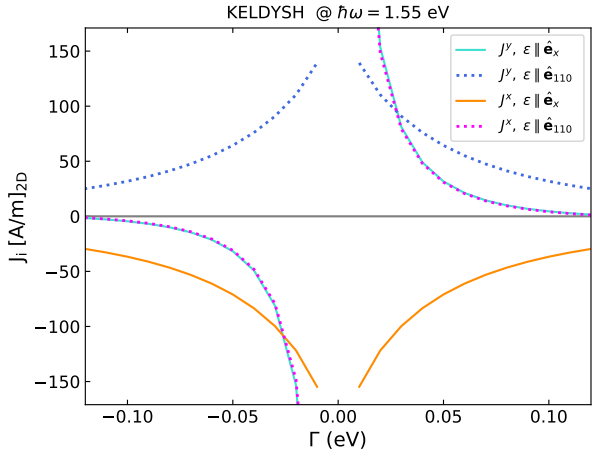


**FIGURE 2.3.** Photocurrent in 2D van-der-Waals magnet $Fe_3GeTe_2$. Odd and even behavior with respect to sign change of the broadening parameter Γ indicates magnetic and non-magnetic photocurrents. A detailed discussion of photocurrents in $Fe_3GeTe_2$ can be found in Chapter 7.

The photoconductivity tensor in Eq. (2.3) describes the dissipation of energy pumped into the system by the laser. The dissipation of energy is often modeled via the constant lifetime approximation, given by the inverse of the broadening parameter Γ, acting on the electronic states. Indeed, this approximation is used in the Keldysh formalism used in this thesis to describe photocurrents as will be discussed in the next Chapter 3. To mimic a time-reversal operation, the sign of the broadening parameter is reversed

$$\Gamma \longrightarrow -\Gamma, \tag{2.5}$$

and the system now dissipates "negative energy", that is, it actually gains

energy. Thus, effectively time is reversed. With Eq. (2.4) in mind, studying the behavior of the photoconductivity w.r.t. a sign change of the broadening parameter, allows one to identify the magnetic and nonmagnetic components of Eq. (2.3). As an example of the different behavior of magnetic and nonmagnetic photocurrents Figure 2.3 shows the components of the photocurrent in 2D van-der-Waals ferromagnet $Fe_3GeTe_2$ for positive and negative broadening values in response to linearly polarized light.

Since $Fe_3GeTe_2$ has no inversion symmetry already in its non-magnetic state, magnetic and non-magnetic photocurrents can be present in the system. Indeed, Figure 2.3 shows even and odd LPGE responses confirming the presence of both magnetic and non-magnetic photocurrents in the system. A detailed discussion of photocurrents in $Fe_3GeTe_2$ can be found in Chapter 7.

### 2.1.3 *Photocurrents as probes of quantum metric*

Historically photocurrents were classified by two fundamental mechanism, the shift and the injection photocurrents[65,82]. The shift photocurrent originates from different expectation values of the position operator of the initial and excited state in real space, *i.e.* electrons are *shifted* in real space by the laser. The second mechanism is the so-called injection current, which originates from a change of the carrier group velocity between initial and excited state. Here the laser directly *injects* velocity into the electronic system. In a more recent work these two effects were identified as insulating contributions[78] with additional metallic contributions present for example in Weyl semimetalls. Characterization of these metallic contributions is ongoing[70,71,77–79,83,84]. Besides this, theoretical efforts are being made to unify the description of photocurrents solely in terms of topological quantities acting as order parameters. Three fundamental mechanisms are suggested: A Drude term associated with the change of the Fermi distribution by the laser perturbation and two geometric terms: a Berry curvature dipole (BCD) term and a second term probing the quantum metric dipole[75,85,86]. Each term has a distinct lifetime broadening $\Gamma$ scaling: the Drude term scales as $\sim 1/\Gamma^2$, the Berry curvature dipole term as $\sim 1/\Gamma$, while the quantum metric dipole term is constant with respect to $\Gamma$[85]. As suggested by Kaplan *et al.*[75] the two geometric terms are both given by derivatives of the quantum geometric tensor[74], which thus could be used as a unified order parameter for geometric photoresponses. Depending on the crystal symmetry only certain terms may be allowed, especially in $\mathcal{PT}$-symmetric antiferromagnets, such as the bulk AFM $Mn_2Au$ discussed in Chapter 8, only the BCD contribution survives[85].

### 2.1.4 *Spin photogalvanic effect and inverse Faraday effect*

Besides the conventional photogalvanic effect in which a charge current is induced, various spin-related photogalvanic effects have been discovered[87]. In certain materials the generation of pure spin photocurrents, *i.e.* currents which are fully spin polarized, have been suggested[87–91]. For example such nonlinear spin currents have been proposed in noncentrosymmetric spin-orbit coupled systems[57]. In the inverse Faraday effect (IFE)[92] a second order electric field induces a nonequilibrium spin density[41,93].

In the next chapter the Keldysh nonequilibrium formalism is introduced and applied to derive expression for the second order photoconductivity $\rho_{ijk}(\omega)$ in Eq. (2.1), spin photocurrents and IFE within a unified framework.

# Chapter 3

# *Nonequilibrium Keldysh formalism*

In this chapter the nonequilibrium Keldysh formalism is used to derive response tensors which are of second order in the applied oscillating laser field, to describe the rectified DC photocurrents discussed in the previous Chapter 2. The Keldysh formalism was first developed by Leonid V Keldysh [94] and in a similar time frame by Kadanoff and Baym [95]. Compared to the more widely adopted Kubo formalism which assumes a ground-state Fermi distribution and hence is best suited to treat weak perturbations, the Keldysh formalism is more suited to describe systems "far away" from their equilibrium state since it assumes a nonequilibrium electron distribution. In the first section of the chapter the Keldysh formalism is motivated by discussing various pictures to describe time-dependent quantum mechanical systems. The second section shows a detailed derivation of second order response tensors as first derived by Freimuth *et al.* in Ref. [28,29]. Towards the end of the chapter various operators are plugged into the formalism to yield expression for the photocurrent, the spin polarized photocurrent and the laser induced nonequilibrium spin density.

## 3.1 Time-dependent systems

This section provides a quantum mechanical treatment of systems described by a time-independent Hamiltonian $H_0$ perturbed by a time-dependent Hamiltonian $H'(t)$ added at some point in time $t_0$ such that the overall Hamiltonian describing the system $\mathscr{H}(t)$ is given by

$$\mathscr{H}(t) = H_0 + H'(t), \tag{3.1}$$

where $H'(t) = 0$ for $t < t_0$. In quantum mechanics time can be introduced as a generic variable and one is left with several choices, categorized into "pictures", how to add the time variable. Three different approaches or pictures are popular: 1) states are time-dependent and operators time independent, this is known as the Schrödinger picture. 2) In the Heisenberg picture the states are time-independent, then the operators have to carry the time evolution of the

system. 3) Make everything, operators and states, time-dependent, known as Dirac or interaction picture.

### 3.1.1 Schrödinger picture

In the Schrödinger picture the system is described by the time-dependent Schrödinger equation

$$i\hbar \left|\dot{\psi}_{\mathcal{S}}(t)\right\rangle = \mathscr{H}(t) \left|\psi_{\mathcal{S}}(t)\right\rangle, \tag{3.2}$$

where the states are time-dependent, while the operators are time independent.

In case of mixed states, the density matrix $\rho_{\mathcal{S}}$ is constructed by

$$\rho_{\mathcal{S}}(t) = \sum_m p_m \left|\psi_m(t)\right\rangle \left\langle\psi_m(t)\right|, \tag{3.3}$$

where $p_m$ is the weight, or expectation value, of basis state $|\psi_m\rangle$. The time evolution of the density matrix is given by

$$\dot{\rho}_{\mathcal{S}}(t) = \frac{i}{\hbar}\left[\rho_{\mathcal{S}}(t), \mathscr{H}(t)\right]. \tag{3.4}$$

In case of a time independent Hamiltonian $\mathscr{H}(t) = H_0$ the expression simplifies to

$$\rho(H) = \left(\mathrm{Tr}\, e^{-\beta H_0}\right)^{-1} e^{-\beta H_0}, \tag{3.5}$$

where $\beta = T^{-1}$ is the inverse of the temperature.

The expectation value of a generic operator $\hat{O}_{\mathcal{S}}$ is given by tracing the product of the operator with the density matrix, in the Schrödinger picture it follows

$$\langle \hat{O}(t)\rangle_{\mathcal{S}} = \mathrm{Tr}\left[\rho_{\mathcal{S}}(t)\hat{O}_{\mathcal{S}}\right], \tag{3.6}$$

however, the density matrix describing the nonequilibrium system $\rho_{\mathcal{S}}(t)$ is often unknown and in practice hard to calculate. To make predictions about the nonequilibrium system without knowledge of the full nonequilibrium density matrix, propagators are introduced. Propagators, also known as Greens functions, are two point correlators between times $t_0$ and $t$. To propagate a state from some point in time $t_0$ to another time $t$ one can implicitly define a Greens function $G_{\mathcal{S}}(t, t_0)$, such that the states of the system at some point $t$ are given by the product of the propagator with the state at point $t_0$

$$\left|\psi_{\mathcal{S}}(t)\right\rangle = G_{\mathcal{S}}(t, t_0)\left|\psi_{\mathcal{S}}(t_0)\right\rangle. \tag{3.7}$$

Since the Greens function connects systems and different times it should fulfill the following properties

$$\begin{aligned} G^{*}_{\mathcal{S}}\left(t, t_0\right) &= G^{-1}_{\mathcal{S}}\left(t, t_0\right) \\ G_{\mathcal{S}}\left(t_0, t_0\right) &= \mathbb{I} \\ G_{\mathcal{S}}\left(t, t_0\right) &= G_{\mathcal{S}}\left(t, t'\right) G_{\mathcal{S}}\left(t', t_0\right). \end{aligned} \tag{3.8}$$

In case of a fully time-independent Hamiltonian $H'(t) = 0,\ \forall t \in \mathbb{R}$ the time evolution is given by the transformation

$$|\psi_{\mathcal{S}}(t)\rangle = G_{\mathcal{S}}\left(t, t_0\right)|\psi_{\mathcal{S}}\left(t_0\right)\rangle = e^{iH_0(t-t_0)/\hbar}|\psi_{\mathcal{S}}\left(t_0\right)\rangle. \tag{3.9}$$

With the time evolution given in Eq. (3.9), the Schrödinger picture is well suited to describe the evolution of time-independent systems. However, for time-dependent systems it is more convenient to work in the Heisenberg or in the interaction picture discussed below.

### 3.1.2 Heisenberg picture

In the Heisenberg picture the states are time-independent, instead the operators change over time. The expectation value of an operator $O_{\mathscr{H}}$ in the Heisenberg picture for the Hamiltonian given by Eq. (3.1) at some point $t > t_0$ is then given by time evolution of a time-independent operator in the Schrödinger picture

$$O_{\mathscr{H}}(t) = e^{i\mathscr{H}t/\hbar}\hat{O}_{\mathcal{S}}e^{-i\mathscr{H}t/\hbar}, \tag{3.10}$$

and the density matrix of the unperturbed system $\rho(H_0)$

$$\langle O_{\mathscr{H}}(t)\rangle = \mathrm{Tr}[\rho(H_0)O_{\mathscr{H}}(t)]. \tag{3.11}$$

The basic idea is then to propagate the system along a contour $c$ on the real time axis from the unperturbed point $t_0$ to a point far in the future $t_1$, at which point one "turns around" and propagates the system through some point $t_1$ back to the starting point $t_0$, as shown in Figure 3.1. This is known as the closed time path contour, first proposed by Schwinger[96].

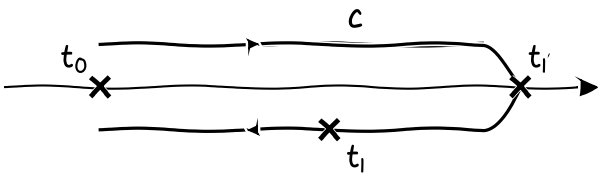


**Figure 3.1.** The closed time path contour.

The Greens function along this contour is called the contour-ordered Greens function and is defined as

$$G\left(1,1'\right) = -i\left\langle T_c\left(\psi_{\mathscr{H}}(1)\psi^{\dagger}_{\mathscr{H}}\left(1'\right)\right)\right\rangle, \tag{3.12}$$

where $T_c$ is the time-ordering operator on the contour $c$ and 1 & $1'$ are different points in time. The time ordering depends on where along the contour the propagator acts

$$T_c\left(\psi_{\mathscr{H}}(1)\psi^{\dagger}_{\mathscr{H}}\left(1'\right)\right) \equiv \begin{cases} \psi_{\mathscr{H}}(1)\psi^{\dagger}_{\mathscr{H}}\left(1'\right) & t_1 >_c t_{1'} \\ -\psi^{\dagger}_{\mathscr{H}}\left(1'\right)\psi_{\mathscr{H}}(1) & t_1 <_c t_{1'} \end{cases}. \tag{3.13}$$

With Eq. (3.13) the contour-ordered Greens function in Eq. (3.12) can be split into two components

$$G\left(1,1'\right) = \begin{cases} G^{>}\left(1,1'\right) & t_1 >_c t_{1'} \\ G^{<}\left(1,1'\right) & t_1 <_c t_{1'} \end{cases}. \tag{3.14}$$

where $G^{>}$ is called the lesser and $G^{<}$ the greater Greens function.

### 3.1.3 Dirac picture

In the Heisenberg picture the expectation value of an operator is given by the unperturbed operator propagated with the full, time-dependent, Hamiltonian

$\mathscr{H}(t)$ as given in Eq. (3.10):

$$\langle O_{\mathscr{H}}(t)\rangle = \mathrm{Tr}[\rho(H)O_{\mathscr{H}}(t)]. \tag{3.15}$$

However, Hamiltonians at different times will in general not commute with each other, which prohibits a perturbative expansion of the Greens function. Since the full Greens function is not necessarily known, especially in numerical simulations, it is desirable to expand the Greens function up to a suitable order to describe a given problem. To achieve this in the interaction picture, also known as Dirac picture, both states and operators are time dependent. A generic operator in the interaction picture $O_H(t)$ is related to the operator in the Heisenberg picture $O_{\mathscr{H}}(t)$ by

$$O_{\mathscr{H}}(t) = u^{\dagger}(t,t_0)\, O_H(t) u(t,t_0)\,, \tag{3.16}$$

with $u(t,t_0) = T\exp\left[-i\int_{t_0}^{t} dt' H'_H(t')\right]$. The Greens function in the interaction picture is given by[97]

$$G(1,1') = -i\left\langle T_c\left(S_c^H \psi_H(1)\psi_H^{\dagger}(1')\right)\right\rangle, \tag{3.17}$$

where $S_c^H = \exp\left[-i\int_c d\tau H'(\tau)\right]$ is the contour integration of the perturbation along the closed time contour shown in Figure 3.1. In order to allow for a perturbative expansion of Eq. (3.17) the expression is reformulated in terms of the unperturbed Hamiltonian $H_0$[97]:

$$\begin{aligned} G(1,1') &= -i\frac{\left\langle T_c\left(S_{c^i} S_c \psi_{H_0}(1)\psi_{H_0}^{\dagger}(1')\right)\right\rangle_0}{\left\langle T_c\left(S_{c^i} S_c\right)\right\rangle_0} \\ &\equiv -i\frac{\mathrm{Tr}\left[e^{-\beta H_0} T_c\left(S_{c^i} S_c \psi_{H_0}(1)\psi_{H_0}^{\dagger}(1')\right)\right]}{\mathrm{Tr}\left[e^{-\beta H_0} T_c\left(S_{c^i} S_c\right)\right]}, \end{aligned} \tag{3.18}$$

where $S_c$ is the contour integral of the unperturbed Hamiltonian, transformed to the interaction picture, along the closed time path contour shown in Figure 3.1 and $S_{c^i}$ along the interaction contour shown in Figure 3.2, such that formally

$$\begin{aligned} S_{c^i} &= \exp\left[-i\int_c d\tau H^i_{H_0}(\tau)\right], \\ S_c &= \exp\left[-i\int_{c^i} d\tau H'_{H_0}(\tau)\right]. \end{aligned} \tag{3.19}$$

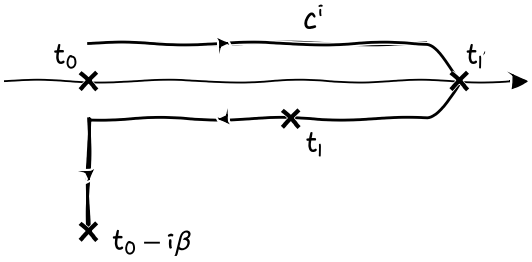


**Figure 3.2.** The interaction contour.

The exponent $e^{-\beta H_0}$ in Eq. (3.18) can then be expanded as a Taylor series allowing one to approximate the time-ordered Greens function up to arbitrary order. Various contours can be picked to perform the integration in Eq. (3.19). In the next section the special contour suggested by Keldysh will be discussed.

## 3.2 Keldysh contour

Compared to the closed time path contour $c_i$ in Figure 3.1, Keldysh let $t_{1'}$ go to infinity, effectively splitting the contour into two detached parts, as shown in Figure 3.3: A forward and a backward branch, depicted as $c_1$ and $c_2$ respectively. Together the forward and backward branch build the Keldysh contour depicted as $c_K$ [94].

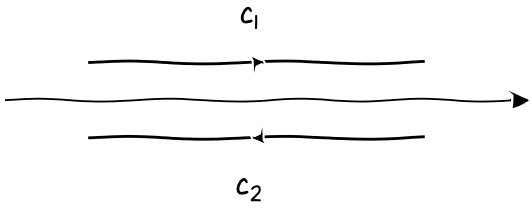


**FIGURE 3.3.** The Keldysh contour consisting of a forward $c_1$ and a backward branch $c_2$.

The contour-order Greens function on the Keldysh contour is mapped into what is known as the $\mathbb{C}^{2\times 2}$ Keldysh space

$$G_{c_K}\left(1,1'\right) \mapsto \widehat{G} \equiv \left\{ \begin{array}{cc} \hat{G}_{11} & \widehat{G}_{12} \\ \widehat{G}_{21} & \hat{G}_{22} \end{array} \right\}, \tag{3.20}$$

where $\hat{G}_{11}$ is the time-ordered Greens function on the forward branch $c_1$ of the Keldysh contour and $\hat{G}_{22}$ the anti-time-ordered Greens function on the backward branch $c_2$, formally given by[97]

$$\begin{aligned} \widehat{G}_{11}\left(1,1'\right) &= -i\left\langle T\left(\psi_{\mathscr{H}}(1)\psi^{\dagger}_{\mathscr{H}}\left(1'\right)\right)\right\rangle, \\ \widehat{G}_{12}\left(1,1'\right) &= G^{<}\left(1,1'\right), \\ \widehat{G}_{21}\left(1,1'\right) &= G^{>}\left(1,1'\right), \\ \widehat{G}_{22}\left(1,1'\right) &= -i\left\langle \widetilde{T}\left(\psi_{\mathscr{H}}(1)\psi^{\dagger}_{\mathscr{H}}\left(1'\right)\right)\right\rangle, \end{aligned} \tag{3.21}$$

where $G^{<}(1,1')$ and $G^{>}(1,1')$ are the lesser and greater Greens function. However, the individual components of Eq. (3.20) are not linearly independent and, thus, Keldysh suggested a rotation in Keldysh space, which results in three linearly independent components

$$\underline{G} = \left\{ \begin{array}{cc} G^{R} & G^{K} \\ 0 & G^{A} \end{array} \right\}, \tag{3.22}$$

where $G^R$ and $G^A$ are the retarded and advanced Greens functions, and $G^K$ is the Keldysh component given by the sum of greater and lesser Greens function[97]

$$\begin{aligned} G^K\left(1,1'\right) &= G^{>}\left(1,1'\right) + G^{<}\left(1,1'\right) \\ &= -i\left\langle\left[\psi_{\mathscr{H}}(1), \psi^{\dagger}_{\mathscr{H}}\left(1'\right)\right]_{\pm}\right\rangle. \end{aligned} \tag{3.23}$$

As shown by Rammer and Smith within the Keldysh formalism the density matrix in case of a periodic perturbation, *i.e.* an electromagnetic field, is given by the lesser Greens function[97]

$$\rho(1) = -iG^{<}(1,1). \tag{3.24}$$

To model responses within the Keldysh formalism one therefore has to approximate the lesser Greens function via perturbative expansion up to desired order.

## 3.3 Rectified second order responses

In this section the Keldysh formalism will be used to derive the expectation value of a generic operator $O$ for a system perturbed by a THz laser pulse. The derivation is closely based on the works by Freimuth published in Ref. [28,29]. To simulate the rectified second order photoresponses as described in the previous Chapter 2, the electric field of the laser is modeled as a coherent wave oscillating with frequency $\omega$ of the kind [29,98]

$$\boldsymbol{E}(t) = -\frac{\partial \boldsymbol{A}(t)}{\partial t} = \mathrm{Re}\left[E_0 \boldsymbol{\varepsilon} e^{-i\omega t}\right], \tag{3.25}$$

where $E_0$ is the field strength, $\boldsymbol{\varepsilon}$ its polarization vector and $\boldsymbol{A}(t)$ is the vector potential. Note that $\boldsymbol{\varepsilon}$ in Eq. (3.25) is complex in case of circularly polarized light. The field is added as a perturbation to the Hamiltonian via the velocity gauge[28]:

$$\delta H(t) = e\boldsymbol{v} \cdot \boldsymbol{A}(t), \tag{3.26}$$

where $\boldsymbol{v}$ is the velocity operator and the vector potential.

### 3.3.1 Expanding the Dyson equation

Within the Keldysh formalism the expectation value of a generic operator can be constructed from Eq. (3.15) and Eq. (3.24). Thus, one is required to find the lesser Greens function of the nonequilibrium system. To obtain $G^{<}$

the laser perturbation Eq. (3.26) is plugged into the Dyson equation on the Keldysh contour[97] and iterated up to the desired order:

$$G\left(1,1'\right) = G_{\mathrm{eq}}\left(1,1'\right) + \int d2 G_{\mathrm{eq}}(1,2)\frac{\delta H(2)}{\hbar} G\left(2,1'\right), \tag{3.27}$$

where 1,1′ and 2 are generic time variables. To model the second order photoresponses the Dyson equation Eq. (3.27) has to be iterated up to terms quadratic in the laser perturbation $\delta H(t)$. Iterating Eq. (3.27) up to second order yields

$$\begin{aligned} G_2(1,1') =& G_{\mathrm{eq}}\left(1,1'\right) \\ &+ \int d2 G_{\mathrm{eq}}(1,2)\frac{\delta H\left(2\right)}{\hbar} G_{\mathrm{eq}}\left(2,1'\right) \\ &+ \int\int d2d3 G_{\mathrm{eq}}(1,2)\frac{\delta H\left(2\right)}{\hbar} G_{\mathrm{eq}}(2,3)\frac{\delta H\left(3\right)}{\hbar} G\left(3,1'\right). \end{aligned} \tag{3.28}$$

Since the photoresponses of interest in this work are of second order in the applied electric field all terms linear or constant in the perturbation $\delta H$ in Eq. (3.28) will be dropped, which simplifies the nonequilibrium Greens function expression to

$$G_2(1,1') = \int\int d2d3 G_{\mathrm{eq}}(1,2)\frac{\delta H\left(2\right)}{\hbar} G_{\mathrm{eq}}(2,3)\frac{\delta H\left(3\right)}{\hbar} G\left(3,1'\right). \tag{3.29}$$

In the next subsection the laser perturbation Eq. (3.26) will be plugged into Eq. (3.29) and a detailed derivation of the second order DC lesser Greens function is performed. The reader is given the option to jump to Section 3.4 directly where the formalism is applied to charge photocurrents.

### 3.3.2 *Derivation of the lesser Greens function*

By employing Langreths theorem $(GGG)^{<} = G^R G^R G^{<} + G^R G^{<} G^A + G^{<} G^{<} G^A$, the triple product of lesser Greens functions in Eq. (3.29) is resolved to

$$\begin{aligned} G_2^{<}(1,1') = \int\int d2d3 [& G_{\mathrm{eq}}^R(1,2)\frac{\delta H(2)}{\hbar} G_{\mathrm{eq}}^R(2,3)\frac{\delta H(3)}{\hbar} G_{\mathrm{eq}}^{<}\left(3,1'\right) \\ &+ G_{\mathrm{eq}}^R(1,2)\frac{\delta H(2)}{\hbar} G_{\mathrm{eq}}^{<}(2,3)\frac{\delta H(3)}{\hbar} G_{\mathrm{eq}}^{A}\left(3,1'\right) \\ &+ G_{\mathrm{eq}}^{<}(1,2)\frac{\delta H(2)}{\hbar} G_{\mathrm{eq}}^{a}(2,3)\frac{\delta H(3)}{\hbar} G_{\mathrm{eq}}^{A}\left(3,1'\right)]. \end{aligned} \tag{3.30}$$

Using the laser vector potential

$$\boldsymbol{A}(t) = \mathrm{Re}\left[\frac{E_0 \boldsymbol{\epsilon} e^{-i\omega t}}{i\omega}\right], \tag{3.31}$$

the product of the laser perturbations in Eq. (3.30) can be expressed as (the Greens function in-between is dropped for better readability, but should be kept in mind)

$$\begin{aligned}\frac{\delta H(2)}{\hbar}\frac{\delta H(3)}{\hbar} &= \frac{e^2}{\hbar^2}\boldsymbol{v}\cdot\mathrm{Re}\left[\frac{E_0\boldsymbol{\epsilon}e^{-i\omega_2 2}}{i\omega_2}\right]\boldsymbol{v}\cdot\mathrm{Re}\left[\frac{E_0\boldsymbol{\epsilon}e^{-i\omega_3 3}}{i\omega_3}\right]\\ &= \frac{e^2}{\hbar^2}\left(\frac{E_0}{\omega_2\omega_3}\right)^2\mathrm{Re}\left[-i(\boldsymbol{v}\cdot\boldsymbol{\epsilon})e^{-i\omega_2 2}\right]\mathrm{Re}\left[-i(\boldsymbol{v}\cdot\boldsymbol{\epsilon})e^{-i\omega_3 3}\right]\\ &= \frac{e^2}{\hbar^2}\left(\frac{E_0}{\omega_2\omega_3}\right)^2\mathrm{Im}\left[(\boldsymbol{v}\cdot\boldsymbol{\epsilon})e^{-i\omega_2 2}\right]\mathrm{Im}\left[(\boldsymbol{v}\cdot\boldsymbol{\epsilon})e^{-i\omega_3 3}\right].\end{aligned} \tag{3.32}$$

Using $z - z^* = \frac{1}{2i}\mathrm{Im}\,[z]$ allows one to get rid of the imaginary part and to combine the exponential functions in a convenient way, as will become apparent later. For Eq. (3.32) it follows

$$\begin{aligned}\frac{\delta H(2)}{\hbar}\frac{\delta H(3)}{\hbar} &= \frac{e^2}{\hbar^2}\left(\frac{E_0}{\omega_2\omega_3}\right)^2(2i)^2\\ &\quad\left[(\boldsymbol{v}\cdot\boldsymbol{\epsilon})e^{-i\omega_2 2} - (\boldsymbol{v}\cdot\boldsymbol{\epsilon}^*)e^{+i\omega_2 2}\right]\left[(\boldsymbol{v}\cdot\boldsymbol{\epsilon})e^{-i\omega_3 3} - (\boldsymbol{v}\cdot\boldsymbol{\epsilon}^*)e^{+i\omega_3 3}\right]\\ &= -4\frac{e^2}{\hbar^2}\left(\frac{E_0}{\omega_2\omega_3}\right)^2\Big[\\ &\quad + (\boldsymbol{v}\cdot\boldsymbol{\epsilon})e^{-i\omega_2 2}(\boldsymbol{v}\cdot\boldsymbol{\epsilon})e^{-i\omega_3 3}\\ &\quad - (\boldsymbol{v}\cdot\boldsymbol{\epsilon})e^{-i\omega_2 2}(\boldsymbol{v}\cdot\boldsymbol{\epsilon}^*)e^{+i\omega_3 3}\\ &\quad - (\boldsymbol{v}\cdot\boldsymbol{\epsilon}^*)e^{+i\omega_2 2}(\boldsymbol{v}\cdot\boldsymbol{\epsilon})e^{-i\omega_3 3}\\ &\quad + (\boldsymbol{v}\cdot\boldsymbol{\epsilon}^*)e^{+i\omega_2 2}(\boldsymbol{v}\cdot\boldsymbol{\epsilon}^*)e^{+i\omega_3 3}\Big].\end{aligned} \tag{3.33}$$

From Eq. (3.35) only the mixed terms containing the laser polarization and its complex conjugates are kept, with the following argument in mind. Since the goal is to describe a rectified DC response one can assume $\omega = \omega_2 = -\omega_3$. From Eq. (3.25) it follows for the product of two electric field components

$$E_i(t)E_j(t) = \frac{E_0^2}{4}\left[\epsilon_i\epsilon_j^* + \epsilon_i^*\epsilon_j + \epsilon_i\epsilon_j e^{-2i\omega t} + \epsilon_i^*\epsilon_j^* e^{2i\omega t}\right]. \tag{3.34}$$

The first two terms in Eq. (3.34) are independent of the fields frequency $\omega$, these are the DC terms. The third and fourth term effectively oscillate with

frequency $2\omega$, these terms describe the second harmonic response. In this thesis the focus is on the rectified DC response, thus, the third and fourth terms are dropped yielding

$$\begin{aligned}\frac{\delta H(2)}{\hbar}\frac{\delta H(3)}{\hbar} = -4\frac{e^2}{\hbar^2}\left(\frac{E_0}{\omega}\right)^2 \Big[ \\ + (\boldsymbol{v}\cdot\boldsymbol{\epsilon})e^{-i\omega 2}(\boldsymbol{v}\cdot\boldsymbol{\epsilon}^*)e^{-i\omega 3} \\ + (\boldsymbol{v}\cdot\boldsymbol{\epsilon}^*)e^{+i\omega 2}(\boldsymbol{v}\cdot\boldsymbol{\epsilon})e^{+i\omega 3}\Big].\end{aligned} \tag{3.35}$$

The perturbation Eq. (3.35) is then plugged into the second order lesser Greens function given in Eq. (3.30), yielding

$$\begin{aligned}G^<_{\mathrm{DC}}(1,1') = -4\frac{e^2}{\hbar^2}\left(\frac{E_0}{\omega}\right)^2 \int\int d2d3[ \\ G^R_{\mathrm{eq}}(1,2)(\boldsymbol{v}\cdot\boldsymbol{\epsilon})e^{-i\omega 2}G^R_{\mathrm{eq}}(2,3)(\boldsymbol{v}\cdot\boldsymbol{\epsilon}^*)e^{-i\omega 3}G^<_{\mathrm{eq}}(3,1') \\ +G^R_{\mathrm{eq}}(1,2)(\boldsymbol{v}\cdot\boldsymbol{\epsilon}^*)e^{+i\omega 2}G^R_{\mathrm{eq}}(2,3)(\boldsymbol{v}\cdot\boldsymbol{\epsilon})e^{+i\omega 3}G^<_{\mathrm{eq}}(3,1') \\ +G^R_{\mathrm{eq}}(1,2)(\boldsymbol{v}\cdot\boldsymbol{\epsilon})e^{-i\omega 2}G^<_{\mathrm{eq}}(2,3)(\boldsymbol{v}\cdot\boldsymbol{\epsilon}^*)e^{-i\omega 3}G^A_{\mathrm{eq}}(3,1') \\ +G^R_{\mathrm{eq}}(1,2)(\boldsymbol{v}\cdot\boldsymbol{\epsilon}^*)e^{+i\omega 2}G^<_{\mathrm{eq}}(2,3)(\boldsymbol{v}\cdot\boldsymbol{\epsilon})e^{+i\omega 3}G^A_{\mathrm{eq}}(3,1') \\ +G^<_{\mathrm{eq}}(1,2)(\boldsymbol{v}\cdot\boldsymbol{\epsilon})e^{-i\omega 2}G^A_{\mathrm{eq}}(2,3)(\boldsymbol{v}\cdot\boldsymbol{\epsilon}^*)e^{-i\omega 3}G^A_{\mathrm{eq}}(3,1') \\ +G^<_{\mathrm{eq}}(1,2)(\boldsymbol{v}\cdot\boldsymbol{\epsilon}^*)e^{+i\omega 2}G^A_{\mathrm{eq}}(2,3)(\boldsymbol{v}\cdot\boldsymbol{\epsilon})e^{+i\omega 3}G^A_{\mathrm{eq}}(3,1')].\end{aligned} \tag{3.36}$$

Eq. (3.36) now only depends on the two-point equilibrium Greens functions and the ground state velocity operator $\boldsymbol{v}$. However, the time-integration is impractical to work with, so next a Fourier transform

$$G^{\{R,A,<\}}_{\mathrm{eq}}(t,t') = \frac{1}{2\pi\hbar}\int_{-\infty}^{\infty} d\mathrm{E}e^{-i\mathrm{E}(t-t')/\hbar}G^{\{R,A,<\}}_{\mathrm{eq}}(\mathrm{E}) \tag{3.37}$$

is applied to convert Eq. (3.36) into a energy dependent expression

$$\begin{aligned}
G^<_{\mathrm{DC}}(1,1') = -4\frac{e^2E_0^2}{8\pi^3\hbar^2\omega^2}\int d\mathrm{E}\int\int d2d3\int\int d\mathrm{E}'d\mathrm{E}''[\\
&G^R_{\mathrm{eq}}(\mathrm{E})e^{i(1-2)/\mathrm{E}\hbar}(\boldsymbol{v}\cdot\boldsymbol{\epsilon})e^{-i\omega 2}G^R_{\mathrm{eq}}(\mathrm{E}')e^{i(2-3)/\mathrm{E}'\hbar}\\
&\quad(\boldsymbol{v}\cdot\boldsymbol{\epsilon}^*)e^{-i\omega 3}G^<_{\mathrm{eq}}(\mathrm{E}'')\,e^{i(3-1')/\mathrm{E}''\hbar}\\
&+G^R_{\mathrm{eq}}(\mathrm{E})e^{i(1-2)/\mathrm{E}\hbar}(\boldsymbol{v}\cdot\boldsymbol{\epsilon}^*)e^{+i\omega 2}G^R_{\mathrm{eq}}(\mathrm{E}')e^{i(2-3)/\mathrm{E}'\hbar}\\
&\quad(\boldsymbol{v}\cdot\boldsymbol{\epsilon})e^{+i\omega 3}G^<_{\mathrm{eq}}(\mathrm{E}'')\,e^{i(3-1')/\mathrm{E}''\hbar}\\
&+G^R_{\mathrm{eq}}(\mathrm{E})e^{i(1-2)/\mathrm{E}\hbar}(\boldsymbol{v}\cdot\boldsymbol{\epsilon})e^{-i\omega 2}G^<_{\mathrm{eq}}(\mathrm{E}')e^{i(2-3)/\mathrm{E}'\hbar}\\
&\quad(\boldsymbol{v}\cdot\boldsymbol{\epsilon}^*)e^{-i\omega 3}G^A_{\mathrm{eq}}(\mathrm{E}'')\,e^{i(3-1')/\mathrm{E}''\hbar}\\
&+G^R_{\mathrm{eq}}(\mathrm{E})e^{i(1-2)/\mathrm{E}\hbar}(\boldsymbol{v}\cdot\boldsymbol{\epsilon}^*)e^{+i\omega 2}G^<_{\mathrm{eq}}(\mathrm{E}')e^{i(2-3)/\mathrm{E}'\hbar}\\
&\quad(\boldsymbol{v}\cdot\boldsymbol{\epsilon})e^{+i\omega 3}G^A_{\mathrm{eq}}(\mathrm{E}'')\,e^{i(3-1')/\mathrm{E}''\hbar}\\
&+G^<_{\mathrm{eq}}(\mathrm{E})e^{i(1-2)/\mathrm{E}\hbar}(\boldsymbol{v}\cdot\boldsymbol{\epsilon})e^{-i\omega 2}G^A_{\mathrm{eq}}(\mathrm{E}')e^{i(2-3)/\mathrm{E}'\hbar}\\
&\quad(\boldsymbol{v}\cdot\boldsymbol{\epsilon}^*)e^{-i\omega 3}G^A_{\mathrm{eq}}(\mathrm{E}'')\,e^{i(3-1')/\mathrm{E}''\hbar}\\
&+G^<_{\mathrm{eq}}(\mathrm{E})e^{i(1-2)/\mathrm{E}\hbar}(\boldsymbol{v}\cdot\boldsymbol{\epsilon}^*)e^{+i\omega 2}G^A_{\mathrm{eq}}(\mathrm{E}')e^{i(2-3)/\mathrm{E}'\hbar}\\
&\quad(\boldsymbol{v}\cdot\boldsymbol{\epsilon})e^{+i\omega 3}G^A_{\mathrm{eq}}(\mathrm{E}'')\,e^{i(3-1')/\mathrm{E}''\hbar}].
\end{aligned}\tag{3.38}$$

Next the exponential functions in Eq. (3.38) are reordered such that each exponential function depends only on a single time variable which allows one to identify $\delta(\mathrm{E}-\mathrm{E}') = \int dt e^{i(\mathrm{E}-\mathrm{E}')t}$ and simplify the expression to

$$\begin{aligned}
G^<_{\mathrm{DC}}(1,1') = -4\frac{e^2E_0^2}{8\pi^3\hbar^2\omega^2}\int d\mathrm{E}\int\int d\mathrm{E}'d\mathrm{E}''e^{+i1\mathrm{E}/\hbar}e^{-i1'\mathrm{E}''/\hbar}[\\
&\delta(\mathrm{E}+\hbar\omega-\mathrm{E}')\delta(\mathrm{E}'-\hbar\omega-\mathrm{E}'')\\
&\quad G^R_{\mathrm{eq}}(\mathrm{E})(\boldsymbol{v}\cdot\boldsymbol{\epsilon})G^R_{\mathrm{eq}}(\mathrm{E}')(\boldsymbol{v}\cdot\boldsymbol{\epsilon}^*)G^<_{\mathrm{eq}}(\mathrm{E}'')\\
&+\delta(\mathrm{E}-\hbar\omega-\mathrm{E}')\delta(\mathrm{E}'+\hbar\omega-\mathrm{E}'')\\
&\quad G^R_{\mathrm{eq}}(\mathrm{E})(\boldsymbol{v}\cdot\boldsymbol{\epsilon}^*)G^R_{\mathrm{eq}}(\mathrm{E}')(\boldsymbol{v}\cdot\boldsymbol{\epsilon})G^<_{\mathrm{eq}}(\mathrm{E}'')\\
&+\delta(\mathrm{E}+\hbar\omega-\mathrm{E}')\delta(\mathrm{E}'-\hbar\omega-\mathrm{E}'')\\
&\quad G^R_{\mathrm{eq}}(\mathrm{E})(\boldsymbol{v}\cdot\boldsymbol{\epsilon})G^<_{\mathrm{eq}}(\mathrm{E}')(\boldsymbol{v}\cdot\boldsymbol{\epsilon}^*)G^A_{\mathrm{eq}}(\mathrm{E}'')\\
&+\delta(\mathrm{E}-\hbar\omega-\mathrm{E}')\delta(\mathrm{E}'+\hbar\omega-\mathrm{E}'')\\
&\quad G^R_{\mathrm{eq}}(\mathrm{E})(\boldsymbol{v}\cdot\boldsymbol{\epsilon}^*)G^<_{\mathrm{eq}}(\mathrm{E}')(\boldsymbol{v}\cdot\boldsymbol{\epsilon})G^A_{\mathrm{eq}}(\mathrm{E}'')\\
&+\delta(\mathrm{E}+\hbar\omega-\mathrm{E}')\delta(\mathrm{E}'-\hbar\omega-\mathrm{E}'')\\
&\quad G^<_{\mathrm{eq}}(\mathrm{E})(\boldsymbol{v}\cdot\boldsymbol{\epsilon})G^A_{\mathrm{eq}}(\mathrm{E}')(\boldsymbol{v}\cdot\boldsymbol{\epsilon}^*)G^A_{\mathrm{eq}}(\mathrm{E}'')\\
&+\delta(\mathrm{E}-\hbar\omega-\mathrm{E}')\delta(\mathrm{E}'+\hbar\omega-\mathrm{E}'')\\
&\quad G^<_{\mathrm{eq}}(\mathrm{E})(\boldsymbol{v}\cdot\boldsymbol{\epsilon}^*)G^A_{\mathrm{eq}}(\mathrm{E}')(\boldsymbol{v}\cdot\boldsymbol{\epsilon})G^A_{\mathrm{eq}}(\mathrm{E}'')].
\end{aligned}\tag{3.39}$$

The Dirac deltas in Eq. (3.39) cancel the primed energy integrals and it follows

$$\begin{aligned} G^<_{\mathrm{DC}}(1,1') = -4\frac{e^2E_0^2}{8\pi^3\hbar^2\omega^2}\int d\mathrm{E}e^{i(1-1')\mathrm{E}/\hbar}[ \\ G^R_{\mathrm{eq}}(\mathrm{E})(\boldsymbol{v}\cdot\boldsymbol{\epsilon})G^R_{\mathrm{eq}}(\mathrm{E}+\hbar\omega)(\boldsymbol{v}\cdot\boldsymbol{\epsilon}^*)G^<_{\mathrm{eq}}(\mathrm{E}) \\ +G^R_{\mathrm{eq}}(\mathrm{E})(\boldsymbol{v}\cdot\boldsymbol{\epsilon}^*)G^R_{\mathrm{eq}}(\mathrm{E}-\hbar\omega)(\boldsymbol{v}\cdot\boldsymbol{\epsilon})G^<_{\mathrm{eq}}(\mathrm{E}) \\ +G^R_{\mathrm{eq}}(\mathrm{E})(\boldsymbol{v}\cdot\boldsymbol{\epsilon})G^<_{\mathrm{eq}}(\mathrm{E}+\hbar\omega)(\boldsymbol{v}\cdot\boldsymbol{\epsilon}^*)G^A_{\mathrm{eq}}(\mathrm{E}) \\ +G^R_{\mathrm{eq}}(\mathrm{E})(\boldsymbol{v}\cdot\boldsymbol{\epsilon}^*)G^<_{\mathrm{eq}}(\mathrm{E}-\hbar\omega)(\boldsymbol{v}\cdot\boldsymbol{\epsilon})G^A_{\mathrm{eq}}(\mathrm{E}) \\ +G^<_{\mathrm{eq}}(\mathrm{E})(\boldsymbol{v}\cdot\boldsymbol{\epsilon})G^A_{\mathrm{eq}}(\mathrm{E}+\hbar\omega)(\boldsymbol{v}\cdot\boldsymbol{\epsilon}^*)G^A_{\mathrm{eq}}(\mathrm{E}) \\ +G^<_{\mathrm{eq}}(\mathrm{E})(\boldsymbol{v}\cdot\boldsymbol{\epsilon}^*)G^A_{\mathrm{eq}}(\mathrm{E}-\hbar\omega)(\boldsymbol{v}\cdot\boldsymbol{\epsilon})G^A_{\mathrm{eq}}(\mathrm{E})]. \end{aligned} \tag{3.40}$$

Using $G^<_{\mathrm{eq}}(\mathrm{E}) = f(\mathrm{E})\left[G^{\mathrm{A}}_{\mathrm{eq}}(\mathrm{E}) - G^{\mathrm{R}}_{\mathrm{eq}}(\mathrm{E})\right]$ Eq. (3.40) can be expressed solely in terms of the equilibrium advanced and retarded Greens functions, which can be easily constructed from band energies and the eigenstates of the system as will be shown below. For Eq. (3.40) it follows

$$\begin{aligned} G^<_{\mathrm{DC}}(1,1') = -4\frac{e^2E_0^2}{8\pi^3\hbar^2\omega^2}\int d\mathrm{E}f(\mathrm{E})e^{i(1-1')\mathrm{E}/\hbar}[ \\ +G^R_{\mathrm{eq}}(\mathrm{E})(\boldsymbol{v}\cdot\boldsymbol{\epsilon})G^R_{\mathrm{eq}}(\mathrm{E}+\hbar\omega)(\boldsymbol{v}\cdot\boldsymbol{\epsilon}^*)G^A_{\mathrm{eq}}(\mathrm{E}) \\ -G^R_{\mathrm{eq}}(\mathrm{E})(\boldsymbol{v}\cdot\boldsymbol{\epsilon})G^A_{\mathrm{eq}}(\mathrm{E}+\hbar\omega)(\boldsymbol{v}\cdot\boldsymbol{\epsilon}^*)G^A_{\mathrm{eq}}(\mathrm{E}) \\ -G^R_{\mathrm{eq}}(\mathrm{E})(\boldsymbol{v}\cdot\boldsymbol{\epsilon})G^R_{\mathrm{eq}}(\mathrm{E}+\hbar\omega)(\boldsymbol{v}\cdot\boldsymbol{\epsilon}^*)G^R_{\mathrm{eq}}(\mathrm{E}) \\ +G^A_{\mathrm{eq}}(\mathrm{E})(\boldsymbol{v}\cdot\boldsymbol{\epsilon})G^A_{\mathrm{eq}}(\mathrm{E}+\hbar\omega)(\boldsymbol{v}\cdot\boldsymbol{\epsilon}^*)G^A_{\mathrm{eq}}(\mathrm{E}) \\ +G^R_{\mathrm{eq}}(\mathrm{E})(\boldsymbol{v}\cdot\boldsymbol{\epsilon}^*)G^R_{\mathrm{eq}}(\mathrm{E}-\hbar\omega)(\boldsymbol{v}\cdot\boldsymbol{\epsilon})G^A_{\mathrm{eq}}(\mathrm{E}) \\ -G^R_{\mathrm{eq}}(\mathrm{E})(\boldsymbol{v}\cdot\boldsymbol{\epsilon}^*)G^A_{\mathrm{eq}}(\mathrm{E}-\hbar\omega)(\boldsymbol{v}\cdot\boldsymbol{\epsilon})G^A_{\mathrm{eq}}(\mathrm{E}) \\ -G^R_{\mathrm{eq}}(\mathrm{E})(\boldsymbol{v}\cdot\boldsymbol{\epsilon}^*)G^R_{\mathrm{eq}}(\mathrm{E}-\hbar\omega)(\boldsymbol{v}\cdot\boldsymbol{\epsilon})G^R_{\mathrm{eq}}(\mathrm{E}) \\ +G^A_{\mathrm{eq}}(\mathrm{E})(\boldsymbol{v}\cdot\boldsymbol{\epsilon}^*)G^A_{\mathrm{eq}}(\mathrm{E}-\hbar\omega)(\boldsymbol{v}\cdot\boldsymbol{\epsilon})G^A_{\mathrm{eq}}(\mathrm{E}) \\ +G^R_{\mathrm{eq}}(\mathrm{E})(\boldsymbol{v}\cdot\boldsymbol{\epsilon})G^A_{\mathrm{eq}}(\mathrm{E}+\hbar\omega)(\boldsymbol{v}\cdot\boldsymbol{\epsilon}^*)G^A_{\mathrm{eq}}(\mathrm{E}) \\ -G^R_{\mathrm{eq}}(\mathrm{E})(\boldsymbol{v}\cdot\boldsymbol{\epsilon})G^R_{\mathrm{eq}}(\mathrm{E}+\hbar\omega)(\boldsymbol{v}\cdot\boldsymbol{\epsilon}^*)G^A_{\mathrm{eq}}(\mathrm{E}) \\ +G^R_{\mathrm{eq}}(\mathrm{E})(\boldsymbol{v}\cdot\boldsymbol{\epsilon}^*)G^A_{\mathrm{eq}}(\mathrm{E}-\hbar\omega)(\boldsymbol{v}\cdot\boldsymbol{\epsilon})G^A_{\mathrm{eq}}(\mathrm{E}) \\ -G^R_{\mathrm{eq}}(\mathrm{E})(\boldsymbol{v}\cdot\boldsymbol{\epsilon}^*)G^R_{\mathrm{eq}}(\mathrm{E}-\hbar\omega)(\boldsymbol{v}\cdot\boldsymbol{\epsilon})G^A_{\mathrm{eq}}(\mathrm{E})]. \end{aligned} \tag{3.41}$$

In Eq. (3.41) two consecutive lines fulfill the relationship $z - z^*$, such that one can use again $z - z^* = \frac{1}{2i}\,\mathrm{Im}\,[z]$ but this time "backwards" to compactify the

expression to

$$
\begin{aligned}
G^{<}_{\mathrm{DC}}(1,1') = i\frac{e^2E_0^2}{8\pi^3\hbar^2\omega^2}\,\mathrm{Im}\int d\mathrm{E}e^{i(1-1')\mathrm{E}/\hbar}2[ \\
&+f(\mathrm{E})G^R_{\mathrm{eq}}(\mathrm{E})(\boldsymbol{v}\cdot\boldsymbol{\epsilon})G^R_{\mathrm{eq}}(\mathrm{E}+\hbar\omega)(\boldsymbol{v}\cdot\boldsymbol{\epsilon}^*)G^A_{\mathrm{eq}}(\mathrm{E}) \\
&-f(\mathrm{E})G^R_{\mathrm{eq}}(\mathrm{E})(\boldsymbol{v}\cdot\boldsymbol{\epsilon})G^R_{\mathrm{eq}}(\mathrm{E}+\hbar\omega)(\boldsymbol{v}\cdot\boldsymbol{\epsilon}^*)G^R_{\mathrm{eq}}(\mathrm{E}) \\
&+f(\mathrm{E})G^R_{\mathrm{eq}}(\mathrm{E})(\boldsymbol{v}\cdot\boldsymbol{\epsilon}^*)G^R_{\mathrm{eq}}(\mathrm{E}-\hbar\omega)(\boldsymbol{v}\cdot\boldsymbol{\epsilon})G^A_{\mathrm{eq}}(\mathrm{E}) \\
&-f(\mathrm{E})G^R_{\mathrm{eq}}(\mathrm{E})(\boldsymbol{v}\cdot\boldsymbol{\epsilon}^*)G^R_{\mathrm{eq}}(\mathrm{E}-\hbar\omega)(\boldsymbol{v}\cdot\boldsymbol{\epsilon})G^R_{\mathrm{eq}}(\mathrm{E}) \\
&+f(\mathrm{E})G^R_{\mathrm{eq}}(\mathrm{E})(\boldsymbol{v}\cdot\boldsymbol{\epsilon})G^A_{\mathrm{eq}}(\mathrm{E}+\hbar\omega)(\boldsymbol{v}\cdot\boldsymbol{\epsilon}^*)G^A_{\mathrm{eq}}(\mathrm{E}) \\
&+f(\mathrm{E})G^R_{\mathrm{eq}}(\mathrm{E})(\boldsymbol{v}\cdot\boldsymbol{\epsilon}^*)G^A_{\mathrm{eq}}(\mathrm{E}-\hbar\omega)(\boldsymbol{v}\cdot\boldsymbol{\epsilon})G^A_{\mathrm{eq}}(\mathrm{E})].
\end{aligned}
\tag{3.42}
$$

With Eq. (3.24) in mind, one assumes $1 = 1'$ to finally arrive at

$$
\begin{aligned}
G^{<}_{\mathrm{DC}} = i\frac{e^2E_0^2}{8\pi\hbar^3\omega^2}\,\mathrm{Im}\int d\mathrm{E}2[ \\
&+f(\mathrm{E})G^R_{\mathrm{eq}}(\mathrm{E})(\boldsymbol{v}\cdot\boldsymbol{\epsilon})G^R_{\mathrm{eq}}(\mathrm{E}+\hbar\omega)(\boldsymbol{v}\cdot\boldsymbol{\epsilon}^*)G^A_{\mathrm{eq}}(\mathrm{E}) \\
&-f(\mathrm{E})G^R_{\mathrm{eq}}(\mathrm{E})(\boldsymbol{v}\cdot\boldsymbol{\epsilon})G^R_{\mathrm{eq}}(\mathrm{E}+\hbar\omega)(\boldsymbol{v}\cdot\boldsymbol{\epsilon}^*)G^R_{\mathrm{eq}}(\mathrm{E}) \\
&+f(\mathrm{E})G^R_{\mathrm{eq}}(\mathrm{E})(\boldsymbol{v}\cdot\boldsymbol{\epsilon}^*)G^R_{\mathrm{eq}}(\mathrm{E}-\hbar\omega)(\boldsymbol{v}\cdot\boldsymbol{\epsilon})G^A_{\mathrm{eq}}(\mathrm{E}) \\
&-f(\mathrm{E})G^R_{\mathrm{eq}}(\mathrm{E})(\boldsymbol{v}\cdot\boldsymbol{\epsilon}^*)G^R_{\mathrm{eq}}(\mathrm{E}-\hbar\omega)(\boldsymbol{v}\cdot\boldsymbol{\epsilon})G^R_{\mathrm{eq}}(\mathrm{E}) \\
&+f(\mathrm{E})G^R_{\mathrm{eq}}(\mathrm{E})(\boldsymbol{v}\cdot\boldsymbol{\epsilon})G^A_{\mathrm{eq}}(\mathrm{E}+\hbar\omega)(\boldsymbol{v}\cdot\boldsymbol{\epsilon}^*)G^A_{\mathrm{eq}}(\mathrm{E}) \\
&+f(\mathrm{E})G^R_{\mathrm{eq}}(\mathrm{E})(\boldsymbol{v}\cdot\boldsymbol{\epsilon}^*)G^A_{\mathrm{eq}}(\mathrm{E}-\hbar\omega)(\boldsymbol{v}\cdot\boldsymbol{\epsilon})G^A_{\mathrm{eq}}(\mathrm{E})].
\end{aligned}
\tag{3.43}
$$

Eq. (3.43) is in good agreement with Eq.(A7) in Ref. [28]. Note that Eq. (A7) has slightly different arguments within the Greens functions which could be a typo in Ref. [28] originating from using the second harmonic energy arguments instead of the DC arguments. Before Eq. (3.42) is used to derive expression for the photocurrents etc., it is convenient to express Eq. (3.42) in terms of the applied laser intensity $I$. The laser intensity $I = \epsilon_0 c E_0^2/2$[28] is quadratic in the laser electric field strength $E_0$ and, thus, Eq. (3.42) scales linearly with the laser intensity. For Eq. (3.42) it follows

$$
\begin{aligned}
G^{<}_{\mathrm{DC}} &= i\frac{e^2E_0^2}{8\pi\hbar}\left(\frac{1}{\hbar\omega}\right)^2\mathrm{Im}\int d\mathrm{E}[2...] \\
&= i\frac{2e^2I}{8\pi\hbar\epsilon_0 c}\left(\frac{1}{\hbar\omega}\right)^2\mathrm{Im}\int d\mathrm{E}[2...] \\
&= i\frac{2e^2}{8\pi\epsilon_0}\frac{I}{\hbar c}\left(\frac{1}{\hbar\omega}\right)^2\mathrm{Im}\int d\mathrm{E}[2...].
\end{aligned}
\tag{3.44}
$$

And by realizing that $4\pi\epsilon_0 = e^2/(a_0 E_h)$ one concludes

$$\begin{aligned} G^<_{\mathrm{DC}} &= i\frac{2e^2 4\pi a_0 E_h}{8\pi e^2}\frac{I}{\hbar c}\left(\frac{1}{\hbar\omega}\right)^2 \mathrm{Im}\int d\mathrm{E}[2...] \\ &= i a_0 E_h \frac{I}{\hbar c}\left(\frac{1}{\hbar\omega}\right)^2 \mathrm{Im}\int d\mathrm{E}[2...] \\ &= i\frac{a_0^2 I}{\hbar c}\left(\frac{E_h}{\hbar\omega}\right)^2 \mathrm{Im}\int d\mathrm{E}[\frac{2}{a_0 E_h}...]. \end{aligned} \tag{3.45}$$

In the final step of Eq. (3.44) the factor $1/(a_0 E_h)$ was moved under the brackets. Everything within the brackets will be defined as the response tensor. This step will become apparent in the units discussion section3.4.1. The expectation value of a generic operator is given by Eq. (3.15), with Eq. (3.44) it follows that

$$\begin{aligned} \langle O\rangle &= \mathrm{Tr}[\rho(H)O] \\ &= \frac{1}{i}\mathrm{Tr}[O(t)G^<_{\mathrm{DC}}] \\ &= \frac{a_0^2 I}{\hbar c}\left(\frac{E_h}{\hbar\omega}\right)^2 \mathrm{Im}\int d\mathrm{E}\mathrm{Tr}[O[\frac{2}{a_0 E_h}...]. \end{aligned} \tag{3.46}$$

The dot products in Eq. (3.42) are evaluated as sums over the vector components such that the $a$-th component of the expectation value of the generic operator $\langle O_a\rangle$ is given by

$$\begin{aligned} \langle O_a\rangle &= \frac{a_0^2 I}{\hbar c}\left(\frac{E_h}{\hbar\omega}\right)^2 \mathrm{Im}\sum_{bc}\left(\hat{\boldsymbol{e}}_b\cdot\boldsymbol{\epsilon}\right)\left(\hat{\boldsymbol{e}}_c\cdot\boldsymbol{\epsilon}^*\right)\int d\mathrm{E}\mathrm{Tr}[O_a[\frac{2}{a_0 E_h}...] \\ &\equiv \frac{a_0^2 I}{\hbar c}\left(\frac{E_h}{\hbar\omega}\right)^2 \mathrm{Im}\sum_{bc}\varepsilon_b\varepsilon_c^*\xi_{abc}, \end{aligned} \tag{3.47}$$

where $\xi_{abc}$ was implicitly defined as the generic rectified second order response to operator $O$ and, thus, is given by

$$\begin{aligned} \xi_{abc} =& \frac{2}{a_0 \mathrm{E_H}}\int\frac{\mathrm{d}^D k}{(2\pi)^D}\int \mathrm{dE}\,\mathrm{Tr}[ \\ & f(\mathrm{E})O_a G^{\mathrm{R}}_{\boldsymbol{k}}(\mathrm{E})v_b G^{\mathrm{R}}_{\boldsymbol{k}}(\mathrm{E}-\hbar\omega)v_c G^{\mathrm{R}}_{\boldsymbol{k}}(\mathrm{E}) \\ & -f(\mathrm{E})O_a G^{\mathrm{R}}_{\boldsymbol{k}}(\mathrm{E})v_b G^{\mathrm{R}}_{\boldsymbol{k}}(\mathrm{E}-\hbar\omega)v_c G^{\mathrm{A}}_{\boldsymbol{k}}(\mathrm{E}) \\ & +f(\mathrm{E})O_a G^{\mathrm{R}}_{\boldsymbol{k}}(\mathrm{E})v_c G^{\mathrm{R}}_{\boldsymbol{k}}(\mathrm{E}+\hbar\omega)v_b G^{\mathrm{R}}_{\boldsymbol{k}}(\mathrm{E}) \\ & -f(\mathrm{E})O_a G^{\mathrm{R}}_{\boldsymbol{k}}(\mathrm{E})v_c G^{\mathrm{R}}_{\boldsymbol{k}}(\mathrm{E}+\hbar\omega)v_b G^{\mathrm{A}}_{\boldsymbol{k}}(\mathrm{E}) \\ & +f(\mathrm{E}-\hbar\omega)O_a G^{\mathrm{R}}_{\boldsymbol{k}}(\mathrm{E})v_b G^{\mathrm{R}}_{\boldsymbol{k}}(\mathrm{E}-\hbar\omega)v_c G^{\mathrm{A}}_{\boldsymbol{k}}(\mathrm{E}) \\ & + f(\mathrm{E}+\hbar\omega)O_a G^{\mathrm{R}}_{\boldsymbol{k}}(\mathrm{E})v_c G^{\mathrm{R}}_{\boldsymbol{k}}(\mathrm{E}+\hbar\omega)v_b G^{\mathrm{A}}_{\boldsymbol{k}}(\mathrm{E})\Big], \end{aligned} \tag{3.48}$$

where $D$ is the dimension of the system and $a$, $b$ and $c$ are spatial indices with $a, b, c \in [1, .., D]$.

### 3.3.3 Constant lifetime approximation

Assuming a constant lifetime broadening $\Gamma$, the $0^{\text{th}}$ retarded Greens function is constructed from the eigenstates $|\boldsymbol{kn}\rangle$ and the eigenenergies $\mathrm{E}_{\boldsymbol{kn}}$ of the Wannier interpolated Hamiltonian

$$\begin{aligned} G^{\mathrm{R}}_{\mathrm{eq},\boldsymbol{k}}(\mathrm{E}) &\equiv \hbar \sum_n \frac{|\boldsymbol{kn}\rangle\langle\boldsymbol{kn}|}{\mathrm{E} - \mathrm{E}_{\boldsymbol{kn}} + i\Gamma}, \\ G^{\mathrm{A}}_{\mathrm{eq},\boldsymbol{k}}(\mathrm{E}) &= [G^{\mathrm{R}}_{\mathrm{eq},\boldsymbol{k}}(\mathrm{E})]^* = \hbar \sum_n \frac{|\boldsymbol{kn}\rangle\langle\boldsymbol{kn}|}{\mathrm{E} - \mathrm{E}_{\boldsymbol{kn}} - i\Gamma}, \end{aligned} \tag{3.49}$$

where the advanced Greens function $G^{\mathrm{A}}_{\mathrm{eq},\boldsymbol{k}}$ is given by the complex conjugate of the retarded Greens function. The nominators is Eq. (3.49) will rotate the generic operator component $O_i$ and the two velocity operators $v_j$, $v_k$ in Eq. (3.48) into their eigenbasis. In the context of Wannier interpolation, see Section 5.5, that means that the operators will be plugged into the Keldysh routines in their Hamiltonian gauge, see also subsection 5.5.1. Assuming Eq. (3.49) the nominators in Eq. (3.48) are energy independent, the energy integration, thus, only effects the energy denominators in Eq. (3.48) introduced by the triple product of Greens functions present in each term. The energy integration can be performed individually for each term in the sum. Terms consisting of a triple product of retarded Greens functions are identified as Fermi sea contributions $\xi^{RRR}$, while the mixed terms with two retarded and one advanced Greens function are the Fermi surface contributions $\xi^{RRA}$:

$$\begin{aligned} &\xi^{RRR}(\mathrm{E}_n, \mathrm{E}_m, \mathrm{E}_l, \hbar\omega, \Gamma, \mathrm{E_f}) \\ &\qquad \equiv \int_{-\infty}^{+\infty} \frac{d\mathrm{E} f(\mathrm{E})}{(\mathrm{E} - \mathrm{E_n} + i\Gamma)(\mathrm{E} \pm \hbar\omega - \mathrm{E_m} + i\Gamma)(\mathrm{E} - \mathrm{E_l} + i\Gamma)} \\ &\xi^{RRA}(\mathrm{E}_n, \mathrm{E}_m, \mathrm{E}_l, \hbar\omega, \Gamma, \mathrm{E_f}) \\ &\qquad \equiv \int_{-\infty}^{+\infty} \frac{d\mathrm{E} f(\mathrm{E})}{(\mathrm{E} - \mathrm{E_n} + i\Gamma)(\mathrm{E} \pm \hbar\omega - \mathrm{E_m} + i\Gamma)(\mathrm{E} - \mathrm{E_l} - i\Gamma)}. \end{aligned} \tag{3.50}$$

Eq. (3.50) can then be integrated numerically, by cutting of the integrals at the lowest and highest energy band respectively. However, numerical integration is expensive since the expressions in Eq. (3.50) have to be sampled over the complete bandstructure and each point in the 3D parameter space spanned by the laser parameters $\{\hbar\omega, \Gamma, \mathrm{E_f}\}$. On the other hand solving Eq. (3.50) analytically allows for a fast evaluation of the energy integrals. The next section

will show that in the zero temperature limit the expressions in Eq. (3.50) are analytically solvable.

### 3.3.4 Analytic energy integration

In the $T = 0$ limit the Fermi distribution is given by a step function $f(\mathrm{E}) = \Theta(\mathrm{E}_f - \mathrm{E})$, thus, the nominator in Eq. (3.50) becomes truly energy independent and the integration has to be performed only up to the Fermi energy. For better readability, the following notation is introduced

$$\xi^{RRR}_{T\to 0}(n, m, l, \mathrm{E_f}) \equiv \int_{-\infty}^{\mathrm{E_f}} \frac{d\mathrm{E}}{(\mathrm{E} - n + i\Gamma)(\mathrm{E} - m + i\Gamma)(\mathrm{E} - l + i\Gamma)}, \tag{3.51}$$

where the band energies $\mathrm{E}_n, \mathrm{E}_m, \mathrm{E}_l$ have been replaced by $n, m, l$.

$$\xi^{RRA}_{T\to 0}(n, m, l, \mathrm{E_f}) \equiv \int_{-\infty}^{\mathrm{E_f}} \frac{d\mathrm{E}}{(\mathrm{E} - n + i\Gamma)(\mathrm{E} - m + i\Gamma)(\mathrm{E} - l + i\Gamma)}. \tag{3.52}$$

Due to the prefactors consisting of energy differences in Eq. (3.51) and Eq. (3.52), numerical instabilities can occur in the cases $n = m \neq l$, $n \neq m = l$, etc.. Even if the system has no degenerate bands, divergences will still be present, since the second argument, here denoted $b$, is not the eigenvalue of the associated band, but the eigenvalue shifted by $\pm\hbar\omega$. Thus, a laser induced band transition will always produce zero energy differences in the denominators. Since the band transitions drive the photoresponses, it is paramount to address the divergences. But first the Fermi sea and surface integral will be solved for the case of non-degenerate bands.

### 3.3.5 Non-degenerate RRR

To perform the integration in Eq. (3.51) and Eq. (3.52) the integrand is first expanded into partial fractions. For the product of two retarded denominators

the partial fraction expansion is considered

$$
\begin{aligned}
&\xi^{RRR}_{T\to 0}(n,m,l,\mathrm{E_f}) \\
&= \int_{-\infty}^{\mathrm{E_f}} \frac{d\mathrm{E}}{(\mathrm{E}-n+i\Gamma)(\mathrm{E}-m+i\Gamma)(\mathrm{E}-l+i\Gamma)} \\
&= \int_{-\infty}^{\mathrm{E_f}} d\mathrm{E} \frac{(n-m)(m-l)(l-n)}{(n-m)(m-l)(l-n)(\mathrm{E}-n+i\Gamma)(\mathrm{E}-m+i\Gamma)(\mathrm{E}-l+i\Gamma)} \\
&= \int_{-\infty}^{\mathrm{E_f}} \frac{d\mathrm{E}}{(n-m)(n-l)(\mathrm{E}-n+i\Gamma)} - \int_{-\infty}^{\mathrm{E_f}} \frac{d\mathrm{E}}{(n-m)(m-l)(\mathrm{E}-m+i\Gamma)} \\
&\quad - \int_{-\infty}^{\mathrm{E_f}} \frac{d\mathrm{E}}{(n-l)(l-m)(\mathrm{E}-l+i\Gamma)}.
\end{aligned}
\tag{3.53}
$$

Eq. (3.53) then consists only of relatively easily solvable integrals of the form

$$
\begin{aligned}
&\int_{-\infty}^{\mathrm{E_f}} \frac{d\mathrm{E}}{(\mathrm{E}-n+i\Gamma)} = \int_{-\infty}^{\mathrm{E_f}} d\mathrm{E} \frac{(\mathrm{E}-n-i\Gamma)}{\left((\mathrm{E}-n)^2-\Gamma^2\right)} \\
&= \int_{-\infty}^{\mathrm{E_f}} d\mathrm{E} \frac{\mathrm{E}-n}{\left((\mathrm{E}-n)^2-\Gamma^2\right)} - \int_{-\infty}^{\mathrm{E_f}} d\mathrm{E} \frac{(+i\Gamma)}{\left((\mathrm{E}-n)^2-\Gamma^2\right)} \\
&= -\frac{1}{2}\ln\left[(n-\mathrm{E})^2-\Gamma^2\right]_{-\infty}^{\mathrm{E}_f} + \frac{1}{i}\arctan\left[\frac{n-\mathrm{E}}{\Gamma}\right]_{-\infty}^{\mathrm{E}_f} \\
&= -\frac{1}{2}\ln\left[(n-\mathrm{E})^2-\Gamma^2\right]_{-\infty}^{\mathrm{E}_f} + \frac{1}{i}\arctan\left[\frac{n-\mathrm{E}_f}{\Gamma}\right] - \frac{\pi}{2i}.
\end{aligned}
\tag{3.54}
$$

And finally plugging Eq. (3.54) into Eq. (3.53) one arrives at the result of Freimuth *et al.* [28]:

$$\begin{aligned}
&\xi^{RRR}_{T\to 0}(n,m,l,\mathrm{E_f}) \\
&= \frac{1}{2\,(n-m)\,(n-l)} \ln\left[1+\frac{\left(n-\mathrm{E}_f\right)^2}{\Gamma^2}\right] \\
&+ \frac{\mathrm{E}_\mathrm{H}^2}{2\,(m-c)\,(m-n)} \ln\left[1+\frac{\left(m-\mathrm{E}_f\right)^2}{\Gamma^2}\right] \\
&+ \frac{1}{2\,(l-n)\,(l-b)} \ln\left[1+\frac{\left(l-\mathrm{E}_f\right)^2}{\Gamma^2}\right] \\
&+ \frac{\mathrm{E}_\mathrm{H}^2}{i\,(n-m)\,(n-l)} \arctan\left[\frac{\mathrm{E}_f-n}{\Gamma}\right] \\
&+ \frac{1}{i\,(m-l)\,(b-a)} \arctan\left[\frac{\mathrm{E}_f-m}{\Gamma}\right] \\
&+ \frac{\mathrm{E}_\mathrm{H}^2}{i\,(c-n)\,(l-m)} \arctan\left[\frac{\mathrm{E}_f-l}{\Gamma}\right].
\end{aligned} \tag{3.55}$$

### 3.3.6 Non-degenerate RRA

In case of the Fermi surface integral in Eq. (3.52) the partial fractional expansion is given by

$$\begin{aligned}
&\xi^{RRA}_{T\to 0}(n,m,l,\mathrm{E_f}) \\
&= \int_{-\infty}^{\mathrm{E_f}} \frac{d\mathrm{E}}{(\mathrm{E}-n+i\Gamma)(\mathrm{E}-m+i\Gamma)(\mathrm{E}-l-i\Gamma)} \\
&= \int_{-\infty}^{\mathrm{E_f}} d\mathrm{E} \frac{(n-m)(-n+l+2i\Gamma)(-m+l+2i\Gamma)}{(n-m)(-n+l+2i\Gamma)(-m+l+2i\Gamma)(\mathrm{E}-n+i\Gamma)(\mathrm{E}-m+i\Gamma)(l-i\Gamma)} \\
&= -\int_{-\infty}^{\mathrm{E_f}} \frac{d\mathrm{E}}{(n-m)(-n+l+2i\Gamma)(\mathrm{E}-n+i\Gamma)} \\
&\quad + \int_{-\infty}^{\mathrm{E_f}} \frac{d\mathrm{E}}{(n-m)(-m+l+2i\Gamma)(\mathrm{E}-m+i\Gamma)} \\
&\quad + \int_{-\infty}^{\mathrm{E_f}} \frac{d\mathrm{E}}{(-n+l+2i\Gamma)(-m+l+2i\Gamma)(l-i\Gamma)}.
\end{aligned} \tag{3.56}$$

From which in a similar fashion as to the Fermi sea integral one can derive[28]

$$
\begin{aligned}
&\xi^{RRA}_{T\to 0}(n,m,l,\mathrm{E_f}) \\
=&\frac{\mathrm{E_H^2}}{2\,(n-m)\,(n-l-2i\Gamma)}\ln\left[1+\frac{(n-\mathrm{E_f})^2}{\Gamma^2}\right] \\
&+\frac{\mathrm{E_H^2}}{2\,(m-l-2i\Gamma)\,(m-n)}\ln\left[1+\frac{(m-\mathrm{E_f})^2}{\Gamma^2}\right] \\
&+\frac{\mathrm{E_H^2}}{2\,(l-n+2i\Gamma)\,(l-m+2i\Gamma)}\ln\left[1+\frac{(l-\mathrm{E_f})^2}{\Gamma^2}\right] \\
&+\frac{i\mathrm{E_H^2}}{(n-m)\,(l-n+2i\Gamma)}\left[\frac{\pi}{2}+\arctan\frac{\mathrm{E_f}-n}{\Gamma}\right] \\
&+\frac{i\mathrm{E_H^2}}{(l-m+2i\Gamma)\,(m-n)}\left[\frac{\pi}{2}+\arctan\frac{\mathrm{E_f}-m}{\Gamma}\right] \\
&+\frac{i\mathrm{E_H^2}}{(l-n+2i\Gamma)\,(l-m+2i\Gamma)}\left[\frac{\pi}{2}+\arctan\frac{\mathrm{E_f}-l}{\Gamma}\right].
\end{aligned}
\tag{3.57}
$$

### 3.3.7 Degenerate bands

In case of $n=m\neq l$ it follows

$$
\begin{aligned}
&\xi^{RRR}_{T\to 0}(n,n,l,\mathrm{E}_f) \\
&=\int_{-\infty}^{\mathrm{E}_f}\frac{d\mathrm{E}}{(\mathrm{E}-n+i\Gamma)^2(\mathrm{E}-l+i\Gamma)} \\
&=\int_{-\infty}^{\mathrm{E}_f}d\mathrm{E}\frac{(n-l)^2(n-l)}{(n-l)^2(n-l)(\mathrm{E}-n+i\Gamma)^2(\mathrm{E}-l+i\Gamma)} \\
&=\int_{-\infty}^{\mathrm{E}_f}\frac{d\mathrm{E}}{(n-l)(\mathrm{E}-n+i\Gamma)^2} \\
&-\int_{-\infty}^{\mathrm{E}_f}\frac{d\mathrm{E}}{(n-l)^2(\mathrm{E}-n+i\Gamma)}+\int_{-\infty}^{\mathrm{E}_f}\frac{d\mathrm{E}}{(n-l)^2(\mathrm{E}-l+i\Gamma)},
\end{aligned}
\tag{3.58}
$$

and with Eq. (3.54)

$$
\begin{aligned}
&=\frac{1}{(n-l)}\left[\frac{1}{(\mathrm{E}-n+i\Gamma)}\right]_{-\infty}^{\mathrm{E}_f} \\
&+\frac{1}{2(n-l)^2}\left(\ln\left[(n-\mathrm{E})^2-\Gamma^2)\right]_{-\infty}^{\mathrm{E}_f}-\ln\left[(l-\mathrm{E})^2-\Gamma^2)\right]_{-\infty}^{\mathrm{E}_f}\right) \\
&-\frac{i}{(n-l)^2}\left(\arctan\left[\frac{n-\mathrm{E}}{\Gamma}\right]_{-\infty}^{\mathrm{E}_f}-\arctan\left[\frac{l-\mathrm{E}}{\Gamma}\right]_{-\infty}^{\mathrm{E}_f}\right).
\end{aligned}
\tag{3.59}
$$

The expressions in Eq. (3.59) then have to be evaluated at the upper bound, which is the Fermi level $\mathrm{E}_f$, and for the lower bound in the minus infinity limit. The first term in Eq. (3.59) is of the form $\sim 1/\mathrm{E}$ and, thus, vanishes at infinity, the arctan is bound by $[-\pi/2, \pi/2]$ and, thus, also converges to a well defined number. However, the logarithms in Eq. (3.59) are more problematic since, although very slowly, the logarithm diverges in the infinity limit.

$$\begin{aligned}
&\xi^{RRR}_{T\to 0}(n,n,l,\mathrm{E}_f)\\
&= \frac{1}{(n-l)}\left[\frac{1}{(\mathrm{E}_f - n + i\Gamma)} - 0\right]\\
&+ \frac{1}{2(n-l)^2}\left(\ln\left[(n-\mathrm{E}_f)^2 - \Gamma^2)\right] - \ln\left[(l-\mathrm{E}_f)^2 - \Gamma^2)\right]\right)\\
&- \frac{i}{(n-l)^2}\left(\arctan\left[\frac{\mathrm{E}_f - n}{\Gamma}\right] - \frac{\pi}{2} - \arctan\left[\frac{\mathrm{E}_f - l}{\Gamma}\right] + \frac{\pi}{2}\right)\\
&- \frac{1}{2(n-l)^2}\left(\lim_{\mathrm{E}\to-\infty}\ln\left[(n-\mathrm{E})^2 - \Gamma^2)\right] - \lim_{\mathrm{E}\to-\infty}\ln\left[(l-\mathrm{E})^2 - \Gamma^2)\right]\right).
\end{aligned} \tag{3.60}$$

From Eq. (3.60) one directly arrives at the final expression

$$\begin{aligned}
\xi^{RRR}_{T\to 0}(n,n,l,\mathrm{E}_f) &= -\frac{1}{(l-n)}\frac{1}{(\mathrm{E}_f - n + i\Gamma)}\\
&- \frac{1}{2(n-l)^2}\left(\ln\left[\frac{((l-\mathrm{E}_f)^2 - \Gamma^2)}{((n-\mathrm{E}_f)^2 - \Gamma^2)}\right]\right)\\
&- \frac{1}{i(n-l)^2}\left(\arctan\left[\frac{\mathrm{E}_f - l}{\Gamma}\right] - \arctan\left[\frac{\mathrm{E}_f - n}{\Gamma}\right]\right).
\end{aligned} \tag{3.61}$$

Eq. (3.61) is in good agreement with the quantity $I_1$ given in Eq.(B6) in the work by Freimuth *et al.* [28]. Eq. (3.55) will also diverge in the special case of $a \neq b = c$ and $a = c \neq b$, these cases can be calculated with Eq. (3.61) by realizing

$$\xi^{RRR}_{T\to 0}(n,n,m,\mathrm{E}_f) = \xi^{RRR}_{T\to 0}(n,m,n,\mathrm{E}_f) = \xi^{RRR}_{T\to 0}(m,n,n,\mathrm{E}_f). \tag{3.62}$$

In the degenerate scenario the Fermi surface energy integrals can be expanded to

$$\begin{aligned}
&\xi^{RRA}_{T\to 0}(n,n,l,\mathrm{E}_f)\\
&=\int_{-\infty}^{\mathrm{E}_f}\frac{d\mathrm{E}}{(\mathrm{E}-n+i\Gamma)^2(\mathrm{E}-l-i\Gamma)}\\
&=\int_{-\infty}^{\mathrm{E}_f}d\mathrm{E}\frac{(-n+l+2i\Gamma)^2(n-l-2i\Gamma)}{(-n+l+2i\Gamma)^2(n-l-2i\Gamma)(\mathrm{E}-n+i\Gamma)^2(\mathrm{E}-l+i\Gamma)}\\
&=\int_{-\infty}^{\mathrm{E}_f}\frac{d\mathrm{E}}{(n-l-2i\Gamma)(\mathrm{E}-n+i\Gamma)^2}\\
&\quad+\int_{-\infty}^{\mathrm{E}_f}\frac{d\mathrm{E}}{(-n+l+2i\Gamma)^2(\mathrm{E}-l+i\Gamma)}\\
&\quad-\int_{-\infty}^{\mathrm{E}_f}\frac{d\mathrm{E}}{(-n+l+2i\Gamma)^2(\mathrm{E}-n+i\Gamma)}.
\end{aligned}\tag{3.63}$$

Eq. (3.64) has a very similar structure to Eq. (3.58) and is therefore not red-erived here, the final expression is directly adopted from Eq. (B7) in the work of Freimuth *et al.*[28]

$$\begin{aligned}
\xi^{RRA}_{T\to 0}(n,n,l,\mathrm{E}_f) &= -\frac{1}{(n-l+2i\Gamma)}\frac{1}{(\mathrm{E}_f-n+i\Gamma)}\\
&-\frac{1}{2(n-l)^2}\left(\ln\left[\frac{(l-\mathrm{E}_f)^2-\Gamma^2}{(a-\mathrm{E}_f)^2-\Gamma^2}\right]\right)\\
&-\frac{1}{i(n-l)^2}\left(\pi+\arctan\left[\frac{\mathrm{E}_f-l}{\Gamma}\right]+\arctan\left[\frac{\mathrm{E}_f-n}{\Gamma}\right]\right).
\end{aligned}\tag{3.64}$$

### 3.3.8 Double degenerate bands

In the special case $n=m=l$ it follows directly that

$$\xi^{RRR}_{T\to 0}(n,n,n,\mathrm{E}_f)=\int_{-\infty}^{\mathrm{E}_f}\frac{d\mathrm{E}}{(\mathrm{E}-n+i\Gamma)^3}=\frac{1}{(\mathrm{E}_f-n+i\Gamma)^2}.\tag{3.65}$$

Code snippets of the analytic energy integrals can be found in Section A.5.

In the next sections various operators will be plugged into Eq. (3.47) and Eq. (3.48) to derive expression for the second order charge photocurrents, spin photocurrents and the laser induced nonequilibrium spin density.

## 3.4 SECOND ORDER CHARGE PHOTOCURRENTS

From Eq. (3.47) it follows directly for the photocurrent density [29]:

$$J_a \equiv \langle ev_a \rangle = \frac{1}{i}\,\mathrm{Tr}[ev_a G^{<}_{\mathrm{DC}}] = \frac{a_0^2 eI}{\hbar c}\left(\frac{\mathrm{E_H}}{\hbar\omega}\right)^2 \mathrm{Im}\sum_{bc}\varepsilon_b\varepsilon_c^*\varphi_{abc}, \tag{3.66}$$

where $a_0$ is the Bohr radius, $e$ is the elementary charge, $\hbar$ is the reduced Planck constant and $I$ is the field intensity. The field intensity is given by $I = \epsilon_0 c E_0^2/2$, where $\epsilon_0$ is the vacuum permittivity. Although $J_i$ is in fact the photocurrent density, for brevity it will be referred to as the photocurrent. Units of the photocurrent will be given in terms of the current density units, namely A/m for 2D and A/m$^2$ for 3D systems respectively. The photoconductivity tensor $\varphi_{ijk}$ is given by plugging the velocity operator $v_i$ into Eq. (3.48)

$$\begin{aligned}\varphi_{abc} =& \frac{2}{a_0\mathrm{E_H}}\int\frac{\mathrm{d}^D k}{(2\pi)^D}\int \mathrm{dE}\,\mathrm{Tr}[\\ & f(\mathrm{E})v_a G^{\mathrm{R}}_{\boldsymbol{k}}(\mathrm{E})v_b G^{\mathrm{R}}_{\boldsymbol{k}}(\mathrm{E}-\hbar\omega)v_c G^{\mathrm{R}}_{\boldsymbol{k}}(\mathrm{E})\\ & -f(\mathrm{E})v_a G^{\mathrm{R}}_{\boldsymbol{k}}(\mathrm{E})v_b G^{\mathrm{R}}_{\boldsymbol{k}}(\mathrm{E}-\hbar\omega)v_c G^{\mathrm{A}}_{\boldsymbol{k}}(\mathrm{E})\\ & +f(\mathrm{E})v_a G^{\mathrm{R}}_{\boldsymbol{k}}(\mathrm{E})v_c G^{\mathrm{R}}_{\boldsymbol{k}}(\mathrm{E}+\hbar\omega)v_b G^{\mathrm{R}}_{\boldsymbol{k}}(\mathrm{E})\\ & -f(\mathrm{E})v_a G^{\mathrm{R}}_{\boldsymbol{k}}(\mathrm{E})v_c G^{\mathrm{R}}_{\boldsymbol{k}}(\mathrm{E}\hbar\omega)v_b G^{\mathrm{A}}_{\boldsymbol{k}}(\mathrm{E})\\ & +f(\mathrm{E}-\hbar\omega)v_a G^{\mathrm{R}}_{\boldsymbol{k}}(\mathrm{E})v_b G^{\mathrm{R}}_{\boldsymbol{k}}(\mathrm{E}-\hbar\omega)v_c G^{\mathrm{A}}_{\boldsymbol{k}}(\mathrm{E})\\ & + f(\mathrm{E}+\hbar\omega)v_a G^{\mathrm{R}}_{\boldsymbol{k}}(\mathrm{E})v_c G^{\mathrm{R}}_{\boldsymbol{k}}(\mathrm{E}+\hbar\omega)v_b G^{\mathrm{A}}_{\boldsymbol{k}}(\mathrm{E})\Big],\end{aligned} \tag{3.67}$$

where $v_a$ is the a-th component of the velocity operator, $D \in [1, 2, 3]$ is the dimensionality of the system, $f(\mathrm{E})$ is the Fermi-Dirac distribution function and $G^{\mathrm{R/A}}_{\boldsymbol{k}}$ is the equilibrium retarded/advanced Greens function as defined in Eq. (3.49).

To compute the photocurrent the integrals in Eq. (3.67) have to be evaluated. At zero temperature the Fermi distribution becomes a step function which allows one to perform the energy integration analytically as discussed above. The integral over the Brillouin zone is performed numerically by summing over a set of $k$-points discretizing the first Brillouin zone.

### 3.4.1 *Units of charge photocurrents*

To derive the units of the charge photocurrents in Eq. (3.66) the units of the response tensor Eq. (3.67) have to be derived first

$$[\varphi_{abc}] = \frac{2}{a_0\mathrm{E_H}}\frac{(1/a_0)^D}{(2\pi)^D}\mathrm{E_H}[v]^3[G^{\mathrm{R/A}}(\mathrm{E})]^3 \tag{3.68}$$

using[99] $[v] = a_0 \mathrm{E_H}/\hbar$ and the definition of the retarded/advanced Greens function Eq. (3.49) it follows

$$\begin{aligned}[\varphi_{abc}] &= \frac{2}{a_0 \mathrm{E_H}} \mathrm{E_H} \frac{(1/a_0)^D}{(2\pi)^D} \frac{a_0^3 \mathrm{E}_h^3}{\hbar^3} \frac{\hbar^3}{\mathrm{E}_h^3} \\ &= \frac{2}{(2\pi)^D} a_0^{2-D}.\end{aligned} \tag{3.69}$$

The dependence on the dimensionality $D$ is required since the current density is calculated which requires to normalize the current with the real space cell volume.

### 3.4.2 Literature correspondence

In literature the photocurrent is often expressed in the form[69]

$$J_a = \mathrm{Re} \sum_{bc} 2\sigma_{abc} E_b E_c^*. \tag{3.70}$$

With Eq. (3.66) the photoconductivity $\sigma_{abc}$ can be expressed in terms of the Keldysh photoconductivity $\varphi_{abc}$

$$\sigma_{abc} := i \frac{a_0^2 e \epsilon_0}{2\hbar} \frac{\varphi_{abc}}{2}. \tag{3.71}$$

### 3.4.3 Fermi sea and surface contributions and the zero frequency limit

The second order conductivity in Eq. 3.67 is given by terms constructed from retarded and advanced Greens functions. Terms solely constructed with the retarded Greens functions can be identified as Fermi sea contributions, while mixed terms are identified as Fermi surface contributions. The second order conductivity is then given by the sum of the two contributions

$$\varphi_{abc}(\hbar\omega) = \varphi_{abc}^{\mathrm{sea}}(\hbar\omega) + \varphi_{abc}^{\mathrm{surf}}(\hbar\omega), \tag{3.72}$$

where

$$\begin{aligned}\varphi_{abc}^{sea}(\hbar\omega) =& \frac{2}{a_0 \mathrm{E_H}} \int \frac{\mathrm{d}^D k}{(2\pi)^D} \int \mathrm{dE}\, \mathrm{Tr}[ \\ & f(\mathrm{E}) v_a G_{\boldsymbol{k}}^{\mathrm{R}}(\mathrm{E}) v_b G_{\boldsymbol{k}}^{\mathrm{R}}(\mathrm{E} - \hbar\omega) v_c G_{\boldsymbol{k}}^{\mathrm{R}}(\mathrm{E}) \\ & + f(\mathrm{E}) v_a G_{\boldsymbol{k}}^{\mathrm{R}}(\mathrm{E}) v_c G_{\boldsymbol{k}}^{\mathrm{R}}(\mathrm{E} + \hbar\omega) v_b G_{\boldsymbol{k}}^{\mathrm{R}}(\mathrm{E})],\end{aligned} \tag{3.73}$$

and

$$\begin{aligned}\varphi^{surf}_{abc}(\hbar\omega) =& \frac{2}{a_0 \mathrm{E_H}} \int \frac{\mathrm{d}^D k}{(2\pi)^D} \int \mathrm{dE}\, \mathrm{Tr}[ \\ & -f(\mathrm{E}) v_a G^{\mathrm{R}}_{\boldsymbol{k}}(\mathrm{E}) v_b G^{\mathrm{R}}_{\boldsymbol{k}}(\mathrm{E}-\hbar\omega) v_c G^{\mathrm{A}}_{\boldsymbol{k}}(\mathrm{E}) \\ & -f(\mathrm{E}) v_a G^{\mathrm{R}}_{\boldsymbol{k}}(\mathrm{E}) v_c G^{\mathrm{R}}_{\boldsymbol{k}}(\mathrm{E}+\hbar\omega) v_b G^{\mathrm{A}}_{\boldsymbol{k}}(\mathrm{E}) \\ & +f(\mathrm{E}-\hbar\omega) v_a G^{\mathrm{R}}_{\boldsymbol{k}}(\mathrm{E}) v_b G^{\mathrm{R}}_{\boldsymbol{k}}(\mathrm{E}-\hbar\omega) v_c G^{\mathrm{A}}_{\boldsymbol{k}}(\mathrm{E}) \\ & + f(\mathrm{E}+\hbar\omega) v_a G^{\mathrm{R}}_{\boldsymbol{k}}(\mathrm{E}) v_c G^{\mathrm{R}}_{\boldsymbol{k}}(\mathrm{E}+\hbar\omega) v_b G^{\mathrm{A}}_{\boldsymbol{k}}(\mathrm{E}) \Big] . \end{aligned} \tag{3.74}$$

In the zero frequency limit $\hbar\omega \longrightarrow 0$ the surface term vanishes

$$\begin{aligned}\varphi^{surf}_{abc}(\hbar\omega \longrightarrow 0) =& \frac{2}{a_0 \mathrm{E_H}} \int \frac{\mathrm{d}^D k}{(2\pi)^D} \int \mathrm{dE}\, \mathrm{Tr}[ \\ & -f(\mathrm{E}) v_a G^{\mathrm{R}}_{\boldsymbol{k}}(\mathrm{E}) v_b G^{\mathrm{R}}_{\boldsymbol{k}}(\mathrm{E}) v_c G^{\mathrm{A}}_{\boldsymbol{k}}(\mathrm{E}) \\ & -f(\mathrm{E}) v_a G^{\mathrm{R}}_{\boldsymbol{k}}(\mathrm{E}) v_c G^{\mathrm{R}}_{\boldsymbol{k}}(\mathrm{E}) v_b G^{\mathrm{A}}_{\boldsymbol{k}}(\mathrm{E}) \\ & +f(\mathrm{E}) v_a G^{\mathrm{R}}_{\boldsymbol{k}}(\mathrm{E}) v_b G^{\mathrm{R}}_{\boldsymbol{k}}(\mathrm{E}) v_c G^{\mathrm{A}}_{\boldsymbol{k}}(\mathrm{E}) \\ & + f(\mathrm{E}) v_a G^{\mathrm{R}}_{\boldsymbol{k}}(\mathrm{E}) v_c G^{\mathrm{R}}_{\boldsymbol{k}}(\mathrm{E}) v_b G^{\mathrm{A}}_{\boldsymbol{k}}(\mathrm{E}) \Big] \\ =& \, 0, \end{aligned} \tag{3.75}$$

while the sea term can still contribute

$$\begin{aligned}\varphi^{sea}_{abc}(\hbar\omega \longrightarrow 0) =& \frac{2}{a_0 \mathrm{E_H}} \int \frac{\mathrm{d}^D k}{(2\pi)^D} \int \mathrm{dE}\, \mathrm{Tr}[ \\ & f(\mathrm{E}) v_a G^{\mathrm{R}}_{\boldsymbol{k}}(\mathrm{E}) v_b G^{\mathrm{R}}_{\boldsymbol{k}}(\mathrm{E}) v_c G^{\mathrm{R}}_{\boldsymbol{k}}(\mathrm{E}) \\ & +f(\mathrm{E}) v_a G^{\mathrm{R}}_{\boldsymbol{k}}(\mathrm{E}) v_c G^{\mathrm{R}}_{\boldsymbol{k}}(\mathrm{E}) v_b G^{\mathrm{R}}_{\boldsymbol{k}}(\mathrm{E})] . \end{aligned} \tag{3.76}$$

Figure 3.4 shows as an example the second order conductivity tensor approaching the zero frequency in the bulk semiconductor GaAs. Since the DFT calculation of GaAs produced a finite bandgap of about 400 meV no photoresponse is expected in GaAs for laser frequencies below $\hbar\omega \lesssim 200$ meV and any response appearing here can be safely considered a numerical divergence raised by the energy denominators of the nonequilibrium Greens function. Note that the experimental bandgap of GaAs is much larger and a scissors shift can be applied within the Wannier basis to remedy the undershooting of bandgap [69], a detailed description of the photoresponses calculated for GaAs can be found in subsection 6.4.2. Figure 3.4 shows the real (blue) and imaginary (red) part of the conductivity tensor. The solid lines represent the Fermi sea contribution while dotted lines show the surface contribution. Laser frequencies in a range from 10 to 500 meV were considered and the broadening fixed to $\Gamma = 100$ meV.

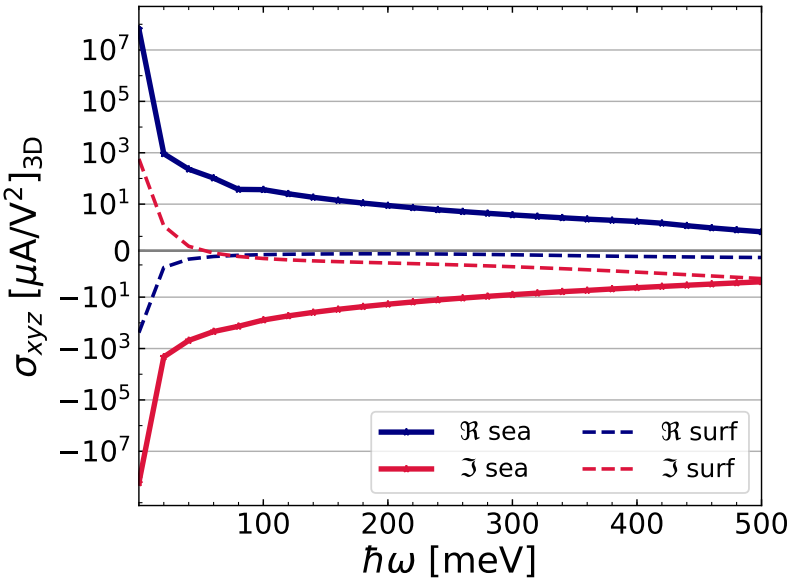


**Figure 3.4.** Real (blue) and imaginary (red) part of the photoconductivity tensor approaching the zero frequency limit in bandgaped semiconductor GaAs. The solid lines show the Fermi sea term while dashed lines indicate the surface contribution.

Figure 3.4 shows that the sea term dominates in the zero frequency limit, for frequencies of $\hbar\omega = 200$ meV or smaller the sea terms conductivity is larger then $10\mu$A/V$^2$ with almost perfect exponential scaling in the range between $\hbar\omega$ =40 and 500 meV. The surface contribution is mostly suppressed and only starts to diverge for Laser frequencies below 100 meV. It is noted that numerical divergencies in the zero frequency limit can, based on heuristic observations of the author, be mitigated by improving the quality of Wannier functions, especially increasing the number of *ab-initio* bands used for the projection onto Wannier functions helped, or by using more $k$-points in the Wannier interpolation. In all systems considered in this work the Fermi surface term was dominating at finite frequencies of $\hbar\omega \gtrsim 600$ meV). Therefore, in many cases it is advisable to focus the discussion on the Fermi surface response.

## 3.5 SPIN PHOTOCURRENTS

In a similar fashion it follows for the spin current density $Q_a^s$

$$Q_a^s = -\frac{a_0^2 I}{4c}\left(\frac{\mathrm{E_H}}{\hbar\omega}\right)^2 \mathrm{Im}\sum_{bc}\varepsilon_b\varepsilon_c^*\phi_{abc}^s, \tag{3.77}$$

where $i$ indicates the direction in which the spin current is flowing and $s$ the direction in which the spins are pointing. $\phi_{abc}^s$ is the second order spin conductivity as given by

$$\begin{aligned}\phi_{abc}^s = \frac{2}{a_0\mathrm{E_H}}\int\frac{\mathrm{d}^D k}{(2\pi)^D}\int \mathrm{dE}\,\mathrm{Tr}[\\ f(\mathrm{E})\,\{v_a,\tau_s\}\,G_{\boldsymbol{k}}^{\mathrm{R}}(\mathrm{E})v_b G_{\boldsymbol{k}}^{\mathrm{R}}(\mathrm{E}-\hbar\omega)v_c G_{\boldsymbol{k}}^{\mathrm{R}}(\mathrm{E})\\ -f(\mathrm{E})\,\{v_a,\tau_s\}\,G_{\boldsymbol{k}}^{\mathrm{R}}(\mathrm{E})v_b G_{\boldsymbol{k}}^{\mathrm{R}}(\mathrm{E}-\hbar\omega)v_c G_{\boldsymbol{k}}^{\mathrm{A}}(\mathrm{E})\\ +f(\mathrm{E})\,\{v_a,\tau_s\}\,G_{\boldsymbol{k}}^{\mathrm{R}}(\mathrm{E})v_c G_{\boldsymbol{k}}^{\mathrm{R}}(\mathrm{E}+\hbar\omega)v_b G_{\boldsymbol{k}}^{\mathrm{R}}(\mathrm{E})\\ -f(\mathrm{E})\,\{v_a,\tau_s\}\,G_{\boldsymbol{k}}^{\mathrm{R}}(\mathrm{E})v_c G_{\boldsymbol{k}}^{\mathrm{R}}(\mathrm{E}+\hbar\omega)v_b G_{\boldsymbol{k}}^{\mathrm{A}}(\mathrm{E})\\ +f(\mathrm{E}-\hbar\omega)\,\{v_a,\tau_s\}\,G_{\boldsymbol{k}}^{\mathrm{R}}(\mathrm{E})v_b G_{\boldsymbol{k}}^{\mathrm{R}}(\mathrm{E}-\hbar\omega)v_c G_{\boldsymbol{k}}^{\mathrm{A}}(\mathrm{E})\\ +f(\mathrm{E}+\hbar\omega)\,\{v_a,\tau_s\}\,G_{\boldsymbol{k}}^{\mathrm{R}}(\mathrm{E})v_c G_{\boldsymbol{k}}^{\mathrm{R}}(\mathrm{E}+\hbar\omega)v_b G_{\boldsymbol{k}}^{\mathrm{A}}(\mathrm{E})\Big],\end{aligned} \tag{3.78}$$

where $\tau_s$ is the $s$-component of the Pauli operator.

### 3.5.1 Units

The spin photoconductivity in Eq. (3.78) is closely related to the charge photoconductivity Eq. (3.67), but instead of the velocity operator it couples the anticommutator of velocity and Pauli operator $\{v_i, \tau_s\}$ to the nonequilibrium electronic system. Since the Pauli operator is dimensionless, the units of the the charge and spin photoconductivity are identical and from Eq. (3.69) it follows directly

$$\left[\phi_{abc}^s\right] = \left[\varphi_{abc}\right] = \frac{2}{(2\pi)^D}a_0^{2-D}. \tag{3.79}$$

## 3.6 NONEQUILIBRIUM SPIN DENSITY

Besides the photocurrents of charge and spin the laser can also directly induce a nonequilibrium spin density $\delta\boldsymbol{S}$ given by the ansatz [28]

$$\delta\boldsymbol{S} = \int d^3r\,\delta\boldsymbol{S}(\boldsymbol{r}) = \frac{\hbar}{2i}\,\mathrm{Tr}\left[\boldsymbol{\tau}G^<\right], \tag{3.80}$$

such that

$$\delta S_a = -\frac{\hbar}{2}\frac{a_0^3 I}{c}\left(\frac{\mathrm{E_H}}{\hbar\omega}\right)^2 \mathrm{Im}\sum_{bc}\varepsilon_b\varepsilon_c^*\chi_{abc}. \tag{3.81}$$

The response tensor $\chi_{abc}$ is then given by plugging the Pauli operator $\boldsymbol{\tau}$ into the second order DC Greens function given in Eq. (3.48):

$$\begin{aligned}\chi_{abc} \equiv & \frac{2}{\mathcal{N}\hbar a_0^2}\sum_k \int d\mathrm{E} \\ & \times \mathrm{Tr}\Big[f(\mathrm{E})\tau_a G_k^{\mathrm{R}}(\mathrm{E})v_b G_k^{\mathrm{R}}(\mathrm{E}-\hbar\omega)v_c G_k^{\mathrm{R}}(\mathrm{E}) \\ & - f(\mathrm{E})\tau_a G_k^{R}(\mathrm{E})v_b G_k^{R}(\mathrm{E}-\hbar\omega)v_c G_k^{A}(\mathrm{E}) \\ & + f(\mathrm{E})\tau_a G_k^{\mathrm{R}}(\mathrm{E})v_c G_k^{\mathrm{R}}(\mathrm{E}+\hbar\omega)v_b G_k^{\mathrm{R}}(\mathrm{E}) \\ & - f(\mathrm{E})\tau_a G_k^{\mathrm{R}}(\mathrm{E})v_c G_k^{\mathrm{R}}(\mathrm{E}+\hbar\omega)v_b G_k^{\mathrm{A}}(\mathrm{E}) \\ & + f(\mathrm{E}-\hbar\omega)\tau_a G_k^{R}(\mathrm{E})v_b G_k^{R}(\mathrm{E}-\hbar\omega)v_c G_k^{A}(\mathrm{E}) \\ & + f(\mathrm{E}+\hbar\omega)\tau_a G_k^{\mathrm{R}}(\mathrm{E})v_c G_k^{\mathrm{R}}(\mathrm{E}+\hbar\omega)v_b G_k^{\mathrm{A}}(\mathrm{E})\Big].\end{aligned} \tag{3.82}$$

### 3.6.1 Units

The units of the nonequilibrium spin density response tensor $\chi_{abc}$ are given by

$$[\chi_{abc}] = \frac{2}{\hbar a_0^2}\mathrm{E_H}[\tau_a] = \frac{2}{\hbar a_0^2}\mathrm{E_H}[-]. \tag{3.83}$$

To derive the units of the nonequilibrium spin density first the laser intensity $I = \epsilon_0 c E_0^2/2$ is plugged into Eq. (3.81)

$$\delta S_a = -\frac{\hbar}{2}\frac{a_0^3\epsilon_0 c E_0^2}{2c}\frac{\mathrm{E_H}}{(\hbar\omega)^2}\,\mathrm{Im}\sum_{bc}\varepsilon_j\varepsilon_k^*\chi_{abc}. \tag{3.84}$$

Realizing that $[E_0] = \mathrm{E_H}/(ea_0)$ the units of Eq. (3.84) are given by

$$\begin{aligned}[\delta S_a] &= -\frac{\hbar}{2}\frac{a_0^3\epsilon_0[E_0]^2}{2}\frac{\mathrm{E_H}}{([\hbar_\omega])^2}[\chi_{abc}] \\ &= -\frac{\hbar}{2}\frac{a_0^3\epsilon_0(\mathrm{E}_h^2/(e^2a_0^2))}{2}\frac{\mathrm{E_H}}{\mathrm{E}_h^2}[\chi_{abc}] \\ &= -\frac{\hbar}{4}\frac{a_0\epsilon_0}{e^2}\mathrm{E_H}[\chi_{abc}].\end{aligned} \tag{3.85}$$

Using the definition of the Bohr radius[99] $a_0 = 4\pi\epsilon_0\hbar^2/(m_e e^2) \Leftrightarrow \epsilon_0 = a_0 m_e e^2/(4\pi\hbar^2)$ it follows

$$[\delta S_a] = -\frac{\hbar}{4}\frac{a_0^2 m_e e^2}{4\pi e^2\hbar^2}\mathrm{E_H}[\chi_{abc}]. \tag{3.86}$$

Finally expressing the Hartree energy as[99] $\mathrm{E_H} = \hbar^2/(m_e a_0^2)$ yields

$$[\delta S_a] = -\frac{1}{4}\frac{a_0^2 m_e}{4\pi\hbar}\frac{\hbar^2}{m_e a_0^2}[\chi_{abc}] = -\frac{\hbar}{4}\frac{1}{4\pi}[2] = -\frac{1}{4\pi}(\frac{\hbar}{2}). \tag{3.87}$$

## 3.7 ORBITAL EFFECTS

In analogy to the laser induced spin density Eq. (3.81) and the spin photocurrents Eq. (3.77) it is possible to calculate the laser induced orbital magnetization and orbital photocurrent by plugin the angular momentum operator, here denoted by $\varsigma_i$, into the Keldysh formalism. The laser induced orbital magnetization is defined as

$$\delta L_a = -\frac{\hbar}{2}\frac{a_0^3 I}{c}\frac{\mathrm{E_H}}{(\hbar\omega)^2}\,\mathrm{Im}\sum_{bc}\varepsilon_b\varepsilon_c^*\tilde{\chi}_{abc}, \tag{3.88}$$

where $\tilde{\chi}_{abc}$ is the orbital magnetization tensor given by replacing the Pauli operator $\tau_s$ in Eq. (3.82) with the angular momentum operator $\varsigma_l$. To distinguish the spin and the orbital the index $s$ was replaced by the index $l$. The laser induced orbital photocurrent is denoted by $J_a^l$ and is given by

$$J_a^l = -\frac{a_0^2 I}{4c}\left(\frac{\mathrm{E_H}}{\hbar\omega}\right)^2\mathrm{Im}\sum_{bc}\varepsilon_b\varepsilon_c^*\tilde{\phi}_{abc}^l, \tag{3.89}$$

where $\tilde{\phi}_{abc}^l$ is the orbital photoconductivity tensor given by replacing the Pauli operator in Eq. (3.78) with the angular momentum operator $\varsigma_l$.

### 3.7.1 *Units*

The units of the laser induced orbital magnetization are in principle the same as for the laser induced spin density. However, the Fleur code[100] writes out the Pauli operator in units of $\hbar/2$, while the angular momentum operator is provided in units of $\hbar$. To compare orbital and spin effects it is advantageous to present both effects in units of $\hbar/2$. Therefore, in the calculation of orbital effects an overall factor 2 has to be applied to the response to match the units of the spin based effects.

## 3.8 Resonant transitions

Resonant transitions are defined as transitions were the initial and final state are the same.

## 3.9 Laser parameters

In order to provide sound predictions of photoresponses to laser sources, it is important to choose reasonable values for the laser intensity $I$ and frequency $\omega$. Throughout this work a 50 fs pulsed laser of intensity I=10 GW/cm$^2$ will be considered, mimicking the parameters of a Ti:sapphire laser [101,102], which is capable of producing light in the near-infrared up to red frequency range. The default laser frequency will therefore be set to $\hbar\omega = 1.55\,\text{eV}$ which corresponds to red light of wavelength $\lambda = 800\,\text{nm}$. Since the laser intensity enters the Keldysh formalism linearly, the presented results can easily be converted to other laser intensities. Results will usually be presented for a range of laser frequencies (usually within $\hbar\omega = 0.2\,\text{eV}$ up to $\hbar\omega = 5.0\,\text{eV}$) to allow experimentalists to tune THz sources such that photoresponses are maximized.

Part III

# Methods

# Chapter 4

# *Density Functional Theory*

In the previous part of the thesis fundamentals of the calculation of (spin) photocurrents with the Keldysh nonequilibrium formalism were derived. In this part the practical methods of calculating laser induced effects are discussed in three chapters. The first chapter focuses on Density functional theory (DFT) calculations performed with the Fleur code [100]. In the second chapter Wannier functions will be introduced and the interface between Fleur and the Wannier90 code [103] will be briefly discussed. In the third chapter the *ju_wip* code will be introduced. This post-processing tool was developed during the course of this PhD, and it performs the Wannier interpolation and calculates various response quantities.

## 4.1 The many-body problem

A crystal can be understood as a collection of electrons and atomic nuclei which interact with each other via the Coulomb interaction. The (unperturbed) crystal's time evolution is given by the Schrödinger equation. The Hamiltonian $H$ contains kinetic energy terms of electrons $T_e$ and nuclei $T_{\text{nuc}}$, interactions within the nucleus $H_{\text{nuc}}$, electron electron interactions $H_{\text{ee}}$ and the interactions of electrons with the nucleus $H_{\text{ee-nuc}}$. The complete Hamiltonian $H$ is then given by the sum of the individual contributions

$$H = T_{\text{nuc}} + H_{\text{nuc}} + T_e + H_{\text{ee}} + H_{\text{ee-nuc}}. \tag{4.1}$$

## 4.2 Born-Oppenheimer Approximation

The full many-body system of the crystal is described by Eq. (4.1), however it can not be solved with current computational hardware. Therefore, approximations have to be made to simplify the Hamiltonian, such that it can be solved in a reasonable time. The mass of an electron $m_e$ is in general much smaller than the mass of a nucleus $m_{\text{nuc}}$ such that

$$m_e << m_{\text{nuc}}, \tag{4.2}$$

thus effectively the electron's mobility is much higher than that of the nucleus, which appear stationary. According to the Born-Oppenheimer approximation the purely ionic contribution $H_{\text{nuc}}$ can thus be detached from Eq. (4.1) and solved individually. The wavefunction of $N_{\text{nuc}}$ cores are then solutions to the Schrödinger equation with the Hamiltonian given in atomic units as

$$H = T_{\text{nuc}} + H_{\text{nuc}} = -\sum_A \frac{1}{2M_A}\nabla_A^2 + \sum_{B>A} \frac{Z_A Z_B}{|R_A - R_B|}, \tag{4.3}$$

where $M_A$ is the mass of the nucleus $A$ with $A = 1, .., N_{\text{nuc}}$, $Z_A$ its atomic number and $R_A$ its position. The wavefunctions of the electrons are solutions to the Schrödinger equation given by the Hamiltonian [104]

$$H = T_e + H_{\text{ee}} + H_{\text{ee-nuc}}, \tag{4.4}$$

where $T_e$ is the kinetic energy, $H_{\text{ee}}$ describes the Coulomb interaction of the electrons and $H_{\text{ee-nuc}}$ accounts for the electrons interaction with the nuclei. The electronic Eq. (4.1) simplifies to

$$H\,|\Psi\rangle = (T_e + H_{\text{ee}} + H_{\text{ee-nuc}})\,|\Psi\rangle = \mathrm{E}\,|\Psi\rangle\,, \tag{4.5}$$

where $|\Psi\rangle$ is the wavefunction of all the $N_e$ electrons in the crystal, which takes the electronic positions as argument

$$|\Psi\rangle = |\Psi(\mathbf{r}_1, \ldots, \mathbf{r}_{N_e})\rangle\,. \tag{4.6}$$

As Kohn pointed out, storing the many body wavefunction in Eq. (4.6), requires at least $N_p$ variables with [105]

$$N_p = p^{3N_e}, \tag{4.7}$$

where $p$ is the number of parameters per electron, usually $3 \leq p \leq 10$. Generously assuming that each parameter can be stored with a single bit, Eq. (4.7) can be used to estimate the memory requirements for a given number of interacting electrons $N_e$. Assuming one has a contemporary 1 Tbit=$1 \times 10^{12}$ bit of storage available the maximum number of electrons would be $\approx 8$. Even the 1kg ultimate black hole laptop [21] mentioned in the introduction (see Section 1.1), whose memory capacity is governed by its entropy, would only be able to handle roughly 22 electrons! Thus, it would be advantageous to decouple the electrons from each other and treat the interactions by some external potential in which the electrons are moving. Assuming the Born-Oppenheimer approximation the interactions of the electrons with the nuclei can be treated as an external potential $V_{\text{ext}}$. Hartree suggested a system of

decoupled electrons, with, assuming atomic units, the wavefunction $|\Psi_i\rangle$ of electron $i$ given by [106]

$$-\frac{1}{2}\nabla^2 |\Psi_i\rangle - V_{\text{ext}}(\mathbf{r}_i) |\Psi_i\rangle + \frac{1}{2}\sum_{i\neq j} \frac{1}{|\mathbf{r}_i - \mathbf{r}_j|} |\Psi_i\rangle = \mathrm{E}_i |\Psi_i\rangle , \tag{4.8}$$

where the first term on the left side describes the kinetic energy of the electron, the second term describes the external potential which accounts for the interaction of the electron $i$ with the atomic nuclei and the third term describes the Coulomb interaction of the electron $i$ with all the other electrons $j$. The many-body wavefunction $|\Psi\rangle$ in Eq. (4.6) is then approximated by, what is known as, the Hartree product [106] of the single particle wavefunctions $|\Psi_i\rangle$ defined as solutions of the Hartree equation Eq. (4.8)

$$|\Psi\rangle \approx \prod_i |\Psi_i\rangle . \tag{4.9}$$

## 4.3 HOHENBERG-KOHN THEOREMS

Since wavefunctions are not observables and only their probability density is, the knowledge of the wavefunction itself is not required to calculate ground state properties of the many-body system. Knowledge of the ground state density of a given many-body ground state $|\Psi_{\text{gs}}\rangle$ defined as

$$n_{\text{gs}}(\mathbf{r}) = \langle\Psi_{\text{gs}}| \sum_i \delta(\mathbf{r} - \mathbf{r}_i) |\Psi_{\text{gs}}\rangle \tag{4.10}$$

is sufficient, and properties such as the system's ground state energy can be expressed as functionals of the density

$$E_{gs} = E_{gs}[n]. \tag{4.11}$$

To describe an interacting electron gas moving in an effective potential $V_{\text{ext}}(\mathbf{r})$ as given in Eq. (4.8) via the density Eq. (4.10) and the ground state energy functional Eq. (4.11), Hohenberg & Kohn formulated the following theorems [107]

1. Uniqueness

   For a system of interacting particles moving in an external potential $V_{\text{ext}}(\mathbf{r})$, the ground state density $n_{\text{gs}}(\mathbf{r})$ uniquely determines the external potential $V_{\text{ext}}(\mathbf{r})$ up to a constant shift. Thus, given a projection $G$, that projects the ground state density $n_{\text{gs}}(\mathbf{r})$ onto the external potential $V_{\text{ext}}(\mathbf{r})$, such that

   $$G[n_{\text{gs}}] = V_{\text{ext}}(\mathbf{r}), \tag{4.12}$$

$G$ is invertible.

2. Variatonal principle

$$\begin{aligned} E_{gs}[n] &> E_{gs} \; \forall n \neq n_{gs} \\ E_{gs}[n_{gs}] &= E_{gs} \end{aligned} \tag{4.13}$$

The variational principle states that in the scenario of a non-degenerate ground state, the ground state energy functional in Eq. (4.11) will always produce energy values larger than the ground state energy $E_0$, unless the ground state density $n_0$ is plugged in. In case of a degenerate ground state, Levy showed that the variational principle holds, however the inequality condition then reads $E_{gs}[n] \geq E_{gs}$ [108,109]. From the variational principle it follows that a universal energy functional $F[n]$, independent of $V_{\text{ext}}$, can be defined, which, when minimized by plugging in the ground state density $n_{gs}$, yields the ground state energy $E_{gs}$.

The theorems by Hohenberg and Kohn allow one to describe a system of interacting particles solely in terms of functionals of the ground state density $n_{gs}$, such that [110]

$$\begin{aligned} E_{\text{gs}}[n] &= \langle \Psi_{\text{gs}}[n] | \, T_e[n] + W[n] \, | \Psi_{\text{gs}}[n] \rangle + \langle \Psi_{\text{gs}}[n] | \, \hat{V}_{\text{ext}} \, | \Psi_{\text{gs}}[n] \rangle \\ &= \langle \Psi_{\text{gs}}[n] | \, F[n] \, | \Psi_{\text{gs}}[n] \rangle + \langle \Psi_{\text{gs}}[n] | \, \hat{V}_{\text{ext}} \, | \Psi_{\text{gs}}[n] \rangle , \end{aligned} \tag{4.14}$$

where $T_e[n]$ is the kinetic energy functional and $W[n]$ is the interaction energy functional which together build the universal functional $F[n] = T_e[n] + W[n]$. Based on the theorems by Hohenberg and Kohn, Kohn and Sham developed an auxiliary system of non-interacting electrons expressed in terms of functionals of the ground state density, which allowed for computational calculation of interacting many-body systems in a self-consistent manner [111].

## 4.4 Kohn-Sham equations

Based on the Hohenberg and Kohn theorem, Kohn and Sham formulated the following energy functional [111]

$$\begin{aligned} E_{\text{gs}}[n] =& \langle \Psi_{\text{gs}}[n] | \, T_e[n] + U_{\text{H}}[n] + E_{xc}[n] \, | \Psi_{\text{gs}}[n] \rangle \\ &+ \langle \Psi_{\text{gs}}[n] | \, \hat{V}_{\text{ext}} \, | \Psi_{\text{gs}}[n] \rangle \\ \equiv& F[n] + \int d\mathbf{r} V_{\text{ext}}(\mathbf{r}) n(\mathbf{r}), \end{aligned} \tag{4.15}$$

where the first part of the right-hand side can be identified as the universal functional $F[n]$ which is independent on the underlying crystal structure. The universal functional of Kohn and Sham is, thus, given by [111]

$$F[n] = T_e[n] + U_{\mathrm{H}}[n] + E_{\mathrm{xc}}[n], \tag{4.16}$$

where $T_e[n]$ is the kinetic energy functional, $U_{\mathrm{H}}[n]$ the Hartree and $E_{xc}[n]$ the exchange-correlation ($xc$) energy functional, with the Hartree energy functional given by

$$U_{\mathrm{H}}[n] = \frac{1}{2}\int\int d\mathbf{r}d\mathbf{r}'\frac{n(\mathbf{r})n(\mathbf{r}')}{|\mathbf{r}-\mathbf{r}'|}. \tag{4.17}$$

Remembering the variatonal principle one can require

$$\frac{\delta\left[E_{\mathrm{gs}}[n(\mathbf{r})] + \mu(N_e - \int d\mathbf{r}n(\mathbf{r}))\right]}{\delta n(\mathbf{r})} = 0, \tag{4.18}$$

where $\mu$ is a Lagrange multiplier introduced to enforce a constant electron count $N_e = \int d\mathbf{r}n(\mathbf{r}) = \text{const}$. Thus, $\mu$ is the true Fermi level of the system. To solve Eq. (4.15) under the requirement of Eq. (4.18) Kohn and Sham proposed the following ansatz: The ground state density $n_{\mathrm{gs}}$ can be represented by the ground state density of a system of noninteracting Kohn-Sham orbitals $\phi_j$ moving in an effective potential $V_{\mathrm{eff}}(\mathbf{r})$. Combining the ansatz with Eq. (4.15) yields the set of Kohn-Sham equations [111]

$$[-\tfrac{1}{2}\nabla^2 + V_{\mathrm{eff}}(\mathbf{r})]\phi_j(\mathbf{r}) = \mathrm{E}_j\phi_j(\mathbf{r}) \tag{4.19}$$

of $N_e$ independent particles moving in the effective potential $V_{\mathrm{eff}}(\mathbf{r}) = V_H(\mathbf{r}) + V_{xc}(\mathbf{r}) + V_{\mathrm{ext}}(\mathbf{r})$, with the ground state density of the interacting system given by the sum over the probability densities of the noninteracting Kohn-Sham orbitals $n(\mathbf{r}) = \sum_{j=1}^{N_e}|\phi_j(\mathbf{r})|^2$. The kinetic energy functional is then evaluated as the sum over the kinetic energy of the Kohn-Sham orbitals

$$T_{\mathrm{KS}}[n] = -\frac{1}{2}\sum_j^{N_e}\langle\phi_j|\,\nabla^2\,|\phi_j\rangle = -\frac{1}{2}\sum_j^{N_e}|\nabla\phi_j(\mathbf{r})|^2. \tag{4.20}$$

$V_H(\mathbf{r})$ in Eq. (4.19) is the Hartree potential [106] describing the Coulomb interaction between electrons and the overall electronic charge density. $V_{xc}(\mathbf{r})$ is the potential describing the exchange and correlation effects of the electronic system. Both potentials are defined as the functional derivative of their counterparts in Eq. (4.16)

$$\begin{aligned} V_H(\mathbf{r}) &= \frac{\delta\left[U_H[n(\mathbf{r})]\right]}{\delta n(\mathbf{r})} = \int d\mathbf{r}'\frac{n(\mathbf{r}')}{|\mathbf{r}-\mathbf{r}'|}, \\ V_{xc}(\mathbf{r}) &= \frac{\delta\left[E_{xc}[n(\mathbf{r})]\right]}{\delta n(\mathbf{r})}. \end{aligned} \tag{4.21}$$

The exchange-correlation functional $E_{xc}[n(\mathbf{r})]$ is so far only implicitly defined as difference between the kinetic energy and potential functionals of the fully interacting many-body system defined in Eq. (4.14) with the kinetic and Hartree energy functionals of the Kohn-Sham auxiliary system defined in Eq. (4.20) and Eq. (4.17). Implicitly $E_{xc}[n(\mathbf{r})]$ is, thus, defined as

$$E_{xc}[n(\mathbf{r})] \equiv (T_e[n] - T_{\mathrm{KS}}[n]) + (W[n] - U_{\mathrm{H}}[n]) \tag{4.22}$$

and in practice has to be approximated. The most prominent approximations for the exchange-correlation energy functional will be discussed in the next section. Eq. (4.19) builds the "Kohn-Sham system of equations" which allows to describe $N_e$ interacting electrons moving in an external potential by solving the set of single particle Schrödinger equations in Eq. (4.19). Summing over the set of Kohn-Sham orbitals $\phi_j(\mathbf{r})$ yields the density which is then plugged into Eq. (4.21) to calculate the electronic potential. To construct the set in Eq. (4.19), knowledge of the density is required to obtain Eq. (4.19) and Eq. (4.21) forcing one to solve the system self consistently with an iterative procedure. For this usually a initial guess of the density $n_0(\mathbf{r})$ is made to setup the potential in Eq. (4.21) which is plugged into the Schrödinger equation Eq. (4.19). Solving the Schrödinger equation yields an updated density $n_1(\mathbf{r})$ from which an updated potential can be calculated and so on. This procedure is then repeated until the updated density meets some convergence criterion

$$\frac{1}{V}\int d\mathbf{r}|n_{i+1}(\mathbf{r}) - n_i(\mathbf{r})| \leq \zeta, \tag{4.23}$$

where $V$ is the volume of the unit cell and $\zeta$ is a generic convergence parameter. Note that Eq. (4.23) is only given here as a trivial example, the convergence criterion in modern DFT codes might be less trivial.

### 4.4.1 Extension to magnetic systems

Since the Fleur code was used in this thesis to calculate collinear magnetic materials as presented in Chapter 7 and Chapter 8, the extension of the above formalism to collinear magnetic systems is briefly outlined here. It is noted that non-collinear magnetism requires more effort to be implemented and is beyond the scope of this work. The interested reader is pointed to [112]. To treat collinear magnetism the Kohn-Sham system is extended from a scalar into the 2×2 Pauli basis spanned by the Pauli matrices $\tau_i$. A magnetization density $\mathbf{m}(\mathbf{r})$ is introduced with is defined as

$$\mathbf{M} = \int d\mathbf{r}\mathbf{m}(\mathbf{r}), \tag{4.24}$$

where $\mathbf{M}$ is the magnetization of the system. Eq. (4.19) is then slightly reformulated to

$$\begin{aligned}
[-\tfrac{1}{2}\nabla^2 + V_{\mathrm{NM}}^{\uparrow\downarrow}(\mathbf{r}) + \mu_0 \boldsymbol{\tau}\cdot\mathbf{B}_{\mathrm{eff}}]\phi_j(\mathbf{r}) &= \mathrm{E}_j\phi_j(\mathbf{r}),\\
n(\mathbf{r}) &= \sum_{j=1}^{N} |\phi_j(\mathbf{r})|^2,\\
\mathbf{m}(\mathbf{r}) &= -\mu_0 \sum_{j=1}^{N} \phi_j^* \boldsymbol{\tau}\phi_j,
\end{aligned} \tag{4.25}$$

where $\boldsymbol{\tau}$ is the Pauli vector and the single-particle wavefunctions were split into an up and down contribution

$$\phi_j = \begin{pmatrix} \phi_j^{\uparrow} \\ \phi_j^{\downarrow} \end{pmatrix}. \tag{4.26}$$

Eq. (4.25) is then solved under the usual constraint of fixed electron number with an additional new constraint requiring the total magnetization as defined in Eq. (4.24) to be fixed. $V_{\mathrm{NM}}^{\uparrow\downarrow}$ in Eq. (4.25) is given by the effective potential describing the non-magnetic system as given in Eq. (4.19), however the exchange-correlation potential will in general depend on the density and the magnetization $\mathrm{E}_{xc} = \mathrm{E}_{xc}[n(\mathbf{r}), \mathbf{m}(\mathbf{r})]$ and thus $V_{\mathrm{NM}}^{\uparrow\downarrow}$ is defined separately for spin-up $V_{\mathrm{NM}}^{\uparrow}$ and spin-down states $V_{\mathrm{NM}}^{\downarrow}$ such that

$$V_{\mathrm{NM}}^{\uparrow\downarrow} = \begin{pmatrix} V_{\mathrm{NM}}^{\uparrow} \\ V_{\mathrm{NM}}^{\downarrow} \end{pmatrix}. \tag{4.27}$$

Differentiating the exchange-correlation functional with respect to the density yields the non-magnetic exchange-correlation potential, while "differentiating" the functional with respect to magnetization yields an effective magnetic field $\mathbf{B}_{xc}$

$$\begin{aligned}
V_{xc}(\mathbf{r}) &= \frac{\delta \mathrm{E}_{xc}[n(\mathbf{r}), \mathbf{m}(\mathbf{r})]}{\delta n(\mathbf{r})},\\
\mathbf{B}_{xc}(\mathbf{r}) &= \frac{\delta \mathrm{E}_{xc}[n(\mathbf{r}), \mathbf{m}(\mathbf{r})]}{\delta \mathbf{m}(\mathbf{r})}.
\end{aligned} \tag{4.28}$$

The effective magnetic field in Eq. (4.25) is then given by the effective field associated to the $xc$-functional plus an optionally applied external magnetic field $\mathbf{B}_{\mathrm{ext}}$

$$\mathbf{B}_{\mathrm{eff}} = \mathbf{B}_{xc} + \mathbf{B}_{\mathrm{ext}}. \tag{4.29}$$

In this work however external magnetic fields will be added to the Wannier interpolated Hamiltonian directly as outlined in subsection 6.3.4 and applied in Chapter 9.

## 4.5 Exchange-correlation potential

The exchange-correlation potential ($xc$-potential) describes the effects of exchange and correlation in the electronic system. Different approximations of the $xc$-functional exist and their respective quality depends in general on the system to be simulated. One of the simplest approximations is to assume that the electrons form a homogeneous electron gas.

### 4.5.1 LDA

The local density approximation (LDA) is the simplest commonly known functional to approximate the $xc$-potential. The LDA assumes electrons to be delocalized and describes them as a homogeneous electron gas (HEG), thus, requiring $n(\mathbf{r}) = \text{const}$.

$$\mathrm{E}_{xc}^{\mathrm{LDA}}[n] = \int d\mathbf{r} n(\mathbf{r}) e_{xc}[n(\mathbf{r})], \tag{4.30}$$

where $e_{xc}[n(\mathbf{r})]$ is the exchange-correlation energy density ($xc$-energy density) consisting of the exchange $e_x$ and the correlation $e_c$ energy density. Within the LDA $e_x$ is given by the exchange energy density of a homogeneous electron gas [111]

$$e_x[n(\mathbf{r})] = -\tfrac{3}{4\pi} k_{\mathrm{F}} = -\tfrac{3}{4}\left(\tfrac{3}{\pi}\right)^{1/3} n^{1/3}, \tag{4.31}$$

where $k_{\mathrm{F}}$ is the Fermi surface given by $k_{\mathrm{F}} = \sqrt{2 m_e \mathrm{E}_{\mathrm{F}}}/\hbar$ with $m_e$ the electron mass, $\mathrm{E}_{\mathrm{F}}$ the Fermi energy and $\hbar$ the reduced Plank constant. The correlation energy density however has to be approximated based on quantum Monte Carlo simulations [113–116]. Within LDA often structural properties, the lattice constant, as well as the bandstructure and density of states are describes with good accuracy. However, LDA has several shortcomings, it overbinds the system [117], it fails to predict the band gap [118–121] and has problems to describe magnetic systems [122–126].

### 4.5.2 GGA

To remedy the aforementioned shortcomings of LDA it was first proposed to expand the $xc$-functional of Eq. (4.30) in powers of the gradient of the density in order to increase accuracy of the exchange-correlation functional

in systems with sufficiently fast varying density. This is known as the gradient expansion approximation (GEA) in which the following ansatz is made

$$\begin{aligned} \mathrm{E}_{xc}^{\mathrm{GEA}}[n] =& \mathrm{E}_{xc}^{\mathrm{LDA}}[n] \\ &+ \tfrac{1}{2} \int d\mathbf{r} \alpha(n(\mathbf{r}))(\nabla n(\mathbf{r}))^2 \\ &+ \tfrac{1}{2} \int d\mathbf{r} \beta(n(\mathbf{r}))(\nabla^2 n(\mathbf{r}))^2 \\ &+ \dots . \end{aligned} \tag{4.32}$$

However the ansatz failed since it was not able to improve the predictive power of LDA and often worsened results [127]. The method was then refined in what is known as the generalized gradient approximation (GGA) [128] in which the gradient of the density and its higher-order derivatives are considered to construct

$$\mathrm{E}_{xc}^{\mathrm{GGA}}[n] = \mathrm{E}_{xc}^{\mathrm{LDA}}[n] + \int d\mathbf{r} f(n, \nabla n, \nabla^2 n, \dots). \tag{4.33}$$

where $f(n, \nabla n, \nabla^2 n, \dots)$ is a parameter dependent mixing of the density and its (higher-order) derivatives. The parameters should then be chosen such that the accuracy of the DFT calculation is improved, on the other hand the dependence of the functional on external parameters foils the first principles or *ab-initio* spirit of the DFT calculation. A widely adopted GGA functional is the one proposed by Perdew-Burke-Ernzerhof (PBE) in which all parameters are constants [129], thus, recovering the *ab-initio* nature of the calculation. The GGA improves the accuracy over the LDA in most scenarios [130], corrects its overbinding [131–133] and is often used for magnetic materials [134,135]. DFT calculations presented in subsection 6.4.2, Chapter 7 and Chapter 8 all used the PBE functional. subsection 6.4.2 is a good example of the underestimation of the bandgap, here by $\sim$ 1 eV in case of the semiconductor GaAs. In that section the influence of the underestimated band gap on the photoresponses is also analyzed.

## 4.6 FLAPW

To conclude the chapter the FLAPW method employed by the Fleur code [100] is outlined. FLAPW is an abbreviation for full-potential linearized augmented-plane-wave method, and it uses a linearized augmented plane wave basis set [136]. Already in 1929 Bloch realized that non-interacting electrons moving in a periodic potential, such as the Coulomb interaction with the cores in a crystal lattice, can be described by plane-waves modulated with a lattice

periodic function[137]

$$\xi_{\mathbf{q}}(\mathbf{r}) = u_{\mathbf{q}}(\mathbf{r})e^{i\mathbf{q}\cdot\mathbf{r}}, \tag{4.34}$$

where $u_{\mathbf{q}}(\mathbf{r})$ has the periodicity of the lattice and $\mathbf{q}$ is the wavevector of the plane wave. Eq. (4.34) later became known as Bloch functions[138]. For a given reciprocal lattice vector $\mathbf{G}$ Eq. (4.34) holds $\xi_{n\mathbf{q}}(\mathbf{r}) = \xi_{n\mathbf{q}+\mathbf{G}}(\mathbf{r})$. Thus, knowledge of the Bloch waves within the first Brillouin zone is enough to describe the complete crystal. In principle with Eq. (4.34) as basis functions a basis set up could be constructed to describe the Kohn-Sham orbitals in Eq. (4.19) and Eq. (4.25), however the $1/r$ Coulomb potential of the cores has poles at the atomic positions which cannot be described well by a pure plane wave basis set. One strategy to remedy the diverging Coulomb attraction is to cut off the $1/r$-potential at some point close to the core and replace it with a non-diverging pseudopotential. Due to its simplicity, the pseudopotential approach is quite popular, but it does not work well for heavy cores and depends in general on the chosen cutoff radius beyond which the Coulomb potential is approximated. Instead, within the FLAPW method a more complex basis set is constructed to handle the diverging potential more efficiently. The idea is to split the basis set in two regions: A region close to the core, in which spherical harmonics are used as basis functions and only in between these core regions plane waves are used. The spheres around the cores are referred to as the muffin-tin spheres, or simply muffin-tins, due to their resemblance with a muffin or cupcake tin (see Figure 4.1). The flat regions in between the muffin-tins are referred to as the interstitial region.

**Figure 4.1.** A muffin or cupcake tin[139].

Assuming $N_{at}$ atoms in the unit cell, positioned at $\boldsymbol{\tau}_a$ with $a \in [1, ..., N_{at}]$, a set of muffin-tin spheres $MT_a$ surrounded by an interstitial region IS is constructed in the FLAPW method. Basis functions are then given for the

muffin-tin spheres and interstitial regions individually [136]

$$\xi_{\mathbf{qG}}(\mathbf{r}) = \begin{cases} \frac{1}{\sqrt{V}} e^{i(\mathbf{q}+\mathbf{G})\cdot\mathbf{r}} & \text{if } \mathbf{r} \in \text{IS} \\ \sum_{l}^{l_{\max,\alpha}} \sum_{m=-l}^{l} Y_{lm}(\mathbf{r}_a) \Big[ \alpha^a_{lm}(\mathbf{q},\mathbf{G}) u^a_l(\|\mathbf{r}_a\|) & \\ \qquad + \beta^a_{lm}(\mathbf{q},\mathbf{G}) \dot{u}^a_l(\|\mathbf{r}_a\|) \Big] & \text{if } \mathbf{r} \in \text{MT}_a \end{cases}, \quad (4.35)$$

where $V$ is the volume of the real space unit cell, $\varkappa$ indicates spin-up or spin-down states, $\|\mathbf{r}\|$ denotes the Euclidean vector norm of a vector $\mathbf{r}$, $l$ and $m$ are the angular and magnetic quantum number and $Y_{lm}(\mathbf{r}_a)$ are the spherical harmonics evaluated for $\mathbf{r}_a = \mathbf{r} - \boldsymbol{\tau}_a$. $u^a_l(\|\mathbf{r}_a\|)$ and $\dot{u}^{a\varkappa}_l(\|\mathbf{r}_a\|)$ are solutions to the radial Schrödinger equation and their energy derivatives respectively. The basis functions in Eq. (4.35) are known as linearized augmented-plane-waves (LAPWs). With Eq. (4.35) a basis set can be constructed via

$$|\psi_{j\mathbf{q}}(\mathbf{r})\rangle = \sum_{\mathbf{G}} c^{\mathbf{G}}_{j\mathbf{q}} |\xi_{\mathbf{q},\mathbf{G}}(\mathbf{r})\rangle, \quad (4.36)$$

where $j$ is the index of Kohn-Sham orbitals considered with $j = 1, .., N_e$ and $c^{\mathbf{G}}_{j\mathbf{q}}$ are the basis coefficients to be determined. The coefficients $\alpha^a_{lm}(\mathbf{q},\mathbf{G})$ and $\beta^a_{lm}(\mathbf{q},\mathbf{G})$ in Eq. (4.35) are chosen such that the overall Bloch function $\psi_{j\mathbf{q}}(\mathbf{r})$ is smooth at the interface between a muffin-tin sphere and the surrounding interstitial region. The basis set in Eq. (4.36) is cut-off at some finite wave vector $G_{\max} > \|\mathbf{q}+\mathbf{G}\|$. The plane wave cut-off $G_{\max}$ and the number of $\mathbf{q}$'s to sample the first Brillouin zone are important convergence parameters for a DFT calculation. To find the basis coefficients $c^{\mathbf{G}}_{j\mathbf{q}}$ a Hamiltonian $H^{\mathbf{q}}_{\mathbf{G}',\mathbf{G}}$ is set up based on Kohn-Sham equations defined in Eq. (4.19) and Eq. (4.25):

$$H^{\mathbf{q}}_{\mathbf{G}',\mathbf{G}} = \langle \xi_{\mathbf{q},\mathbf{G}'} | \hat{T}_{\mathbf{s}} + V_{\text{eff}}(\mathbf{r}) | \xi_{\mathbf{k},\mathbf{G}} \rangle . \quad (4.37)$$

Besides using the LAPW basis set given by Eq. (4.35), within the FLAPW method the effective potential of the Kohn-Sham system in Eq. (4.19) is expanded in the LAPW basis as well such that

$$V(\mathbf{r}) = \begin{cases} \sum_{\mathbf{G}} V^{\mathbf{G}}_I e^{i\mathbf{G}\mathbf{r}} & \text{if } \mathbf{r} \in \text{IS} \\ \sum_L V^L_{MT}(r) Y_L(\hat{\mathbf{r}}) & \text{if } \mathbf{r} \in \text{MT}_a, \end{cases} \quad (4.38)$$

where $V^{\mathbf{G}}_I$ is the Fourier transform of the effective potential in the interstitial region, $V^L_{MT}(r)$ the effective potential within the muffin-tin spheres and $\hat{\mathbf{r}}$ a unit vector along the vector $\mathbf{r}$. Due to Eq. (4.38) additional cut-offs for the

plane wave expansion of the potential and an additional cut-off for the expansion of the exchange-correlation potential $g_{\max}$ and $g_{\max,xc}$ are introduced. Eq. (4.35), Eq. (4.37) and Eq. (4.38) outline the FLAPW method, a detailed description of the method and the potential setup within the individual regions is omitted here, since it would go beyond the scope of this work, the interested reader is pointed to [136].

### 4.6.1 Relativistic effects

In the field of spintronics the spin-orbit coupling (SOC) is a crucial mechanism which connects the electronic to the spin degrees of freedom [56]. Laser induced spin-based effects, such as the inverse Faraday effect (IFE), heavily depend on spin-orbit interaction [41], since the laser's electromagnetic field couples to the electronic system and requires SOC to induce the magnetization associated with the IFE. The reader is pointed here to recent reports suggesting a direct coupling of a laser pulse's orbital angular momentum to spin degrees of freedom in [140]. SOC effects in Fleur are included by first setting up a scalar relativistic Hamiltonian in the muffin-tins. After solving the scalar relativistic Hamiltonian the overall Hamiltonian including the SOC contribution is expanded in terms of the eigenvectors of the scalar relativistic Hamiltonian. Diagonalizing the SOC Hamiltonian then yields the final eigenstates and eigenenergies. This is known as the second variation treatment of spin orbit coupling within Fleur [100].

### 4.6.2 Wannier functions within FLAPW

The generation of maximally localized Wannier functions with the Fleur code [100] and its interface to Wannier90 [103] as given by Freimuth *et al.* [141] will be outlined in the next chapter.

# Chapter 5

## *Wannier Functions*

In this work Wannier functions are used to calculate second order photoresponses by means of the nonequilibrium Keldysh formalism introduced in Chapter 3. To calculate photoresponses such as the photocurrent, the velocity operator and band energies have to be known on a set of sufficiently dense $k$-points sampling the Brillouin zone [142]. Often at least 256 $k$-points per dimensions are required, resulting in more than one million $k$-points to be calculated in total for a 3D material. Due to the large basis size of an *ab-initio* DFT calculation performed with the Fleur code [100], a direct computation of second order photoresponses in the DFT basis set on millions of $k$-points is computationally very expensive, but not impossible [41]. In the approach presented here the $k$-point mesh used to converge the density matrix, $k_{\mathrm{DFT}}$, is rather coarse, often only 8 to 16 $k_{\mathrm{DFT}}$-points per dimension are used, which

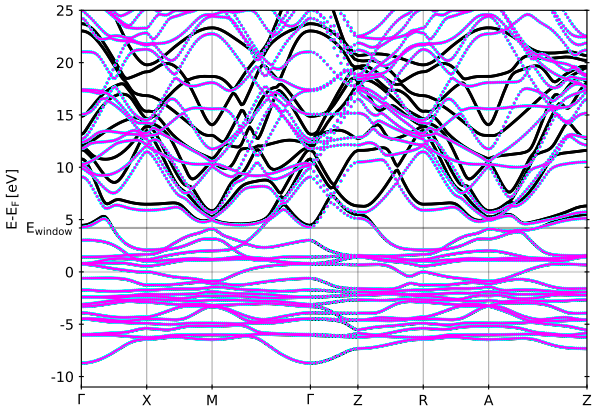


**Figure 5.1.** Example of a Wannier interpolated bandstructure, here the bandstructure of bulk AFM $Mn_2Au$. The *ab-initio* bandstructure obtained with Fleur is shown in cyan and magenta for spin-up and spin-down states, respectively. The Wannier interpolated bands are given in black. The frozen energy window was set to 4.2 eV above the true Fermi level and is indicated in the plot.

is not enough to even converge first order responses. To remedy the lack of $k$-points available in the DFT calculation, one can use the technique of Wannier interpolation (WI) to interpolate additional $k$-points in between the $k_{\mathrm{DFT}}$ points.

To deploy the Wannier interpolation technique, one has to set up the Wannier functions first, which are defined as a backward Fourier transform of the Bloch states from reciprocal to real space. The Wannier functions allow one to extract a real space basis set, which within a given energy region, known as frozen energy window, gives an accurate representation of the Bloch states. In a second step the real space basis set is Fourier transformed again, this time onto a sufficiently dense $k$-mesh $k_{\mathrm{WI}}$, such that the desired photoresponse tensors are converged when integrating over all $k_{\mathrm{WI}}$-points. To avoid confusion between the *ab-initio* and the interpolated $k$-mesh and keep the notation simple, the *ab-initio* $k$-points will be referred to as $q$-points throughout this chapter, $\mathbf{k}_{\mathrm{DFT}} \equiv \mathbf{q}_{\mathrm{DFT}}$, and the interpolation mesh points as $\mathbf{k}_{\mathrm{WI}} = \mathbf{k}$, such that

$$N_{k_{\mathrm{DFT}}} = N_{q_{\mathrm{DFT}}} << N_k = N_{k_{\mathrm{WI}}}. \tag{5.1}$$

This step is known as the Wannier interpolation, since the dense $k_{\mathrm{WI}}$-mesh interpolates $k$-points in between the original mesh points $\mathbf{q}_{\mathrm{DFT}}$. As an example Figure 5.1 shows the bandstructure of 54 Wannier functions extracted from a DFT calculation of the metallic antiferromagnet $Mn_2Au$. Up to the frozen energy window, indicated by $E_{\mathrm{window}}$, the Fleur bands and the Wannier bands are perfectly on top of each other. However above the energy window deviations between *ab-initio* and interpolated bands are visible.

In this chapter the construction and interpolation of maximally localized Wannier functions [143,144] with the Wannier90 code [103] is outlined, with an emphasis on the interface between Fleur [100] and Wannier90 [141].

## 5.1 Introduction

Wannier functions were originally defined by Gregory H. Wannier as Fourier Transform of the Bloch states from a set of $N_{\mathbf{q}}$ $\mathbf{q}$-points onto a lattice of $N_{\mathbf{R}} = N_{\mathbf{q}}$ real space cells at points $\mathbf{R}$ [145]. Due to the properties of the Fourier Transform smooth functions in $\mathbf{q}$-space result in well localized Wannier functions in real space, which is a necessary requirement to obtain smooth functions in the aforementioned Wannier interpolated $\mathbf{k}$-space given by the inverse Fourier Transformation of the real space Wannier functions [142]. Assuming a set of $N$ Bloch states, the Wannier function of band $n \in [1, .., N]$

in real space cell $\mathbf{R}$ is given by [143,144]

$$|\mathbf{R}j\rangle = \frac{V}{(2\pi)^3}\int d\mathbf{q} e^{-i\mathbf{q}\cdot\mathbf{R}}\,|\psi_{j\mathbf{q}}\rangle\,, \tag{5.2}$$

where $V$ is the volume of the unit cell and $|\psi_{n\mathbf{q}}\rangle$ is the $n$-th Bloch state at $\mathbf{q}$.

There is, however, no unique set of Wannier functions associated with the Hamiltonian, due to the invariance of the Schrödinger equation under a phase change. The Bloch wave function $|\psi_{n\mathbf{q}}\rangle$ multiplied with a phase factor $\varphi_n(\mathbf{q})$

$$|\tilde{\psi}_{n\mathbf{q}}\rangle := e^{i\varphi_n(\mathbf{q})}\,|\psi_{n\mathbf{q}}\rangle \tag{5.3}$$

is still a solution to the Hamiltonian. This is known as "gauge freedom" of the Bloch waves, since expectation values are independent of the chosen gauge. Wannier functions are not observables (although their probability density is) and can be influenced by choice of gauge. A choice of gauge is defined as a set of unitary rotation matrices $U_{mn}(\mathbf{q}) \in \mathbb{C}^{N\times N}$ which change the phase of the wave functions via

$$|\tilde{\psi}_{n\mathbf{q}}\rangle = \sum_{m=1}^{N} U_{mn}^{(\mathbf{q})}\,|\psi_{n\mathbf{q}}\rangle\,, \tag{5.4}$$

also known as "gauge transformation". Combining Eq. (5.2) with Eq. (5.4) yields the transformed Wannier function

$$|\widetilde{\mathbf{R}n}\rangle = \frac{V}{(2\pi)^3}\int d\mathbf{q} e^{-i\mathbf{q}\cdot\mathbf{R}}\sum_{m=1}^{N} U_{mn}(\mathbf{q})\,|\psi_{n\mathbf{q}}\rangle\,. \tag{5.5}$$

This gauge freedom raises the question of an ideal choice of gauge. In case of smooth Bloch functions Eq. (5.2) would already produce well localized Wannier functions. However, if the Bloch functions are calculated numerically, for example by a DFT code such as the Fleur code [100], a problem arises: At each $\mathbf{q}$-point a matrix inversion has to be performed to obtain the eigenvalues and the coefficients of the Hamiltonian in the Bloch basis. Usually the inversion is done by optimized matrix libraries such as Lapack [146], which allow for a fast computation of the inverse but, due to the invariance of the Hamiltonian to a phase factor, introduce random phases at each $\mathbf{q}$-point [141]. Due to the random phase factor the resulting Bloch waves are in general not smooth over the Brillouin zone, resulting in poorly localized Wannier functions in real space. To remedy this problem, the gauge transformation of the Wannier functions given in Eq. (5.5) can be utilized. The idea is to find a set of gauge transformations $U_{mn}(\mathbf{q})$ at each $\mathbf{q}$-point such that the resulting Wannier functions $|\widetilde{\mathbf{R}n}\rangle$ are well localized in real space. Since the $\mathbf{q}$ mesh is

often rather coarse and only a few Wannier functions will be extracted, such an optimization can be performed in a reasonable time. In the next section the spread of the Wannier functions will be introduced as a metric to characterize the localization of the Wannier functions in real space. Further, the procedure of finding the maximally localized Wannier functions (MLWFs) by minimizing the spread will be outlined.

## 5.2 MLWF

Often a gauge is chosen such that the real space spread of the Wannier functions is minimized. Good localization within the real space supercell spanned by lattice vectors **R** will improve the smoothness of the interpolated $k$-space quantities. The maximally localized Wannier functions (MLWF)[143,144] are defined as Wannier functions with a gauge choice that minimizes the spread of the Wannier functions and, thus, maximizes the localization of the WFs and the quality of interpolated quantities. The spread $\Omega$ of the Wannier functions is defined as[144]

$$\Omega := \sum_n \left[ \left\langle r^2 \right\rangle_n - \overline{\mathbf{r_n}}^2 \right], \tag{5.6}$$

where $\left\langle r^2 \right\rangle_n$ is the squared position operator and $\overline{\mathbf{r_n}} = \langle \mathbf{R}n \,|\, \mathbf{r} \,|\, \mathbf{0}n \rangle$ the center of the $n$-th Wannier function at lattice cite **R**. The spread defined in Eq. (5.6) can be split into a gauge independent part $\Omega_\mathrm{I}$ and the remaining gauge dependent contribution $\widetilde{\Omega}$[143] such that $\Omega = \Omega_\mathrm{I} + \widetilde{\Omega}$. The gauge independent part $\Omega_\mathrm{I}$ is given by

$$\Omega_\mathrm{I} = \sum_n \left[ \left\langle r^2 \right\rangle_n - \sum_{\mathbf{R}m} |\langle \mathbf{R}m|\mathbf{r}|\mathbf{0}n\rangle|^2 \right]. \tag{5.7}$$

Since $\Omega_\mathrm{I}$ is by definition invariant under any gauge transformation, minimizing the overall spread $\Omega$ given in Eq. (5.6) simplifies to finding a gauge transformation which minimizes the gauge dependent contribution $\widetilde{\Omega}$ given by[143]

$$\widetilde{\Omega} = \sum_n \sum_{\mathbf{R}m \neq \mathbf{0}n} |\langle \mathbf{R}m|\mathbf{r}|\mathbf{0}n\rangle|^2. \tag{5.8}$$

To minimize the gauge dependent contribution it is practical to further split Eq. (5.8) into a band diagonal contribution $\widetilde{\Omega}_\mathrm{D}$[143]

$$\widetilde{\Omega}_\mathrm{D} = \sum_n \sum_{\mathbf{R} \neq \mathbf{0}} |\langle \mathbf{R}n|\mathbf{r}|\mathbf{0}n\rangle|^2 \tag{5.9}$$

and the remaining off-diagonal contribution

$$\widetilde{\Omega}_{\mathrm{OD}} = \sum_{m \neq n} \sum_{\mathbf{R}} |\langle \mathbf{R}m|\mathbf{r}|\mathbf{0}n\rangle|^2. \tag{5.10}$$

Since most *ab-initio* codes, including the Fleur code, work in momentum space a momentum space formulation of Eq. (5.6) is desirable. First the lattice periodic part of the Bloch function $u_{n\mathbf{q}}(\mathbf{r})$ is defined as

$$u_{n\mathbf{q}}(\mathbf{r}) := e^{-i\mathbf{q}\cdot\mathbf{r}}\psi_{n\mathbf{q}}(\mathbf{r}). \tag{5.11}$$

As Blount realized the real space position operator translates into a derivative in momentum space [147], so that for the Wannier centers it follows

$$\overline{\mathbf{r_n}} = -\frac{V}{(2\pi)^3}\int \mathrm{d}\mathbf{q}\left\langle u_{n\mathbf{q}}\middle|\nabla_{\mathbf{q}}\middle|u_{m\mathbf{q}}\right\rangle. \tag{5.12}$$

In analogy the square position operator is given by a second derivative in momentum space

$$\left\langle r^2\right\rangle_n = -\frac{V}{(2\pi)^3}\int \mathrm{d}\,\mathbf{q}e^{i\mathbf{q}\cdot\mathbf{R}}\left\langle u_{n\mathbf{q}}\middle|\nabla^2_{\mathbf{q}}\middle|u_{n\mathbf{q}}\right\rangle. \tag{5.13}$$

Combining Eq. (5.12) and Eq. (5.13) allows one to formulate Eq. (5.6) in reciprocal space

$$\Omega = -\frac{V}{(2\pi)^3}\int \mathrm{d}\,\mathbf{q}\sum_n\left[\left\langle u_{n\mathbf{q}}\middle|\nabla^2_{\mathbf{q}}\middle|u_{n\mathbf{q}}\right\rangle - \left\langle u_{n\mathbf{q}}\middle|\nabla_{\mathbf{q}}\middle|u_{m\mathbf{q}}\right\rangle^2\right]. \tag{5.14}$$

The $q$-space derivatives in Eq. (5.14) are then evaluated numerically by means of finite differences [141] at each $q$-point directly by the *ab-initio* code. To evaluate Eq. (5.14) on a mesh of $N$ $\mathbf{q}$-points in the Brillouin zone, the transformation

$$\frac{V}{(2\pi)^3}\int d\mathbf{q} \to \frac{1}{N}\sum_{\mathbf{q}} \tag{5.15}$$

is used yielding

$$\Omega = -\frac{1}{N}\sum_{\mathbf{q}}\sum_n\left[\left\langle u_{n\mathbf{q}}\middle|\nabla^2_{\mathbf{q}}\middle|u_{n\mathbf{q}}\right\rangle - \left\langle u_{n\mathbf{q}}\middle|\nabla_{\mathbf{q}}\middle|u_{m\mathbf{q}}\right\rangle^2\right]. \tag{5.16}$$

Calculating the spread in Eq. (5.16) by finite difference, requires knowledge of the overlap between a given $q$-point $\mathbf{q}$ with its neighboring $q$-points $\mathbf{q}_{\mathrm{neigbhor}} = \mathbf{q} + \mathbf{b}$, connected by the vector $\mathbf{b}$. Therefore, the overlap matrix $M_{mn}$ is formally defined as

$$M_{mn}(\mathbf{q}, \mathbf{b}) := \langle u_{\mathbf{q}m}|u_{\mathbf{q}+\mathbf{b}n}\rangle. \tag{5.17}$$

The $M_{mn}$ matrix in Eq. (5.17) is calculated by the *ab-initio* code and then passed to the Wannier90 code which handles the optimization problem of finding the MLWFs. Given the $M_{mn}$ matrix all relevant quantities can be approximated by means of finite differences. For example the Wannier centers defined in Eq. (5.12) can be approximated by [141,144]

$$\begin{aligned}\langle \mathbf{r} \rangle_n &= -\frac{1}{N} \sum_{\mathbf{q}} \langle u_{n\mathbf{q}} \,|\, \nabla_{\mathbf{q}} \,|\, u_{n\mathbf{q}} \rangle \\ &\approx -\frac{1}{N} \sum_{\mathbf{q},\mathbf{b}} w_{\mathbf{b}} \mathbf{b} \Im \ln M_{nn}(\mathbf{q}, \mathbf{b}).\end{aligned} \tag{5.18}$$

In the same fashion it follows for the squared position operator from Eq. (5.13)

$$\left\langle \mathbf{r}^2 \right\rangle_n = \frac{1}{N} \sum_{\mathbf{q},\mathbf{b}} w_{\mathrm{b}} \left[ 1 - \left| M_{nn}(\mathbf{q}, \mathbf{b}) \right|^2 + \left( \Im \ln M_{nn}(\mathbf{q}, \mathbf{b}) \right)^2 \right]. \tag{5.19}$$

To obtain MLWFs only the gauge dependent part has to be minimized. In practice it is split into the band diagonal and off-diagonal parts, introduced in Eq. (5.9) & Eq. (5.10), and expressed in terms of the overlap matrix [143]

$$\widetilde{\Omega}_{\mathrm{OD}} = \frac{1}{N} \sum_{\mathbf{q},\mathbf{b}} w_b \sum_{m \neq n} \left| M_{mn}^{(\mathbf{q},\mathbf{b})} \right|^2, \tag{5.20}$$

$$\widetilde{\Omega}_{\mathrm{D}} = \frac{1}{N} \sum_{\mathbf{q},\mathbf{b}} w_b \sum_{n} \left( - \operatorname{Im} \ln M_{nn}^{(\mathbf{q},\mathbf{b})} - \mathbf{b} \cdot \overline{\mathbf{r}_n} \right)^2. \tag{5.21}$$

The gauge dependent contributions of the spread $\widetilde{\Omega}$ can be interpreted as measure for how much the Wannier functions differ from the eigenfunctions of the position operator [143,144], minimizing this disparity is of grave importance in transport calculations, such as the Keldysh photoresponses discussed in Chapter 3, since the formalisms rely on the velocity operator which is given by the derivative of the position operator. The Wannier90 code minimizes the overall spread by minimizing Eq. (5.20) and Eq. (5.21) by means of a steepest descent optimization scheme [143,148]. For that unitary transformations are applied to the $M_{mn}$ matrix which transforms like [141]

$$\widetilde{M}_{mn}(\mathbf{q}, \mathbf{b}) = \sum_{m'} \sum_{m''} \left( U_{m'm}(\mathbf{q}) \right)^* U_{m''n}(\mathbf{q} + \mathbf{b}) M_{m'm''}(\mathbf{q}, \mathbf{b}), \tag{5.22}$$

where $\widetilde{M}_{mn}$ denotes the transformed $M_{mn}$ matrix. Minimizing Eq. (5.20) and Eq. (5.21) by finding an optimal set of unitary matrices $U_{mn}(\mathbf{q})$ is the main objective of the Wannier90 code [103] and often referred to as the "wannierization".

The gauge independent contribution $\Omega_{\mathrm{I}}$ is given by [143]

$$\begin{aligned}\Omega_{\mathrm{I}} &= \frac{1}{N}\sum_{\mathbf{k},\mathbf{b}} w_b \left( J - \sum_{mn} \left| M_{mn}^{(\mathbf{q},\mathbf{b})} \right|^2 \right) \\ &= \frac{1}{N}\sum_{\mathbf{k},\mathbf{b}} w_b \,\mathrm{tr}\left[ P^{(\mathbf{q})} Q^{(\mathbf{q}+\mathbf{b})} \right],\end{aligned} \tag{5.23}$$

where $J$ is the number of bands considered and $P^{(\mathbf{q})} = \Sigma_n \left| u_{n\mathbf{k}} \right\rangle \left\langle u_{n\mathbf{k}} \right|$ the projection operator at point $\mathbf{q}$ of the Brillouin zone from all states onto of the group of bands considered creating the Wannier functions. The $Q^{(\mathbf{q})}$ operator is defined as the complementary projection operator $Q^{(\mathbf{q})} = 1 - P^{(\mathbf{q})}$ and since $\Omega_{\mathrm{I}}$ only depends on the projection operator $P^{(\mathbf{q})}$ and its complement $Q^{(\mathbf{q}+\mathbf{b})}$, it is directly apparent that $\Omega_{\mathrm{I}}$ is gauge independent for a group of $J$ isolated bands projected onto $J$ Wannier functions. Thus, $\Omega_{\mathrm{I}}$ can be interpreted as a measure for how much the band projection operator changes within the Brillouin zone. In the next section the more general scenario of entangled bands is discussed, where a set of Wannier functions is extracted from a larger group of bands.

### 5.2.1 *Entangled bands*

The above discussion assumes that $N_{wf}$ Wannier functions will be extracted as the Fourier transform of $N_{wf}$ Bloch waves. A reasonable assumption if the Wannier functions are extracted from an isolated group of bands [143]. However, for metallic systems it is often impossible to extract an integer number of bands within a given energy window, since the number of bands included in the window in general depends on the $k$-point. The formalism was thus extended to also treat entangled bands [144]. The main idea is to extract a subset of $N_{wf}$ Wannier functions from a set of $N$ Bloch states by requiring

$$\left| \mathbf{R}n \right\rangle = \frac{1}{N_{\mathbf{q}}} \sum_{\mathbf{q}} e^{-i\mathbf{q}\cdot\mathbf{R}} \sum_{m} \widetilde{U}_{mn}(\mathbf{q}) \left| \psi_{\mathbf{q}m} \right\rangle, \tag{5.24}$$

where $\widetilde{U}_{mn}(\mathbf{q}) \in \mathbb{C}^{N \times N_{wf}}$. Eq. (5.23) which measures the dispersion of the band projection operator becomes dependent on the choice of the $\widetilde{U}_{mn}(\mathbf{q})$ matrices. For details on the optimization procedure of $\Omega_{\mathrm{I}}$ the reader is pointed to [144].

## 5.3 Fleur Interface

To minimize the spread of the Wannier functions Wannier90 requires two quantities from the *ab-initio* code: The $M_{mn}$ matrix provides the overlaps of the Bloch states between neighboring $\mathbf{q}$-points and is used to calculate the spread via Eq. (5.20), Eq. (5.21) and Eq. (5.23). Minimizing the spreads then becomes a global optimization problem of finding the optimal unitary rotation matrices $U_{mn}(\mathbf{q})$. The Wannier90 code splits the optimization by first minimizing $\Omega_\mathrm{I}$ and in a second step $\widetilde{\Omega}$ [144]. Global optimization problems are in general sensitive to the chosen initial guess, for example if the initial guess is near a local minimum that is not the global minimum, the optimizer might get "trapped" in a local minimum. Therefore, one usually provides an initial guess for the rotation $U_{mn}(\mathbf{q})$ which is expected to be close to the global optimum. Often atomic orbitals localized at the atomic sites are used as initial projections, since these functions are solutions in a non-interacting scenario. For a given set of Bloch states $|\psi_{\mathbf{q}m}\rangle$ the projection onto localized orbitals $|g_n\rangle$ is given by [141]

$$|\phi_{\mathbf{q}n}\rangle = \sum_m |\psi_{\mathbf{q}m}\rangle \langle\psi_{\mathbf{q}m}|g_n\rangle = \sum_m A_{mn}(\mathbf{q})\,|\psi_{\mathbf{q}m}\rangle\,, \tag{5.25}$$

where the $A_{mn}(\mathbf{q})$ is the projection operator resulting in the transformed Bloch states $|\phi_{\mathbf{q}n}\rangle$. Like the $M_{mn}$ matrix the $A_{mn}(\mathbf{q})$ matrix will be calculated by the *ab-initio* code and passed to Wannier90. By using Löwdin's orthogonalization procedure [149] an orthonormal basis set is constructed [149]

$$|\tilde{\psi}_{\mathbf{q}n}\rangle = \sum_m \left[\left(S(\mathbf{q})\right)^{-1/2}\right]_{mn} |\phi_{\mathbf{q}m}\rangle\,, \tag{5.26}$$

where $S_{mn}(\mathbf{q}) = \langle\phi_{\mathbf{q}m}|\phi_{\mathbf{q}n}\rangle$ [141] is the overlap within the projected Bloch space in Eq. (5.25). Eq. (5.26) is then Fourier transformed via Eq. (5.2) to construct the initial guess of Wannier functions.

A good starting point for many systems is to project onto *s*-, *p*- and *d*-orbitals on each atomic site, which can, in case of small systems, results in less than 100 Wannier functions to describe the whole system near the Fermi level. Too large spreads of the Wannier functions or a stark misalignment of the Wannier centers with the atomic centers indicate Wannier functions of poor quality. In such scenarios, clearly the chosen set of initial guesses does not represent the electronic system well. To improve the quality of the Wannier functions one could first try to increase the basis size by including *f*-orbitals to the initial guess. On the other hand Wannier functions centered far from the atomic cites indicate strong hybridization in the system, in which

case it is usually better to use *sp*-hybrid orbitals centered on the bonds as initial guesses. The initial guess is not always straight forward, good guesses are heavily system dependent. On top of that the quality of the Wannier functions depends on the chosen frozen energy window and a "good" window has to be found for a given set of trial orbitals. It is noted here that in a recent publication Cancès *et al.* suggested scenarios in which the trial orbital method might not always find the MLWFs and proposed an optimization scheme which works with a random initial guess [150].

## 5.4 REAL SPACE BASIS SET

After the wannierization in Wannier90 is completed, Wannier90 can write out the Hamiltonian and position operators as real space quantities defined in the Wannier basis. Implicitly the real space basis set is defined as the inverse Fourier transform of the *ab-initio* $\mathbf{q}$-mesh onto the real space cell mesh $\mathbf{R}$

$$\begin{aligned} \langle \mathbf{0}n | \hat{H} | \mathbf{R}m \rangle &= \frac{1}{N_q^3} \sum_{\mathbf{q}} e^{-i\mathbf{q}\cdot\mathbf{R}} H_{nm}^{(W)}(\mathbf{q}) \\ \langle \mathbf{0}n | \hat{r}_\alpha | \mathbf{R}m \rangle &= \frac{1}{N_q^3} \sum_{\mathbf{q}} e^{-i\mathbf{q}\cdot\mathbf{R}} A_{nm,\alpha}^{(W)}(\mathbf{q}). \end{aligned} \tag{5.27}$$

Within a given energy window, known as the frozen energy window, defined here as the energy interval $[\mathrm{E}_{\min}, \mathrm{E}_{\text{window}}]$, the Hamiltonian operator $H_{nm}^{(\mathrm{W})}(\mathbf{q})$ in Eq. (5.27) is given by Hamiltonian evaluated within the Bloch basis [144]

$$H_{nm}^{(\mathrm{W})}(\mathbf{q}) = \langle u_{\mathbf{q}n} | \hat{H}(\mathbf{q}) | u_{\mathbf{k}m} \rangle \leftrightarrow \mathrm{E}_{n\mathbf{q}}, \mathrm{E}_{m\mathbf{q}} \in [\mathrm{E}_{\min}, \mathrm{E}_{\text{window}}]. \tag{5.28}$$

The superscript $(W)$ indicates that the resulting Hamiltonian is in the Wannier gauge and intents to clarify that $H_{nm}^{(\mathrm{W})}(\mathbf{q})$ is only accurately reproducing the eigenenergies of the Bloch states in the frozen energy window. Note for the previously discussed scenario of an isolated group of bands no frozen energy window has to be specified. The lower bound of the frozen energy window is usually chosen such that no bands are below $\mathrm{E}_{\min}$. Choosing a reasonable upper bound of the frozen energy can be challenging however, and is a critical, user dependent step required in the wannierization procedure. If the Wannier functions are used to calculate photoresponses to an applied laser with frequency $\omega$, the frozen energy windows upper bound $\mathrm{E}_{\text{window}}$ should be at least

$$\mathrm{E}_{\text{window}} > \mathrm{E}_{\mathrm{F}} + \hbar\omega, \tag{5.29}$$

where $E_F$ is the true Fermi level. Figure 5.1 showcases a Wannier interpolated bandstructure alongside the ab-inito band structure in the metallic bulk AFM $Mn_2Au$ computed with Fleur (more details on $Mn_2Au$ can be found in Chapter 8 and Chapter 9). The figure shows that up to the upper bound of the frozen energy window the colored *ab-initio* bands are perfectly atop the Wannier interpolated bands (black). Above the frozen energy window, clear discrepancies between the *ab-initio* and the interpolated bandstructure are visible.

Remembering that the Wannier centers in Eq. (5.18) can be computed by means of finite differences acting on the overlap matrix, the generalization to the off-diagonal elements required to compute the position operator $\langle \mathbf{0}n | \hat{r}_\alpha | \mathbf{R}m \rangle$ in Eq. (5.27) is straight forward

$$A^{(W)}_{nm,\alpha}(\mathbf{q}) \approx i \sum_{\mathbf{b}} w_b b_\alpha \left( M_{mn}(\mathbf{q}, \mathbf{b}) - \delta_{nm} \right). \tag{5.30}$$

The Fleur code is capable of computing additional observables in the real space basis, especially it is possible to write the Pauli and angular momentum operator in the real space basis [100]

$$\begin{aligned} \langle \mathbf{0}n | \hat{\tau}_i | \mathbf{R}m \rangle &= \frac{1}{N_q^3} \sum_{\mathbf{q}} e^{-i\mathbf{q}\cdot\mathbf{R}} S^{(W)}_{nm,i}(\mathbf{q}) \\ \langle \mathbf{0}n | \hat{v}_i | \mathbf{R}m \rangle &= \frac{1}{N_q^3} \sum_{\mathbf{q}} e^{-i\mathbf{q}\cdot\mathbf{R}} L^{(W)}_{nm,i}(\mathbf{q}). \end{aligned} \tag{5.31}$$

## 5.5 Wannier Interpolation

Given a Hamiltonian, position operator and potential other operators such as the Pauli operator $\hat{\tau}_i$ in the real space basis defined in Eq. (5.27), one can forward Fourier transform the real space basis onto an arbitrarily dense $k$-mesh [142]

$$\begin{aligned} H^{(W)}_{nm}(\mathbf{k}) &= \sum_{\mathbf{R}} e^{i\mathbf{k}\cdot\mathbf{R}} \langle \mathbf{0}n | \hat{H} | \mathbf{R}m \rangle, \\ A^{(W)}_{nm,a}(\mathbf{k}) &= \sum_{\mathbf{R}} e^{i\mathbf{k}\cdot\mathbf{R}} \langle \mathbf{0}n | \hat{r}_a | \mathbf{R}m \rangle, \\ S^{(W)}_{nm,i}(\mathbf{k}) &= \sum_{\mathbf{R}} e^{i\mathbf{k}\cdot\mathbf{R}} \langle \mathbf{0}n | \hat{\tau}_i | \mathbf{R}m \rangle, \end{aligned} \tag{5.32}$$

where $H^{(W)}_{nm}(\mathbf{k})$ is the Wannier interpolated Hamiltonian at $k$-point $\mathbf{k}$, $A^{(W)}_{nm,a}(\mathbf{k})$ is the Berry connection defined as $A_{nm,\alpha}(\mathbf{k}) := i \langle u_n | \partial_\alpha | u_m \rangle$ and

$S^{(W)}_{nm,i}(\mathbf{k})$ is the Wannier interpolated Pauli operator. From Eq. (5.32) the $k$-derivative of the Hamiltonian can easily be computed

$$\begin{aligned} H^{(W)}_{nm,\alpha}(\mathbf{k}) &= \frac{\partial}{\partial k_\alpha} H^{(W)}_{nm}(\mathbf{k}) \\ &= \sum_{\mathbf{R}} \left( \frac{\partial e^{i\mathbf{k}\cdot\mathbf{R}}}{\partial k} \right)_\alpha \langle \mathbf{0}n|\hat{H}|\mathbf{R}m\rangle \\ &= \sum_{\mathbf{R}} (iR_\alpha) e^{i\mathbf{k}\cdot\mathbf{R}} \langle \mathbf{0}n|\hat{H}|\mathbf{R}m\rangle \,. \end{aligned} \tag{5.33}$$

Since the Berry curvature is defined as the curl of the Berry connection $\boldsymbol{\Omega}_n(\mathbf{k}) = \boldsymbol{\nabla} \times \mathbf{A}_n(\mathbf{k})$, using the same approach as in Eq. (5.33) the curvature can be shown to be given by [142]

$$\Omega^{(W)}_{nm,ab}(\mathbf{k}) = \sum_{\mathbf{R}} e^{i\mathbf{k}\cdot\mathbf{R}} (iR_a \langle \mathbf{0}n|\hat{r}_b|\mathbf{R}m\rangle - iR_b \langle \mathbf{0}n|\hat{r}_a|\mathbf{R}m\rangle). \tag{5.34}$$

The $(W)$ superscript indicates that the interpolated quantities are given in their Wannier gauge, the gauge transformation of these quantities to the Hamiltonian Gauge $(H)$ will be discussed in the next section.

### 5.5.1 Hamiltonian gauge

Diagonalizing the interpolated Hamiltonian from Eq. (5.32) yields the eigenenergies $\mathrm{E}^{(H)}_{n\mathbf{k}}$ and eigenstates $U_{nm}(\mathbf{k})$, where $U(\mathbf{k})$ is a unitary matrix with $U(\mathbf{k}) \in \mathbb{C}^{N_{wf} \times N_{wf}}$ such that

$$H^{(H)}_{nm}(\mathbf{k}) = (U^\dagger(\mathbf{k}) H^{(W)}(\mathbf{k}) U(\mathbf{k}))_{nm} = \mathrm{E}^{(H)}_{n\mathbf{k}} \delta_{nm}. \tag{5.35}$$

Note that $U(\mathbf{k})$ in Eq. (5.35) is different from the $U$ matrix in Eq. (5.5), however, to emphasize that both matrices are unitary they are depicted by $U$. In case of the Hamiltonian the transformation from Wannier to Hamiltonian gauge is thus simply the rotation into the eigenbasis. After the diagonalization the other interpolated operators (think velocity, spin, etc.) have to be transferred to the Hamiltonian gauge too. For a given operator $O$ the operator rotated by the unitary matrices is defined as

$$\bar{O}^{(H)} = U^\dagger O^{(W)} U. \tag{5.36}$$

If the observable $O$ is gauge covariant the rotation alone is enough to yield the operator in the Hamiltonian gauge and $O^{(H)} = \bar{O}^{(H)}$ holds. The gauge transformation of gauge-contravariant objects, for example quantities which include partial derivatives acting on the phase space, is less straight forward. For

example in case of the Berry connection, which is defined as the $k$-derivative of the Bloch waves, a correction term has to be introduced

$$\begin{aligned} A_\alpha^{(H)} &= U^\dagger A_\alpha^{(W)} U + iU^\dagger \partial_\alpha U \\ &= \bar{A}_\alpha^{(H)} + iU^\dagger \partial_\alpha U. \end{aligned} \tag{5.37}$$

In a similar fashion the Berry curvature defined in Eq. (5.34) can be expressed in the Hamiltonian gauge as [142]

$$\Omega_{nm,\alpha\beta}^{(H)} = \bar{\Omega}_{nm,\alpha\beta}^{(\mathrm{H})} - \left[D_{nm,\alpha}^{(\mathrm{H})}, \bar{A}_{nm,\beta}^{(\mathrm{H})}\right] + \left[D_{nm,\beta}^{(\mathrm{H})}, \bar{A}_{nm,\alpha}^{(\mathrm{H})}\right] - i\left[D_{nm,\alpha}^{(\mathrm{H})}, D_{nm,\beta}^{(\mathrm{H})}\right], \tag{5.38}$$

where

$$D_{nm,\alpha}^{(\mathrm{H})} \equiv \left(U^\dagger \partial_\alpha U\right)_{nm} = \begin{cases} \frac{\bar{H}_{nm,\alpha}^{(\mathrm{H})}}{\mathrm{E}_m^{(\mathrm{H})} - \mathrm{E}_n^{(\mathrm{H})}} & \text{if } n \neq m \\ 0 & \text{if } n = m \end{cases}. \tag{5.39}$$

For convenience the Berry curvature in Eq. (5.38) is also defined in its vector form as

$$\Omega_{n,\gamma}^{(H)}(\mathbf{k}) \equiv \varepsilon_{\alpha\beta\gamma}\Omega_{nn,\alpha\beta}^{(H)}(\mathbf{k}), \tag{5.40}$$

where $\varepsilon_{\alpha\beta\gamma}$ is the Levi-Civita symbol.
The velocity operator $\hat{v}_\alpha = (\frac{\partial H}{\partial k})_\alpha$ as given in Eq. (5.33) is defined as the $k$-derivative of the Hamiltonian, thus, a correction term has to be introduced here as well. The correction term is proportional to the Berry connection and often referred to as the "anomalous" velocity contribution [142]

$$v_{nm,\alpha}^{(H)}(\mathbf{k}) = \frac{1}{\hbar}\bar{H}_{nm,\alpha}^{(H)}(\mathbf{k}) - \frac{i}{\hbar}\left(\mathrm{E}_m^{(H)}(\mathbf{k}) - \mathrm{E}_n^{(H)}(\mathbf{k})\right)\bar{A}_{nm,\alpha}^{(H)}(\mathbf{k}). \tag{5.41}$$

The Wannier interpolated velocity operator Eq. (5.41) and eigenenergies $\mathrm{E}_{n\mathbf{k}}^{(H)}$ defined in Eq. (5.35) can then be used to calculate response tensors such as the photoconductivity derived in Chapter 3.

# Chapter 6

## *The ju_wip code*


**Figure 6.1.** The logo of the *ju_wip* code.

In the course of the thesis a Wannier interpolation code focused on calculating second order responses based on the Keldysh formalism, as described in Chapter 3, was developed in Fortran90, utilizing a MPI and OpenMP hybrid parallelization. The code was dubbed *ju_wip*, an abbreviation for **Ju**elich **W**annier **I**nterpolation **P**rogram. In short the *ju_wip* code implements the Wannier interpolation procedure outlined in Section 5.5 and subsection 5.5.1 to interpolate the velocity operator and the band energies within a reduced Wannier basis. In this chapter the workflow and features of the *ju_wip* code will be outlined. Towards the end of the chapter some results obtained with the *ju_wip* will be compared to results previously presented in literature. For the interested reader in Chapter VI some additional information about compiling the *ju_wip* code, it's input file, parallel scaling as well as implementation details is provided.

## 6.1 Workflow

The *ju_wip* has two basic modi operandi: A bandstructure mode which interpolates along a list of $k$-points provided by an external file and the core mode were no $k$-points are explicitly provided by the user, but instead a Monkhorst-Pack mesh [151] is set up automatically. The bandstructure mode can be used to plot the Wannier interpolated bandstructure, but also allows visualizing photocurrents band resolved (see for example Figure 2.2). The core mode is designed to integrate response tensors over the whole Brillouin zone. Figure 6.2 shows a flowchart of the *ju_wip* workflow. A real space basis set is the starting point of a *ju_wip* calculation. The code can run with just a Hamiltonian provided (without position operator), thus, a real space basis sets can be generated by hand for example from a tight-binding model. Most calculations presented in this work, however, were calculated from *ab-initio* with Fleur [100] and its interface to Wannier90 [141,148]. Many available DFT codes have an interface to Wannier90 [103], giving users of the *ju_wip* a broad choice of DFT codes to perform the *ab-initio* calculation. The reader is informed that the spin and orbital real space files are written by Fleur [100] and have to be converted to the Fleur specific file format if another DFT code is used. However, all *ab-initio* calculations presented in this work were performed with the Fleur code [100]. The interpolation step is performed with an MPI parallelization, here the real space basis set will be Fourier transformed onto a sufficiently fine $k$-mesh to converge for example a photocurrent calculation. Finally a good stir (read: gauge transformation) of the $k$-space quantities from Wannier to Hamiltonian gauge is performed to obtain the single band properties required by the Keldysh formalism in the Hamiltonian gauge. After the single band properties are interpolated, *ju_wip* enters the response tensor calculation phase. To allow for maximum flexibility of usage, all matrix operations and response tensor calculations are implemented with an OpenMP parallelization. At the end of a given calculation an MPI reduction is performed which handles the $k$-point integration.

## 6.2 Response tensors

The *ju_wip* code was mostly developed to evaluate the second order Keldysh response tensors as presented in Chapter 3. However, the code is capable of calculating various other response tensors of first and second order, such as the first order optical conductivity and the second order photocurrent tensor based on the Kubo formalism. In this section all response tensors are outlined.

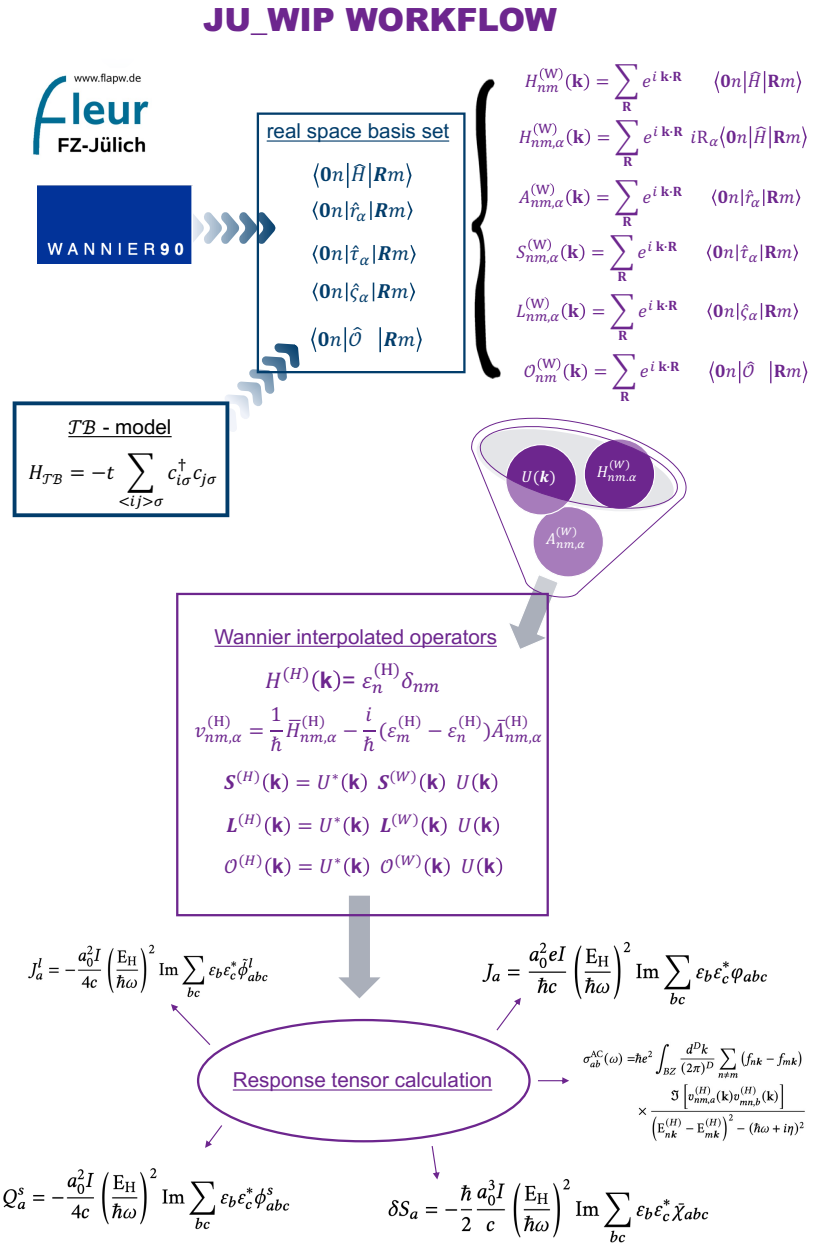


**FIGURE 6.2.** Sketch of the workflow of a calculation performed with the *ju_wip* code.

*ju_wip* requires an input file named `input.cfg`, formatted in the configuration file format, to be present in the root folder of the calculation. The real space ba-

sis set exported by Wannier90 has to be provided in a subfolder `./w90files`. By setting the associated flags in the input file to `true` the calculation of a given response tensor will be activated. For details on the input file please check Chapter VI.

After finishing the tensor calculation the code will write out the tensor as numpy [152] files (.npy) which can be directly read within a numpy python script. To write out the tensors as numpy files a publicly available open source library was used developed within the Jülich institute [153]. For most tensors basic plotting scripts are provided in `ju_wip/scripts/plotting/`, the plotting scripts are written in python and use pythons matplotlib [154].

### 6.2.1 MEP

The magneto electric polarization (MEP) was the subject of the author's master thesis [155], in which the magnetoelectric polarization was calculated in a toy model. The response tensor calculation routines were integrated into the *ju_wip* code to allow for *ab-initio* calculations of the magnetoelectric polarization. The magnetoelectric polarization $\boldsymbol{P}'$ in a $D$-dimensional insulating material is given by [156]

$$\boldsymbol{P}' = -\int \frac{d^D k}{(2\pi)^D} \sum_{n\in \text{occ.}} \left[ \frac{1}{2} (\Omega_{nn}^{(H)}(\mathbf{k}) \cdot \mathbf{A}_{nn}^{(H)})(\mathbf{k}) \boldsymbol{B} + \boldsymbol{a}_n'(\mathbf{k}) \right], \tag{6.1}$$

where $n$ are occupied bands, $\Omega_{nn}^{(H)}$ the Berry curvature, $\mathbf{A}_{nn}^{(H)}$ the Berry connection and $\boldsymbol{B}$ is an applied magnetic field. The first summand in Eq. (6.1) is known as the Chern Simons term, and it accounts for the field induced change in phase-space volume. The second term $\boldsymbol{a}'$ describes the field induced positional shift of the semiclassical wavepacket [157] and its $a$-th component is given by [156]

$$a_a'(\mathbf{k}) = F_{ab}(\mathbf{k}) B_b + G_{ab}(\mathbf{k}) E_b. \tag{6.2}$$

Please note that only the response to a external magnetic field is implemented, *i.e.* only the response tensor $F_{i\beta}$ in Eq. (6.2) but not $G_{ab}$. The response tensor $F_{ab}$ is given by [156]

$$F_{ab}(\mathbf{k}) = \text{Im} \sum_{m\neq n} \frac{v_{nm,a}^{(H)}(\mathbf{k}) \omega_{mn,b}(\mathbf{k})}{\left( \mathrm{E}_{n\mathbf{k}}^{(H)} - \mathrm{E}_{m\mathbf{k}}^{(H)} \right)^2}, \tag{6.3}$$

with

$$\omega_{mn,a}(\mathbf{k}) = -i\varepsilon_{abc} \sum_{m'\neq n} \frac{\left[ v_{mm',b}^{(H)}(\mathbf{k}) + v_{mm',b}^{(H)}(\mathbf{k}) \delta_{mm'} \right] v_{m'n,c}^{(H)}(\mathbf{k})}{\mathrm{E}_{m\mathbf{k}} - \mathrm{E}_{n\mathbf{k}}}, \tag{6.4}$$

where $\varepsilon_{abl}$ is the Levi-Civita symbol. To calculate the magnetoelectric polarizability with *ju_wip* set the `do_mep` flag in the *jobs* section of the input file to `true`. The components of the response tensor are written out individually: `out/mep_bands_cs.npy` is the Chern-Simons contribution, while `out/mep_bands_ic.npy` and `out/mep_bands_lc.npy` are the two contribution to $F_{ij}$ in Eq. (6.3). The magnetoelectric polarization is only defined properly in an insulating material and in case of the MEP routines the number of valence bands has to be given by the user in the *MEP* section of the input file. The output tensors will be written out valence band resoled and have the shape $a'(a, b,$`valence_bands`$)$ where $a, b \in [1, .., 3]$.

### 6.2.2 Optical conductivity

The optical conductivity tensor is the first order response tensor to the perturbation of an AC electric field, oscillating with frequency $\omega$, given by the following Kubo expression [158,159]

$$\begin{aligned}\sigma_{ab}^{\mathrm{AC}}(\omega) =& \hbar e^2 \int_{BZ} \frac{d^D k}{(2\pi)^D} \sum_{n\neq m} \left(f_{n\boldsymbol{k}} - f_{m\boldsymbol{k}}\right) \\ &\times \frac{\Im\left[v_{nm,a}^{(H)}(\mathbf{k}) v_{mn,b}^{(H)}(\mathbf{k})\right]}{\left(\mathrm{E}_{n\boldsymbol{k}}^{(H)} - \mathrm{E}_{m\boldsymbol{k}}^{(H)}\right)^2 - (\hbar\omega + i\eta)^2},\end{aligned} \tag{6.5}$$

where $\eta$ is a numerical broadening parameter, $v_{nm,a}^{(H)}(\mathbf{k})$ is component $a$ of the Wannier interpolated velocity operator defined in Eq. (5.41), $\mathrm{E}_{m\boldsymbol{k}}^{(H)}$ are the eigenenergies of the Wannier functions as defined in Eq. (5.35) and $f_{n\mathbf{k}}$ is the Fermi distribution of the $n$-th Wannier function at point $\mathbf{k}$. To calculate the optical conductivity with *ju_wip*, set the `do_ahc` flag in the *jobs* section of the input file to `true`. In the sections *Fermi* and *Laser*, the number of parameter points on which the tensor is calculated can be specified. The optical conductivity is written out as a 5D complex tensor representing Eq. (6.5) with the following structure $\sigma(a, b,$ `N_hw`, `N_eta_smr+N_eta_smr2`, `N_ef`$)$ where $a, b \in [1, .., 3]$ are the spatial indices. The tensor is written out as a .npy file to `out/ahc_AC_tens.npy`. Basic python matplotlib plotting scripts can be found in the folder `ju_wip/scripts/plotting/ahc/` of the *ju_wip* code.

### 6.2.3 AHC

The anomalous Hall conductivity (AHC) can be understood as the DC-limit ($\omega \longrightarrow 0$) of the optical conductivity tensor in Eq. (6.5) and is given by inte-

grating the Wannier interpolated Berry curvature[142] defined in Eq. (5.40)

$$\sigma_{ab}^{\mathrm{DC}} = -\frac{e^2}{\hbar}\sum_n \int_{\mathrm{BZ}} \frac{d^D k}{(2\pi)^D} f_{n\mathbf{k}} \varepsilon_{abc} \Omega_{n,c}^{(H)}(\mathbf{k}), \tag{6.6}$$

where $\varepsilon_{abc}$ is the Levi-Civita symbol. The AHC routine is activated by setting `do_ahc` and `do_wip_curv` to true. The tensor will be written to `out/ahc_DC_tens.npy`. Requiring

$$\sigma_{ab}^{\mathrm{AC}}(\omega \to 0, \eta) = \sigma_{ab}^{\mathrm{DC}} \tag{6.7}$$

allows one to determine reasonable value for the numerical broadening $\eta$ in Eq. (6.5).

### 6.2.4 *Keldysh*

Calculating the second order DC response to an applied oscillating electric field within the Keldysh nonequilibrium formalism is the main objective of this code. Only the final expressions are repeated here, for a detailed derivation of the second order response tensors with the nonequilibrium Keldysh formalism please refer to Chapter 3. The Hamiltonian gauge band energies, velocity operators, etc. are plugged into the derived response tensor expressions. The code is capable of calculating the second order photocurrent (see also Eq. (3.66))

$$J_a = \frac{a_0^2 e I}{\hbar c}\left(\frac{\mathrm{E_H}}{\hbar\omega}\right)^2 \mathrm{Im}\sum_{bc} \varepsilon_b \varepsilon_c^* \varphi_{abc}, \tag{6.8}$$

the spin polarized photocurrent (see also Eq. (3.77))

$$Q_a^s = -\frac{a_0^2 I}{4c}\left(\frac{\mathrm{E_H}}{\hbar\omega}\right)^2 \mathrm{Im}\sum_{bc} \varepsilon_b \varepsilon_c^* \phi_{abc}^s \tag{6.9}$$

and the induced spin density (see also Eq. (3.81))

$$\delta S_a = -\frac{\hbar}{2}\frac{a_0^3 I}{c}\left(\frac{\mathrm{E_H}}{\hbar\omega}\right)^2 \mathrm{Im}\sum_{bc} \varepsilon_b \varepsilon_c^* \bar{\chi}_{abc}. \tag{6.10}$$

Note that by overwriting the real space Pauli file (`w90files/rspauli.1`) with the real angular momentum operator (`w90files/ranlgmom.rs`), it is also possible to calculate the Laser induced orbital magnetization and the orbital photocurrent. The user should keep in mind, that an additional

factor 2 has to be applied to the machinery if the angular momentum operator is used, since it is written in units of $\hbar$ by Fleur, while the spin operator is given in units of $\hbar/2$. By setting `do_keldysh` to `true` in the *jobs* section in combination with setting `do_kely_epC` to `true` in the *Keldysh* section the calculation of the photocurrent tensor is activated. With `do_kely_spC` in the *Keldysh* section the spin photocurrents can be activated and with `do_kely_pauli` the inverse Faraday effect. Just like for the previously discussed tensors, the parameter space is controlled by the *Fermi* and *Laser* section of the input file. The *ju_wip* code will output the activated Keldysh response tensors as 6D (7D in case of the spin photocurrent) complex tensors of form $\varphi(a, b, c$,`N_hw`,`N_eta_smr`+`N_eta_smr2`, `N_ef`) where $a, b, c \in [1, .., 3]$ are the spatial indices. The photocurrent tensor for example is written to `out/kely_epC_SUM.npy` and can be directly visualized with the scripts provided in `ju_wip/scripts/plotting/photocurrents/Keldysh/`. Further, the sea and surface components of the tensor will be written out as `out/kely_epC_sea.npy` and `out/kely_epC_surf.npy` respectively.

### 6.2.5 Nagaosa expression

A Kubo based expression for the second order photoconductivity was derived by Nagaosa *et al.* recently[71]. Since the calculation of the Kubo based 2nd order response tensor is faster than the Keldysh routines it allows the user a quick sanity check of a full Keldysh run as presented in subsection 6.2.4. For the photocurrent defined as $J_c = \sigma^c_{ab} E^*_a E_b$, where $E_a$ are the components of the laser's electric field, the second order photoconductivity in the Kubo formalism $\sigma^c_{ab}$ is given by[71]

$$\sigma^c_{ab}(\omega) = \frac{|e|^3}{\omega^2}\,\mathrm{Re}\left\{\phi_{ab}\sum_{\Omega=\pm\omega}\sum_{l,m,n}\int_{BZ}\frac{d^Dk}{(2\pi)^D}\left(f_{l\mathbf{k}}-f_{n\mathbf{k}}\right)\right.$$
$$\left.\frac{v^{(H)}_{nl,a}(\mathbf{k})\,v^{(H)}_{lm,b}(\mathbf{k})\,v^{(H)}_{mn,c}(\mathbf{k})}{\left(\mathrm{E}^{(H)}_{n\mathbf{k}}-\mathrm{E}^{(H)}_{m\mathbf{k}}-i\delta\right)\left(\mathrm{E}^{(H)}_{n\mathbf{k}}-\mathrm{E}^{(H)}_{l\mathbf{k}}+\hbar\Omega-i\delta\right)}\right\}, \tag{6.11}$$

where $\delta$ is a broadening parameter and $\phi_{ab}$ is the phase relation between the electric field components $E_a$ and $E_b$. By setting `do_photoC` to `true` in the *jobs* section of the input file the tensor defined in Eq. (6.11) is calculated. The *ju_wip* code will output a 6D complex tensor representing Eq. (6.11) which is structured as $\sigma(a, b, c$,`N_hw`,`N_eta_smr`+`N_eta_smr2`, `N_ef`) where $a, b, c \in [1, .., 3]$ are the spatial indices. The tensor is written to `out/photoC2_naga.npy` and

can be directly visualized with the scripts provided in `ju_wip/scripts/plotting/photocurrents/Nagaosa/`.

### 6.2.6 Other

For completeness the author would like to inform the reader that some additional tensors are included with the code, however, these implementations are unfinished, incomplete and often untested and can not be switched on from the input file. Future developers of the code might find information about these "limbo" modules useful though and, thus, a brief overview is given here: In `ju_wip/src/kubo_mep.f90` a experimental generalization of the MEP tensor form subsection 6.2.1 to metallic systems is implemented. In `ju_wip/src/bcd_photo.f90` some of the second order photocurrent tensors presented by Sodemann *et al.* in [78] are implemented. In `ju_wip/src/gyro.f90` some of the response tensors presented by Souza *et al.* [70] are implemented.

### 6.2.7 *k*-space integration

The response tensors given above, as well as the photoresponse tensors derived in Chapter 3 require an integration over the first Brillouin zone. The *ju_wip* code performs this integration numerically by replacing the integral over a $D$-dimensional $k$-space with a weighted sum over $N_k$ $k$-points, such that

$$\int_{BZ} \frac{d^D k}{(2\pi)^D} \rightarrow \frac{1}{N_k} \sum_k . \tag{6.12}$$

## 6.3 SPECIAL FEATURES

The code has some specialized features implemented which will be outlined in this section. How to activate and configure these features will be described in greater detail in Section A.2.

### 6.3.1 Model calculations

By setting the `use_kspace_ham` flag in the *wannBase* section of the input file the usage of a Hamiltonian setup directly in $k$-space can be activated. Thus, for these types of calculations no real space basis set has to be provided by the user. These model Hamiltonians are implemented directly as FORTRAN

source code and only a small number of models is provided. The integer input parameter `k_space_ham_id` selects which model is used. The supported $k$-space models are listed below.

| id | $k$-space model |
|---|---|
| 0 | magnetic Rashba model, see also subsection 6.4.1 |
| 1 | Hamiltonian filled with random numbers for testing purposes |

Another option is to provide a tight-binding model setup in real space. In this scenario the user has to set up the tight-binding Hamiltonian and provide it to the code in form of a Wannier90 Hamiltonian real space file (Wannier90 `seedname`_hr.dat file). This approach was used to calculate a tight-binding model of $\gamma$-FeMn, for details see Section 10.2.

### 6.3.2 Bandstructure mode

By setting `plot_bands` in the *jobs* section of the input.cfg file to `true`, the bandstructure mode is activated. In this mode the code does not set up a Monkhorst-Pack mesh and instead interpolates $k$-points along a path specified in a special input file. The $k$-point list file along which the bandstructure is interpolated can be generated with the kptsgen.pl script written by A. Schindlmayr, which was the default script used to set up $k$-points paths in older version of Fleur (think $\leq 0.26g$). The script is provided in the repository of the *ju_wip* code and can be found under `scripts/kspace_gen/kptsgen.pl`. The *ju_wip* code will output the interpolated bandstructure to a fixed format file `out/eBands.dat`, which can be directly plotted with the script `scripts/plotting/plot_bandStruct.py`. The Keldysh responses as given in subsection 6.2.4 can be calculated band resolved within the bandstructure mode. In this scenario the Keldysh response tensor is written out band- and $k$-resolved along the given path.

### 6.3.3 Atom projection

For an operator given in the Wannier gauge $\hat{O}^{(W)}$, the code is capable of projecting the operator onto a number of atomic sites which can be defined by the user via the input file (for details see Chapter VI). The projector onto atomic site *at* is given by the identity matrix, however, only the diagonal elements whose associated Wannier centers are closest to atomic cite $\boldsymbol{\tau}_{at}$ are non-zero. The projector is given by

$$\hat{P}_{nm}(at) = \delta_{nm} \begin{cases} 1 & \text{if } \min_{\forall at \in [1,..,N_{at}]} |\overline{\mathbf{r_n}} - \boldsymbol{\tau}_{at}| \\ 0 & \text{else}, \end{cases} \tag{6.13}$$

where $\overline{\mathbf{r_n}}$ is the center of the $n$-th Wannier function and $\boldsymbol{\tau}_{at}$ is the atomic position onto which the Wannier function is projected. A generic operator might not commute with the projector, Thus, to ensure correctness the projection operator is applied from both sides of the operator

$$\hat{O}^{(W)}(at) = \frac{1}{2}\left[\hat{P}(at)\hat{O}^{(W)} + \hat{O}^{(W)}\hat{P}(at)\right]. \tag{6.14}$$

A good check that the projector is working as intended is to calculate the atom projected response and then sum it over all atomic sites which should yield the fully integrated response.

### 6.3.4 *Zeeman field*

The code can apply an external magnetic field, denoted here as Zeeman field $\mathbf{B}_{\text{Zeeman}}$, to the Wannier gauge Hamiltonian of Eq. (5.32)

$$\tilde{H}^{(W)}_{nm}(\mathbf{k}) = H^{(W)}_{nm}(\mathbf{k}) + \mu_0\left(\mathbf{S}^{(W)}_{nm}(\mathbf{k}) \cdot \mathbf{B}_{\text{Zeeman}}\right), \tag{6.15}$$

where $\mathbf{S}^{(W)}_{nm}(\mathbf{k})$ is the Wannier interpolated Pauli operator defined in Eq. (5.32). The code then diagonalizes the modified Hamiltonian $\tilde{H}^{(W)}_{nm}(\mathbf{k})$, thus, not only the band energies but also the eigenvectors and the velocities in the Hamiltonian gauge from Eq. (5.41) will be modified by the Zeeman term.

### 6.3.5 *k-resolved responses*

All Keldysh response tensors can be written out $k$-point resolved, allowing the user to visualize the response quantity resolved in the Brillouin zone. $k$-resolved calculations are also possible in the bandstructure mode, allowing the user to plot a bandstructure resolved photoresponse along some (high-symmetry) path of the Brillouin zone.

## 6.4 Testing in known systems

Since the *ju_wip* code was build from scratch in this work, testing if the code provides correct results was imperative. For that purpose the photocurrent was tested in two different systems, the magnetic Rashba model and in an *ab-initio* calculation of GaAs. Both test results are briefly reported here.

### 6.4.1 Metallic 2D Rashba model

To test the *ju_wip* code it was first checked if the magnetic photogalvanic effect in the magnetic Rashba model reported in Ref. [29] could be reproduced. Testing a model system first is advantageous, since no position operator will be interpolated and interpolation errors of the Hamiltonian in earlier steps of the calculation, *i.e.* the wannierization, can be ruled out. Further, in case of the 2D Rashba model only two states are considered reducing the matrix size to 2×2 allowing for fast calculations. Since the Rashba model is 2D the total number of $k$-points calculated might be lower compared to a 3D system. The Hamiltonian presented in Eq.6 of Ref. [29] was used to model a ferromagnetic 2D Rashba model

$$H = \frac{-\hbar^2}{2m_e}\Delta - i\alpha(\nabla \times \hat{\mathbf{e}}_z)\cdot\sigma + \frac{\Delta V}{2}\sigma\cdot\hat{\mathbf{n}}(\mathbf{r}), \tag{6.16}$$

where $\alpha$ is the Rashba coupling strength, $\delta V$ the applied exchange field strength and $\hat{\mathbf{n}}(\mathbf{r})$ the direction of the magnetization. The resulting band-structure is shown in Figure 6.3 for various showcases.

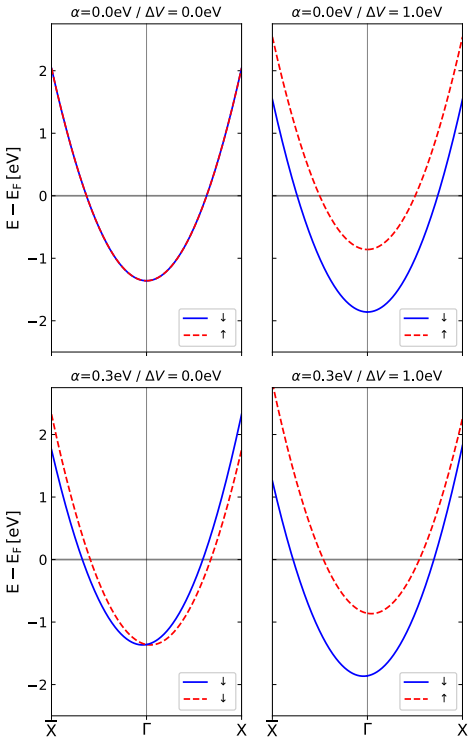


**FIGURE 6.3.** Bandstructure of Eq. (6.16) for different model parameters. In case of no Rashba coupling and no exchange interaction, $a_R = V_{ex} = 0$, bands are degenerate. The exchange interaction splits bands in the energy domain (y-axis), while the Rashba coupling shifts the parabola with respect to the Γ-point (x-axis). If both interactions are switched on a combination of both shifts is present.

For an easy identification of the effect, the Rashba coupling was set to $\alpha = 0.3$ eV or 0 eV in Figure 6.3. For all other calculations discussed below the Rashba coupling was fixed to $\alpha = 0.1$ eV.

Figure 6.4 shows the photocurrent calculated with the *ju_wip* code for the Rashba model given by Eq. (6.16). The Rashba coupling strength was set to $\alpha_R = 0.1$ eV and the exchange interaction to $V_{ex} = 1.0$ eV with magnetic moments pointing along the $y$-direction. The parameters were chosen to match the parameters used by Freimuth *et al.* and to compare to results presented in Fig. 2 of [29]. Figure 6.4 shows very good agreement with the results previously obtained by Freimuth *et al.* presented in [29], with the peak of the helicity independent $J_x$ current (red and black curves on top of each other) in response to circularly polarized light at $J_x(\Gamma \rightarrow 0; \sigma^{\pm}) \approx 2.6\,\mathrm{A/m^2}$ and the switchable $J_y$ response with a peak value of $J_y \approx 0.24\,\mathrm{A/m^2}$ located at $\Gamma = 0.18$ eV (note that the $J^y$ response is scaled for better visibility in Figure 6.4 by a factor 10).

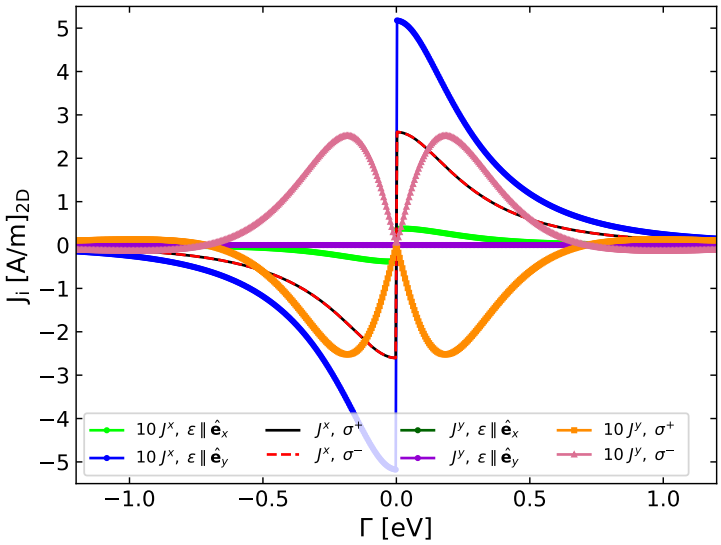


**FIGURE 6.4.** Photocurrent in the magnetic Rashba model (see Eq. (6.16)) with parameters set to $\alpha_R = 0.1$ eV, $V_{ex} = 1.0$ eV, plotted versus positive and negative broadening $\Gamma$. The magnetization was set to point along the $y$-direction. The Fermi level was set to $E_F$=1.36 eV and the laser frequency to $\hbar\omega = 1.55$ eV.

Figure 6.4 also shows the photoresponse at negative broadening values. Considering negative broadening values in a dissipative process such as the photocurrent effectively reverses the energy dissipation, thus, pumping energy into the system. It mimics the effects of a time reversal operation, which also reverses magnetic moments, and is thus suited to identify magnetic photocurrents as outlined in Sec.2.1.2. A magnetic LPGE current is expected to switch sign under reversal of the broadening parameter, while the CPGE currents are even under sign reversal.

### 6.4.2 *Shift current in bulk semiconductor GaAs*

In the previous section it was confirmed that the *ju_wip* code produces accurate photoresponses if the Hamiltonian is directly provided as a $k$-space model. In this section the full *ab-initio* pipeline, that is the interface to the real space basis set written by Wannier90 and the Wannier interpolation within *ju_wip*, are tested. As benchmark material the 3D bulk semiconductor GaAs was chosen, since photoresponses were heavily studied in the past in GaAs[65,80,160–163] allowing for a qualitative and quantitative evaluation of the

approach presented in this work. In a recent work Azpiroz *et al.* reported on the implementation of shift current in Postwannier90[103] and presented the photoconductivity $\sigma_{xyz}$ (see Eq. (3.71) for the definition of $\sigma_{xyz}$) associated with the shift current in GaAs[69]. DFT calculations by Azpiroz *et al.* were performed with the VASP code[69] based on the pseudopotential method.

To make the test as robust as possible, a set of 16 *s* and *p* Wannier orbitals was generated with the Fleur code. The generated Wannier functions were then wannierized with the Wannier90 code and in the same fashion as Azpiroz *et al.* a scissors shift of 1.15 eV was applied within Wannier90 to correct the underestimation of the band gap. Figure 6.5 shows the resulting photoconductivity calculated with the *ju_wip* code, as defined in Eq. (3.71), plotted versus the applied laser frequency. The conductivity was evaluated at the true Fermi level, and the broadening was set to $\Gamma = 40$ meV to match the broadening selected by Azpiroz.

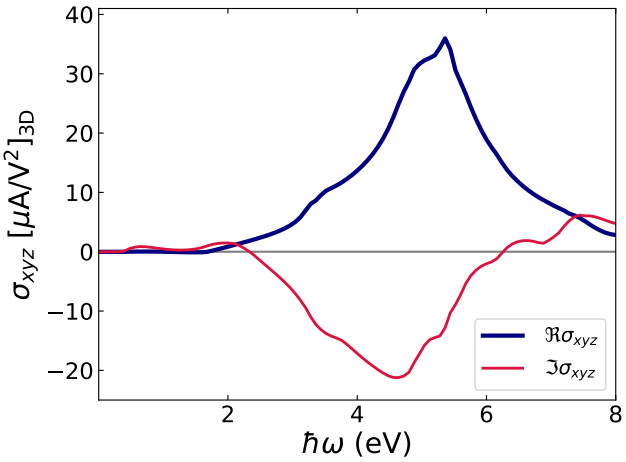


**FIGURE 6.5.** Photoconductivity versus applied laser frequency. A scissors shift of 1.15 eV was applied to the Hamiltonian to correct the band gap, which is underestimated by the DFT calculation.

Figure 6.5 is in good agreement with Fig.3(a) of[69], the maximum of roughly $\sigma_{xyz} \approx 40\,\mu\text{A/V}^2$ is located at $\hbar\omega \approx 5.3$ eV in both results. Slight differences in the smoothness and the absence of smaller features such as the small spike appearing in Azpiroz results at $\hbar\omega \approx 7$ eV can be attributed to the different underlying DFT methods of the VASP and Fleur code. The broadening parameter in the Keldysh formalism $\Gamma$ also has a different physical interpretation than the broadening parameter used by Azpiroz *et al.* Tuning the Keldysh broadening $\Gamma$ could be used to match the smoothness better, with

smaller broadening values leading in general to less smooth photoresponses when plotted versus the laser frequency or the band filling.

As discussed in subsection 2.1.2 magnetic/non-magnetic photocurrents will be odd/even under change of the broadening parameter Γ. This is quickly tested in Figure 6.6 for GaAs, where magnetic contributions are forbidden. Figure 6.6 shows the broadening dependence of the $x$-component of the photocurrent evaluated at the true Fermi level for an applied laser frequency of $\hbar\omega = 4.20$ eV. In the legend of the figure the various laser polarizations are indicated. In case of circular polarized light $\varepsilon \circlearrowright \lambda_y^z$ denotes light rotating clockwise in the plane spanned by the $z$- and the $y$-direction, likewise $\varepsilon \circlearrowleft \lambda_y^z$ denotes counterclockwise rotation in the same plane.

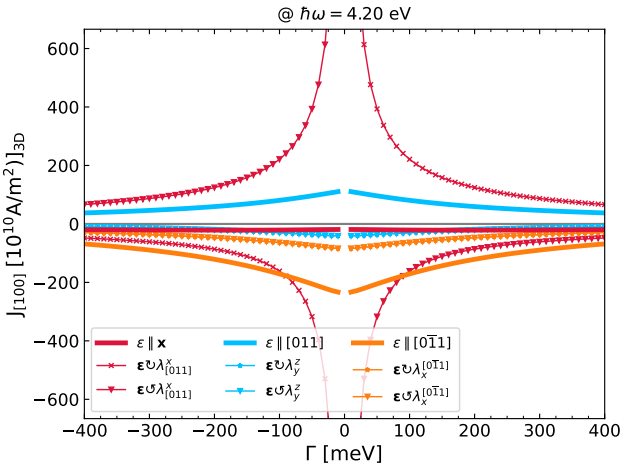


**FIGURE 6.6.** Dependence of the photocurrent on the broadening parameter. The clean limit is approached from positive and negative broadening values. Since GaAs is a nonmagnetic semiconductor, an even behavior with respect to change of sign of the broadening parameter is expected for linearly polarized light. This holds for all 3 linearly independent linearly polarized fields shown.

As expected from the existing theory, all LPGE photocurrent are even under change of sign of the broadening in Figure 6.6. Non magnetic CPGE responses on the other hand all do switch sign under reversal of Γ which is consistent with the existing theory as given in subsection 2.1.2. Note that helicity independent responses to circularly polarized light are averages of LPGE currents and, thus, behave like LPGE currents. Only helicity switchable responses do switch sign under a sign reversal of Γ. This is to be expected since the time-reversal operation, here mimicked by the reversal of broadening parameter, flips the sense of rotation of the circularly polarized field.

Part IV

# Photogalvanic effects in magnetic materials

# Chapter 7

# *Laser effects in $Fe_3GeTe_2$*

In this part of the thesis optical responses, calculated with the *ju_wip* code, in various magnetic systems are presented. In the first chapter the 2D van-der-Waals $Fe_3GeTe_2$ is discussed. The following two chapters present results obtained for 3D antiferromagnetic $Mn_2Au$.

This chapter and the herein presented results are mostly adapted from [1]. The goal of this chapter is to represent and extend the discussion of photoresponses in $Fe_3GeTe_2$ (FGT), with an emphasis on identifying magnetic and non-magnetic photocurrents by means of the *ju_wip* code. Further, the chapter aims to compare photoresponses in this system qualitatively and quantitatively to various other materials studied in this thesis. The author acknowledges that Wannier functions used to obtain the photoresponses presented in this chapter were provided by coauthors Dr. Dongwook Go and Dr. Tom Saunderson of [1], who performed the DFT calculations with the Fleur code [100] as well as the wannierization with the wannier90 code. Dr. Go and Dr. Saunderson provided the real space basis set of the Wannier functions. The calculation of charge and spin photocurrents which are the main result of the publication [1] were obtained solely by the author of this work by means of the *ju_wip* code developed in the course of this thesis. Wannier interpolated bandstructures were constructed by means of the *ju_wip* code as well.

## 7.1 Introduction

2D van-der-Waals materials have picked up a large interest in the recent years, since the weak van-der-Waals bonds between individual layers allows for stacking of functional layers of various chemical composition to design complex functional multilayer systems [58–61]. $Fe_3GeTe_2$ has emerged as a good candidate hosting such van-der-Waals layers and is of particular interest, due to its ferromagnetic configuration in the single layer limit [58], with the Curie temperature far above room temperature [164]. Complex magnetic structures, such as skyrmions, can be realized within FGT, highlighting the material as a good platform for a rich set of complex magnetic phenomena [165–167]. FGT

was suggested to host large current induced spin-orbit torques oscillating between individual layers of the bulk configuration which can be unveiled in the single layer limit [168,169]. Thus, studying the photoresponses in FGT can provide relevant insight into how to utilize FGT in the context of ultrafast spintronics.

Figure 7.1 a) and b) show the considered single layer structure of $Fe_3GeTe_2$, the magnetic moments of the Fe atoms are indicated by the red arrows.

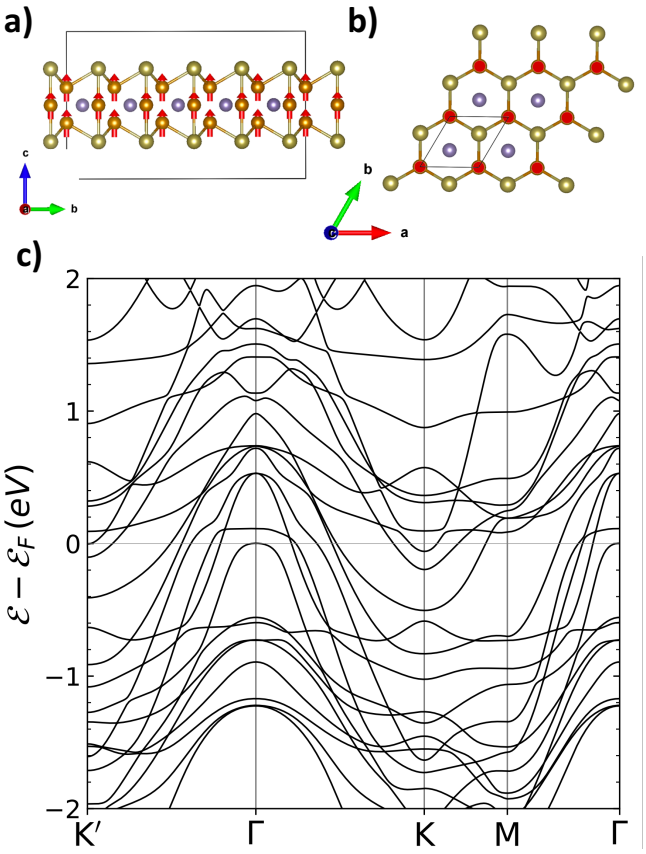


**FIGURE 7.1.** Crystal and bandstructure of a single layer of FGT (reprinted from [1], ©2021 CC BY 4.0). a) and b) show the considered layer of $Fe_3GeTe_2$, red arrows indicate the magnetic moments of the iron atoms. c) shows the resulting Wannier interpolated bandstructure.

In agreement with experimental observations, a ferromagnetic configuration was considered with the magnetization vector pointing along the *z*-direction [58]. For a detailed description of the *ab-initio* calculation with the

Fleur code [100] and the construction of the maximally localized Wannier functions of the single layer FGT the reader is pointed to Ref. [1]. Here it is only mentioned that $d$-orbitals on the Fe atoms and $p$-orbitals on the Ge and Te sites were used as initial projection in the construction of the Wannier functions resulting in a total of 48 Wannier functions, allowing for an accurate description of the single layer of FGT within a reasonable energy window around the true Fermi level. Figure 7.1 c) shows the Wannier interpolated band structure around the true Fermi level. The K′ point denotes the negative K point.

Figure 7.1 c) highlights the complex orbital nature of FGT near the true Fermi level. The broken inversion symmetry of the system can be directly identified in the bandstructure by comparing bands at the K and K′ point. For example at the K′ point a band is present at the true Fermi level, while the same band is shifted by about $-200$ meV at the K point. Due to the broken inversion symmetry, photocurrents are allowed in the system. In the next section the broadening dependence of photocurrents in FGT will be analyzed, and the various photoresponses will be classified into magnetic and non-magnetic.

## 7.2 NON-MAGNETIC AND MAGNETIC PHOTOCURRENTS

Figure 7.2 shows the broadening dependence of the components of the photocurrent as defined in Eq. (3.66) for an applied laser light of frequency $\hbar\omega = 1.55$ eV, linearly polarized along the $x$-direction, with intensity fixed to $I = 10\text{GW/cm}^2$. The photoresponses were evaluated at the true Fermi level. Broadening values in the range of $\Gamma = 25$ meV up to 300 meV were considered in the main figure, while the inset shows the dirty limit for broadening values between 100 and 600 meV. Within the inset the response was multiplied by a factor of $\Gamma$, such that a scaling law can be identified.

At room temperature broadening of $\Gamma = 25$ meV, the photocurrents presented in Figure 7.2 reach an amplitude of about 50 A/m, which is an order of magnitude larger than the photocurrents in the magnetic Rashba model as presented in Ref. [29]. For details on the magnetic Rashba model the reader is pointed to subsection 6.4.1. Figure 7.2 suggests a quick decay of both photoresponses for broadening values above $\Gamma = 100$ meV. At $\Gamma = 100$ meV the $J_y$ response (blue curve) has decreased by an order of magnitude when compared to the response at $\Gamma = 25$ meV. The $x$-component of the photocurrent $J_x$ is reduced by roughly a factor of 2.5 at $\Gamma = 100$ meV. In the inset of Figure 7.2 the responses are multiplied with a factor of $\Gamma$. For broadening values above $\Gamma = 250$ meV both responses are almost perfect

flat lines, suggesting a $1/\Gamma$ scaling of both photoresponses towards the large broadening values presented. For smaller broadening values the decay is more rapid.

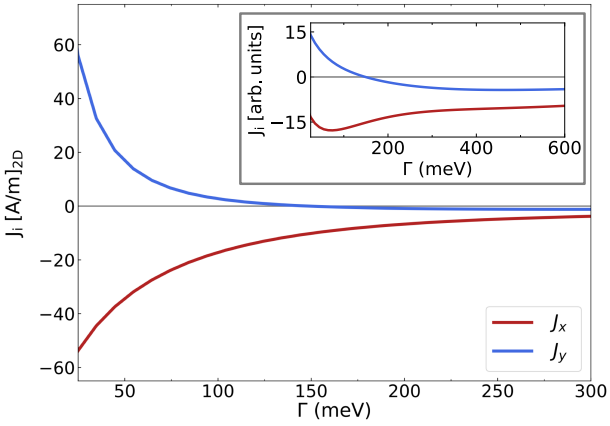


**Figure 7.2.** Broadening dependence of the charge photocurrent (reprinted from [1], ©2021 CC BY 4.0). The responses were evaluated at the true Fermi level and the laser frequency was fixed to $\hbar\omega = 1.55$ eV. The inset shows the photocurrents multiplied by a factor of $\Gamma$.

As discussed in subsection 2.1.2 magnetic photocurrents in response to linearly polarized light behave antisymmetric under a sign change of the lifetime broadening $\Gamma$, while nonmagnetic components are symmetric.

In order to identify magnetic and non magnetic photocurrents in FGT, Figure 7.3 shows the $x$- and $y$-component of the photocurrent in response to light linearly polarized along the $x$- and [110]-direction respectively. The laser frequency was kept at $\hbar\omega = 1.55$ eV and the band filling was set to the true Fermi level. Figure 7.3 shows that both magnetic and non-magnetic photocurrents are present. From Figure 7.3 $J_y(\varepsilon \parallel \hat{\mathbf{e}}_x)$ and $J_x(\varepsilon \parallel \hat{\mathbf{e}}_{110})$ can be identified as magnetic photocurrents. The identification of the magnetic photocurrents via the negative broadening is consistent with the symmetry analysis provided by coauthor Frank Freimuth presented in Eq.(3) of Ref. [1]. The magnetic responses are described by the symmetry tensor $\chi^{(a,2)}_{ijkl}$ in Ref. [1], where the superscript indicates an axial or pseudo vector, switching sign under a magnetization reversal. The nonmagnetic responses on the other hand are given by the polar tensor $\chi^{(p,1)}_{ijk}$. Figure 7.3 suggests that a 45° rotation of the linear polarization from the $x$ to the [110]-direction allows one to "swap" the magnetic photocurrent from flowing along the $x$-direction to flowing along the $y$-direction. FGT is the only material considered in this thesis were one can easily switch components of the photocurrent to become

sensitive to magnetization reversal by simply rotating the linear polarization vector by 45° within the $xy$-plane.

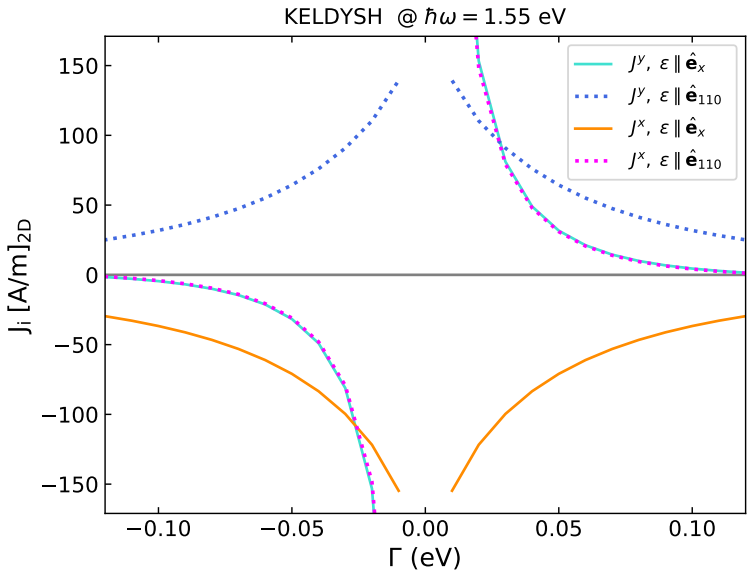


**FIGURE 7.3.** Clean limit of the components of the charge photocurrent for different orientations of the laser's linear polarization. Even responses indicate non-magnetic photocurrents, while odd responses are identified as magnetic photocurrents.

For example in the magnetic Rashba model discussed in Figure 6.4, the $x$-component of the photocurrent was always non-magnetic, irrespective of the orientation of linearly polarized light. Only the helicity dependent response in $y$-direction was identified to be of magnetic origin. However, one key difference was that the magnetization in the Rashba model was set in the plane along the $y$-direction, while for the here discussed FGT the scenario of magnetization out-of-plane along the $z$-direction was considered. In the next section both magnetic and non-magnetic components of the photocurrent will be analyzed in terms of their frequency and band filling dependence.

## 7.3 SPECTRAL PROPERTIES

In order to compare the strength of photocurrents in $Fe_3GeTe_2$ to the amplitude of photoresponses reported in other 2D systems and make predictions on the robustness of the photoconductivity, the spectral properties of magnetic and non magnetic photocurrents are discussed in this section for a large

range of broadening values.

Figure 7.4 a) shows the frequency dependence of the photoconductivity tensor defined in Eq. (3.71), the tensor is defined such that the photocurrent is given by $J_i = \mathrm{Re}\sum_{jk} 2\sigma_{ijk}E_jE_k^*$ to allow for a direct comparison of the conductivity to literature. The left column shows the non-magnetic photoconductivity along $x$-direction, the right column the magnetic tensor. Frequency values in the range of $\hbar\omega = 0.3$ eV up to $\hbar\omega = 3.1$ eV were considered at the true Fermi level for various broadening values varying from $\Gamma = 25$ meV up to $\Gamma = 400$ meV. The responses for the respective broadening values are indicated by the color coding. Figure 7.4 a) shows that both, non-magnetic (left) and magnetic photoconductivity (right) oscillate up to a frequency of $\hbar\omega \approx 1.8$ eV, above this frequency both tensors are negative in sign but still show a stark modulation with respect to the applied frequency. The non-magnetic photoconductivity is maximized in terms of its absolute amplitude at a frequency of $\hbar\omega = 1.5$ eV with an amplitude of $\sim 80\ \mu A/V^2$ for a broadening of $\Gamma = 25$ meV. The magnetic photoconductivity tensor reaches values of almost $200\ \mu A/V^2$ for frequencies around $\hbar\omega = 0.75$ eV. Another spike of $\sim 100\ \mu A/V^2$ is visible at $\hbar\omega = 1.7$ eV, thus, exceeding the maximum of the non-magnetic tensor in the left column. With amplitudes of the magnetic conductivity tensor reaching $200\ \mu A/V^2$ at room-temperature broadening the response is competitive in terms of amplitude with photoconductivities reported in literature. For example a photoconductivity of $\sim 100\ \mu A/V^2$ was reported for non-magnetic monolayer GeS [69] and a similar value in $WS_2$ [170], likewise a value of $200\ \mu A/V^2$ was reported in 2D AFM $CrI_3$ [50].

To confirm that the reported photoresponses are experimentally accessible, the dependence on the band-filling around the true Fermi level is analyzed next. Figure 7.4 b) shows the non-magnetic $J_x$(red curves) and magnetic photocurrent $J_y$ (blue curves) at a fixed frequency of $\hbar\omega = 1.55$ eV for light linearly polarized along the $x$-direction. The color coding represents the various broadening values considered (same as in a)). Band fillings in the range from $-3$ eV up to $+1$ eV around the true Fermi level $\varepsilon_F$ are considered. Above the true Fermi level both components are almost constant, however, the signals quickly decay with respect to broadening. Below the true Fermi level both components quickly decrease with respect to band filling, with amplitudes, especially of the $J_y$ component, mostly suppressed at $-0.5$ eV. Between $-0.5$ eV and $-1.0$ eV both components are almost constant again with amplitudes around 25 A/m for each component. At $-1.5$ eV an almost complete suppression of both components is visible. Therefore, the overall photocurrent is almost zero at this band filling.

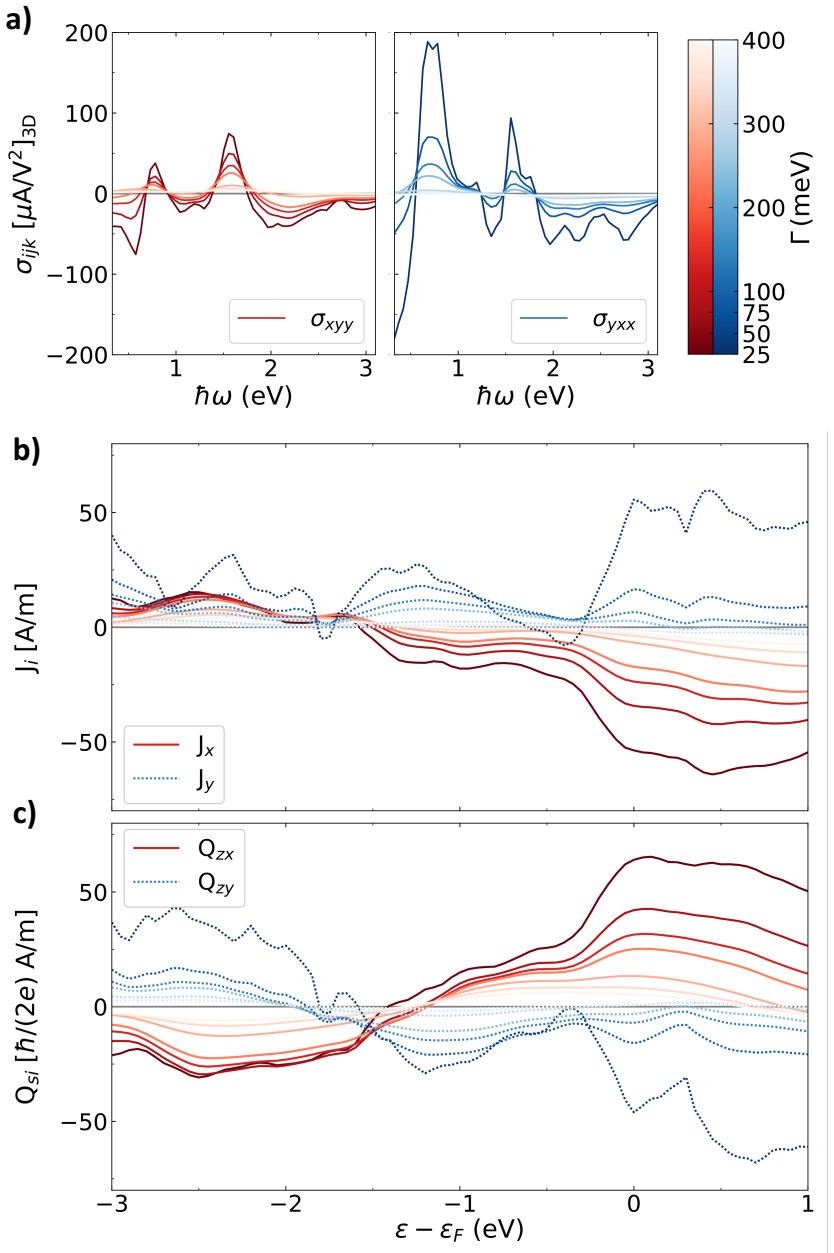


**FIGURE 7.4.** Spectral properties of FGT (reprinted from[1], ©2021 CC BY 4.0). a) Frequency dependence of the photoconductivity tensor as defined in Equation 3.71. b) Band filling dependence of the charge photocurrent in response to light polarized along the $x$-direction with frequency $\hbar\omega = 1.55$ eV evaluated at $\Gamma = 25$ meV. c) same as b) but for the spin-polarized photocurrents, with spins aligned parallel to the magnetization, which points out-of-plane along the $z$-direction.

Beneath this point both components regain amplitude, however, a qualitative change is visible: the $J_x$ current becomes positive in sign, while the $J_y$ component remains positive throughout the presented frequency range. The overall photocurrent is expected to rotate by about 90°, due to the change of sign of the $x$-component since both $x$- and $y$-component remain comparable in amplitude.

Figure 7.4 c) shows the dependence on the band-filling of the spin polarized photocurrent in response to the same laser field as in b), spin currents flowing in the $xy$-plane with spin polarization along the $z$-direction were considered, denoted by $Q_{zx}$ and $Q_{zy}$ respectively. Since both charge and spin photocurrents are present in $x$- and $y$-direction, the ratio between charge and spin responses with respect to each other indicates how strong the spin-polarization of the two photocurrents is. In an energy window of about ±1 eV around the true Fermi level a strong correlation in their dependence on band-filling and broadening is apparent between the spin-polarized and unpolarized photocurrents. For band fillings beneath 1.5 eV under the true Fermi level, however, a qualitative difference can be seen for in case of the magnetic spin photocurrent $Q_{zy}$ which undergoes a sign change, while its charge photocurrent counterpart $J_y$ stays positive. Therefore, the ratio between spin-polarized and unpolarized photocurrents is non-trivial and depends in general on the band-filling, since only transitions in an energy window defined by the laser frequency around the selected band-filling can be activated. Additionally, the ratio depends on the chosen disorder strength Γ, as can for example be seen in case of the nonmagnetic currents flowing along $x$ in the region from -2 to -3 eV, here the spin-polarized component appears more pronounced towards smaller broadening values compared to the charge photocurrent.

The findings suggest a non-trivial interplay between spin and charge photocurrents in FGT which are not just linked via a constant conversion factor. Instead, the ratio between charge and spin photocurrents can be manipulated by modification of the band filling, as well as by variation of the disorder parameter. While the change of the band-filling alters the possible transitions between states, the change in disorder is more associated with the variable strength of individual, competing, transitions. To further analyze the connection between charge and spin photocurrents, in the next section both responses will be analyzed in terms of their reciprocal space distribution in the first Brillouin zone.

## 7.4 MICROSCOPIC ORIGIN

In the previous section, charge and spin photocurrents were found to be intimately linked at the true Fermi level. To confirm the close relation of both types of responses, in this section their respective reciprocal space distribution in the first Brillouin zone is analyzed.

Figure 7.5 shows the reciprocal space distribution of charge photocurrents along the a) $x$-direction and b) along the $y$-direction. In the second column the distribution of the spin photocurrent is shown again along a) $x$-direction and b) $y$-direction. In both scenarios spin photocurrents with spin-polarization along the $z$-direction are shown. Red colors indicate regions of positive amplitude, blue colors regions of negative response. As above the laser frequency was fixed to $\hbar\omega = 1.55\,\text{eV}$, all responses were evaluated with the broadening fixed to $\Gamma = 25\,\text{meV}$.

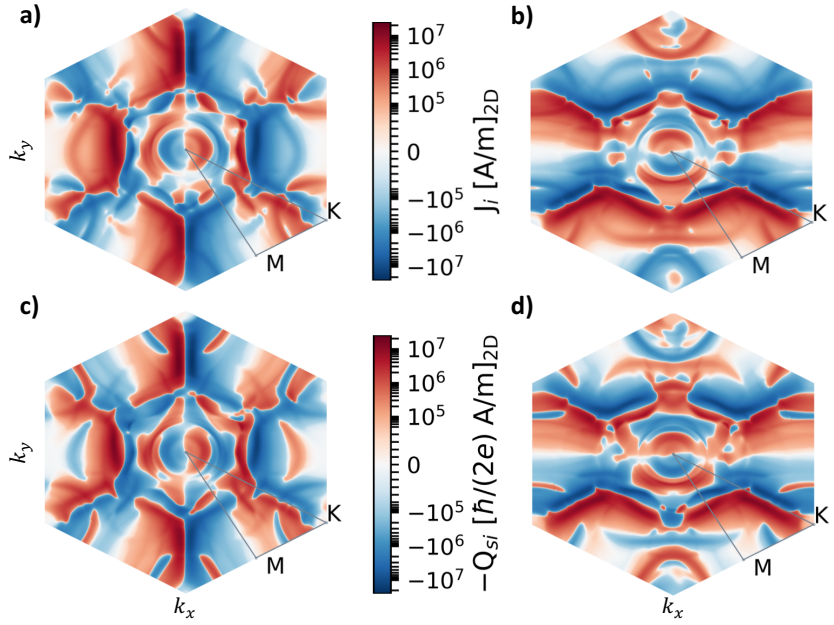


**FIGURE 7.5.** Brillouin zone resolved charge and spin photocurrent in response to light of frequency $\hbar\omega = 1.55\,\text{eV}$ linearly polarized along the $x$-direction (reprinted from[1], ©2021 CC BY 4.0). a) shows the charge photocurrent flowing in $x$-direction $J_x$, b) shows the $J_y$ current. In c) the spin photocurrent $Q_{zx}$ is shown, d) shows the $Q_{zy}$ component of the spin photocurrent. All responses were evaluated at the true Fermi level with the broadening set to $\Gamma = 25\,\text{meV}$.

Comparing the two charge photocurrents presented in Figure 7.5 a) and b) some qualitative similarities become apparent. In both scenarios the Brillouin

zone (BZ) is split into two regions of opposite sign which are connected by an antisymmetric mirror symmetry. The mirror line aligns perpendicular to the flow of the current. However, the mirror symmetry is not perfect, in that case the two regions would cancel each other and the photocurrent given by the integral over the BZ would vanish. In both a) and b) certain features are more pronounced than their mirror counterparts, thus, these regions do not cancel each other upon integration and a finite overall response is present. One example of the non-cancelling mirror regions can be seen in a): the blue regions of negative sign are more pronounced than their red symmetry counterparts, resulting in an overall negative response.

Figure 7.5 c) and d) show the spin-polarized photocurrents flowing along c) $x$ and d) $y$-direction, with spin polarization along $z$ in both scenarios, resolved in the first Brillouin zone. Comparing the spin photocurrents to the charge photocurrents shown in a) and b) the overall distribution of positive and negative regions is similar. Some differences between charge and spin photocurrents do occur, however. For example the spin photocurrent in c) $Q_{zx}$ shows pockets of opposing sign at the edges of the first BZ which are not present in case of the charge photocurrents. The large competing regions in Figure 7.5, which are presented for both charge and spin photocurrents, suggest that both effects could be further increased in amplitude by introducing a bias, for example via chemical deposition, which enhances one region over the other.

In summary this chapter unveiled FGT as a promising platform to generate sizeable photocurrents of charge and spin. The complex dependence on applied laser frequency allows for an accessible modulation of both types of photocurrents. The strong sensitivity of the photoresponses to manipulation of band-filling and disorder as well as the orientation of linearly polarized light highlight the versatility of photoresponses of charge and spin in this material but also suggest that careful experimental setup has to be done in order to obtain predictable photocurrents. In the context of spintronics, the magnetic photocurrents could be used as proxy to determine the orientation of the magnetization vector.

# Chapter 8

# *Collinear AFM $Mn_2Au$*

In this chapter various laser induced effects in the bulk antiferromagnet $Mn_2Au$ (manganese two gold) will be discussed. Within this chapter the analysis is focused on the scenario of collinear alignment of the opposing magnetic moments on the two Mn sublattices. In the next chapter the effect of canting of the magnetic moments on the photogalvanic effects will be discussed. Central results of both chapters were published and are adopted with the permission of AIP Publishing from Ref. [2]. All results were produced with the Keldysh formalism implemented in the *ju_wip* code as described in Chapter 6.

## 8.1 Introduction

Due to its desirable properties such as high predicted Néel temperature above 1000K [171–173] and a relatively simple chemical composition [174], $Mn_2Au$ has emerged as a promising material platform for the exploration of various spin-orbit effects which are accessible at room temperature. Electric switching of the AFM order parameter was demonstrated by means of Néel type spin-orbit torques [175–177]. More recently the field was further driven towards all optical switching of $Mn_2Au$, the optical readout of the order parameter was demonstrated [178] and manipulation of the Néel vector was suggested via a combined application of THz laser pulses and strain [179]. In the following chapter various photogalvanic effects will be analyzed in $Mn_2Au$ in terms of their dependence on the Néel vector, their magnetic nature and their microscopic origin. Further the spectral properties will be analyzed for various band fillings and laser frequencies. The findings highlight the power of photocurrents as experimentally easily accessible proxies for the detection of the Néel vector orientation. Further the laser induced spin density, also known as the inverse Faraday effect, will be analyzed and a large staggered response on the Mn sublattices will be identified. Finally the laser induced spin photocurrents will be analyzed and an interpretation in conjunction with the perpendicular flowing charge photocurrents as a *photospin Hall effect*

will be established. The *photospin Hall effect* allows to determine size and orientation of the sizeable spin-polarized photocurrent by measuring the more accessible perpendicular flowing charge photocurrent and thus helps establish $Mn_2Au$ as a source of large optically generated spin currents.

## 8.2 Crystal and Electronic Structure

$Mn_2Au$ has as tetragonal unit cell with space group $I4/mmm$ [174], as shown in Figure 8.1 a). The lattice constant was fixed to the experimental value of $a = 6.291$ a.u. and $c = 16.142$ a.u. [174]. The magnetization in the two Mn sublayers has collinear antiferromagnetic ordering [172] and is, if not specified otherwise, assumed to be along the [110]-direction, which is the magnetic easy axis. Figure 8.1 a) shows the assumed tetragonal unit cell containing 6 atoms, Figure 8.1 b) shows an equivalent reduced unit cell containing only 3 atoms. Electronic structure calculations were performed with the Fleur code [100]. For self-consistent calculations the plane-wave cutoff, see Section 4.6, was set to 4.0 a.u.$^{-1}$. 12 $k$-points per dimension were used resulting in a total of 1728 $k$-points sampling the 3D Brillouin zone. The plane wave cutoffs for the potential ($g_{max}$) and exchange-correlation potential ($g_{max,xc}$) were set to 12.0 and 12.0 a.u.$^{-1}$, respectively. The muffin-tin radii for Mn and Au atoms were set to 2.53 a.u. and 2.60 a.u., respectively. The nonrelativistic PBE [180] exchange-correlation functional discussed in subsection 4.5.2 was used, spin-orbit coupling was included in second variation. Figure 8.1 c) shows the resulting bandstructure of the 3 atom unit cell shown in b).

*s*-,*p*-,*d*-orbitals on both the Mn sites and the Au site were used as initial guess for the projection onto maximally localized Wannier functions which were generated by the Wannier90 code [103], resulting in 54 Wannier functions in case of the 3 atom cell and 108 in case of the 6 atom tetragonal cell and thus reduces the computational load in case of the 3 atom cell by at least a factor 2. The complete simulation workflow is demonstrated in Section 6.1. The *ab-initio* bands are plotted in cyan and magenta for the spin-up and down states, respectively. Wannier interpolated bands are plotted in black. Within the frozen energy window, set to $E_{frozen} = E_F + 4.2$ eV, the Wannier interpolated bands show no visible deviation from the *ab-initio* band structure. In the panels left and right to the centered bandstructure panel, the *ab-initio* density of states is plotted for spin-up and spin-down states respectively. The DOS is plotted atom resolved and uses the same color coding as the unit cell cartoons in a) and b), the contribution from the interstitial region is given in dark green.

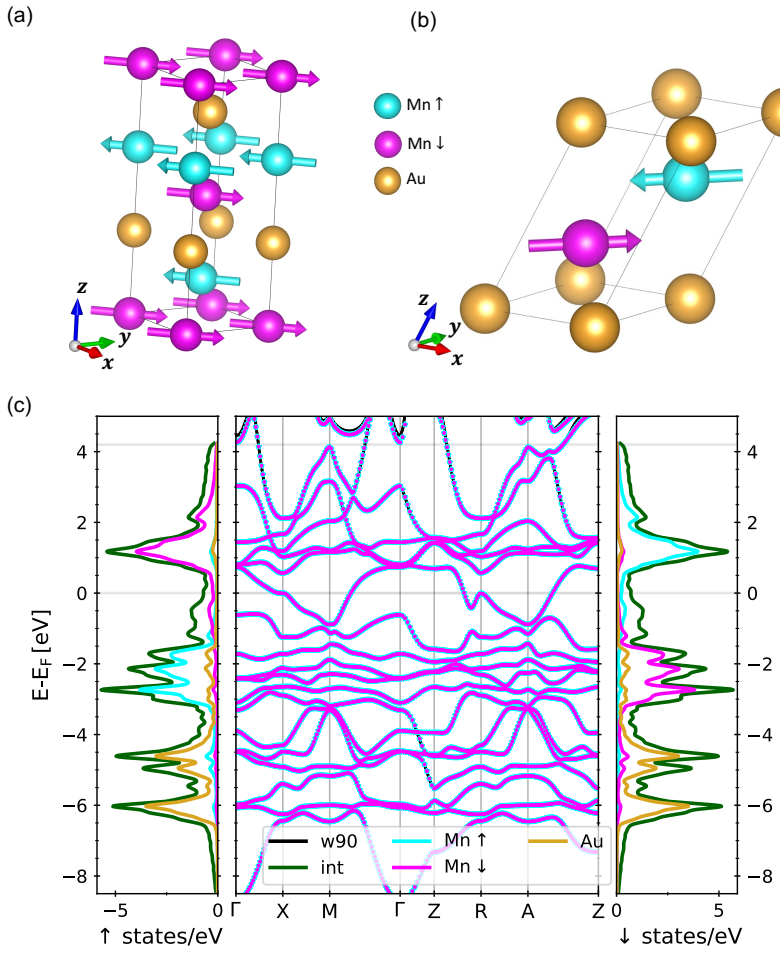


**FIGURE 8.1.** Unit cell and ground state electronic properties of the bulk antiferromagnet $Mn_2Au$ (reprinted from [2], ©2023 CC BY 4.0). a) regular, tetragonal unit cell of $Mn_2Au$ consisting of 6 atoms in the unit cell. Cyan and magenta spheres indicate the Mn spin-up and spin-down sublattices respectively. Gold atoms are indicated by golden spheres. b) irreducible unit cell with only 3 atoms in the unit cell. c) shows the density of the spin-up and spin-down states on the outer left and outer right panels respectively. In the center panel the DFT bandstructure is indicated by cyan and magenta dots for up and down states respectively. The Wannier interpolated bandstructure is plotted in black. Only above the frozen energy window, set to 4.2 eV above the true Fermi level, discrepancies between the interpolated and the DFT bands are visible.

The spatial inversion symmetry $\mathcal{P}$ is broken in $Mn_2Au$ by the opposing magnetic moments on the Mn sublattices. The magnetic moments also break the time reversal symmetry $\mathcal{T}$, however, combining a time reversal operation with a spatial inversion $\mathcal{P}$ recovers the original unit cell. The combined sym-

metry operation of $\mathcal{P}\&\mathcal{T}$ is known as the $\mathcal{PT}$-symmetry. $\mathcal{PT}$-symmetric antiferromagnets have certain characteristic properties, for example Kramers band degeneracy is recovered [181,182] as can be seen from the bandstructure presented in Figure 8.1c). In the context of second order photoresponses, the $\mathcal{PT}$-symmetry is expected to suppress extrinsic contributions like the side-jump and skew-scattering contributions [85], while allowing intrinsic photocurrents of purely magnetic origin [183], making $Mn_2Au$ the ideal candidate to study photocurrents of pure magnetic origin. Another example for a $\mathcal{PT}$-symmetric collinear antiferromagnet is CuMnAs [184].

As already outlined in Section 2.1, photoresponses are driven by bandstructure transitions from some initial to a final state. A transition can only occur if the energy difference between the initial and final state is equal to the applied laser frequency $\hbar\omega$. Besides this hard requirement however, the rate of transitions is strongly dependent on the density of states at the final state's energy level. A large DOS at a given energy level means many final states are available, thus, increasing the transition probability. As will be discussed below in subsection 8.4.2 one can thus make predictions on optimal laser frequencies based on the DOS available around the true Fermi level. The DOS shows a large spike of almost 10 states/eV at 1.2 eV above the Fermi level and a group of similar large spikes ranging from about -1.6eV to -3.2eV with the largest spike at −2.8 eV below the Fermi level. Focusing on the two Mn curves (red and blue) it is visible that the sites undergo a spin flip when crossing from the previously mentioned group beneath the Fermi level to states above the Fermi level, *i.e.* the red Mn curve flips from spin down (right panel) to spin up (left panel) at about -1eV below the Fermi level. Throughout the presented energy range the interstitial contribution dominates the DOS. However, the atomic contributions are comparable in size and the atomic DOS is dominated in an energy region of $E_F \pm 4$ eV by the Mn sublattices.

## 8.3 Néel vector dependence of photocurrents

The inversion symmetry $\mathcal{P}$ in $Mn_2Au$ is broken only by the magnetization on the Mn sublattices and not the crystal structure itself, thus, the resulting photocurrents are expected to be purely magnetic. The orientation of the magnetic photocurrent is expected to depend directly on the orientation of the Néel vector, indeed in a recent experiment the magnetic linear dichroism was found to have a distinctive dependence on the relative orientation of the linearly polarized light and the Néel vector orientation [185]. Further, the nonlinear anomalous Hall effect was recently proposed to measure the Néel vector orientation [73,183].

In this section the photocurrent is analyzed with the Néel vector lying in the (001)-plane for the two scenarios of the Néel vector along the $x$- and $y$-direction respectively. Figure 8.2 shows the photocurrent at the true Fermi level for the Néel vector oriented along the a) $x$- and b) $y$-direction in response to linearly polarized light of frequency $\hbar\omega = 3.00\,\text{eV}$, with the polarization vector rotating in the (001)-plane. The broadening was set to $\Gamma = 25\,\text{meV}$. The first row shows the $x$-component $J_x$ of the photocurrent, the second row shows $J_y$. In case of the Néel vector aligned along $x$ presented in Figure 8.2 a) the $J_y$ component shows the largest response of almost $90\,\text{A/m}^2$ when the linear light polarization is along $y$, for light polarized along $x$ the current response switches sign and is reduced to a amplitude of $\sim 70\,\text{A/m}^2$. When the Néel vector is aligned along $y$ the $J_x$ is maximal as shown in Figure 8.2 b).

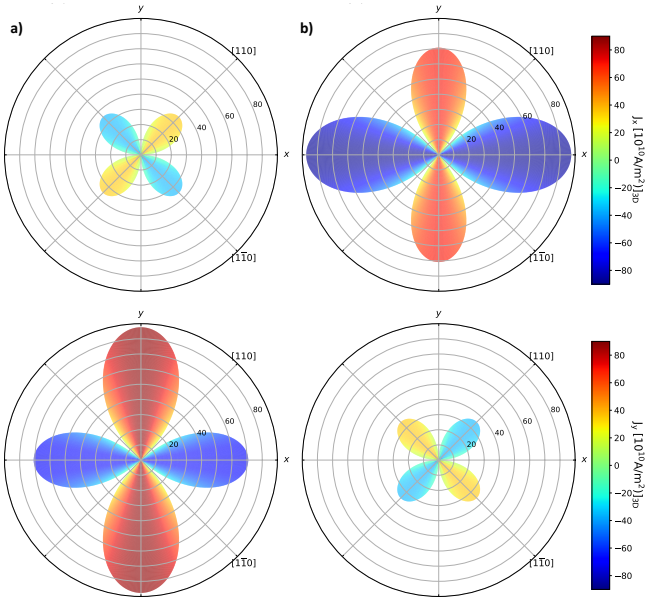


**FIGURE 8.2.** Photocurrent in response to linearly polarized light for staggered magnetization along a) $x$- and b) $y$-direction. The linear polarization is rotated in the (001) plane. A laser frequency of $\hbar\omega = 3.00\,\text{eV}$ was chosen and the broadening set to $\Gamma = 25\,\text{meV}$.

The angular dependence of the linear polarization is shifted by 90° between the two scenarios with an additional sign reversal of the resulting current, *i.e.*

$$\begin{aligned} J_y(\mathbf{N} \parallel x; \varepsilon \parallel y) &= -J_x(\mathbf{N} \parallel y; \varepsilon \parallel x) \\ J_y(\mathbf{N} \parallel x; \varepsilon \parallel x) &= -J_x(\mathbf{N} \parallel y; \varepsilon \parallel y). \end{aligned} \tag{8.1}$$

The response perpendicular to the Néel vector is dominating in both scenarios. A smaller parallel response of $\sim 35\,\text{A/m}^2$ can be driven by linearly polarized

light, if the light polarization is not aligned parallel or perpendicular to the Néel vector, but instead rotated by 45° with respect to the Néel vector. As will be discussed latter, this "off axis" alignment of the linear polarization vector not only drives a photocurrent but also a nonequilibrium spin density. To confirm the relations in Eq. (8.1) are a fundamental property of the system, Figure 8.3 shows the in-plane photocurrents as presented in Figure 8.2, but in response to laser light of frequency $\hbar\omega = 1.55\,\text{eV}$ with a more relaxed broadening value of $\Gamma = 100\,\text{meV}$ versus the band filling for both scenarios of Néel vector orientation. Responses to linearly and circularly polarized light along the $x$-,$y$- and $z$-direction are presented.

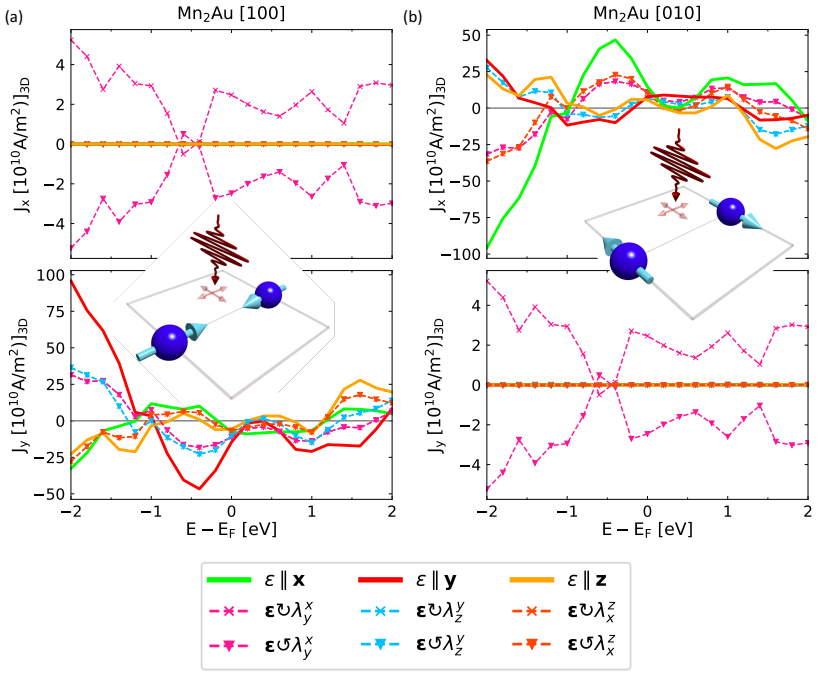


**FIGURE 8.3.** Photocurrent in Mn2Au for different directions of the staggered magnetization, for red laser light with $\hbar\omega = 1.55\,\text{eV}$ (reprinted from [2], ©2023 CC BY 4.0). The broadening was set to $\Gamma = 100\,\text{meV}$. a) photocurrent vs true Fermi level for staggered magnetization along $\hat{x}$-direction. b) same as a) but with staggered magnetization along $\hat{y}$-direction.

Figure 8.3 confirms the relations in Eq. (8.1) are generic with respect to the band filling throughout the presented energy range. The circular responses in Figure 8.3 have two distinct origins: the component perpendicular to the Néel vector in response to circularly polarized light is helicity independent and guided by the two linear responses spanning the plane of rotation. Considering for example the orange curves, which show the response to light

rotating in the plane spanned by the $z$- and the $x$-axis, the figure suggests that the orange responses are the average of the linear responses in $z$ (thick yellow curve) and $x$-direction (thick green curve). The observation was explicitly checked and confirmed by the author and holds for all currents perpendicular to the Néel vector in response to circularly polarized light. Since these responses are just averages of the linear responses, they are identified as MLPGE responses as defined in subsection 2.1.2. The components perpendicular to the Néel vector respond only to light rotating in the $xy$-plane and are helicity switchable, thus, revealing their MCPGE origin. It is noted that the MCPGE responses are an order of magnitude smaller than the LPGE effects.

## 8.4 PHOTOCURRENTS FOR MAGNETIZATION ALONG EASY AXIS

As discussed in the previous section, the photocurrents in $Mn_2Au$ directly depend on the orientation of the Néel vector and follow the Néel vector when rotated in the $xy$-plane. Therefore, from here on out, photocurrents will be discussed relative to the Néel vector orientation which will be fixed to the [110]-direction, as it is the magnetic easy axis [186]. For this scenario the following notation is introduced: The $z$-axis will be referred to as the out-of-plane direction since it stands perpendicular on the Mn-sublattices and is along the magnetic hard axis [186]. Responses in the $xy$-plane will be refereed to as in-plane. In the $xy$-plane the [110] direction will be denoted by $\parallel \mathbf{N}$ and the $[1\bar{1}0]$ direction as $\perp \mathbf{N}$. Photocurrents and laser polarization will be given in terms of their components w.r.t. the linearly independent directions $\{\parallel \mathbf{N}, \perp \mathbf{N}, z\}$.

### *8.4.1 Symmetry considerations*

In Section 3.8 resonant transitions were defined as the special case where the initial and final state of the in general 3-band process describing the second order Keldysh responses is assumed. The LPGE is given by such resonant transitions [50], while the CPGE effects can only be described by non-resonant transitions. It was checked by the author that, indeed, the magnetic LPGE currents $J_{\perp\mathbf{N}}$ presented in Figure 8.9 a) and b) are solely given by resonant transitions, while the magnetic CPGE currents $J_{\parallel\mathbf{N}}$ and $J_z$ are purely non-resonant transitions. To study the properties of such resonant transitions, a band-resolved analysis can be utilized.

Figure 8.4 shows the a) parallel and b) perpendicular photocurrent for $\hbar\omega = 3.0\,\mathrm{eV}$ band resolved for linear polarization parallel (first row) and perpendicular to the Néel vector (second row). The Fermi level was set to

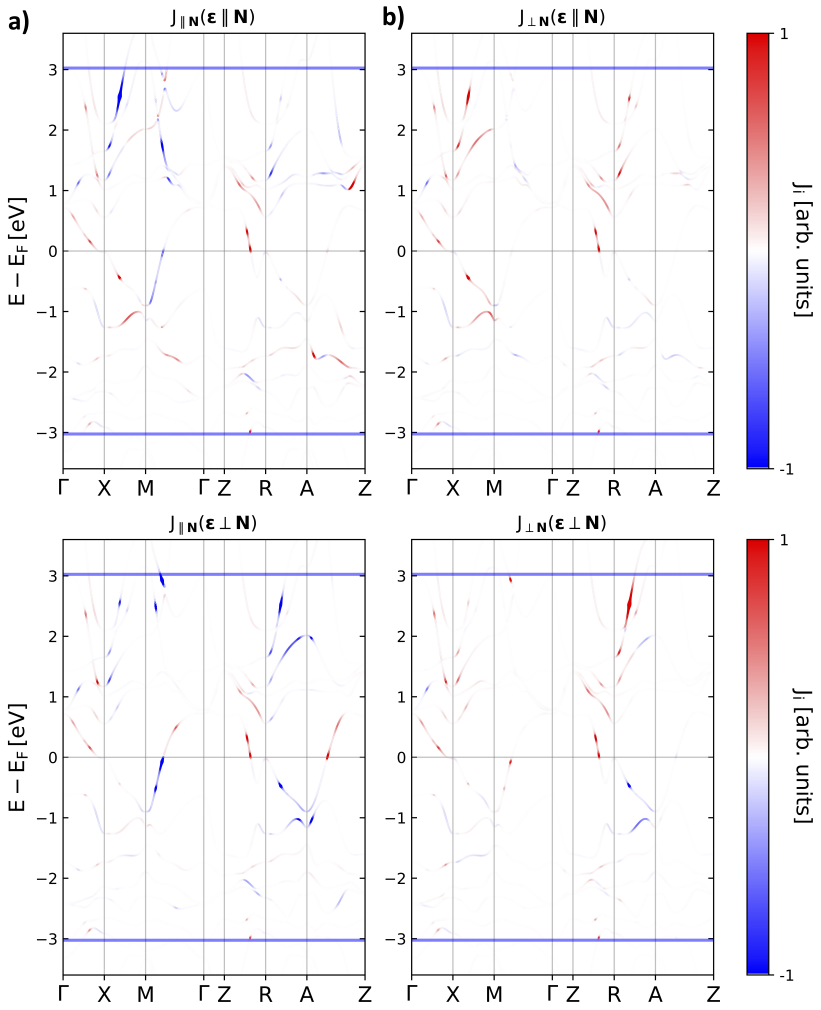


**FIGURE 8.4.** Band transitions along a high symmetry path of the a) parallel and b) perpendicular photocurrent for linearly polarized laser light parallel (upper) and perpendicular (lower panels) to the Néel vector for a laser frequency of $\hbar\omega = 3.0\,\mathrm{eV}$ (reprinted from [2], ©2023 CC BY 4.0). The Fermi level is indicated by the horizontal gray line, the edges of the selected energy interval $[\mathrm{E_F} - \hbar\omega, \mathrm{E_F} + \hbar\omega]$ are indicated by the blue bars.

the true Fermi level and a broadening of $\Gamma = 25$ meV used. The strength of the photoresponse at a given $k$-point is indicated by band thickness and the color coding. The energy region of bands contributing is determined by the selected Fermi level and the applied laser frequency $\pm\hbar\omega$ and marked by the thick blue lines at $E = E_F \pm 3.0$ eV. As discussed in the previous section the component of the photocurrent parallel to the Néel vector integrates to zero over the first Brillouin zone, however, strong transitions are visible not only in the perpendicular scenario shown in b) but also in case of the parallel component of scenario a). The sizeable resonant transitions of the parallel component suggest that a reduction of symmetry might unlock the response, as will be discussed further in the following sections and demonstrated in the next chapter. For now the discussion will be focused on the comparison of the bandstructure transitions for the various scenarios shown in Figure 8.4. Comparing first the two scenarios for light polarized along the Néel vector $\varepsilon \parallel \mathbf{N}$ in the upper panel of Figure 8.4 transitions happen at the same $k$ values and between bands which are separated by the laser frequency of 3.0 eV. For example a large transition between the X and M point from ~-0.3 eV to ~2.7 eV is visible in a) and b).

In case of the nonvanishing perpendicular current in b), however, both bands contribute with positive values, while in a) the conduction band shows a negative current response while the valence band has a positive response. In other regions of the BZ both current responses are very similar in strength and sign, for example from Γ to the X point the band transitions are the same for $J_{\perp\mathbf{N}}$ and $J_{\parallel\mathbf{N}}$. The transitions in the region between Z and R, which lay above Γ and X respectively, are also indistinguishable. From R to A the transitions are of comparable strength between a) and b) but of opposite sign. The region from M to Γ and from A to Z is more pronounced for the $J_{\parallel\mathbf{N}}$. In case of linearly polarized light with the light polarization perpendicular to the Néel vector shown in the second row of Figure 8.4 the qualitative behavior is the same for most transitions, however, other regions of the BZ seem to contribute more. Especially transitions for the upper slice of the BZ, the $\overline{ZRA}$ path, are dominant. Another large transition is visible in the path from M to Γ for both currents.

In conclusion transitions in response to linearly polarized light are visible along the high symmetry path presented in Figure 8.4 for both cases of $J_{\parallel\mathbf{N}}$ and $J_{\perp\mathbf{N}}$ often at the same $k$ points with only difference in sign and strength of the transition. Transitions do happen also in case of the symmetry forbidden response $J_{\parallel\mathbf{N}}$, which suggests that they are cancelled by opposing transitions in other regions of the BZ. To check how different regions of the BZ act with respect to each other in the above discussed scenarios, the photocurrent will now be analyzed in 3 slices parallel to the (001)−plane of the BZ. The first

and third slice are taken at a constant $|k_z|$ amplitude with negative (1st) and positive (3rd slice) values of $k_z$ respectively. The second slice is located in the middle of the BZ with $k_z = 0$. Figure 8.5 shows the parallel (left column) and perpendicular (right column) photocurrent as contour plots over these slices.

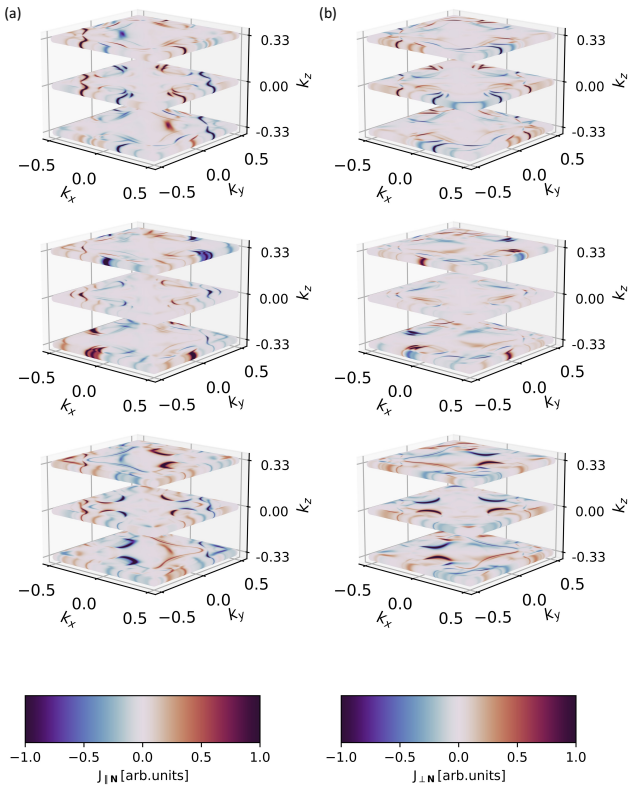


**FIGURE 8.5.** Brillouin zone resolved photocurrents in different $k_z$-layers for blue laser light with $\hbar\omega = 3.0$ eV and $\Gamma = 25$ meV. The left column shows the parallel photocurrent $J_{\parallel \mathbf{N}}$, which integrates to zero. The right column shows the non-vanishing perpendicular photocurrent $J_{\perp \mathbf{N}}$ (reprinted from [2], ©2023 CC BY 4.0).

Figure 8.5 shows that in case of the parallel response $k_z$ layers in the upper and lower half of the Brillouin zone cancel each other upon integration, while for the perpendicular current they add up. Figure 8.6 shows the response band resolved when following a path in the $k_z = 0$ layer from the negative M point, denoted M′, at (-.5,-.5) to the positive M point at (.5,.5) (coordinates given in relative units).

In case of the overall nonvanishing $J_{\perp \mathbf{N}}$ Figure 8.6 shows perfect mirror symmetry between the negative and positive $k$ region. For $J_{\parallel \mathbf{N}}$ transitions are mirrored as well but are of opposite sign in the two halves of the BZ

and cancel each other when integrating over the whole BZ. With this it is clear why the bandstructure transitions shown in Figure 8.4 alone cannot reveal the qualitative symmetry properties, at least not if only one quadrant of the Brillouin zone was considered. Since the presented high symmetry path is completely located in a region of positive $k$ in the BZ. Considering regions of positive and negative $\mathbf{k}$ easily reveals the effects of symmetry on the photocurrent as demonstrated as well in Figure 8.5. Figure 8.6 follows the photocurrent along the path from the negative to the positive M point.

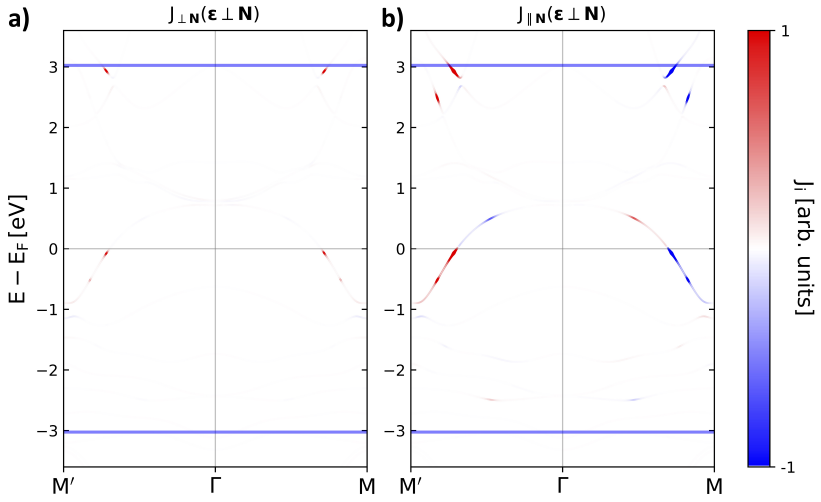


**FIGURE 8.6.** Band transitions of the photocurrent for linearly polarized laser light when crossing from negative to positive $k$-values, with the polarization perpendicular to the Néel vector in the $xy$-plane. a) photocurrent flowing in the $xy$-plane perpendicular to the Néel vector. b) photocurrent in the $xy$-plane parallel to the Néel vector.

In scenario a), showing the perpendicular component of the photocurrent, M and M′ contribute equally. However, in the symmetry forbidden scenario b) the responses in negative regions of the BZ cancel the positive regions.

### 8.4.2 *Spectral properties*

In order to compare the strength of the photocurrents to other materials presented in literature it is convenient to study the second order conductivity tensor $\sigma_{ijk}$, as defined in Eq. (3.71) such that the photocurrent is given by $J_i = \mathrm{Re} \sum_{jk} 2\sigma_{ijk} E_j E_k^*$. Based on the discussion in Section 8.3 the conductivity tensor was projected onto the dominating response perpendicular to the Néel

vector via $\sigma_{\perp \mathbf{N} jk} \equiv (\sigma_{xjk} - \sigma_{yjk})/\sqrt{2}$ and the following sum rules were used

$$\begin{aligned}
\sigma_{\perp\mathbf{N}}(\varepsilon \parallel \mathbf{N}) &\equiv \tfrac{1}{2}(\sigma_{\perp\mathbf{N}xx} + \sigma_{\perp\mathbf{N}yy}) + \tfrac{1}{2}(\sigma_{\perp\mathbf{N}xy} + \sigma_{\perp\mathbf{N}yx}) \\
\sigma_{\perp\mathbf{N}}(\varepsilon \perp \mathbf{N}) &\equiv \tfrac{1}{2}(\sigma_{\perp\mathbf{N}xx} + \sigma_{\perp\mathbf{N}yy}) - \tfrac{1}{2}(\sigma_{\perp\mathbf{N}xy} + \sigma_{\perp\mathbf{N}yx}) \\
\sigma_{\perp\mathbf{N}}(\varepsilon \parallel \mathbf{z}) &\equiv \sigma_{\perp\mathbf{N}zz},
\end{aligned} \tag{8.2}$$

to get the conductivity for the linear polarization parallel and perpendicular to the Néel vector. Figure 8.7 shows the frequency dependence of the perpendicular conductivity tensor as defined in Eq. (8.2). The tensor was evaluated at the true Fermi level and a broadening of $\Gamma = 25$ meV, corresponding to the thermal smearing at room temperature was used to allow for a reasonable comparison to values in literature.

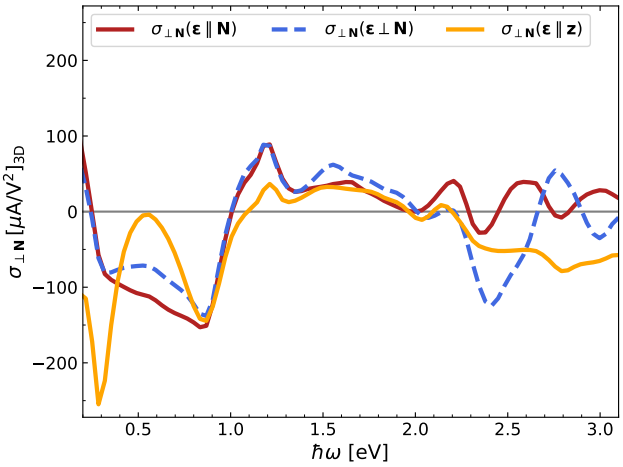


**FIGURE 8.7.** Frequency dependence of the conductivity tensor projected onto the $(1\bar{1}0)$ direction for different linear light polarizations (reprinted from [2], ©2023 CC BY 4.0). A broadening of $\Gamma = 25$ meV was used to mimic room temperature and the Fermi level was set to the true Fermi level.

Figure 8.7 shows sizeable photoconductivity for all orientations of the laser polarization across the complete presented frequency band of $\hbar\omega \in [0.20, 3.10]$ eV.

As discussed in subsection 3.4.3, divergences of physical and numerical origin can occur when approaching the zero frequency limit. Since it is nontrivial to disentangle these divergences and potentially a lot of computational effort is required to cure numerical instabilities, the discussion was confined to laser frequencies above 200 meV. After discussions with experimental colleagues which suggested that the experimental accessible frequency range

starts roughly at $\hbar\omega = 1.00$ eV, it was concluded that the chosen frequency range is reasonable.

For laser frequencies smaller than $\hbar\omega = 1.00$ eV the conductivity is negative for all linearly polarized fields. At a laser frequency of $\hbar\omega = 0.80$ eV the conductivity shows a (negative) peak of $\sim -150\ \mu A/V^2$ similar in amplitude for all presented polarizations. Another peak of about $100\ \mu A/V^2$ is present at $\hbar\omega = 1.20$ eV if the laser light is linearly polarized within the $xy-$plane, while the conductivity in response to linearly along $z$ polarized light (golden curve) shows a much smaller peak at this frequency.

Therefore, the conductivity in Figure 8.7 is comparable in size to values reported in literature, *i.e.* Azpiroz *et al.* reported a maximum conductivity of $\sim 40\ \mu A/V^2$ for the bulk semiconductor GaAs[69], and more recently Zhang *et al.* predicted a photoconductivity of almost $100\ \mu A/V^2$ in the 2D van-der-Waals AFM $CrI_3$ [50]. In the range of $\hbar\omega \in [1.20, 2.00]$ eV the conductivity is positive for all orientations of the linear polarization. At $\hbar\omega = 2.00$ eV the two in-plane polarized conductivities (blue and red curve) are completely suppressed and start to oscillate w.r.t. frequency in the frequency band of $\hbar\omega \in [2.00, 3.10]$ eV. At a laser frequency of $\hbar\omega = 3.00$ eV the conductivity $\sigma_{\perp \mathbf{N}}$ can be switched almost perfectly between $\sim \pm 25\ \mu A/V^2$, by simply rotating the linear polarization vector by 90° in the $xy$-plane. The largest response at frequency $\hbar\omega = 3.00$ eV of $\sim 75\ \mu A/V^2$ however is in response to light linearly polarized along the $z$-direction.

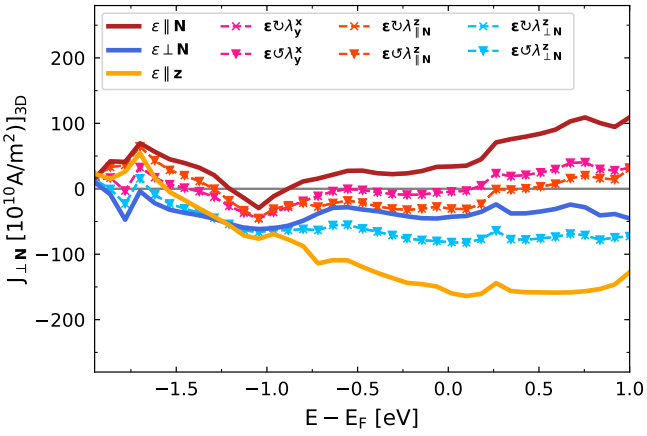


**FIGURE 8.8.** Dependence of the in-plane perpendicular component of the photocurrent on the band filling for a laser frequency of $\hbar\omega = 3.00$ eV and a broadening of $\Gamma = 25$ meV (reprinted from[2], ©2023 CC BY 4.0).

Fixing the laser frequency at $\hbar\omega = 3.00\,\text{eV}$ Figure 8.8 shows the photocurrent $J_{\perp\mathbf{N}}$ associated with Eq. (8.2) for different band fillings. As indicated by Figure 8.7, when evaluated at the true Fermi level the photocurrent can be switched between roughly $\pm 50 \times 10^{10}\,\text{A/m}^2$. This can also be seen when examining the response to circularly polarized light rotating in the $xy$-plane indicated by the magenta curve. In Section 8.3 these responses were identified as averages of the linearly polarized in-plane responses. At the true Fermi level the averaged circular response vanishes, thus, confirming the opposite nature of the linear responses. This feature is robust almost over the entire presented energy range, although above the true Fermi level the parallel polarized response (thick red curve) slightly dominates. Beneath the true Fermi level the perpendicular polarization (thick blue curve) is pronounced over the parallel polarization. Only at 1 eV below the true Fermi level a dip of the parallel polarized response is visible and both responses are negative.

In conclusion, it was shown that the photocurrents in $Mn_2Au$ are comparable in size to various other prominent materials and if the laser frequency is fixed to $\hbar\omega = 3.0\,\text{eV}$ the dominating in-plane perpendicular component of the photocurrent can be switched by simply rotating the linear polarization by 90° within the $xy$-plane. It was confirmed that this feature is robust with respect to the band filling in a range of almost 2 eV around the true Fermi level. Due to the convenient switching behavior between in-plane linear responses, which can often only be achieved with, experimentally harder to handle, circularly polarized light, the frequency of $\hbar\omega = 3.0\,\text{eV}$ will be used as default value for the remaining discussion in this chapter. In the next paragraph the broadening dependence will be analyzed.

### 8.4.3 *Dependence on broadening & switchability*

In this paragraph the dependence of the photocurrents on the broadening $\Gamma$ is analyzed when approaching the clean limit ($\Gamma \to 0$). Based on arguments in subsection 2.1.2, positive and negative broadening values are considered to identify magnetic photogalvanic currents. In the second part of this paragraph a scaling law will be identified to draw conclusion on the microscopic origin of the photocurrent.

As discussed in subsection 2.1.2 magnetic and nonmagnetic LPGE currents should show opposite behavior under a time reversal operation $\mathcal{T}$. Nonmagnetic LPGE currents are expected to be even, while their magnetic counterparts switch sign under a time reversal operation. The picture is reversed in case of CPGE currents, since not only the magnetization is reversed but also the light's sense of rotation. In dissipative processes, such as the here

discussed photocurrent, the time reversal operation can be mimicked by considering negative broadening parameters. To confirm that all photocurrents are purely magnetic, as dictated by the $\mathcal{PT}$-symmetry of the system [183] and explicitly proposed for $Mn_2Au$ [50].

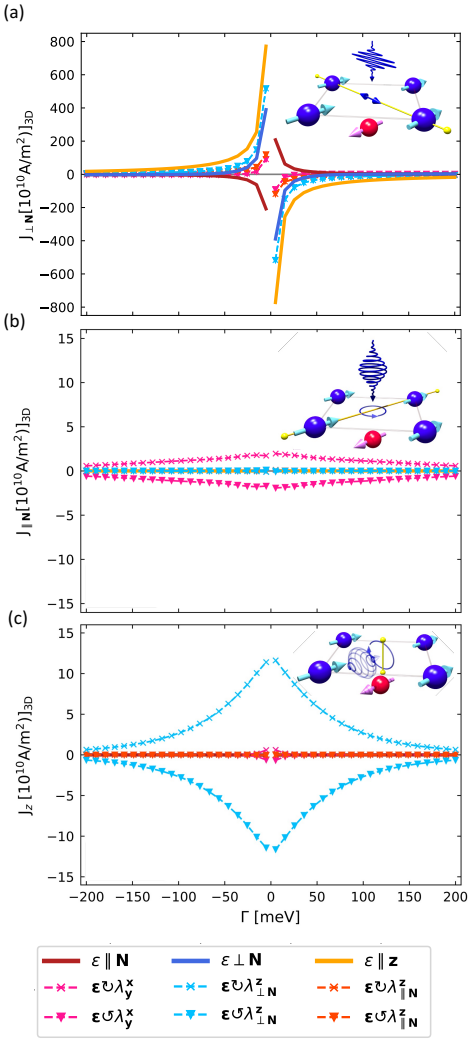


**FIGURE 8.9.** Dependence of the photocurrent on the broadening parameter $\Gamma$ for different linearly and circularly polarized laser sources, evaluated at the true Fermi level with a laser frequency of $\hbar\omega = 3.00\,\mathrm{eV}$ (reprinted from [2], ©2023 CC BY 4.0). The clean limit is approached from positive and negative smearing values to mimic the effect of a Néel vector reversal.

Figure 8.9 shows the components of the photocurrent in response to linearly

and circularly polarized light plotted against positive and negative broadening values with amplitudes between 5 to 200 meV. The Fermi level was set to the true Fermi level and the applied laser frequency kept at $\hbar\omega = 3.00$ eV. In Figure 8.9 the photocurrents in $Mn_2Au$ are plotted against the lifetime broadening for positive and negative values of $\Gamma$, mimicking a Néel vector switch via a time-reversal operation. Indeed, the linear photocurrent $J_{\perp\mathbf{N}}$ is odd with respect to the broadening, while the circular responses $J_{\parallel\mathbf{N}}$ and $J_z$ are even, confirming both types to be of magnetic origin as expected from the $\mathcal{PT}$-symmetry of the system. Therefore, the LPGE like photocurrents can be switched by a reversal of the magnetic moments on the Mn sublattices or, at certain applied laser frequencies, also by changing the orientation of the linearly polarized laser light, making them a good proxy to gauge the state of the Néel vector. The CPGE photocurrents can only be switched by changing the lights helicity and are one order of magnitude smaller compared to the LPGE photocurrents. By analyzing the scaling of the photocurrent it is possible to identify different quantum geometric quantities[75,85,86]. Three terms can be identified by their scaling behavior with respect to the quasiparticle lifetime: a Drude term quadratic in the lifetime broadening $\tau$, a term probing the Berry curvature dipole which is linear in the lifetime broadening and a term probing the quantum metric dipole independent on the lifetime broadening[85,85]. However, the Berry curvature itself and therefore the Berry curvature dipole term is expected to vanish in $\mathcal{PT}$-symmetric systems[85], leaving only the Drude and the quantum metric dipole term. Figure 8.10 shows again the broadening dependence of the dominating in-plane perpendicular photocurrent, fitted with the non-linear least squares algorithm, as implemented in the `scipy.optimize.curve\_fit` routine[187], to the model function $f(\Gamma) = c + a\Gamma^2$. The fitted coefficients $a$ and $c$ are shown in the legend for each linearly independent orientations of the linear polarization vector. Figure 8.10 suggest that, at the given frequency of $\hbar\omega = 3.00$ eV, the Drude term is dominating by several orders of magnitude over the geometric contribution associated with quantum metric dipole. These findings are in line with recent theoretical predictions by Sodemann *et al.*[78], suggesting that geometrical contributions dominate only in the low frequency limit $\hbar\omega \leq \Gamma$ and are suppressed strongly towards larger frequencies.

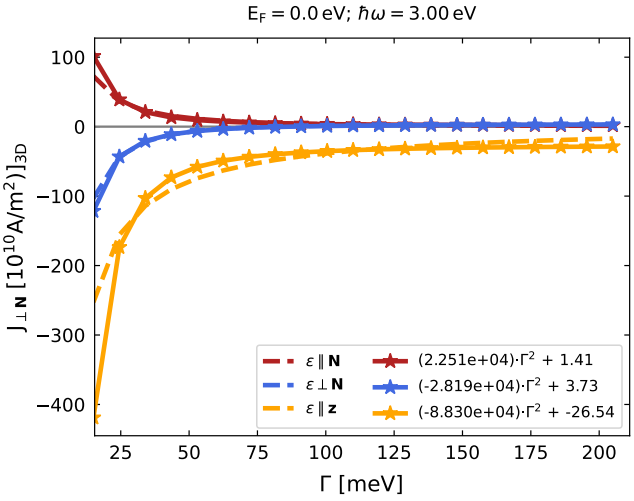


**FIGURE 8.10.** Broadening dependence of $J_{\perp \mathbf{N}}$(solid curves) and a fit to the $f(\Gamma) = c + a\Gamma^2$ (dashed curves). The resulting fitting coefficients are given in the legend.

## 8.5 INVERSE FARADAY EFFECT

In this section the laser induced spin density defined in Eq. (3.81), known as the inverse Faraday effect, upon radiation with circularly polarized light[92], is analyzed in $Mn_2Au$. The inverse Faraday Effect is expected to be play a crucial role for the ultrafast optical switching of AFMs[28,40,41,43,92,188].

Due to the special, symmetric breaking, role of the opposing magnetization in $Mn_2Au$ not only the overall induced spin density is analyzed, but also the staggered response on the Mn sublattices defined by

$$\delta \mathbf{S}^- := \frac{\delta \mathbf{S}(\mathrm{Mn}_\uparrow) - \delta \mathbf{S}(\mathrm{Mn}_\downarrow)}{2}. \tag{8.3}$$

To avoid confusion, the induced spin density, summed over all atomic cites including the Au cite, is denoted as $\delta S^+$. Figure 8.11 a) shows the broadening dependence of the components of the overall induced spin density $\delta S^+$ and b) of the staggered response $\delta S^-$. As for the previously discussed photocurrents the nonequilibrium spin density is projected onto the $\{\| \mathbf{N}, \perp \mathbf{N}, z\}$-directions. The induced spin density was evaluated at the true Fermi level for a laser frequency of $\hbar\omega = 3.00$ eV. In case of the overall response broadening values $\Gamma$ in the range from 10 to 1000 meV were considered. To save computation time the staggered responses were only analyzed up to a broadening of 400 meV. For both scenarios the broadening is plotted on a logarithmic scale. The

in-plane components of the uniform induced spin density in Figure 8.11 a) only respond to circularly polarized light and are comparable in amplitude, with responses of $\sim 1 \times 10^{-6}\,\hbar/2$ at $\Gamma$ =25 meV room temperature broadening. As the cartoons indicate, both components are finite when the direction of the nonequilibrium spin density is along the normal of the plane of rotation. In case of the integrated response along the Néel vector $\delta S^{+}_{\parallel \mathbf{N}}$ the magnetic moments on the Mn sublattices are uniformly modulated in amplitude. Due to the opposing orientation of the magnetization on the Mn sublattices and the uniform modulation, $\delta S^{+}_{\parallel \mathbf{N}}$ results in the formation of a very slightly ferrimagnetic configuration.

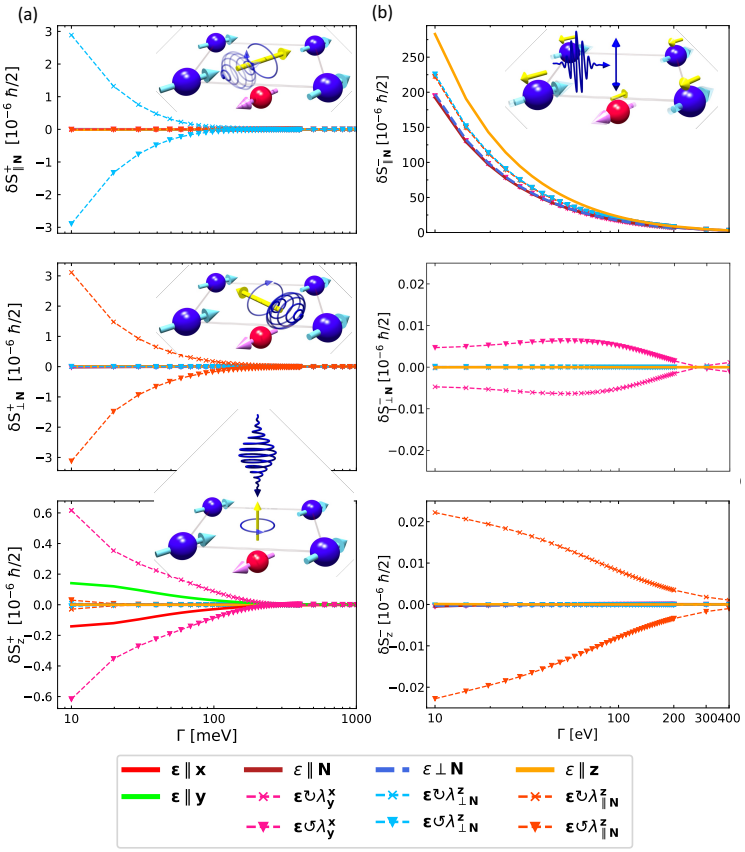


**FIGURE 8.11.** Broadening dependence of the a) overall and b) staggered laser induced spin density $\delta S^{\pm}$, for a laser frequency of $\hbar\omega = 3.00$ eV evaluated at the true Fermi level (reprinted from [2], ©2023 CC BY 4.0). The figure shows the spin density projected onto the $\{\parallel \mathbf{N}, \perp \mathbf{N}, z\}$-directions. Cartoons indicate the required laser alignment to induce the respective components.

The $\delta S^{+}_{\perp \mathbf{N}}$ response results in the formation of a small ferromagnetic

moment along the $\perp$ **N** direction, thus, exerting a uniform torque, which effectively cants the magnetic moments on the Mn sublattices. The same is true for the out-of-plane component $\delta S_z^+$, which requires an equivalent geometric setup in terms of laser orientation as the in-plane components, however, the amplitude is reduced: at 25 meV broadening the $z$-component $\delta S_z \approx 0.35 \times 10^{-6}\,\hbar/2$ is more than two times smaller than the in-plane components. On the other hand $\delta S_z^+$ shows the slowest decay towards larger broadening values and is comparable in amplitude to the in-plane-component for broadening values above 100 meV. In the range of $\Gamma = 20$ meV up to almost $\Gamma = 200$ meV the $z$-component shows almost perfect linear scaling, indicating a $\sim \log(\Gamma)$ behavior. The overall responses $\delta S^+$ can all be helicity switched as expected from the existing IFE theory[41,92]. From Figure 8.11 it can be seen that the overall $z$-component not only responds to circularly polarized light, but also to linearly polarized light. If the light is linearly polarized along the **x**-direction a finite response of $\approx 0.15 \times 10^{-6}\,\hbar/2$ at $\Gamma = 25$ meV is present and a equally strong, but reversed in sign, response for light polarized along the **y**-direction.

Similar to the IFE in response to circularly polarized light, which is helicity switchable, the here presented nonequilibrium spin density in response to linearly polarized light can be switched by rotating the linear polarization by 90° in the $xy$-plane. The response to these "off-axis" linearly polarized fields is surprising in the context of the IFE, which is historically only associated with circularly polarized light[92]. However, the here presented findings are in good agreement with recent predictions made by Freimuth *et al.*[189], who predicted a laser-induced torque in $Mn_2Au$ for the scenario of the Néel vector along the [110]-direction in response to linearly polarized light along the $x$- and $y$-direction. In terms of their symmetry requirements the laser induced spin density and the laser induced torque are equivalent since both torque and spin operator are axial vectors. The response of $\delta S_z^+$ to linearly polarized light along $x$ and $y$ is, therefore, directly governed by the symmetry tensors #4 and #27 given in Table 1 in the work of Freimuth[189]. Since linearly polarized light is experimentally more accessible than circularly polarized light, this raises the question if a similar response to "off-axis" linearly polarized light can be found for the in-plane components $\delta S_{\parallel \mathbf{N}}^+$ & $\delta S_{\perp \mathbf{N}}^+$.

Figure 8.12 shows the a) $\delta S_{\parallel \mathbf{N}}^+$ component in response to linearly polarized light rotating in the plane whose normal is along the Néel vector. In a similar fashion Figure 8.12 b) shows the $\delta S_{\perp \mathbf{N}}^+$ component in response to linearly polarized light rotating in the plane spanned by the Néel vector with the $z$-axis, which is again the plane whose normal is along the induced spin density. Figure 8.12 c) shows the same analysis for the $z$-component, here the linear polarization is rotated within the $xy$-plane. Figure 8.12 suggest

that the in-plane components of the overall spin density can be driven by "off-axis" linearly polarized light as well and are by a factor 4 larger than the out-of-plane off-axis response. A 90° rotation of the linear polarization in the respective plane of rotation allows one to switch the responses between positive and negative sign, thus, mimicking the behavior of a helicity switchable circular response by means of linearly polarized light.

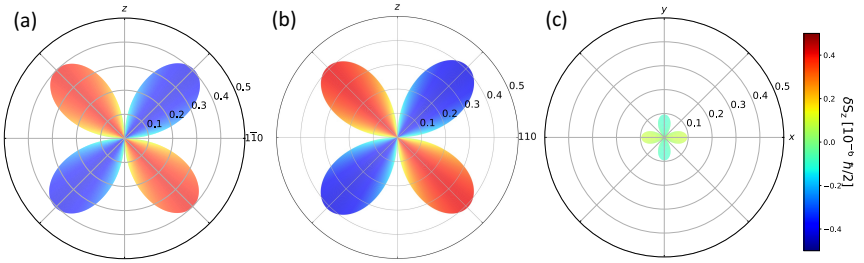


**FIGURE 8.12.** Angular dependence of the laser induced spin density in response to linearly polarized light rotating in the plane whose normal is along the induced spin density (reprinted from [2], ©2023 CC BY 4.0). a) shows the in-plane parallel component $\delta S^+_{\parallel \mathbf{N}}$, b) the perpendicular component $\delta S^+_{\perp \mathbf{N}}$ and c) the out-of plane component $\delta S^+_z$. The laser frequency was set to $\hbar\omega = 3.00$ eV, the broadening fixed to $\Gamma = 25$ meV and the responses were evaluated at the true Fermi level. The absolute amplitude is indicated by the radius and the amplitude by the color code, both radius and color coding are normalized such that all three components can be directly compared.

The discussion is now focused on the staggered responses $\delta\mathbf{S}^-$ defined in Eq. (8.3) and presented in Figure 8.11 b). The staggered component perpendicular to the Néel vector $\delta S^-_{\perp \mathbf{N}}$ and the out-of-plane component $\delta S^-_z$ are two orders of magnitude smaller than their respective overall responses presented in Figure 8.11 a) and, therefore, are considered negligible and omitted from the remaining discussion. However, the staggered response along the Néel vector $\delta S^-_{\parallel \mathbf{N}}$ is sizeable, in fact with amplitudes reaching $\sim 125 \times 10^{-6}\,\hbar/2$ at $\Gamma = 25$ meV the parallel component of the staggered response is two orders of magnitude larger than all previously discussed uniform responses. Further $\delta S^-_{\parallel \mathbf{N}}$ in response to circularly polarized light is helicity independent, unlike the integrated responses, and maximized by means of linearly polarized light. Similar to the perpendicular charge photocurrent $J_{\perp \mathbf{N}}$ the staggered spin response parallel to the Néel vector $\delta S^-_{\parallel \mathbf{N}}$ behaves like a LPGE effect, while all other induced spin components (staggered and integrated) are of CPGE character.

In Ref. [190] a strong electrically induced staggered spin density on the Mn sublattices was identified as the origin of an ultrafast spin-axis reorientation in $Mn_2Au$. However, in this case the induced spin density was not aligned with the magnetic moments of Mn and, thus, a torque of op-

posing sign exerted on the respective magnetic moments. These staggered torques are known as Néel -order spin orbit torque (NSOT)[190,191] and are subject of ongoing research in the context of electrical and optical switching of AFMs[39,44,176,192,193]. However, as Figure 8.11 b) suggests the staggered components required to drive a NSOT are effectively suppressed upon optical excitation in $Mn_2Au$. On the other hand, a large staggered IFE was recently reported in AFM CrPt[43], were a direct quenching of the magnetic moments on the Cr sublattices was achieved by applying circularly polarized light. The reported quenching was identified as the origin of ultrafast optical switching of the Néel vector in CrPt[43], highlighting the importance of direct modulation of the magnetic moments via staggered spin responses for the switching of AFM materials. Here the quenching of the Néel vector is not only finite for circularly polarized light, but can also be driven by means of linearly polarized light. In fact the strongest quenching is induced by light linearly polarized along the $z$-direction. Due to the importance of the staggered nonequilibrium spin density in the context of ultrafast switching of the AFM order, $\delta S^{-}_{\|\mathbf{N}}$ is next analyzed in terms of its frequency dependence. Figure 8.13 b) shows the frequency dependence of $\delta S^{-}_{\|\mathbf{N}}$, for reference the frequency dependence of the overall largest uniform spin response $\delta S^{+}_{\perp\mathbf{N}}$ is also presented. Laser frequencies in the range of $\hbar\omega \in [0.2, 4.1]$ eV were considered, the broadening was fixed to room temperature and the band filling set to match the true Fermi level. Figure 8.13 highlights the fundamentally different behavior of the uniform and the staggered response. The uniform response shows characteristic IFE behavior: it is driven by circularly polarized light, helicity switchable, and oscillates with respect to frequency. The staggered component on the other hand behaves like an LPGE effect and while its response to circularly polarized is sizeable, it is helicity independent and can thus be interpreted as averages of the associated responses to linearly polarized light. Further, the staggered response always quenches the magnetic moments in the presented frequency range, no sign change, which would result in an enhancement of the local moments, is present.

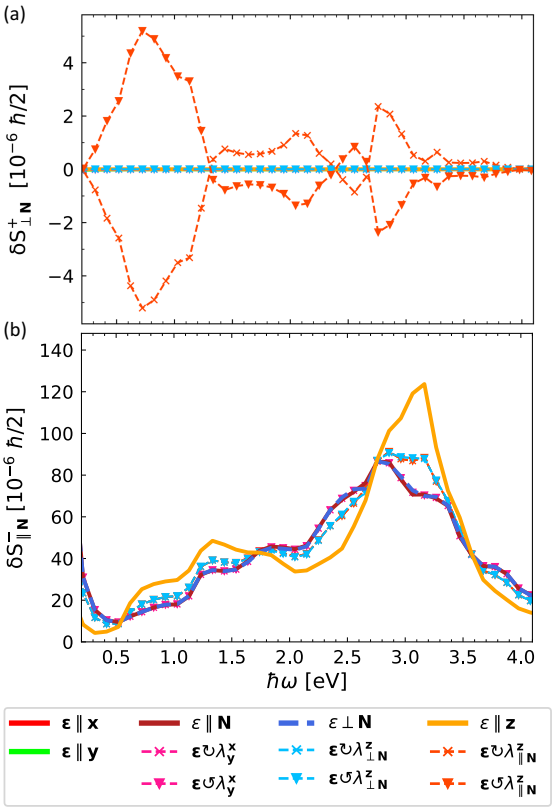


**FIGURE 8.13.** Laser induced a) overall and b) staggered spin density $\delta S^{\pm}$. Evaluated at the true Fermi level with a broadening of $\Gamma = 25$ meV in response to circularly and linearly polarized light, respectively (reprinted from [2], ©2023 CC BY 4.0). Frequencies in the range from $\hbar\omega = 0.2$,eV to 4.1 eV were considered.

The largest integrated response of about $5 \times 10^{-6}\,\hbar/2$ is achieved at $\hbar\omega = 0.7$ eV. At this frequency the staggered response is mostly suppressed, before showing an almost perfect monotonic increase of the amplitude up to its maximum of about $85{\times}10^{-6}\,\hbar/2$ in response to light polarized in the $xy$-plane at a frequency of $\hbar\omega = 2.8$ eV and about $125{\times}10^{-6}\,\hbar/2$ in response to light polarized linearly out-of plane at a frequency of $\hbar\omega = 3.1$ eV. For frequencies above $\hbar\omega = 3.1$ eV the staggered response rapidly drops off.

## 8.6 Laser induced spin currents

Nonmagnetic semiconductors were historically the first material class found to host sizeable, electrically induced, spin currents by means of the spin Hall effect [194]. The spin Hall effect describes the generation of a fully spin-polarized current flowing perpendicular to an electrically induced charge current by spin orbit coupling which deflects the spin-up and spin-down charge carriers in opposing directions perpendicular to the flow of the unpolarized current [194]. Optical detection of these pure spin currents by means of Kerr rotation was confirmed in a similar time frame [195]. Later optical generation of spin currents in semiconductors due to the transfer of optical orbital angular momentum of the light to the charge carriers was demonstrated later [196]. More recently the second order photogalvanic effect was theoretically predicted to induce gigantic spin currents in ferromagnets [98]. $\mathcal{PT}$-symmetric collinear AFMs, such as the here discussed $Mn_2Au$, were proposed as efficient spin current generators by means of the nonlinear Hall effect [91], and in case of $\mathcal{PT}$-symmetric antiferromagnetic insulators a large spin circular photogalvanic effect was predicted [89]. In non-centrosymmetric systems which still hold a mirror symmetry, pure bulk spin currents can even be generated by means of linearly polarized light [90].

In this section laser induced spin-polarized photocurrents, or spin photocurrents, defined in Eq. (3.77), are investigated in $Mn_2Au$ for both circularly and linearly polarized light and compared to the previously discussed charge photocurrents. Figure 8.14 shows the laser induced spin polarized photocurrents as defined in Eq. (3.77) calculated in $Mn_2Au$ vs the broadening $\Gamma$ evaluated at the true Fermi Level for a laser frequency of $\hbar\omega = 3.0\,\mathrm{eV}$. Only in-plane spin photocurrents are shown, the left column shows the spin currents flowing parallel to the Néel vector, the right column the currents flowing perpendicular to the Néel vector. The first, second and third row show the components of the spin polarization parallel, perpendicular and out-of-plane relative to the Néel vector respectively. Cartoons in the panels show the geometry of the individual responses. The most sizeable spin currents in Figure 8.14 are the currents with spins aligned parallel to the Néel vector in response to circularly polarized light, *i.e.* $Q^{\|\mathbf{N}}_{\|\mathbf{N}}(\lambda^z_{\|\mathbf{N}})$ and $Q^{\|\mathbf{N}}_{\perp\mathbf{N}}(\lambda^z_{\perp\mathbf{N}})$, with amplitudes reaching $\sim 150\,\hbar/(2\mathrm{e})\,\mathrm{A/m^2}$ at room temperature smearing ($\Gamma = 25\,\mathrm{meV}$). Both responses are sensitive to the light's helicity and, therefore, can be classified as CPGE-like spin currents. As the cartoons indicate in both scenarios the laser light rotates in the plane spanned by the direction of current flow with the $z$-axis. Suggesting that the flow of the spin polarized current, with spin polarization along the Néel vector, in response to circu-

larly polarized light can be arbitrarily manipulated by rotating the angle of incident of the light within the $xy$-plane. A similar symmetry is apparent for the CPGE-like spin currents $Q^{\perp\mathbf{N}}_{\parallel\mathbf{N}}(\lambda^z_{\perp\mathbf{N}})$ & $Q^{\perp\mathbf{N}}_{\perp\mathbf{N}}(\lambda^z_{\parallel\mathbf{N}})$ presented in the second row of Figure 8.14, however here the light rotates in the plane whose normal is parallel to the flow of the spin polarized current. Compared to the responses shown in the first row the amplitude of the spin currents is reduced to $\sim\pm 50\,\hbar/(2e)\,\mathrm{A/m^2}$ at $\Gamma = 25$ meV.

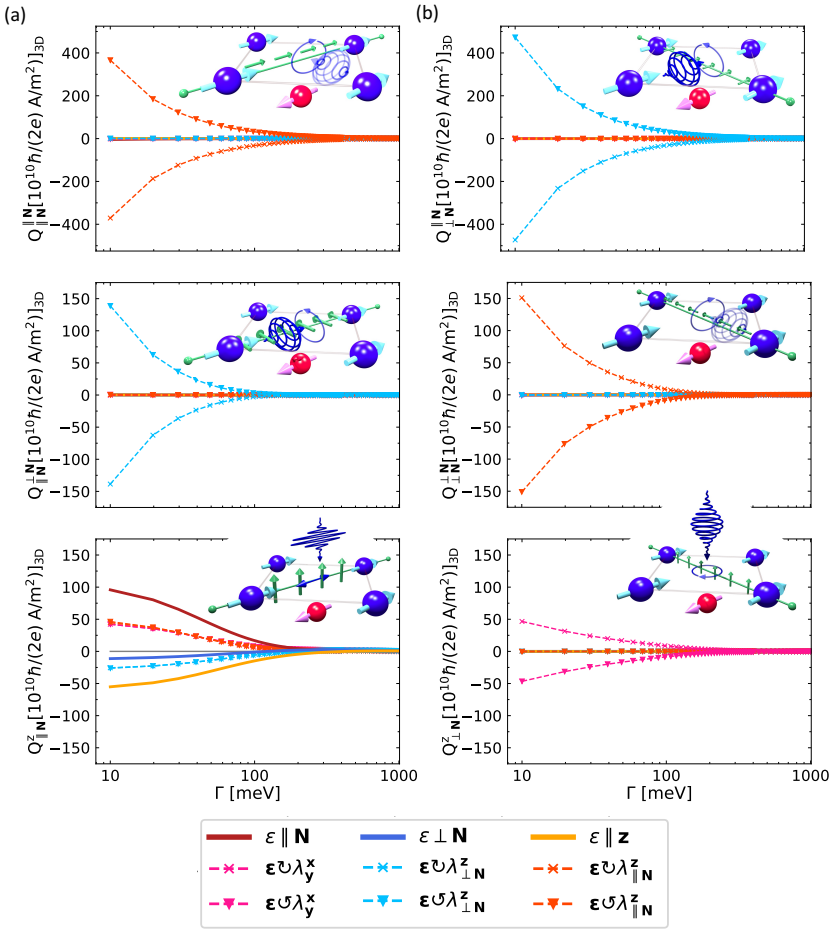


**FIGURE 8.14.** Laser induced in-plane spin currents evaluated at the true Fermi level versus the broadening Γ, for a laser frequency of $\hbar\omega = 3.00$ eV (reprinted from [2], ©2023 CC BY 4.0). The left column shows the spin currents flowing parallel to the Néel vector, the right column currents perpendicular to the Néel vector. Each row represents a different orientation of the spin polarization.

The third row of Figure 8.14 shows the spin currents flowing in the plane but with spins polarized out-of-plane along the $z$-direction. The spin current

flowing parallel to the Néel vector with spins pointing along the $z$-direction $Q^z_{\|\mathbf{N}}$ is the only in-plane component showing LPGE-like behavior, as indicated by the responses to linearly polarized light reaching $\sim 75\,\hbar/(2e)\,\mathrm{A/m^2}$ at $\Gamma = 25$ meV and the helicity independent responses to circularly polarized light. It was confirmed by the author that the circular responses are indeed the averages of the linearly polarized responses. The LPGE-like $Q^z_{\|\mathbf{N}}$ decays much slower w.r.t. to $\Gamma$ than the CPGE like spin currents. This is the same qualitative behavior as shown by the magnetic LPGE charge photocurrents discussed above, other similarities to the LPGE charge currents are apparent: the spin polarized current $Q^z_{\|\mathbf{N}}$ changes sign when rotating the in-plane linear polarization by 90° (thick red and blue curve), however the switching is not perfect, since the response to light polarized parallel to the Néel vector is an order of magnitude larger than the response to light polarized perpendicular to the Néel vector. Therefore, a given linearly polarized field not only induces a charge current flowing perpendicular to the Néel vector $J_{\perp\mathbf{N}}$, but also a spin-polarized current $Q^z_{\|\mathbf{N}}$ flowing perpendicular to the spin-unpolarized charge photocurrent, which can be interpreted as a nonlinear photogalvanic equivalent of the Spin Hall effect. In the following subsection 8.6.2 this idea will be outlined in greater detail.

For completeness Figure 8.15 shows the remaining components of the spin photocurrents flowing out of the plane along the $z$-direction for different orientations of the spin polarization. Figure 8.15 a) shows the scenario of the spin photocurrent flowing along $z$ with spins aligned parallel to the Néel vector $Q_z^{\|\mathbf{N}}$. The response behaves LPGE like and thus can also be interpreted as a photogalvanic spin Hall effect in combination with the in-plane charge current $J_{\perp\mathbf{N}}$, however at room temperature smearing $Q_z^{\|\mathbf{N}}$ is the weakest of all presented responses with $Q_z^{\|\mathbf{N}} \approx -35 \times 10^{10}\,[\hbar/(2e)\,A/m^2]$. Figure 8.15 b) shows the remaining two, CPGE-like, components $Q_z^{\perp\mathbf{N}}$ and $Q_z^z$ only for the respective circularly polarized field which activates the response. At $\Gamma = 25$ meV the responses reach $Q_z^z \approx \pm 70 \times 10^{10}\hbar/(2e)\,\mathrm{A/m^2}$ and $Q_z^{\perp\mathbf{N}} \approx \pm 35 \times 10^{10}\hbar/(2e)\,\mathrm{A/m^2}$ and decay towards larger broadening values. For $\Gamma > 200$ meV both responses are almost completely suppressed. From Figure 8.14 and Figure 8.15 two symmetry relations can be identified: first all spin currents of type $Q^a_a$, with $a \in \{\| \mathbf{N}, \perp \mathbf{N}, z\}$, only respond to circularly polarized light $\varepsilon \circlearrowleft \lambda^{\mathbf{z}}_{\|\mathbf{N}}$ rotating in the plane spanned by the Néel -vector and the $z$-axis. Second spin currents of type $Q^b_a$ always respond to the same field as currents $Q^a_b$ for $a \neq b \in \{\| \mathbf{N}, \perp \mathbf{N}, z\}$.

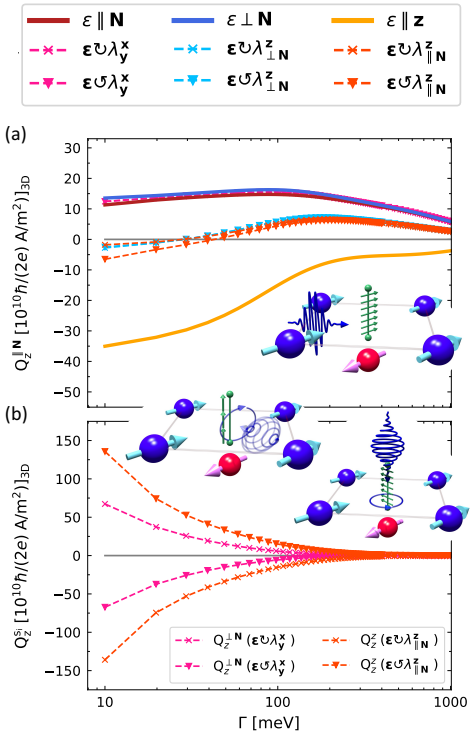


**FIGURE 8.15.** Laser induced spin currents vs the broadening $\Gamma$ for a laser frequency of $\hbar\omega = 3.00\,\text{eV}$ (reprinted from [2], ©2023 CC BY 4.0). a) spin currents flowing in the plane parallel to the Néel vector for different orientations of the spin polarization. b) spin currents flowing perpendicular to the Néel vector in the plane.

### 8.6.1 *Magnetic origin*

The LPGE charge photocurrents presented in Figure 8.9 were found to be odd under sign reversal of the broadening, while CPGE charge photocurrents showed an even behavior, identifying both as purely magnetic photocurrents. To perform a similar analysis for the spin currents two representative responses are shown in Figure 8.16, namely a) shows the CPGE-like spin photocurrent $Q^{\|\mathbf{N}}_{\|\mathbf{N}}$ and b) the LPGE-like $Q^{z}_{\|\mathbf{N}}$, approaching the clean limit of the lifetime broadening $\Gamma$ from positive and negative values. Broadening values in the range of $\pm[10, 200]$ meV were considered.

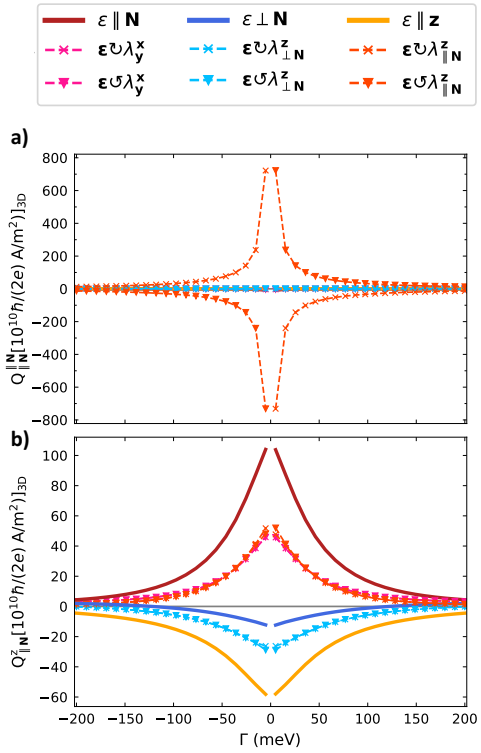


**FIGURE 8.16.** Laser induced spin currents flowing parallel to the Néel vector in the clean limit of the broadening Γ, approached from positive and negative broadening values, respectively. In a) the spin currents flowing parallel to the Néel vector with spins aligned parallel to the Néel vector are shown in response to circularly polarized light rotating in the plane spanned by the Néel vector with the $z$-axis. In b) the scenario of linearly polarized light is shown.

Figure 8.16 shows an even behavior w.r.t. sign reversal of the broadening for the LPGE-like response. The CPGE-like spin current is odd under broadening. It was checked and confirmed by the author that all other LPGE-like and CPGE-like responses show the same qualitative behavior. Therefore, the behavior is reversed compared to the charge LPGE and CPGE effects shown in Figure 8.9. As derived in Chapter 3 charge photocurrents are calculated in the Keldysh formalism by coupling the velocity operator $v_i$ to the laser induced nonequilibrium state of the electronic system. In case of spin-polarized photocurrents instead the spin-velocity operator $\{v_i, \sigma_s\}$ is coupled to the same nonequilibrium state. Since $\sigma_s$ is odd under a time reversal operation $\mathcal{T}$, the time reversal switches the direction of the spin photocurrent and its spin polarization. Thus, the negative broadening behavior is reversed for spin photocurrents when compared to the charge photocurrents and magnetic LPGE-like spin photocurrents are expected to be even under sign reversal

of Γ and magnetic CPGE-like spin photocurrents odd. With that in mind, Figure 8.16 confirms all LPGE- and CPGE-like spin photocurrents to be of purely magnetic origin.

### 8.6.2 *Photospin Hall Effect*

In the previous sections laser induced photocurrents of charge and spin were analyzed in response to linearly and circularly polarized light. Most components of charge and spin photocurrent were found to respond only to circularly polarized light. As discussed in Section 8.3 and Section 8.4 for various Néel vector orientations within the $xy$-plane, the resulting, magnetic, charge photocurrent $J_{\perp\mathbf{N}}$ in response to linearly polarized light is confined to the $xy$-plane and flows perpendicular to the Néel vector. In Section 8.6 two spin-polarized currents were found in response to linearly polarized light: a small spin photocurrent flowing out-of-plane with spins polarized parallel to the Néel vector $Q_z^{\parallel\mathbf{N}}$ and larger response flowing in-plane parallel to the Néel vector with spin polarization out-of-plane $Q^z_{\parallel\mathbf{N}}$. Both spin-polarized currents flow perpendicular to the spin-unpolarized charge photocurrent $J_{\perp\mathbf{N}}$ and, thus, abide the geometry of the spin Hall effect (SHE), as shown in Figure 8.17.

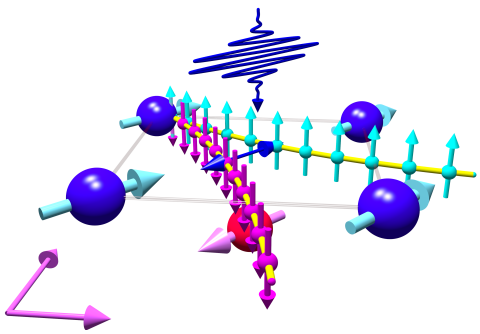

**FIGURE 8.17.** Sketch of charge and spin photocurrents in $Mn_2Au$ (reprinted from [2], ©2023 CC BY 4.0).

In the context of spin Hall effects, the weaker spin photocurrent flowing out-of-plane $Q_z^{\parallel\mathbf{N}}$ hints at a strong anisotropy of the SHE [197] in $Mn_2Au$. Since the electrically induced spin Hall effect was experimentally confirmed in $Mn_2Au$ recently [198], the interpretation of the charge photocurrent and the perpendicular flowing spin photocurrents as a photogalvanic version of the SHE becomes apparent. The geometry of the effect is sketched in Figure 8.17. The combination of charge and spin photocurrents can be identified as a

*photospin Hall effect* (PSHE) and was first proposed in Ref. [2]. To characterize the photospin Hall effect a *photospin Hall angle* $\Theta_{\mathrm{PSH}}$ (PSHA) can be defined as the ratio between the in-plane spin and charge photocurrent

$$\Theta_{\mathrm{PSH}} = \arctan \frac{Q^z_{\parallel \mathbf{N}}}{J_{\perp \mathbf{N}}}. \tag{8.4}$$

The PSHA defined in Eq. (8.4) allows for experimental quantification of spin photocurrents using the more accessible charge photocurrent as a proxy. Since both the charge photocurrent $J_{\perp \mathbf{N}}$ and the spin photocurrent $Q^z_{\parallel \mathbf{N}}$ are of magnetic origin, both currents are reversed when the Néel vector is switched. Thus, the PSHA is expected to be constant upon reversal of the Néel vector.

In the following section the spectral properties and the microscopic origin of the PSHE in $Mn_2Au$ will be discussed. Figure 8.18 shows the frequency dependence of the a) charge and b) spin photocurrent components used in Eq. (8.4) in response to light linearly polarized along the $\{\parallel \mathbf{N}, \perp \mathbf{N}, z\}$-directions. The right column shows the photospin Hall angle as defined in Eq. (8.4) plotted versus c) the band filling at frequency $\hbar\omega = 3.00\,\mathrm{eV}$ and d) at the true Fermi level versus the applied laser frequency. All responses were evaluated at room-temperature broadening $\Gamma = 25\,\mathrm{meV}$. Comparing the unpolarized photocurrent in Figure 8.18 a) with the spin polarized photocurrent in b) some similarities in the frequency dependence are apparent. Both charge and spin photocurrent change sign at a frequency of $\hbar\omega = 1.00\,\mathrm{eV}$, for smaller frequencies the responses are comparable in amplitude in case of in-plane polarization (red and blue curve). In the frequency band of $\hbar\omega \approx 2.00\,\mathrm{eV}$ to $\hbar\omega \approx 3.5\,\mathrm{eV}$ a strong oscillatory behavior with respect to laser frequency is present when using light linearly polarized in the $xy$-plane (red and blue curve). At $\hbar\omega = 2.8\,\mathrm{eV}$ the spin photocurrent in Figure 8.18 b) is maximized with a strong spike for light linearly polarized along the Néel vector (red curve) and an negative spike for light polarized linearly along the $z$-direction (golden curve), with amplitudes reaching about $\pm 80 \times 10^{10}\,\hbar/2e\mathrm{A/m}$ respectively. At the same frequency the staggered laser induced spin density presented in Figure 8.13 in response to light polarized within the $xy$-plane was maximized, suggesting that the spin photocurrent and the staggered spin density on the Mn sublattices are intimately related at least for the given frequency and polarization. Indeed, in semiconductors uniform nonequilibrium spin densities induced by circularly polarized light are known to drive photocurrent by means of the inverse spin galvanic effect (ISGE)[199]. ISGE and spin Hall effects share the same geometric setup and can both be present in materials lacking inversion symmetry[56]. In case of magnetic materials a charge current can be driven by an electrically induced spin accumulation by means of the inverse Edelstein effect[200,201]. Therefore,

a generalization to the second order photoeffects seems reasonable.

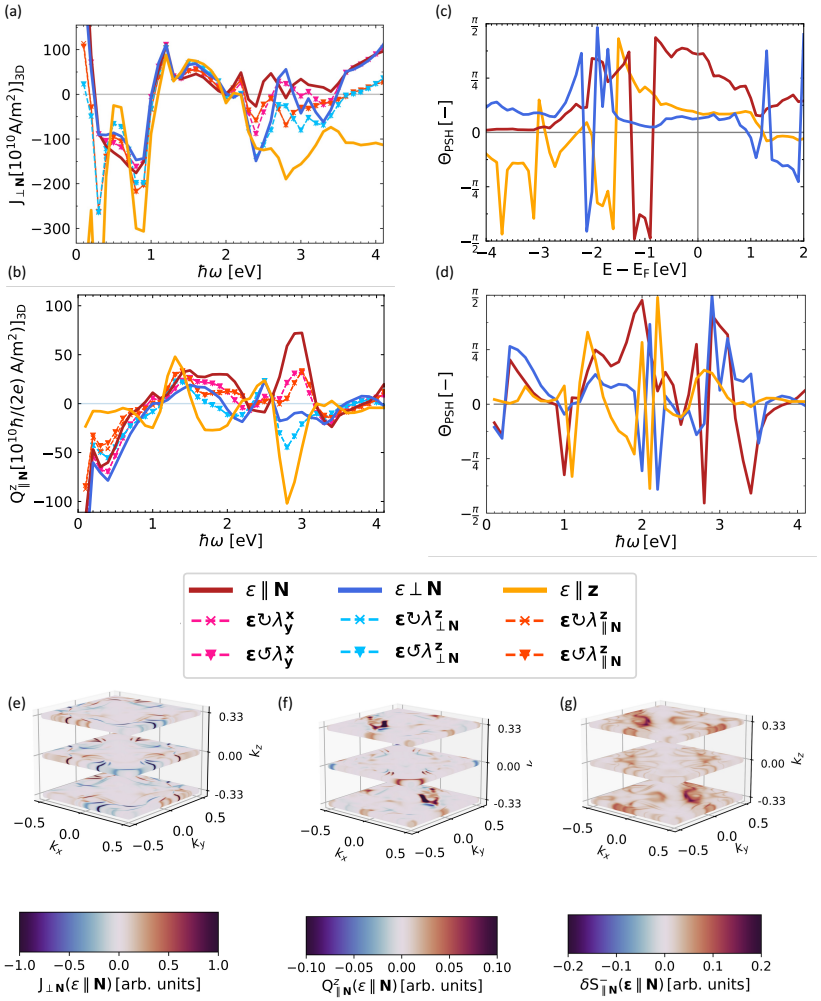


**FIGURE 8.18.** The spin Hall angle as defined in Eq. (8.4) evaluated in $Mn_2Au$ (reprinted from [2], ©2023 CC BY 4.0). The broadening $\Gamma$ was fixed to 25meV. a) shows the frequency dependence of the charge photocurrent and b) of the spin photocurrent. c) Shows the dependence on the band filling of the photospin Hall angle $\Theta_{PSH}$ evaluated for a laser frequency of $\hbar\omega = 3.00$ eV at different band fillings around the true Fermi level. d) Shows the dependence of PSHA at the true Fermi level on the laser frequency. Panels e)-f) show the Brillouin zone resolved distribution of the e) charge photocurrent f) spin photocurrent and g) spin density associated with the PSHE.

Disentangling spin Hall like and inverse spin-galvanic effects however is difficult, the reader should keep in mind, that in principle both mechanism can be present in the here presented $Mn_2Au$ and might be differently weighted

depending on laser polarization and frequency. For example in the case of linearly polarized light along the $z$-direction with frequency $\hbar\omega = 1.2$ eV both spin and charge photocurrent as well as the staggered nonequilibrium spin density show a spike, hinting at a shared microscopic origin of all three responses. In the scenario of $\hbar\omega = 1.2$ eV the induced photogalvanic effect can be accounted for as a Drude like response, since a large number of states is available 1.2 eV above the true Fermi level, as shown in Figure 8.1.

Figure 8.18 c) shows that a sizeable spin Hall angle is presented at the true Fermi level for all orientations of linearly polarized laser light. In a window of about ±1 eV around the true Fermi level the spin Hall angle is almost constant without any significant changes. This robustness around the true Fermi level of the PSHA suggests that the PSHA in conjunction with the experimentally accessible charge photocurrent can be used as a proxy to determine the size of the spin photocurrents. Next Figure 8.18 d) fixes the band filling to the true Fermi level and shows the dependence of the spin Hall angle on the applied laser frequency. In the frequency band of $\hbar\omega \approx [1.5, 3.5]$ eV the spin Hall angle is largest. At $\hbar\omega = 2.00$ eV the angle can be switched by changing the orientation of the in-plane linear polarization (red curve and blue curve).

To further explore the origin of PSHE Figure 8.18 e)-f) shows the Brillouin zone resolved charge and spin photocurrent and the staggered nonequilibrium spin density Brillouin zone resolved, for light of frequency $\hbar\omega = 3.00$ eV linearly polarized parallel to the Néel vector. The Brillouin zone resolved charge photocurrent $J_{\perp\mathbf{N}}$ is presented in Figure 8.18 e), showing competing regions of positive and negative sign. Figure 8.18 f) shows the spin photocurrent $Q^z_{\parallel\mathbf{N}}$ BZ resolved. Compared to the charge photocurrents the spin polarized photocurrents show a qualitatively different origin in the BZ. Instead of competing regions of positive and negative sign the spin photocurrent is mostly driven by two hotspots present in the $k_z$-up and $k_z$-down layer which both contribute with the same sign but are and order of magnitude smaller compared to the charge photocurrent hotspots. The hotspots are symmetry related via a mirror inversion along $k_z$ and a second mirror operation in the plane along the $\perp \mathbf{N}$ direction. The area of these hotspots of the spin photocurrent however does not contribute at all to the charge photocurrents. Hotspots of the charge photocurrent are located closer to the edges of the BZ and are of competing sign w.r.t. each other. Instead, similar hotspots are present in the BZ resolved plot of the staggered spin response, presented in Figure 8.1 g), suggesting that spin photocurrent and induced spin density have a shared microscopic origin in the considered scenario of $\hbar\omega = 3.00$ eV and light polarization along the Néel vector.

In conclusion the charge and spin photocurrent in response to linearly polarized light appear closely related to the staggered spin response on the

Mn sublattices.

## 8.7 Orbital effects

It was theoretically predicted that antiferromagnetic materials can host not only sizeable laser induced spin densities, but also a large laser induced orbital magnetization. For example in the synthetic antiferromagnet Fe the orbital magnetization dominates the response and, unlike the spin response, does not require any spin-orbit coupling [41]. Spin-orbit-coupling is not required to induce orbital magnetization since the laser directly couples to the electronic degrees of freedom. Laser induced orbital effects thus open up a avenue of new, light, materials in the realm of ultrafast spintronics, also referred to as orbitronics in this context [202,203]. In a recent publication laser induced orbital effects were calculated within the nonequilibrium Keldysh formalism, further pushing the idea of ultrafast orbitronics [204]. Very recently orbital pumping by means of the inverse orbital Hall effect was reported [205]. In this section the laser induced orbital magnetization and orbital polarized photocurrent, in short orbital photocurrent, is analyzed in $Mn_2Au$. The laser induced orbital magnetization is given by Eq. (3.89) within the Keldysh formalism. In analogy to the previously discussed laser induced nonequilibrium spin density, an overall and a staggered orbital magnetization $\delta L^{\pm}$ is defined as for the spin density in Eq. (8.3).

Figure 8.19 shows the frequency dependence of the components of the a) overall laser induced orbital magnetization $\delta L^{+}$ and b) staggered orbital response $\delta L^{-}$ on the Mn sublattices. The components were projected onto the $\{\parallel \mathbf{N}, \perp \mathbf{N}, z\}$-directions. To allow for a direct comparison with induced spin density discussed in Section 8.5, the induced orbital magnetization was evaluated at the true Fermi level and room temperature broadening $\Gamma = 25$ meV. Comparing the orbital components in Figure 8.19 with the components of the spin density presented in Figure 8.11, it is directly apparent that for a given laser polarization the induced orbital magnetization and spin density are parallel to each other. This is expected since both spin and orbital effects are equivalent in terms of their symmetry requirements. The uniform orbital magnetization shown in Figure 8.19 a) is an order of magnitude larger than its spin counterpart. Similar to the overall spin density, the largest orbital magnetization is induced in the $xy$-plane and the orbital in-plane components $\delta L^{+}_{\parallel \mathbf{N}}$ and $\delta L^{+}_{\perp \mathbf{N}}$ have a comparable frequency dependence with amplitudes reaching $\delta L^{+}_{\parallel \mathbf{N}} \approx \delta L^{+}_{\perp \mathbf{N}} \approx 38 \times 10^{-6}\, \hbar/2$ at a laser frequency of $\hbar\omega = 1.7$ eV. Comparing the frequency dependence of the integrated orbital magnetization with the frequency dependence of the overall nonequilibrium spin density

$\delta S^+$ presented in Figure 8.13 a), a qualitative difference can be identified: The spin response oscillates within the presented frequency range unlike the orbital responses which do not switch sign for a given helicity. This is not true for the out-of-plane response $\delta L_z^+$, which shows a sign crossing in the region around $\hbar\omega = 2.0\,\text{eV}$.

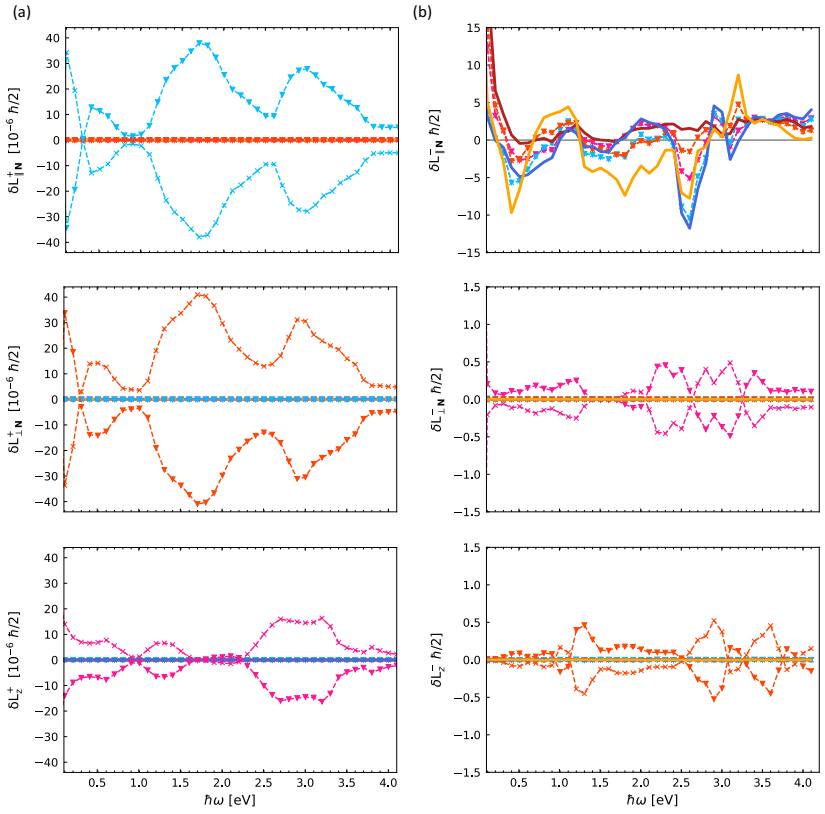


**FIGURE 8.19.** Frequency dependence of components of the a) uniform and b) staggered nonequilibrium orbital magnetization in response linear and circularly polarized laser fields. The responses were evaluated at the true Fermi level with a broadening of $\Gamma = 25\,\text{meV}$.

It is noted that the in-plane components of the orbital magnetization do switch sign in the low frequency limit, however this might be due to numerical instability when approaching $\hbar\omega = 0$. In case of the staggered orbital response presented in Figure 8.19 b) the only sizeable staggered response is induced parallel to the Néel vector $\delta L^-_{\perp\mathbf{N}}$ in response to linearly polarized light. The staggered orbital response however is roughly an order of magnitude smaller than the staggered spin response $\delta S^-_{\perp\mathbf{N}}$ presented in Figure 8.13 b). Unlike the

staggered spin response the staggered orbital response oscillates with respect to frequency. In summary the overall nonequilibrium orbital magnetization does not oscillate with respect to frequency unlike the overall spin response but is an order of magnitude larger compared to the spin density. For the staggered responses the situation is reversed, the staggered spin response is an order of magnitude larger than the staggered orbital magnetization. While the staggered spin response does not oscillate with respect to frequency the staggered orbital magnetization does. Due to the dominance of the spin effect, the combined effect of nonequilibrium spin density and orbital magnetization is expected to results in a quenching of the magnetic moments at all considered frequencies.

In 8.6.2 the staggered spin response was found to be closely related to the overall induced spin photocurrent. This raises the question whether the one order of magnitude smaller staggered orbital magnetization will result in less pronounced orbital photocurrent as well. The frequency dependence of the laser induced orbital photocurrents, as defined in Eq. (3.89), are therefore analyzed next. Figure 8.20 shows the laser induced orbital photocurrents flowing in the $xy$-plane. The columns represent the orientation of the orbital polarization. Figure 8.20 a) shows the orbital photocurrent flowing parallel to the Néel vector, b) shows the perpendicular flowing currents. As was the case for the previously discussed laser induced orbital magnetization, the individual components of the orbital photocurrent respond to the same laser fields as their spin photocurrent counterparts presented in Figure 8.14. Both CPGE- and LPGE-like orbital photocurrents oscillate with respect to frequency and show maximum amplitudes of $\sim 50 \times 10^{10}\, \hbar/(2e)$ A/m. The CPGE orbital currents are thus roughly a factor of 2 to 3 smaller than their spin counterparts. In case of the LPGE like orbital photocurrent $J^z_{\|\mathbf{N}}$ the largest amplitude of $\sim 35 \times 10^{10}\, \hbar/(2e)$ A/m is reached in response to light of frequency $\hbar\omega \approx 2.7$ eV in response to light linearly polarized along the Néel vector. Interestingly this is the same frequency and polarization for which the LPGE like spin photocurrent $Q^z_{\|\mathbf{N}}$ was maximized, although the spin response presented in Figure 8.18 b) reached amplitudes of $\sim 100 \times 10^{10}\, \hbar/(2e)$ A/m. The frequency dependence of the components of the orbital photocurrent flowing out-of-plane are presented in Figure 8.21. Compared to their spin counterparts presented in Figure 8.15, the CPGE-like responses are smaller in amplitude, as was the case for the in-plane orbital photocurrents. On the other hand the LPGE-like orbital photocurrent $J_z^{\|\mathbf{N}}$ with amplitudes of about $\sim 40 \times 10^{10}\, \hbar/(2e)$ A/m in response to light linearly polarized along the Néel vector is comparable to its spin counterpart as presented in Figure 8.16.

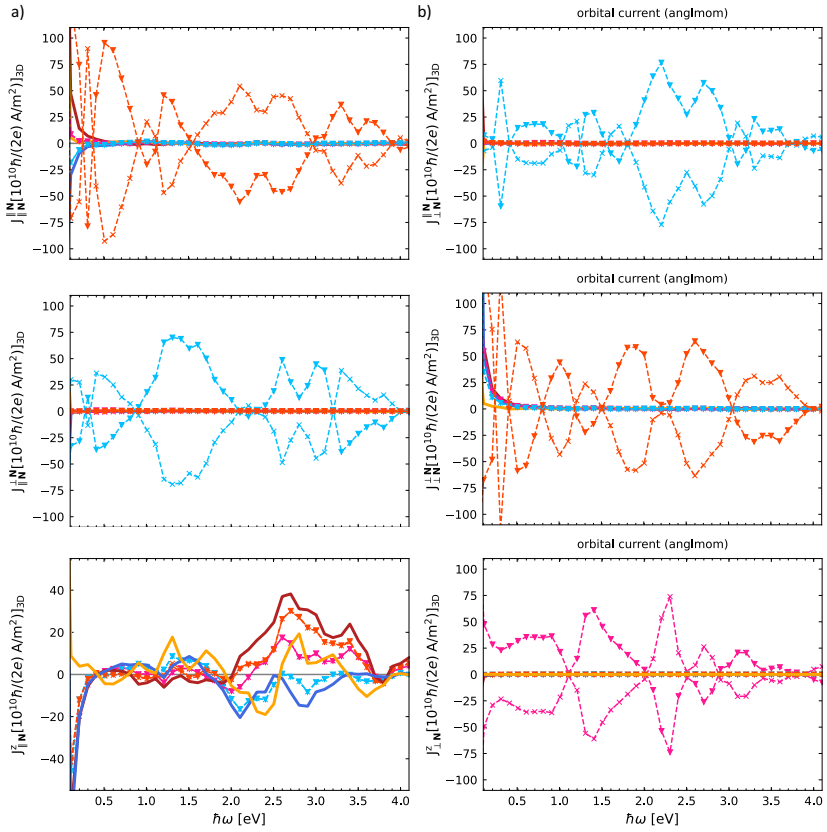


**FIGURE 8.20.** Frequency dependence of the components of the orbital photocurrent flowing in the $xy$-plane a) along the Néel vector and b) perpendicular to the Néel vector in response to linearly and circularly polarized laser fields. The responses were evaluated at the true Fermi level with a broadening of $\Gamma = 25$ meV.

Unlike in the scenario of spin polarized photocurrents were the in-plane current $Q^z_{\|\mathbf{N}}$ was an order of magnitude larger than the out-of-plane response $Q^z_{\|\mathbf{N}}$, in case of their orbital counterparts, $J_z^{\|\mathbf{N}}$ and $J^z_{\|\mathbf{N}}$, both responses are comparable in amplitude. In conclusion when compared to the spin-polarized counterparts orbital photocurrents in $Mn_2Au$ are in general less pronounced, or at best of similar amplitude. This is somewhat expected from the special, symmetry-breaking, role of the staggered magnetization in $\mathcal{PT}$-symmetric AFMs. As discussed in the previous sections, in $Mn_2Au$ the inversion symmetry breaking required to open up a finite photocurrent is achieved by the opposing magnetization on the Mn sublattices. The symmetry breaking therefore "happens" in spin space and has to be mediated by means of spin-orbit coupling to the electronic system. In this sense the spin based photoeffects in $Mn_2Au$ are coupled directly to the symmetry breaking, while the orbital

effects have to be mediated via SOC.

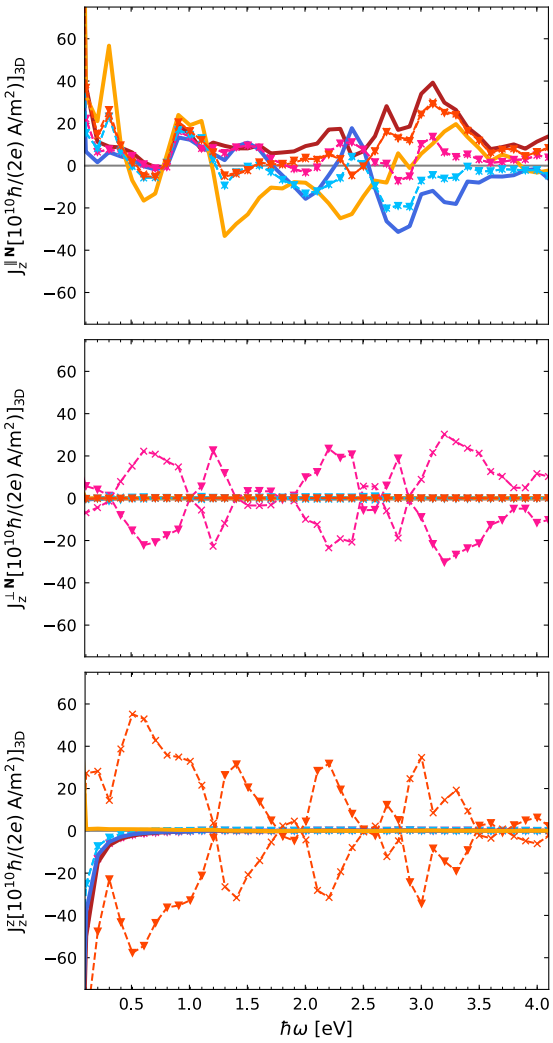


**FIGURE 8.21.** Frequency dependence of the components of the orbital photocurrent flowing along the $z$-direction in response to linearly and circularly polarized laser fields. The responses were evaluated at the true Fermi level with a broadening of $\Gamma = 25$ meV.

In 8.6.2 the photospin Hall effect was proposed. Since the orbital photocurrent has components in response to linearly polarized light along the spin photocurrents the concept of the photo-orbital Hall effect is introduced here to quantify the ratio between the charge photocurrent $J_{\perp \mathbf{N}}$ and the perpendicular flowing orbital photocurrents. In the same fashion as for the photospin Hall angle defined in Eq. (8.4) a photo-orbital Hall $\Theta_{\mathrm{POH}}$ angle

can be defined. Since the two orbital photocurrents in response to linearly polarized light $J_z^{\parallel \mathbf{N}}$ and $J_{\parallel \mathbf{N}}^z$ are comparable in amplitude, an in-plane (IP) photo-orbital Hall angle $\Theta_{\mathrm{POH}}^{\mathrm{IP}}$ and an out-of-plane (OOP) angle $\Theta_{\mathrm{POH}}^{\mathrm{OOP}}$ are defined as

$$\begin{aligned} \Theta_{\mathrm{POH}}^{\mathrm{IP}} &= \arctan\left(\frac{J_{\parallel \mathbf{N}}^z}{J_{\perp \mathbf{N}}}\right) \\ \Theta_{\mathrm{POH}}^{\mathrm{OOP}} &= \arctan\left(\frac{J_z^{\parallel \mathbf{N}}}{J_{\perp \mathbf{N}}}\right). \end{aligned} \tag{8.5}$$

Figure 8.22 compares both photo-orbital Hall angles defined in Eq. (8.5) in terms of their frequency dependence. To allow for a direct comparison with the photospin Hall effect, Figure 8.22 a1) shows the frequency dependence of the spin-polarized photocurrent $Q_{\parallel \mathbf{N}}^z$ in response to linearly polarized light again. Figure 8.22 b1) shows the resulting photospin Hall angle. Figure 8.22 a2) shows the matching orbital photocurrent and b2) the resulting photo-orbital Hall angle $\Theta_{\mathrm{POH}}^{\mathrm{IP}}$. In Figure 8.22 a3)and b3) the out-of-plane photo-orbital current and angle are presented. Although the amplitude of the orbital photocurrents is in general weaker than the spin photocurrent, the photo-orbital Hall angles are comparable in size to the photospin Hall angle for certain frequencies. Some shared features can be identified in all three presented angles. For example all angles show a negative spike for light polarized along the Néel vector (red curve) at frequency $\hbar\omega = 2.7$ eV. Another shared spike is visible at $\hbar\omega = 2.9$ eV for light polarized perpendicular to the Néel vector (blue curve). In both cases the Hall angles are maximized to an absolute value of $\pi/2$. These spikes originate from zero crossings of the charge photocurrent $J_{\perp \mathbf{N}}$ for the respective frequency and polarization as can be seen in Figure 8.7. Overall the photo-orbital Hall angles however do not necessarily correlate with the photospin Hall angle. In case of the in-plane photo-orbital Hall angles the photospin Hall angle dominates at lower frequencies. From $\hbar\omega \approx 1.0$ eV to about $\hbar\omega = 2.0$ eV the in-plane photospin and photo-orbital Hall angle compete, however the spin response mostly prevails. For frequencies above $\hbar\omega \approx 1.8$ eV however both are comparable in amplitude and oscillate quickly with respect to frequency. The out-of-plane photo-orbital Hall angle is more sizeable at lower frequencies when compared to its in-plane counterparts (and to the out-of-plane photospin Hall angle which is not shown). Above a frequency of $\hbar\omega = 3.5$ eV all photo Hall angles are mostly suppressed.

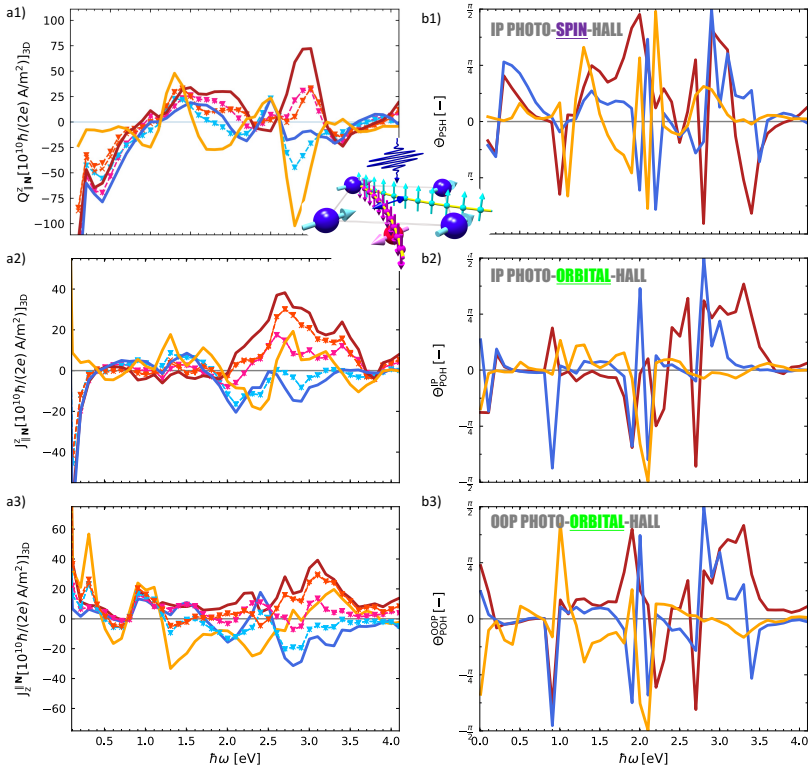


**FIGURE 8.22.** Frequency dependence of the in-plane photospin Hall angle compared to the in-plane and out-of-plane photo-orbital Hall angle. a1) Shows the spin photocurrent driving the photospin Hall effect. a2) and a3) show the frequency dependence of the orbital photocurrent flowing in- and out-of-plane respectively. b1) - b3) Show the frequency dependence of the resulting b1) in-plane photospin, b2) in-plane photo-orbital and b3) out-of-plane photo-orbital Hall effect respectively.

In conclusion laser induced orbital effects can be similar in amplitude to their spin counterparts in $Mn_2Au$. The interplay between spin and orbital responses is rather complex and depends on the applied laser frequency and polarization. In some scenarios orbital and spin photocurrents are concordant, in other scenarios the effects compete or compensate each other. Overall the orbital responses should therefore be taken into consideration when discussing spin responses.

# Chapter 9

# *Chiral effects in antiferromagnets*

In this chapter the effect of canting of the magnetic moments in antiferromagnetic materials will be analyzed. Canting of the opposing moments in collinear antiferromagnets introduces a finite vector chirality and various first order effects were found to directly depend on this vector chirality. For example a chiral Hall effect was found in $Mn_2Au$ in response to a DC electric field [4]. Similarly, a chiral flavored magneto-optical effect of first order in the applied electric field can be induced at finite frequency, as will be discussed in the first section of this chapter. Next the effect of canting will be discussed in the context of the second order photogalvanic effects in bulk antiferromagnet $Mn_2Au$. Various *chiral photogalvanic effects* will be identified in $Mn_2Au$. Chiral charge photocurrents could be used to characterize the Néel spin-orbit torque switching processes in antiferromagnets. The chapter is concluded with the discussion of *chiral spin photocurrents*, which, albeit the small canting angles, excel their collinear counterparts by an order of magnitude, highlighting the importance of chiral effects in AFMs for spintronic applications.

## 9.1 Chiral magneto-optical effect in $SrRuO_3$

This section is adapted from works presented in [3] and [4], were the crystal [206] and chiral magneto-optical effect were identified in a monolayer of antiferromagnetic $SrRuO_3$. In both publications the author of this thesis acted as a co-author and performed the calculations of the crystal and chiral magneto-optical conductivity by means of the *ju_wip* code developed within this thesis (see subsection 6.2.2 and subsection 6.3.4). The extraction of the Wannier functions describing the AFM monolayer of $SrRuO_3$ was performed by Kartik Samantha, who kindly provided the Wannier functions for the collinear as well as for the canted scenarios to the author of this thesis. For details on the construction of the Wannier functions the reader is pointed to [3]. The main intention of this section is to motivate the chiral photogalvanic effects, which can be understood as a generalization of the chiral Hall and mangeto-optical (MO) effects to the realm of second order photogalvanic effects.

Figure 9.1 shows the crystal (orange curve) and chiral (purple) magneto-optical effect induced in a monolayer of antiferromagnetic $SrRuO_3$ for the scenario of a) canting along the $y$- and b) along the $z$-direction. A canting angle of $\Theta = \pm 5^\circ$ was considered. For reference the gray curve indicates the magneto-optical conductivity in the collinear scenario.

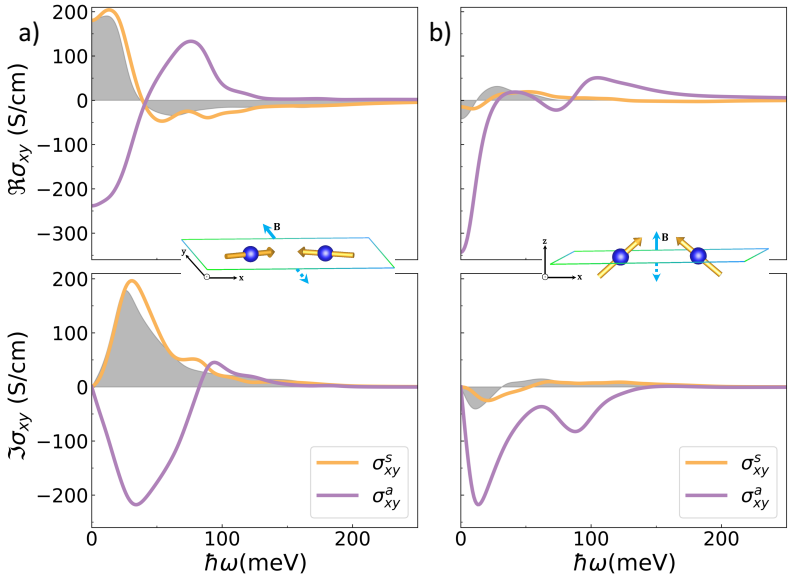


**FIGURE 9.1.** Frequency dependence of the crystal (orange) and chiral (purple) magneto-optical conductivity in a monolayer of antiferromagnetic $SrRuO_3$ in the scenario of a) canting along the $y$-direction and b) along the $z$-direction (reprinted from [4], ©2021 CC BY 4.0). The gray curves show the collinear scenario. In the first and second column the real and imaginary part of the conductivity are shown respectively.

Figure 9.1 shows that the crystal- and chiral-magneto-optical conductivities are comparable in amplitude already for the small canting angles of 5°. In both canting scenarios the real part of the optical conductivity is dominated by the chiral response in the DC-limit ($\hbar\omega \to 0$). In case of canting along the $z$-direction presented in Figure 9.1 b) the imaginary part of the chiral MO conductivity is an order of magnitude larger compared to its crystal counterparts.

Arguably the first order magneto-optical conductivity is dominated by the chiral flavored responses already for the small canting angle of 5° considered, raising the question how the chiral flavored photoresponses compare to the collinear effects.

## 9.2 Analysis of canting in $Mn_2Au$

In Ref. [4] a chiral Hall effect was identified in $Mn_2Au$ for the scenario of the Néel vector aligned along the magnetic hard axis (along the $z$-direction) when a Zeeman field applied was along the $y$-direction. For the rest of this chapter the effect of canting in $Mn_2Au$ will be analyzed in the context of the second order photogalvanic effects for the scenario of the Néel vector along the [110]-direction. For the following discussion the effect of canting is mimicked by applying a Zeeman term to the Wannier interpolated Hamiltonian as described in subsection 6.3.4. This approach allows for a quick variation of the canting angle and is computationally cheap when compared to the more rigorous approach of performing separate noncollinear DFT calculations for each canting scenario. To illustrate the effects of the canting on the symmetry of the system Figure 9.2 shows the effect of a 100meV Zeeman field applied along the $z$-direction on the bandstructure of $Mn_2Au$. The bands of the canted system are presented in cyan and magenta for spin-up and spin-down states respectively. For comparison the bands of the collinear scenario are presented in black. The reader is reminded that, as discussed in Section 8.2, in the collinear scenario bands are spin degenerate, due to the $\mathcal{PT}$-symmetry of the system.

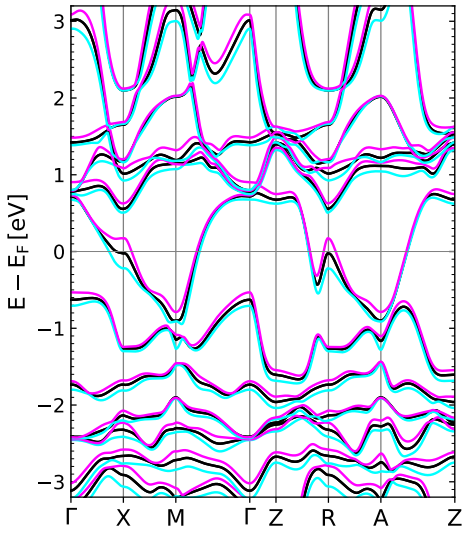


**Figure 9.2.** Combined bandstructure of $Mn_2Au$ for the collinear case (black bands) and canted case (colorized bands). Cyan and magenta colored bands represent the spin-up and -down states, respectively, in the scenario of a 200 meV Zeeman field applied along the $z$-direction.

From Figure 9.2 it is clear that in the canted scenario the spin degeneracy of the bandstructure is lifted. The canting induced by the Zeeman term effectively introduces a small ferromagnetic moment along the $z$-direction, which in turn breaks the $\mathcal{PT}$-symmetry, thus, lifting the spin degeneracy of the bandstructure. The reduced symmetry of the canted system leads to additional finite photoresponses when compared to the collinear scenario as will be demonstrated below.

### 9.2.1 Chiral photocurrents

In 8.4.1 it was demonstrated for the collinear scenario, that the charge photocurrent along the Néel vector $J_{\parallel \mathbf{N}}$ can be sizeable in regions of the Brillouin zone, however, due to a mirror symmetry connecting regions antiparallel, the overall response was canceled out. As Figure 9.2 shows, the Zeeman field reduces the symmetry of the crystal. Thus, it can potentially unlock the before hidden responses such as the charge photocurrent $J_{\parallel \mathbf{N}}$. As for the chiral-magneto optical effects[4], to analyze the effect of the Zeeman field on the charge photocurrents a symmetric and antisymmetric photocurrent $J^{a/s}$ is defined as

$$J^{a/s} = \frac{J(+\theta) \pm J(-\theta)}{2}, \tag{9.1}$$

where $J(\pm\theta)$ is the photocurrent defined in Eq. (3.66) evaluated in the system with canting angle $\pm\theta$ applied. The symmetric photocurrents $J^s$ are closely related to the photocurrents found in the collinear scenario discussed in Chapter 8, however, additional components can occur which are not present in the collinear scenario. These components of the symmetric photocurrent are due to the symmetry lowering, but do not directly couple to the chirality of the spins. Since such components were found to be small and only in response to circularly polarized light, they will be omitted from the discussion, which focuses on the chiral flavored photoresponses. The antisymmetric photocurrent $J^a$, dubbed as the *chiral photocurrent*, will be analyzed in two scenarios: First for a Zeeman field applied along the $z$-direction leading to a canting of the magnetic moments out-of-the plane towards the $z$-direction. Second for in-plane canting, where the field is applied in the $xy$-plane along the $\perp \mathbf{N}$ direction. In principle the field can also be applied parallel to the Néel vector, however, this only makes the material slightly ferrimagnetic and does not introduce a canting of the magnetic moments. It is noted here that it might be worth to consider the effect of a staggered Zeeman field applied along the Néel vector to characterize the system in the scenario of direct switching identified in the context of the staggered IFE in Section 8.5. As of now staggered Zeeman fields are not implemented in the *ju_wip* code and remain

a topic for future discussions. To get a feeling for the effect of the Zeeman field on the photocurrents, the discussion of chiral photocurrents is initiated by studying their dependence on the strength of the applied Zeeman field. Figure 9.3 shows the dependence of the components of the antisymmetric photocurrent $J^{(a)}$, defined in Eq. (9.1), on the strength of the Zeeman field applied a) in-plane and b) out-of-plane.

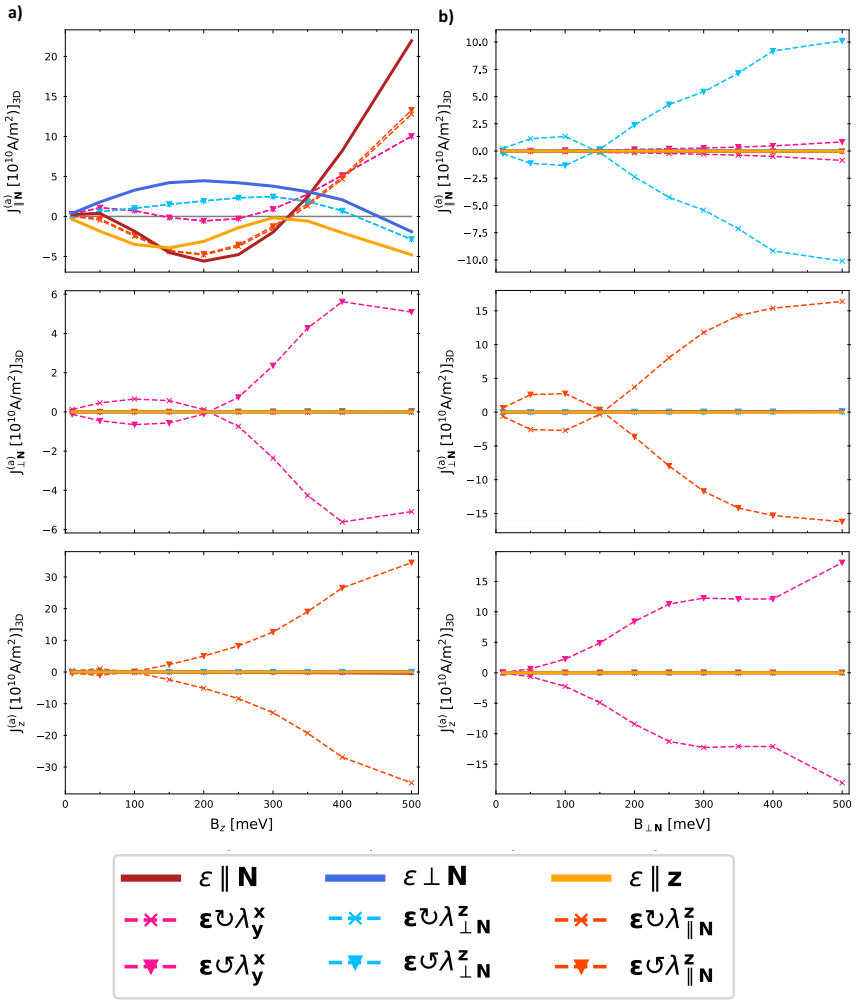


**FIGURE 9.3.** Antisymmetric/chiral components of the photocurrent plotted versus the applied Zeeman field strength, with the field applied along a) the out-of-plane direction and b) in-plane direction.

Zeeman fields in the range of 10 meV up to 500 meV were considered. The laser frequency was fixed to $\hbar\omega = 3.00$ eV, room temperature broadening

$\Gamma = 25$ meV was assumed and the band filling corresponds to the true Fermi level.

For the scenario of canting applied along the $z$-direction presented in Figure 9.3 a), a chiral photocurrent is present flowing parallel to the Néel vector. As conjectured above, indeed the Zeeman field unlocks the photocurrent parallel to the Néel vector when applied along $z$ by lowering the crystal symmetry. The response shows LPGE behavior where circular responses are also present but are averages of the linearly polarized responses. The dependence on the applied Zeeman field strength is, depending on the orientation of the linear polarization, only linear up to a Zeeman field strength of $B_z = 100$ meV to $B_z \approx 200$ meV. Up to an applied field strength of about 200 meV the responses to the two in-plane polarizations ($\varepsilon \parallel \mathbf{N}$ and $\varepsilon \perp \mathbf{N}$) are of opposite sign and scale roughly linearly with the applied field strength. At 200 meV Zeeman field for example the current is about $J^{(a)}_{\parallel \mathbf{N}}(B_z) \sim \pm 5 \times 10^{10}$ A/m$^2$. Between 200 and 350 meV $J^a_{\perp \mathbf{N}}$ undergoes a sign change for both in-plane linearly polarized fields (thick red and blue curve respectively). Above $B_z = 350$ meV the dependence of the chiral photocurrent on the Zeeman field becomes linear again. The other two components of the chiral photocurrent in Figure 9.3 a) are of comparable amplitude and only respond to circularly polarized light. They are switchable by reversing the lights sense of rotation.

Figure 9.3 b) shows the components of the antisymmetric photocurrent for a Zeeman field applied in the plane perpendicular to the Néel vector. Interestingly, in this scenario no antisymmetric photocurrents are present in response to linearly polarized light and only responses to circularly polarized light remain finite. Further the two in-plane components $J^{(a)}_{\parallel \mathbf{N}, \perp \mathbf{N}}(B_{\perp \mathbf{N}})$ indicate an apparent symmetry of the chiral photocurrent. A switchable chiral in-plane photocurrent along $\mathbf{b} \in \{\parallel \mathbf{N}, \perp \mathbf{N}\}$ $\mathbf{J}^{(a)}_{\mathbf{b}}$ is present in response to circularly polarized light when the laser polarization rotates in the plane whose normal is along the $\mathbf{b}$ vector. Since already in the collinear scenario photocurrents in response to circularly polarized light are present in all components of the current and the chiral photocurrents in response to circularly polarized light are mostly suppressed in the regime up to $B_z \sim 200$ meV, the discussion is now focused on the chiral photocurrent in response to linearly polarized light $J^{(a)}_{\parallel \mathbf{N}}$ in the scenario of canting towards the magnetic hard axis along $z$. For the rest of the discussion the Zeeman field will be fixed to 200 meV, up to which most responses, especially the spin-based effects as will be seen later, show a linear scaling w.r.t. the applied field. Before the spin based effects are discussed, the frequency dependence of the chiral photocurrents at 200 meV canting field strength will be presented.

Figure 9.4 shows the frequency dependence of the in-plane symmetric (first column) and antisymmetric (second column) photocurrent components

for a 200 meV Zeeman field applied along the $z$-direction.

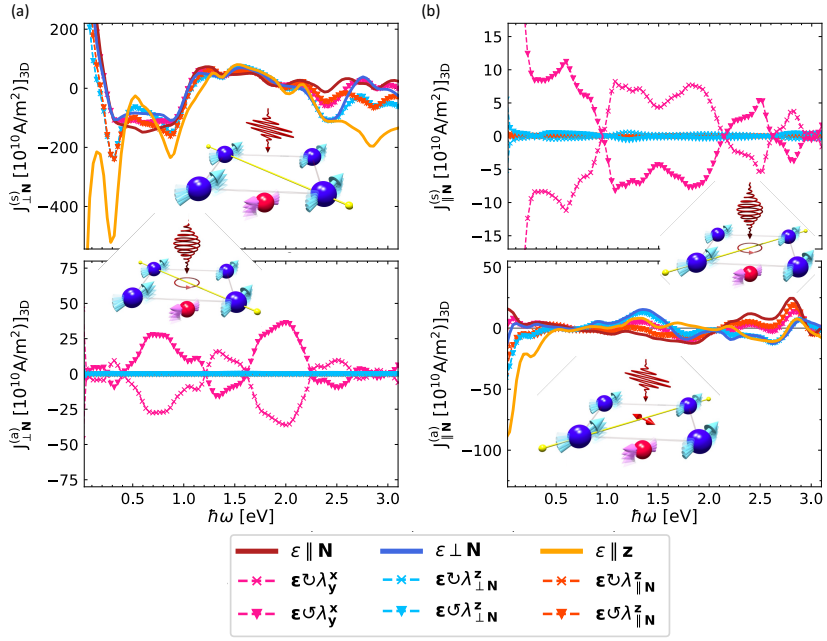


**FIGURE 9.4.** Symmetric (upper panel) and antisymmetric (lower panel) photocurrent for a 300 meV Zeeman field along $z$-direction flowing a) perpendicular and b) parallel to the Néel vector plotted vs the laser frequency $\omega$. Only the Fermi surface contribution to the photocurrent is shown, since the Fermi sea term does not contribute. The cartoons indicate direction and nature of the laser field and the yellow bar shows the direction along which the photocurrent is measured.

Due to the small canting angles the symmetric perpendicular current $J^{(s)}_{\perp}$ presented in Figure 9.4 a) is comparable in amplitude and shape to the photocurrent $J_{\perp \mathbf{N}}$ in the collinear scenario presented in Figure 8.7, thus confirming the Zeeman field of 200 meV acts only as a weak perturbation. Still the chiral photocurrent in response to linearly polarized light $J^{(a)}_{\parallel \mathbf{N}}$ is sizeable, with amplitudes reaching $\sim 25 \times 10^{10}$ A/m$^2$ at a frequency of $\hbar\omega = 2.7$ eV for light linearly polarized along the Néel vector (thick red curve). It is noted that the chiral photocurrents $J^{(a)}_{\perp \mathbf{N}}$ and $J^{(a)}_{\parallel \mathbf{N}}$ respond to the same laser fields (in terms of polarization) as the collinear spin photocurrents $Q^{\perp \mathbf{N}}_{\parallel \mathbf{N}}$ and $Q^{z}_{\parallel \mathbf{N}}$, since both effects can be understood, at least in terms of their symmetry requirements, as a photocurrent perturbed by a spin polarization. Another way to look at it is, that the before fully spin polarized spin photocurrents of the collinear scenario get slightly unpolarized in the canted scenario.

### 9.2.2 Spin dependent effects

In this section the influence of the canting on the spin dependent photogalvanic effects, namely the laser induced nonequilibrium spin density and the spin photocurrents will be analyzed. In the same spirit as for the chiral charge photocurrents defined in Eq. (9.1), only the antisymmetric (dubbed *chiral*) effects will be considered. As for the chiral charge photocurrents in Eq. (9.1) a symmetric and antisymmetric with respect to positive/negative canting of the nonequilibrium spin density and spin photocurrent is defined by

$$\begin{aligned} \delta S^{a/s} &= \frac{\delta S(+\theta) \pm \delta S(-\theta)}{2} \\ Q^{a/s} &= \frac{Q(+\theta) \pm Q(-\theta)}{2}. \end{aligned} \tag{9.2}$$

Figure 9.5 shows the dependence of the antisymmetric nonequilibrium spin density $\delta S^{(a)}$ from Eq. (9.2) for a) in-plane and b) out-of-plane canting. Linearly and circularly polarized light of frequency $\hbar\omega = 3.00$ eV was considered with a broadening of $\Gamma = 25$ meV. In both scenarios the chiral spin density was evaluated at the true Fermi level. Figure 9.5 shows that the component of the spin density along the direction of the applied Zeeman field is sizeable for any laser polarization considered and both orientations of the Zeeman field. The other components are not shown since they are an order of magnitude smaller than their collinear counterparts and, therefore, hard to disentangle from collinear responses in experiment. In both scenarios the nonequilibrium spin density scales almost perfectly linearly throughout the presented field range when the laser light is polarized within the $xy$-plane (thick blue and red curves). If instead the laser light is linearly polarized along the $z$-direction (golden curve), the nonequilibrium spin density is of opposite sign and shows linear scaling up to a field strength of $|\mathbf{B}| = 200$ meV at which the response reaches an amplitude of $-15\times10^{-6}\,\hbar/2$. Towards larger Zeeman fields the response to light polarized along $z$ decreases in amplitude until it switches sign at a applied Zeeman field strength of about 350 meV.

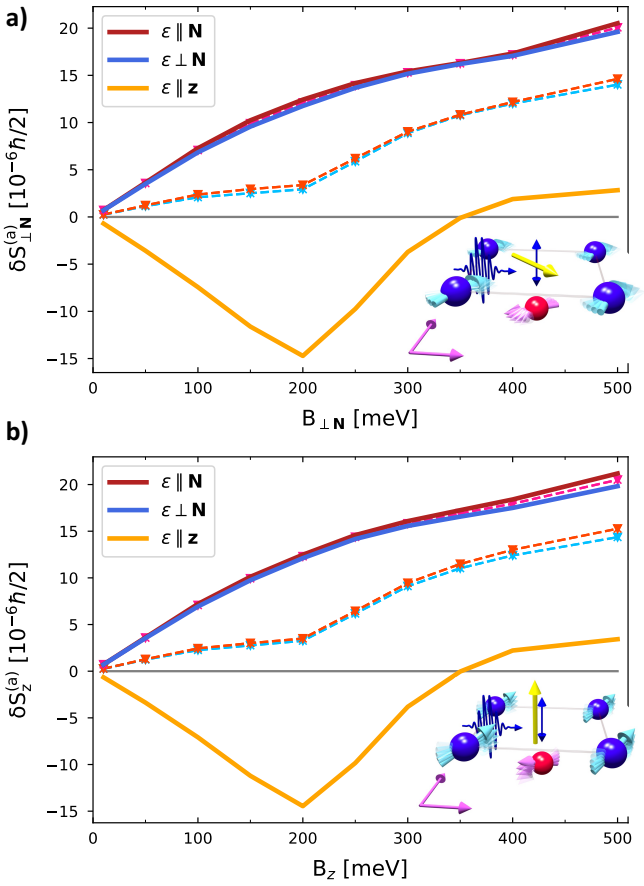


**FIGURE 9.5.** Dependence of the antisymmetric laser induced spin density on the applied Zeeman field strength. a) Zeeman field applied in the $xy$-plane perpendicular to the Néel vector to introduce in-plane canting of the magnetic moments on the Mn sublattices. b) Zeeman field applied along $z$-direction to achieve out-of-plane canting.

Comparing Figure 9.5 a) and b) it is apparent that the antisymmetric spin density is isotropic in the plane spanned by the $z$- and the $\perp$ **N**-directions. The responses in Figure 9.5 a) and b) are virtually identical for all types of applied laser fields over the complete range of Zeeman field strength considered.

In Figure 9.6 the dependence of the antisymmetric component of the spin-polarized photocurrent flowing out of the plane on the strength of the applied Zeeman field is shown. Two scenarios are presented: Figure 9.6 a) shows the spin current for in-plane canting of the magnetic moments and b) the out-of-plane canting scenario. In both cases only the most sizeable components of the spin current are shown.

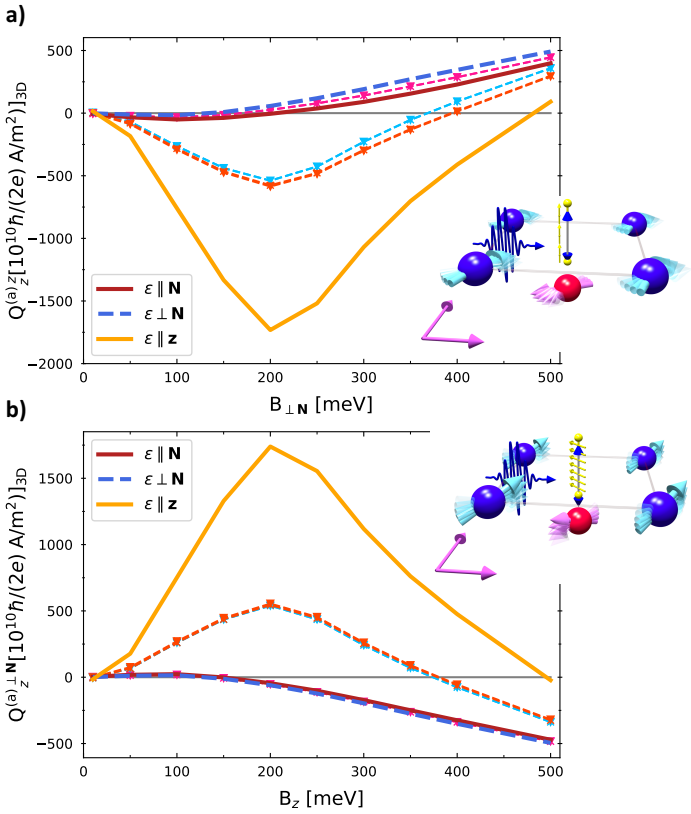


**FIGURE 9.6.** Dependence of the chiral spin photocurrent flowing along the $z$-direction on the strength of the applied Zeeman field. a) Zeeman field applied in the plane perpendicular to the Néel vector. b) Zeeman field applied along z-direction.

The spin currents dependence on the Zeeman field in Figure 9.6 is very similar to the antisymmetric nonequilibrium spin density presented in Figure 9.5. For example the extremum at 200 meV Zeeman field strength in response to linearly polarized light along $z$ (golden curve) is present for spin currents and nonequilibrium spin density. However, the antisymmetric spin density was induced directly along the direction of the applied Zeeman field, denoted here as the **b**-direction, while the chiral spin photocurrents have a spin polarization along $\mathbf{b} \times \mathbf{N}$. In stark contrast to the antisymmetric spin density the sign of the chiral spin photocurrents is reversed between the two respective scenarios presented in Figure 9.6 a) and b). While the spin density is unaltered between the two scenarios, the sign reversal of the chiral spin photocurrent suggests that the spin photocurrent completely vanishes in the direction of the average of the $z$- and the $\perp$ **N**-direction. The vanishing spin current could be explained by the symmetry of the crystal forbidding a photocurrent in this direction.

The antisymmetric spin current peaks at $\sim \pm 1750 \times 10^{10}\, \hbar/(2e)\, \mathrm{A/m^2}$ for a laser frequency of $\hbar\omega = 3.0\,\mathrm{eV}$ with $\Gamma = 25\,\mathrm{meV}$, which is an order of magnitude larger than the spin currents in the collinear scenario as discussed in the previous Chapter 8. On the other hand, for light linearly polarized within the $xy$-plane represented by the thick blue and red curve, the chiral spin photocurrents are suppressed below Zeeman fields of 100 meV and show linear scaling only above that field strength. The chiral spin density showed linearly scaling across the entire presented range of Zeeman field strength.

The similarities between the dependence of the antisymmetric spin density and chiral spin photocurrent on the applied Zeeman field suggest that both effects are intimately related and arguably share their microscopic origin. In contrast to the spin effects the chiral charge photocurrents presented in Figure 9.3 showed a fundamentally different dependence on the applied Zeeman field and were overall less pronounced, especially when compared to the large chiral spin photocurrents. To further analyze the close relation between laser induced chiral spin density and spin photocurrent, the dependence on the applied laser frequency is discussed next.

Figure 9.7 a) shows the frequency dependence of the antisymmetric spin density defined in Eq. (9.2) induced in the $z$-direction when the Zeeman field is applied along $z$. The Zeeman field strength was set to 200 meV up to which the response scales linearly with the applied field strength, as can be seen again in the inset of Figure 9.7, which shows the dependence of the antisymmetric spin density on the Zeeman field for field strength from 10 up to 200 meV. The second column shows the related spin photocurrent flowing along $z$ with spin polarization along the $\perp \mathbf{N}$-direction. To emphasize that both responses are generic with respect to the orientation of the Zeeman field, the scenario of the Zeeman field along the $\perp \mathbf{N}$-direction is shown in Figure 9.7 b). In both scenarios the LPGE-like spin density is along $\mathbf{i}$, where $\mathbf{i}$ is the direction of the Zeeman field, and the chiral spin photocurrent has spin polarization along $\mathbf{i} \times \mathbf{N}$ and flows along $z$-direction. Comparing responses in a) and b) one quickly realizes that their frequency dependence is identical in the two scenarios over the complete presented frequency range from $\hbar\omega = 0.1\,\mathrm{eV}$ up to $\hbar\omega = 4.1\,\mathrm{eV}$. However, one difference already present in Figure 9.5 and Figure 9.6 is apparent: the chiral spin photocurrent has a reversed sign compared to the spin photocurrent in a), while the induced spin density is identical in both cases. Both responses are insensitive to the orientation of the linearly polarized light if confined to the $xy$-plane.

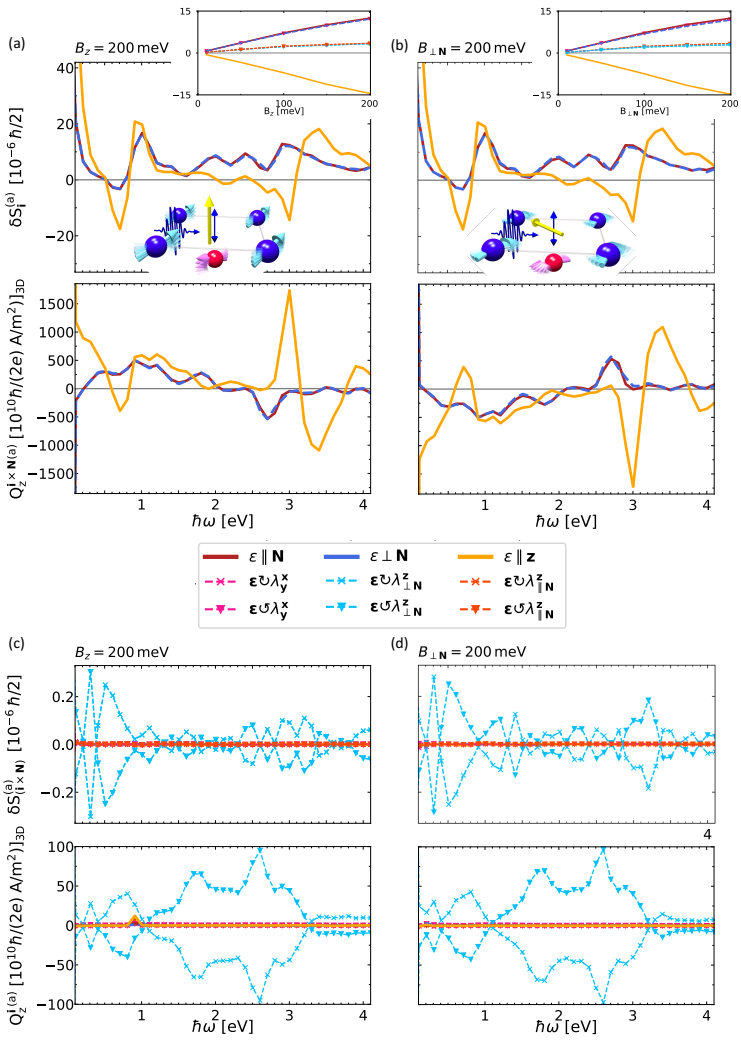


**FIGURE 9.7.** Frequency dependence for the most relevant chiral spin density and chiral spin-polarized photocurrent (reprinted from [2], ©2023 CC BY 4.0). The left column shows responses in the scenario of a Zeeman field of 200 meV applied along the $z$-direction, the right column a 200 meV Zeeman field applied in-plane. a) LPGE like chiral spin density and spin photocurrent. b) Same as a) but for the Zeeman field applied in-plane. In c) and d) the CPGE like chiral effects appearing perpendicular to their LPGE-like counterparts in a) and b) respectively are shown.

Up to a frequency of $\hbar\omega = 1.6$ eV the antisymmetric spin density has the same sign for both linear polarization along $z$ and within the $xy$-plane. At $\hbar\omega = 1.6$ eV both responses are almost completely suppressed, for larger frequencies up to $\hbar\omega \approx 3.1$ eV the response is of opposite sign for the two distinct laser polarization orientations. A similar behavior can be seen for the

chiral spin photocurrent in this frequency region, the responses to linearly polarized light along $z$ and within the $xy$-plane oscillate, here, however, not around zero but instead there appears to be a linear offset. For frequencies above $\hbar\omega = 3.1$ eV the chiral spin photocurrent in response to linearly polarized light in the $xy$-plane is almost completely suppressed, while the respective spin density remains finite at these frequencies. Both spin responses are maximized for light linearly polarized along $z$.

The antisymmetric spin density has two negative peaks of about -$18{\times}10^{-6}\,\hbar/2$ at laser frequencies of $\hbar\omega = 0.7$ eV and $\hbar\omega = 3.0$ eV. Positive peaks of about $20 \times 10^{-6}\,\hbar/2$ are present at $\hbar\omega = 0.8$ eV and $\hbar\omega = 3.4$ eV. The chiral spin photocurrent in response to light polarized along $z$ shows peaks at the same frequencies, although they show a stronger modulation of their amplitude with some switching sign when compared to the peaks of the spin density. The relation between antisymmetric spin density and photocurrent is, thus, not constant and in general depends on the applied laser frequency. Although the effects show strong correlation over the complete presented frequency range. At $\hbar\omega = 0.7$ eV the chiral spin photocurrent peaks with an amplitude of about $-300 \times 10^{10}\,\hbar/(2e)\mathrm{A/m}^2$, while the peak at $\hbar\omega = 3.0$ eV has reversed sign and is dramatically enhanced with amplitudes of $1760 \times 10^{10}\,\hbar/(2e)\mathrm{A/m}^2$. In case of light linearly polarized in the $xy$-plane the largest spin photocurrent response is achieved at a laser frequency of $\hbar\omega = 2.7$ eV and a second peak of comparable amplitude, however, of opposite sign, is present at $\hbar\omega \approx 0.8$ eV. At $\hbar\omega = 3.0$ eV where the largest response to light linearly polarized along $z$ is achieved, the spin photocurrent response to light polarized within the $xy$-plane is almost completely suppressed.

Overall in the presented frequency range the chiral spin density and spin photocurrent show a very similar dependence on the frequency which suggests that both effects are of the same microscopic origin and that the underlying effect is generic with respect to the orientation and strength of the applied Zeeman field. The chiral spin density can be interpreted as an effective canting of the staggered magnetic moments on the Mn sites, which results in an effective ferromagnetic moment along the direction of the chiral spin density $\delta S^-$. Due to the presence of the effective magnetic moment, which acts as a exchange field, a spin-polarized photocurrent can be driven via the spin galvanic effect [199].

Figure 9.7 c) and d) shows the frequency dependence of the antisymmetric spin density along the direction $\mathbf{i} \times \mathbf{N}$ and the antisymmetric spin photocurrent flowing along $z$ with spins polarized along $\mathbf{i}$, where $\mathbf{i}$ is pointing along the direction of the applied exchange field along c) the $z$-direction and d) the $\perp \mathbf{N}$ direction. The presented components show CPGE-like behavior and as the LPGE-like effects are generic with respect to the direction of the applied

Zeeman field, however, unlike for the LPGE-like chiral effects, the frequency dependence of spin density and spin photocurrent do not correlate. Compared to the LPGE-like chiral responses presented in a) and b) the magnitude of the effects is about one to two orders smaller. Therefore, these CPGE-like effects seem to have different microscopic origins and can be understood as the result of the overall symmetry lowering, due to the applied Zeeman field, which in turn introduces a bias between competing band transitions.

In summary sizeable chiral photocurrents and spin photocurrents were found in response to linearly polarized light. The chiral photocurrents could be used as proxies to track the evolution of the magnetic moments during non-direct, torque driven, switching processes. Even for the small canting angles considered, chiral spin photocurrents were found to be gigantic with respect to their collinear counterparts and highlight antiferromagnets under reordering of the intrinsic magnetic moments as viable candidates as spin current sources in the realm of optospintronic applications. With the end of this chapter the results part of this thesis is concluded. In the following part a brief outlook on possible future research directions will be given.

Part V

# Outlook

# Chapter 10

# *Outlook*

This chapter aims to give a brief outlook of future research directions in which the *ju_wip* code could be further applied and extended.

## 10.1 Orbital photoeffects

Besides spintronics, orbitronics have emerged as a field of interest and ongoing research. In orbitronics the orbital magnetization, instead of using the spin degree of freedom, is utilized as information carrier[203]. With the *ju_wip* code the orbital pendants to the spin based photogalvanic effects can be calculated. Indeed, in Chapter 8 the orbital photocurrents were benchmarked against spin photocurrents in $Mn_2Au$. Here spin based effects proved to be of larger magnitude, since the symmetry breaking which allows for a photoresponse is happening in spin space and has to be mediated to the orbital degree of freedoms via spin orbit coupling. One advantage of orbitronics over spintronics is however, that in materials with suitable symmetry lowering, the laser perturbation can directly act on the orbital degree of freedom, without the requirement of strong spin orbit coupling to achieve sizeable effects. This opens up a new class of light materials suitable for orbitronic device applications[203]. The author of this thesis is excited to report that indeed research into orbital photoresponses with the *ju_wip* code is ongoing and spearheaded by Theodoros Adamantopoulos, see for example Ref. [204].

## 10.2 FeMn noncollinear AFMs - FeMn tight-binding model

Another interesting study for the future could be the interplay between photoresponses and noncollinear antiferromagnets. As shown in this work, magnetic photocurrents can act as ultrafast proxies to determine the orientation of the Néel vector in $\mathcal{PT}$-symmetric collinear antiferromagnets such as $Mn_2Au$. This raises the question if they could be leveraged in a similar way for noncollinear AFMs, especially since anomalous Hall[207,208] and spin Hall effects[209] arising from the noncollinear spin structure have already been

discovered. As a proof of concept, photocurrents are calculated here for a tight-binding model of the noncollinear AFM $Fe_xMn_{1-x}$ [159,210]. A Rashba term was added to the model by Feng *et al.* [159] to break inversion symmetry [211].

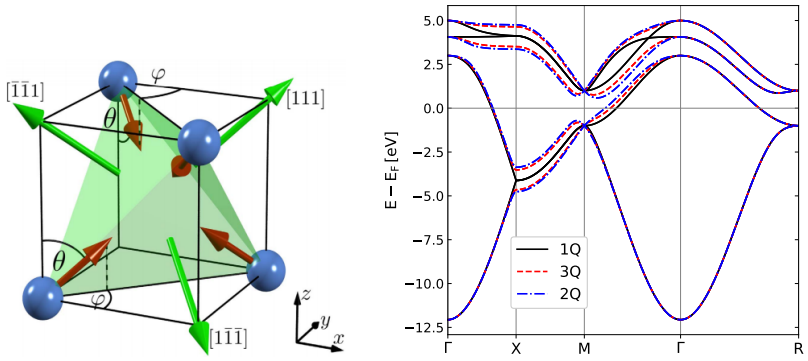


**FIGURE 10.1.** Geometry and electronic structure of 3D $\gamma$-$Fe_xMn_{1-x}$ (FeMn). On the left the unit cell of FeMn (adapted from [210], ©2017 CC BY 4.0). The spin configuration characterized by the angles $\Theta$ and $\phi$ can be controlled by varying the Fe concentration $x$. Fixing $\varphi = 45°$, $\Theta = 0$ corresponds to the 1Q state, $\Theta = 54.7°$ to the 3Q state and $\Theta = 90°$. (b) bandstructure of the 1Q (black), 3Q (red) and 2Q (blue) configuration.

The tight-binding Hamiltonian is given by

$$H = -\sum_{<ij>} c^{\dagger}_{i\alpha} t_{ij} c_{j\alpha} - J \sum_{i} c^{\dagger}_{i\alpha} (\tau_{\alpha\beta} \cdot \mathbf{S}_i) c_{i\beta} + i\lambda_R \sum_{<ij>} c^{\dagger}_{i} (\mathbf{S}_i \times \mathbf{d}_{ij})_z c_j, \quad (10.1)$$

where $c^{\dagger}_{i\alpha}$ and $c_{i\alpha}$ are the creation and annihilation operators of electron $i$ with spin $\alpha$, $t_{ij}$ are the hopping parameters between electronic states $i$ and $j$, $J$ is the exchange coupling strength, $\tau_{\alpha\beta}$ the Pauli operator and $\mathbf{S}_i$ a unit vector pointing along the direction of magnetization of electron $i$. $< ij >$ indicates summation over states only within a layer. The last term accounts for the added Rashba term [211], with $\lambda_R$ the Rashba coupling strength and $d_{ij}$ the vector connecting electron site $i$ and $j$. The hopping parameter $t_{ij}$ and the exchange coupling $J$ where fixed to 1 eV, the Rashba parameter $\lambda_R$ was set to 300 meV if not specified otherwise. With Eq. (10.1) various magnetic configuration can be studied. As shown in the left panel of Figure 10.1 the magnetic state can be parametrized by angles $\Theta$ & $\varphi$. The azimuthal angle $\varphi$ is fixed to $\varphi = 45°$ and the polar $\Theta$ varied to change to antiferromagnetic configuration. For $\Theta = 0$ the AFM configuration is collinear, also referred to as 1Q state since the configuration can be described by a spin-wave solely determined by a single wave vector $\mathbf{Q}$. $\Theta = 90°$ corresponds to a non-coplanar configuration and can be interpreted as a 2Q state. For $\Theta = 54.7°$

the system is in a 3Q state and has maximized scalar spin chirality $\kappa$ given by $\kappa = S_i \cdot (S_j \times S_k)$.

Figure 10.2 shows a comparison between the band resolved photocurrents of the 3Q state without and with Rashba coupling respectively. The Rashba coupling strength was set to 300 meV in the right panel.

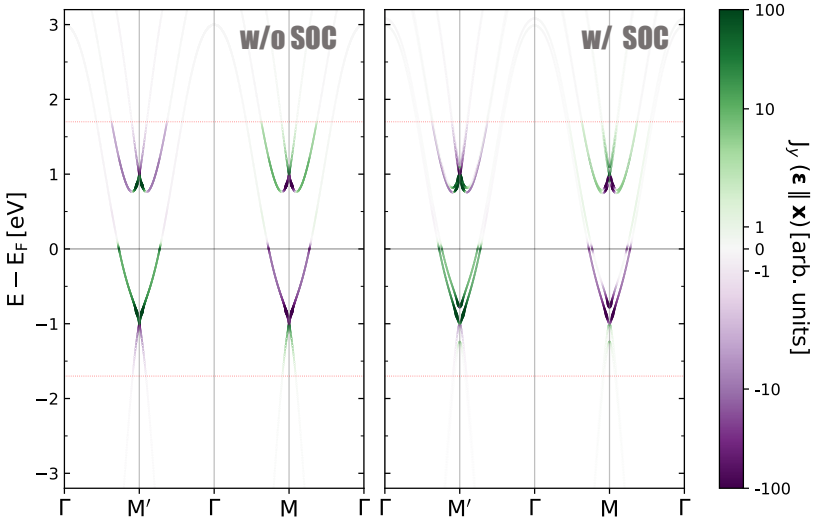


**Figure 10.2.** FeMn bandstructure resolved photocurrent with and without spin-orbit coupling for a laser frequency of $\hbar\omega = 1.7$ eV and a broadening of $\Gamma = 25$ meV.

Figure 10.2 shows that already in the system without Rashba coupling strong photocurrents are induced at the M point and the negative M point M′. However, the contributions from M and M′ are perfectly antisymmetric and "cancel each other out" when integrated over all regions of the Brillouin zone. Thus, some asymmetry has to be introduced to pronounce on point over the other. One option to achieve this is to introduce a Rashba coupling, as shown in[211]; however other options such as introducing strain might also be possible. On the right-hand side, Figure 10.2 shows the band resolved photocurrents for the system with Rashba coupling enabled. As the figure shows the Rashba coupling lifts the band degeneracy and introduces asymmetries between the responses at M and M′, note for example how the green inner band of the parabola at about −0.5 eV is more pronounced on the M′ point, while on the positive M point the purple inner band shows almost no transitions. These asymmetries are picked up and yield a finite photocurrent upon integration over the complete Brillouin zone.

To confirm the symmetry breaking effect of the Rashba term in Eq. (10.1),

Figure 10.3 shows the integrated photocurrent plotted against the applied Rashba coupling strength. The Laser frequency was set to $\hbar\omega = 1.7$ eV, the broadening fixed to $\Gamma = 25$ meV and a $544 \times 544\times$ interpolation $k$-mesh used, which provides well converged results for lifetime broadening larger than $\Gamma = 10$ meV.

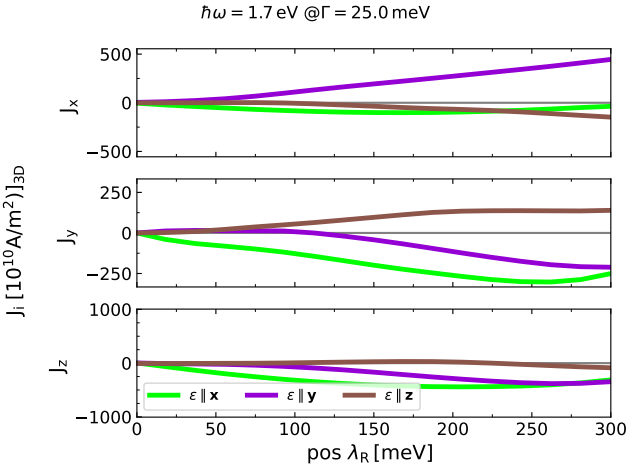


**Figure 10.3.** Effect of spin orbit coupling on the components of the photocurrent.

Figure 10.3 indicates that already moderate spin orbit coupling values can open up a sizeable photocurrent, with $J_x(\lambda_r = 150\,\text{meV}) \approx 250\,\text{A/m}^2$. In order to characterize the magnetic configuration by means of photocurrent their magnetization dependent components have to be identified. These components depend heavily in there sign, size and orientation on the magnetic configuration, as discussed in Section 8.3.

To identify magnetic photocurrents the negative broadening behavior of the photocurrents is presented in Figure 10.4. From Figure 10.4 the $J_y$ response and in case of light linearly polarized along $z$ also the $J_z$ photocurrent can be identified as magnetic photocurrents and should thus be best suited to determine the magnetic configuration.

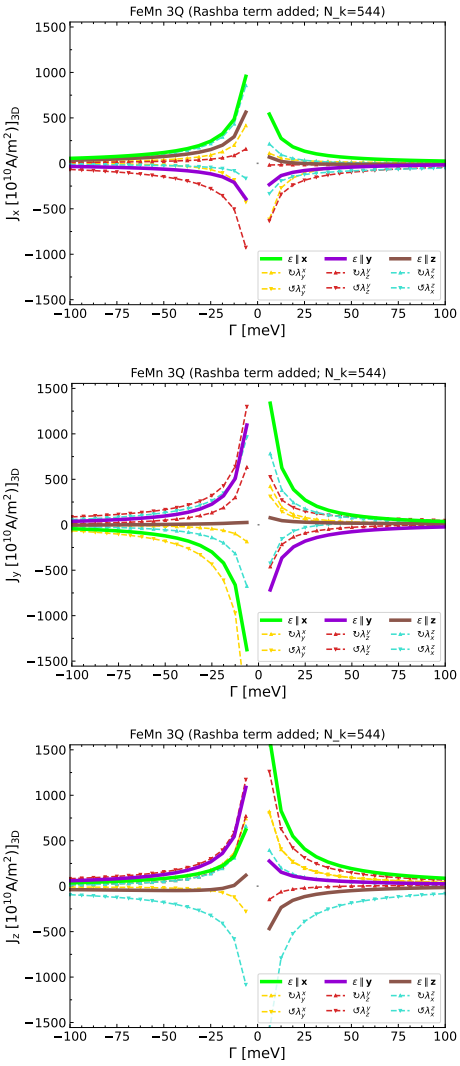


**Figure 10.4.** Broadening dependence of the photocurrents for positive and negative values of the broadening $\Gamma$ in the range from 10 to 100 meV. The columns show the $x, y$ and $z$ component of the photocurrent respectively. $J_x$ and $J_z$ are even (nonmagnetic) in case of linearly polarized light, while $J_y$ is odd (magnetic) w.r.t. to the broadening $\Gamma$. Note that the $J_z$ response to linearly polarized light along z is odd (magnetic), while for the other linear polarization the response is even (nonmagnetic).

The left panel of Figure 10.5 shows frequency dependence of the magnetic component $J_y$ when in the 3Q state ($\Theta = 54.7°$) evaluated at the Fermi level with room temperature broadening. Various linear and circular laser polarizations were considered as indicated by the legend. $J_y$ shows a strong

dependence on the applied laser frequency $\hbar\omega$, with amplitudes reaching as high as $200\text{A/m}^2$, although the predictive power here is limited since only a model calculation was performed. Full *ab-initio* calculations could be a topic for future investigations to better quantify the photoresponses. In the frequency range from 1.0 up to 2.1 eV the photocurrent oscillates with respect to frequency and strongly depends on the applied laser polarization. In this frequency range the response can be almost perfectly switched by changing the orientation of the linear polarization from the $x$ (green curve) to the $y$-direction (purple curve). The strong dependence on frequency and polarization suggests the photocurrent acts as good proxy for the magnetic state of the system.

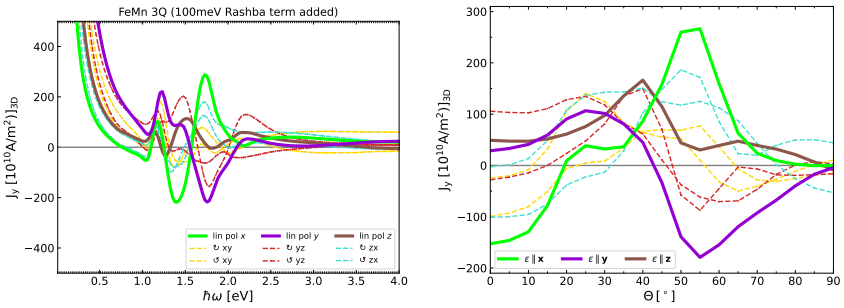


**FIGURE 10.5.** Spectral properties of the photocurrents. In the left panel the frequency dependence of the magnetic component $J_y$ in the 3Q configuration with a strong peak visible at $\hbar\omega = 1.7$ eV, evaluated at the Fermi level with room temperature broadening $\Gamma = 25$ meV. The right panels show the magnetic $J_y$ component with frequency fixed to $\hbar\omega = 1.7$ eV plotted vs the AFM spin-configuration characterized by the angle $\Theta$, as shown in Figure 10.1.

The right panel of Figure 10.5 fixes the laser frequency to $\hbar\omega = 1.7$ eV and instead changes the magnetic state by varying the orientation of the magnetic moments with respect to the angle $\Theta$. The figure shows that for laser light linearly polarized in the $xy$-plane (thick green and purple curve) the $J_y$ component of the photocurrent spikes around the 3Q configuration at $\Theta = 54.7°$, suggesting that the photocurrent is sensitive to the scalar spin chirality and could indeed be used as an experimental proxy to determine the scalar spin chirality.

## 10.3 GPU COMPUTE VIA OPENMP

With the ever-increasing popularity of GPU compute [13,14], the *ju_wip* code might have to be ported to GPU at some point to stay relevant. Note that dur-

ing the course of the authors PhD, no access to GPU machines was available and, therefore, GPU based computation was not yet relevant for this work. Besides the widely adopted CUDA API[212], the device offloading implemented in OpenMP 4.5 (and newer standards)[213] would allow for a relatively straight extension of the already existing OpenMP parallelization implemented in the *ju_wip* code.

With this the thesis is concluded.

# Chapter 11

# *References*


[1] Maximilian Merte, Frank Freimuth, Theodoros Adamantopoulos, Dongwook Go, Thomas Gauntlett Saunderson, Mathias Kläui, L Plucinski, Olena Gomonay, Stefan Blügel, and Yuriy Mokrousov. *Photocurrents of charge and spin in monolayer $Fe_3GeTe_2$*. Physical Review B **104** (22), L220405 (2021). Cited on page/s xi, 8, 93, 94, 95, 96, 99, 101.

[2] Maximilian Merte, Frank Freimuth, Dongwook Go, Theodoros Adamantopoulos, Fabian R. Lux, Lukasz Plucinski, Olena Gomonay, Stefan Blügel, and Yuriy Mokrousov. *Photocurrents, inverse Faraday effect, and photospin Hall effect in $Mn_2Au$*. APL Materials **11** (7), 071106 (2023). Cited on page/s xi, 6, 7, 8, 103, 105, 108, 110, 112, 114, 115, 117, 120, 122, 124, 126, 128, 130, 131, 132, 152.

[3] Kartik Samanta, Marjana Ležaić, Maximilian Merte, Frank Freimuth, Stefan Blügel, and Yuriy Mokrousov. *Crystal Hall and crystal magneto-optical effect in thin films of $SrRuO_3$*. Journal of applied physics **127** (21), 213904 (2020). Cited on page/s xi, 8, 141.

[4] Jonathan Kipp, Kartik Samanta, Fabian R Lux, Maximilian Merte, Dongwook Go, Jan-Philipp Hanke, Matthias Redies, Frank Freimuth, Stefan Blügel, Marjana Ležaić, *et al. The chiral Hall effect in canted ferromagnets and antiferromagnets*. Communications Physics **4** (1), 1–12 (2021). Cited on page/s xi, 8, 141, 142, 143, 144.

[5] Nicola Jones *et al. How to stop data centres from gobbling up the world's electricity*. Nature **561** (7722), 163–166 (2018). Cited on page/s 3.

[6] Anja Feldmann, Oliver Gasser, Franziska Lichtblau, Enric Pujol, Ingmar Poese, Christoph Dietzel, Daniel Wagner, Matthias Wichtlhuber, Juan Tapiador, Narseo Vallina-Rodriguez, *et al. The lockdown effect: Implications of the COVID-19 pandemic on internet traffic*. In *Proceedings of the ACM internet measurement conference* pages 1–18 (2020). Cited on page/s 3.

[7] Mark Bohr. *A 30 year retrospective on Dennard's MOSFET scaling paper*. IEEE Solid-State Circuits Society Newsletter **12** (1), 11–13 (2007). Cited on page/s 3.

[8] Gordon E Moore. *Cramming more components onto integrated circuits*. Proceedings of the IEEE **86** (1), 82–85 (1998). Cited on page/s 3.

[9] Rajeev Muralidhar, Renata Borovica-Gajic, and Rajkumar Buyya. *Energy Efficient Computing Systems: Architectures, Abstractions and Modeling to Techniques and Standards*. ACM Comput. Surv. **54** (11s) (2022). ISSN 0360-0300. Cited on page/s 3, 4.

[10] David P Rodgers. *Improvements in multiprocessor system design*. ACM SIGARCH Computer Architecture News **13** (3), 225–231 (1985). Cited on page/s 3.

[11] Gene M. Amdahl. *Validity of the Single Processor Approach to Achieving Large Scale Computing Capabilities*. In *Proceedings of the April 18-20, 1967, Spring Joint Computer Conference* AFIPS '67 (Spring) page 483–485 New York, NY, USA (1967). Association for Computing Machinery. ISBN 9781450378956. Cited on page/s 3.

[12] Tekla S. Perry. *Move Over, Moore's Law: Make Way for Huang's Law*. Ieee Spectrum pages 82–85 (2018). Cited on page/s 3.

[13] John D Owens, Mike Houston, David Luebke, Simon Green, John E Stone, and James C Phillips. *GPU computing*. Proceedings of the IEEE **96** (5), 879–899 (2008). Cited on page/s 3, 162.

[14] Mohamed Taher. *Accelerating scientific applications using GPU's*. In *2009 4th International Design and Test Workshop (IDT)* pages 1–6. IEEE (2009). Cited on page/s 3, 162.

[15] Carlos Carvalho. *The gap between processor and memory speeds*. In *Proc. of IEEE International Conference on Control and Automation* (2002). Cited on page/s 3.

[16] John L Hennessy and David A Patterson. *A new golden age for computer architecture*. Communications of the ACM **62** (2), 48–60 (2019). Cited on page/s 4.

[17] Tim Ansell and Mehdi Saligane. *The missing pieces of open design enablement: A recent history of Google efforts*. In *Proceedings of the 39th International Conference on Computer-Aided Design* pages 1–8 (2020). Cited on page/s 4.

[18] Richard York. *Ecological paradoxes: William Stanley Jevons and the paperless office*. Human Ecology Review pages 143–147 (2006). Cited on page/s 4.

[19] Diana Bauer and Kathryn Papp. *Book Review Perspectives: The Jevons Paradox and the Myth of Resource Efficiency Improvements*. Sustainability: Science, Practice, & Policy **5** (1), 48–54 (2009). Cited on page/s 4.

[20] Richard York and Julius Alexander McGee. *Understanding the Jevons paradox*. Environmental Sociology **2** (1), 77–87 (2016). Cited on page/s 4.

[21] Seth Lloyd. *Ultimate physical limits to computation*. Nature **406** (6799), 1047–1054 (2000). Cited on page/s 4, 52.

[22] TOP500. *NEWS ORNL's Frontier First to Break the Exaflop Ceiling* (2022). Cited on page/s 4.

[23] Stuart A Wolf and Daryl Treger. *Spintronics: A new paradigm for electronics for the new millennium*. IEEE Transactions on Magnetics **36** (5), 2748–2751 (2000). Cited on page/s 4.

[24] Eric Beaurepaire, J-C Merle, A Daunois, and J-Y Bigot. *Ultrafast spin dynamics in ferromagnetic nickel*. Physical review letters **76** (22), 4250 (1996). Cited on page/s 5.

[25] Andrei Kirilyuk, Alexey V. Kimel, and Theo Rasing. *Ultrafast optical manipulation of magnetic order*. Rev. Mod. Phys. **82**, 2731–2784 (2010). Cited on page/s 5.

[26] Jakob Walowski and Markus Münzenberg. *Perspective: Ultrafast magnetism and THz spintronics*. Journal of Applied Physics **120** (14), 140901 (2016). Cited on page/s 5.

[27] Bernard Dieny, Ioan Lucian Prejbeanu, Kevin Garello, Pietro Gambardella, Paulo Freitas, Ronald Lehndorff, Wolfgang Raberg, Ursula Ebels, Sergej O Demokritov, Johan Akerman, *et al. Opportunities and challenges for spintronics in the microelectronics industry*. Nature Electronics **3** (8), 446–459 (2020). Cited on page/s 5.

[28] Frank Freimuth, Stefan Blügel, and Yuriy Mokrousov. *Laser-induced torques in metallic ferromagnets*. Physical Review B **94**, 144432 (2016). Cited on page/s 5, 19, 26, 32, 37, 38, 39, 40, 45, 119.

[29] Frank Freimuth, Stefan Blügel, and Yuriy Mokrousov. *Laser-induced currents of charge and spin in the Rashba model*. arXiv preprint arXiv:1710.10480 (2017). Cited on page/s 5, 7, 19, 26, 41, 85, 86, 95.

[30] Olena Gomonay, T Jungwirth, and Jairo Sinova. *Concepts of antiferromagnetic spintronics*. physica status solidi (RRL)–Rapid Research Letters **11** (4), 1700022 (2017). Cited on page/s 5.

[31] Tomas Jungwirth, X Marti, P Wadley, and J Wunderlich. *Antiferromagnetic spintronics*. Nature nanotechnology **11** (3), 231–241 (2016). Cited on page/s 5.

[32] T Jungwirth, J Sinova, Aurelien Manchon, X Marti, J Wunderlich, and C Felser. *The multiple directions of antiferromagnetic spintronics*. Nature Physics **14** (3), 200–203 (2018).

Cited on page/s 5.

[33] Tobias Kosub, Martin Kopte, Ruben Hühne, Patrick Appel, Brendan Shields, Patrick Maletinsky, René Hübner, Maciej Oskar Liedke, Jürgen Fassbender, Oliver G Schmidt, *et al. Purely antiferromagnetic magnetoelectric random access memory*. Nature communications **8** (1), 1–7 (2017). Cited on page/s 5.

[34] Kamil Olejník, Vivien Schuler, Xavi Martí, Vít Novák, Zdeněk Kašpar, Peter Wadley, Richard P Campion, Kevin W Edmonds, Bryan L Gallagher, Javier Garcés, *et al. Antiferromagnetic CuMnAs multi-level memory cell with microelectronic compatibility*. Nature communications **8** (1), 15434 (2017). Cited on page/s 5.

[35] William A. Borders, Hisanao Akima, Shunsuke Fukami, Satoshi Moriya, Shouta Kurihara, Yoshihiko Horio, Shigeo Sato, and Hideo Ohno. *Analogue spin–orbit torque device for artificial-neural-network-based associative memory operation*. Applied Physics Express **10** (1), 013007 (2016). Cited on page/s 5.

[36] Aleksandr Kurenkov, Shunsuke Fukami, and Hideo Ohno. *Neuromorphic computing with antiferromagnetic spintronics*. Journal of Applied Physics **128** (1), 010902 (2020). Cited on page/s 5.

[37] Andrea Coluccio, Antonia Ieva, Fabrizio Riente, Massimo Ruo Roch, Marco Ottavi, and Marco Vacca. *RISC-Vlim, a RISC-V Framework for Logic-in-Memory Architectures*. Electronics **11** (19) (2022). ISSN 2079-9292. Cited on page/s 5.

[38] Peter Wadley, Bryn Howells, J Železný, Carl Andrews, Victoria Hills, Richard P Campion, Vit Novák, K Olejník, F Maccherozzi, SS Dhesi, *et al. Electrical switching of an antiferromagnet*. Science **351** (6273), 587–590 (2016). Cited on page/s 5.

[39] Kamil Olejník, Tom Seifert, Zdeněk Kašpar, Vít Novák, Peter Wadley, Richard P. Campion, Manuel Baumgartner, Pietro Gambardella, Petr Němec, Joerg Wunderlich, Jairo Sinova, Petr Kužel, Melanie Müller, Tobias Kampfrath, and Tomas Jungwirth. *Terahertz electrical writing speed in an antiferromagnetic memory*. Science Advances **4** (3), eaar3566 (2018). Cited on page/s 5, 123.

[40] K Vahaplar, AM Kalashnikova, AV Kimel, Denise Hinzke, Ulrich Nowak, R Chantrell, A Tsukamoto, A Itoh, A Kirilyuk, and Th Rasing. *Ultrafast path for optical magnetization reversal via a strongly nonequilibrium state*. Physical review letters **103** (11), 117201 (2009). Cited on page/s 5, 119.

[41] Marco Berritta, Ritwik Mondal, Karel Carva, and Peter M. Oppeneer. *Ab Initio Theory of Coherent Laser-Induced Magnetization in Metals*. Physical Review Letters **117**, 137203 (2016). Cited on page/s 5, 17, 62, 63, 119, 121, 134.

[42] Marion M. S. Barbeau, Mikhail Titov, Mikhail I. Katsnelson, and Alireza Qaiumzadeh. *Nonequilibrium Magnons from Hot Electrons in Antiferromagnetic Systems* (2022). Cited on page/s 5.

[43] Tobias Dannegger, Marco Berritta, Karel Carva, Severin Selzer, Ulrike Ritzmann, Peter M. Oppeneer, and Ulrich Nowak. *Ultrafast coherent all-optical switching of an antiferromagnet with the inverse Faraday effect*. Physical Review B **104**, L060413 (2021). Cited on page/s 5, 6, 119, 123.

[44] Tomas Janda, T Ostatnický, P Němec, E Schmoranzerová, R Campion, V Hills, V Novák, Z Šobáň, and Jörg Wunderlich. *Ultrashort spin–orbit torque generated by femtosecond laser pulses*. Scientific Reports **12** (1), 21550 (2022). Cited on page/s 5, 6, 123.

[45] BSD Ch S Varaprasad, YK Takahashi, M Cinchetti, K Hono, Y Fainman, M Aeschlimann, *et al. All-optical control of ferromagnetic thin films and nanostructures*. Science **345** (6202), 1337–1340 (2014). Cited on page/s 5.

[46] Robin John, Marco Berritta, Denise Hinzke, Cai Müller, Tiffany Santos, Henning Ulrichs, Pablo Nieves, Jakob Walowski, Ritwik Mondal, Oksana Chubykalo-Fesenko, *et al. Magnetisation switching of FePt nanoparticle recording medium by femtosecond laser*

*pulses*. Scientific reports 7 (1), 4114 (2017). Cited on page/s 5.

[47] Fei Xue and Paul M Haney. *Intrinsic staggered spin-orbit torque for the electrical control of antiferromagnets: Application to CrI 3*. Physical Review B **104** (22), 224414 (2021). Cited on page/s 6.

[48] Tobias Kampfrath, Alexander Sell, Gregor Klatt, Alexej Pashkin, Sebastian Mährlein, Thomas Dekorsy, Martin Wolf, Manfred Fiebig, Alfred Leitenstorfer, and Rupert Huber. *Coherent terahertz control of antiferromagnetic spin waves*. Nature Photonics **5** (1), 31–34 (2011). Cited on page/s 6.

[49] P. Němec, M. Fiebig, T. Kampfrath, and A.V. Kimel. *Antiferromagnetic opto-spintronics*. Nature Physics **14** (3), 229–241 (2018). Cited on page/s 6.

[50] Yang Zhang, Tobias Holder, Hiroaki Ishizuka, Fernando de Juan, Naoto Nagaosa, Claudia Felser, and Binghai Yan. *Switchable magnetic bulk photovoltaic effect in the two-dimensional magnet CrI3*. Nature communications **10** (1), 1–7 (2019). Cited on page/s 6, 11, 12, 98, 109, 115, 117.

[51] Anatolii E Fedianin, Alexandra M Kalashnikova, and Johan H Mentink. *Selection rules for ultrafast laser excitation and detection of spin correlations in a cubic antiferromagnet*. arXiv preprint arXiv:2212.14698 (2022). Cited on page/s 6.

[52] Andrej Farkas, Kamil Olejnik, Miloslav Surynek, Petr Nemec, Vit Novak, and Tomas Jungwirth. *Optical Control of Magnetic Configuration of an antiferromagnetic CuMnAs*. In *Frontiers in Optics + Laser Science 2022 (FIO, LS)* page FW7C.3. Optica Publishing Group (2022). Cited on page/s 6.

[53] Qiong Ma, Roshan Krishna Kumar, Su-Yang Xu, Frank HL Koppens, and Justin CW Song. *Photocurrent as a multiphysics diagnostic of quantum materials*. Nature Reviews Physics **5** (3), 170–184 (2023). Cited on page/s 6, 11, 12.

[54] Dominik Hamara, Gunnar F Lange, Farhan Nur Kholid, Anastasios Markou, Claudia Felser, Robert-Jan Slager, and Chiara Ciccarelli. *Helicity-dependent Ultrafast Photocurrents in Weyl Magnet Mn _3 Sn*. arXiv preprint arXiv:2302.07286 (2023). Cited on page/s 6.

[55] Albert Fert. *The present and the future of spintronics*. Thin Solid Films **517** (1), 2–5 (2008). ISSN 0040-6090. Fifth International Conference on Silicon Epitaxy and Heterostructures (ICSI-5). Cited on page/s 6.

[56] Jairo Sinova, Sergio O Valenzuela, Jörg Wunderlich, CH Back, and T Jungwirth. *Spin hall effects*. Reviews of modern physics **87** (4), 1213 (2015). Cited on page/s 6, 62, 131.

[57] Keita Hamamoto, Motohiko Ezawa, Kun Woo Kim, Takahiro Morimoto, and Naoto Nagaosa. *Nonlinear spin current generation in noncentrosymmetric spin-orbit coupled systems*. Physical Review B **95** (22), 224430 (2017). Cited on page/s 6, 17.

[58] Bevin Huang, Genevieve Clark, Efrén Navarro-Moratalla, Dahlia R. Klein, Ran Cheng, Kyle L. Seyler, Ding Zhong, Emma Schmidgall, Michael A. McGuire, David H. Cobden, Wang Yao, Di Xiao, Pablo Jarillo-Herrero, and Xiaodong Xu. *Layer-dependent ferromagnetism in a van der Waals crystal down to the monolayer limit*. Nature **546** (7657), 270–273 (2017). ISSN 1476-4687. Cited on page/s 7, 93, 94.

[59] Cheng Gong and Xiang Zhang. *Two-dimensional magnetic crystals and emergent heterostructure devices*. Science **363** (6428), eaav4450 (2019). Cited on page/s 7, 93.

[60] Cheng Gong, Lin Li, Zhenglu Li, Huiwen Ji, Alex Stern, Yang Xia, Ting Cao, Wei Bao, Chenzhe Wang, Yuan Wang, Z. Q. Qiu, R. J. Cava, Steven G. Louie, Jing Xia, and Xiang Zhang. *Discovery of intrinsic ferromagnetism in two-dimensional van der Waals crystals*. Nature **546** (7657), 265–269 (2017). ISSN 1476-4687. Cited on page/s 7, 93.

[61] M. Gibertini, M. Koperski, A. F. Morpurgo, and K. S. Novoselov. *Magnetic 2D materials and heterostructures*. Nature Nanotechnology **14** (5), 408–419 (2019). ISSN 1748-3395. Cited on page/s 7, 93.

[62] M. Bass, P. A. Franken, J. F. Ward, and G. Weinreich. *Optical Rectification*. Physical Review Letters **9**, 446–448 (1962). Cited on page/s 11.

[63] Viktor Iosifovich Belinicher and Boris Itskhakovich Sturman. *The photogalvanic effect in media lacking a center of symmetry*. Soviet Physics Uspekhi **23** (3), 199 (1980). Cited on page/s 11, 12, 13, 14.

[64] Ralph von Baltz and Wolfgang Kraut. *Theory of the bulk photovoltaic effect in pure crystals*. Physical Review B **23** (10), 5590 (1981). Cited on page/s 11, 12.

[65] J. E. Sipe and A. I. Shkrebtii. *Second-order optical response in semiconductors*. Physical Review B **61**, 5337–5352 (2000). Cited on page/s 11, 14, 16, 87.

[66] T. Choi, S. Lee, Y. J. Choi, V. Kiryukhin, and S.-W. Cheong. *Switchable Ferroelectric Diode and Photovoltaic Effect in $BiFeO_3$*. Science **324** (5923), 63–66 (2009). Cited on page/s 11.

[67] SY Yang, Jan Seidel, SJ Byrnes, P Shafer, C-H Yang, MD Rossell, P Yu, Y-H Chu, JF Scott, JW Ager Iii, *et al. Above-bandgap voltages from ferroelectric photovoltaic devices*. Nature nanotechnology **5** (2), 143–147 (2010). Cited on page/s 11.

[68] Ilya Grinberg, D Vincent West, Maria Torres, Gaoyang Gou, David M Stein, Liyan Wu, Guannan Chen, Eric M Gallo, Andrew R Akbashev, Peter K Davies, *et al. Perovskite oxides for visible-light-absorbing ferroelectric and photovoltaic materials*. Nature **503** (7477), 509–512 (2013). Cited on page/s 11.

[69] Julen Ibañez Azpiroz, Stepan S. Tsirkin, and Ivo Souza. *Ab initio calculation of the shift photocurrent by Wannier interpolation*. Physical Review B **97**, 245143 (2018). Cited on page/s 11, 42, 43, 88, 98, 115.

[70] Stepan S Tsirkin, Pablo Aguado Puente, and Ivo Souza. *Gyrotropic effects in trigonal tellurium studied from first principles*. Physical Review B **97** (3), 035158 (2018). Cited on page/s 11, 16, 82.

[71] Yang Zhang, Hiroaki Ishizuka, Jeroen van den Brink, Claudia Felser, Binghai Yan, and Naoto Nagaosa. *Photogalvanic effect in Weyl semimetals from first principles*. Physical Review B **97**, 241118 (2018). Cited on page/s 11, 16, 81.

[72] Boris Itskhakovich Sturman. *Ballistic and shift currents in the bulk photovoltaic effect theory*. Physics-Uspekhi **63** (4), 407 (2020). Cited on page/s 11.

[73] Ding-Fu Shao, Shu-Hui Zhang, Gautam Gurung, Wen Yang, and Evgeny Y Tsymbal. *Nonlinear anomalous Hall effect for Néel vector detection*. Physical Review Letters **124** (6), 067203 (2020). Cited on page/s 12, 106.

[74] Ran Cheng. *Quantum geometric tensor (fubini-study metric) in simple quantum system: A pedagogical introduction*. arXiv preprint arXiv:1012.1337 (2010). Cited on page/s 12, 16.

[75] Daniel Kaplan, Tobias Holder, and Binghai Yan. *Unification of Nonlinear Anomalous Hall Effect and Nonreciprocal Magnetoresistance in Metals by the Quantum Geometry*. arXiv preprint arXiv:2211.17213 (2022). Cited on page/s 12, 16, 118.

[76] Takahiro Morimoto and Naoto Nagaosa. *Topological nature of nonlinear optical effects in solids*. Science advances **2** (5), e1501524 (2016). Cited on page/s 12.

[77] Fernando De Juan, Adolfo G Grushin, Takahiro Morimoto, and Joel E Moore. *Quantized circular photogalvanic effect in Weyl semimetals*. Nature communications **8** (1), 15995 (2017). Cited on page/s 12, 16.

[78] O. Matsyshyn and I. Sodemann. *Nonlinear Hall Acceleration and the Quantum Rectification Sum Rule*. Physical Review Letters **123**, 246602 (2019). Cited on page/s 12, 16, 82, 118.

[79] Junyeong Ahn, Guang-Yu Guo, Naoto Nagaosa, and Ashvin Vishwanath. *Riemannian geometry of resonant optical responses*. Nature Physics **18** (3), 290–295 (2022). Cited on page/s 12, 16.

[80] EL Ivchenko, Yu B Lyanda-Geller, and GE Pikus. *Magneto-photogalvanic effects in noncentrosymmetric crystals*. Ferroelectrics **83** (1), 19–27 (1988). Cited on page/s 14, 87.

[81] HANS Grimmer. *General relations for transport properties in magnetically ordered crystals*. Acta Crystallographica Section A: Foundations of Crystallography **49** (5), 763–771 (1993). Cited on page/s 14.

[82] Claudio Aversa and JE Sipe. *Nonlinear optical susceptibilities of semiconductors: Results with a length-gauge analysis*. Physical Review B **52** (20), 14636 (1995). Cited on page/s 16.

[83] Junyeong Ahn, Guang-Yu Guo, and Naoto Nagaosa. *Low-frequency divergence and quantum geometry of the bulk photovoltaic effect in topological semimetals*. Physical Review X **10** (4), 041041 (2020). Cited on page/s 16.

[84] ZZ Du, CM Wang, Hai-Peng Sun, Hai-Zhou Lu, and XC Xie. *Quantum theory of the nonlinear Hall effect*. Nature communications **12** (1), 5038 (2021). Cited on page/s 16.

[85] Hikaru Watanabe and Youichi Yanase. *Nonlinear electric transport in odd-parity magnetic multipole systems: Application to Mn-based compounds*. Phys. Rev. Research **2**, 043081 (2020). Cited on page/s 16, 106, 118.

[86] Tobias Holder, Daniel Kaplan, Roni Ilan, and Binghai Yan. *Mixed axial-gravitational anomaly from emergent curved spacetime in nonlinear charge transport*. arXiv preprint arXiv:2111.07780 (2021). Cited on page/s 16, 118.

[87] EL Ivchenko and SD Ganichev. *Spin-dependent photogalvanic effects (A Review)*. arXiv preprint arXiv:1710.09223 (2017). Cited on page/s 17.

[88] Motoi Kimata, Hua Chen, Kouta Kondou, Satoshi Sugimoto, Prasanta K Muduli, Muhammad Ikhlas, Yasutomo Omori, Takahiro Tomita, Allan MacDonald, Satoru Nakatsuji, *et al. Magnetic and magnetic inverse spin Hall effects in a non-collinear antiferromagnet*. Nature **565** (7741), 627–630 (2019). Cited on page/s 17.

[89] Ruixiang Fei, Wenshen Song, Lauren Pusey-Nazzaro, and Li Yang. *PT-Symmetry-Enabled Spin Circular Photogalvanic Effect in Antiferromagnetic Insulators*. Physical Review Letters **127**, 207402 (2021). Cited on page/s 17, 125.

[90] Haowei Xu, Hua Wang, Jian Zhou, and Ju Li. *Pure spin photocurrent in non-centrosymmetric crystals: bulk spin photovoltaic effect*. Nature Communications **12** (1), 1–9 (2021). Cited on page/s 17, 125.

[91] Satoru Hayami, Megumi Yatsushiro, and Hiroaki Kusunose. *Nonlinear spin Hall effect in $\mathcal{PT}$-symmetric collinear magnets*. arXiv preprint arXiv:2203.03754 (2022). Cited on page/s 17, 125.

[92] J. P. van der Ziel, P. S. Pershan, and L. D. Malmstrom. *Optically-Induced Magnetization Resulting from the Inverse Faraday Effect*. Physical Review Letters **15**, 190–193 (1965). Cited on page/s 17, 119, 121.

[93] Marco Battiato, G Barbalinardo, and Peter M Oppeneer. *Quantum theory of the inverse Faraday effect*. Physical review B **89** (1), 014413 (2014). Cited on page/s 17.

[94] Leonid V Keldysh *et al. Diagram technique for nonequilibrium processes*. Sov. Phys. JETP **20** (4), 1018–1026 (1965). Cited on page/s 19, 24.

[95] L.P. Kadanoff and G. Baym. *Quantum Statistical Mechanics: Green's Function Methods in Equilibrium and Nonequilibrium Problems*. CRC Press. Boca Raton (1962). Cited on page/s 19.

[96] Julian Schwinger. *Quantum Electrodynamics. I. A Covariant Formulation*. Phys. Rev. **74**, 1439–1461 (1948). Cited on page/s 21.

[97] J. Rammer and H. Smith. *Quantum field-theoretical methods in transport theory of metals*. Rev. Mod. Phys. **58**, 323–359 (1986). Cited on page/s 23, 25, 26, 27.

[98] Frank Freimuth, Stefan Blügel, and Yuriy Mokrousov. *Charge and spin photocurrents in the Rashba model*. Physical Review B **103**, 075428 (2021). Cited on page/s 26, 125.

[99] E Richard Cohen, Ian M Mills, Tom Cvitas, Jeremy G Frey, Martin Quack, Bertil Holström, and Kozo Kuchitsu. *Quantities, units and symbols in physical chemistry*. Royal

Society of Chemistry (2007). Cited on page/s 42, 47.
[100] *The FLEUR project*. Cited on page/s 47, 51, 59, 62, 63, 64, 65, 72, 76, 93, 95, 104.
[101] Peter F Moulton. *Spectroscopic and laser characteristics of Ti: Al 2 O 3*. JOSA B **3** (1), 125–133 (1986). Cited on page/s 48.
[102] TJ Huisman, RV Mikhaylovskiy, JD Costa, F Freimuth, E Paz, J Ventura, PP Freitas, S Blügel, Y Mokrousov, Th Rasing, *et al. Femtosecond control of electric currents in metallic ferromagnetic heterostructures*. Nature nanotechnology **11** (5), 455–458 (2016). Cited on page/s 48.
[103] Giovanni Pizzi, Valerio Vitale, Ryotaro Arita, Stefan Blügel, Frank Freimuth, Guillaume Géranton, Marco Gibertini, Dominik Gresch, Charles Johnson, Takashi Koretsune, *et al. Wannier90 as a community code: new features and applications*. Journal of Physics: Condensed Matter **32** (16), 165902 (2020). Cited on page/s 51, 62, 64, 68, 76, 88, 104, A-4.
[104] M Born and R Oppenheimer. *Ann. Physik*. (1927). Cited on page/s 52.
[105] Walter Kohn. *Nobel Lecture: Electronic structure of matter—wave functions and density functionals*. Reviews of Modern Physics **71** (5), 1253 (1999). Cited on page/s 52.
[106] Douglas R Hartree. *The wave mechanics of an atom with a non-Coulomb central field. Part I. Theory and methods*. **24** (1), 89–110 (1928). Cited on page/s 53, 55.
[107] Pierre Hohenberg and Walter Kohn. *Inhomogeneous electron gas*. Physical review **136** (3B), B864 (1964). Cited on page/s 53.
[108] Mel Levy. *Universal variational functionals of electron densities, first-order density matrices, and natural spin-orbitals and solution of the v-representability problem*. Proceedings of the National Academy of Sciences **76** (12), 6062–6065 (1979). Cited on page/s 54.
[109] Mel Levy. *Electron densities in search of Hamiltonians*. Physical Review A **26** (3), 1200 (1982). Cited on page/s 54.
[110] Richard M Martin. *Electronic structure: basic theory and practical methods*. Cambridge university press (2020). Cited on page/s 54.
[111] W. Kohn and L. J. Sham. *Self-Consistent Equations Including Exchange and Correlation Effects*. Phys. Rev. **140**, A1133–A1138 (1965). Cited on page/s 54, 55, 58.
[112] Ph Kurz, F Förster, Lars Nordström, Gustav Bihlmayer, and Stefan Blügel. *Ab initio treatment of noncollinear magnets with the full-potential linearized augmented plane wave method*. Physical Review B **69** (2), 024415 (2004). Cited on page/s 56.
[113] David M Ceperley and Berni J Alder. *Ground state of the electron gas by a stochastic method*. Physical review letters **45** (7), 566 (1980). Cited on page/s 58.
[114] Seymour H Vosko, Leslie Wilk, and Marwan Nusair. *Accurate spin-dependent electron liquid correlation energies for local spin density calculations: a critical analysis*. Canadian Journal of physics **58** (8), 1200–1211 (1980). Cited on page/s 58.
[115] John P Perdew and Alex Zunger. *Self-interaction correction to density-functional approximations for many-electron systems*. Physical Review B **23** (10), 5048 (1981). Cited on page/s 58.
[116] John P Perdew and Yue Wang. *Accurate and simple analytic representation of the electron-gas correlation energy*. Physical review B **45** (23), 13244 (1992). Cited on page/s 58.
[117] A Van de Walle and G Ceder. *Correcting overbinding in local-density-approximation calculations*. Physical Review B **59** (23), 14992 (1999). Cited on page/s 58.
[118] John P. Perdew, Robert G. Parr, Mel Levy, and Jose L. Balduz. *Density-Functional Theory for Fractional Particle Number: Derivative Discontinuities of the Energy*. Physical Review Letters **49**, 1691–1694 (1982). Cited on page/s 58.
[119] R. O. Jones and O. Gunnarsson. *The density functional formalism, its applications and prospects*. Rev. Mod. Phys. **61**, 689–746 (1989). Cited on page/s 58.

[120] Fabien Tran and Peter Blaha. *Accurate band gaps of semiconductors and insulators with a semilocal exchange-correlation potential*. Physical review letters **102** (22), 226401 (2009). Cited on page/s 58.

[121] J. A. Camargo-Martínez and R. Baquero. *Performance of the modified Becke-Johnson potential for semiconductors*. Physical Review B **86**, 195106 (2012). Cited on page/s 58.

[122] B L Gyorffy, A J Pindor, J Staunton, G M Stocks, and H Winter. *A first-principles theory of ferromagnetic phase transitions in metals*. Journal of Physics F: Metal Physics **15** (6), 1337 (1985). Cited on page/s 58.

[123] C. S. Wang, B. M. Klein, and H. Krakauer. *Theory of Magnetic and Structural Ordering in Iron*. Physical Review Letters **54**, 1852–1855 (1985). Cited on page/s 58.

[124] P.H. Dederichs, R. Zeller, H. Akai, and H. Ebert. *Ab-initio calculations of the electronic structure of impurities and alloys of ferromagnetic transition metals*. Journal of Magnetism and Magnetic Materials **100** (1), 241–260 (1991). ISSN 0304-8853. Cited on page/s 58.

[125] M. M. Steiner, R. C. Albers, and L. J. Sham. *Quasiparticle properties of Fe, Co, and Ni*. Physical Review B **45**, 13272–13284 (1992). Cited on page/s 58.

[126] MI Katsnelson and AI Lichtenstein. *LDA++ approach to the electronic structure of magnets: correlation effects in iron*. Journal of Physics: Condensed Matter **11** (4), 1037 (1999). Cited on page/s 58.

[127] John P Perdew. *Accurate density functional for the energy: Real-space cutoff of the gradient expansion for the exchange hole*. Physical Review Letters **55** (16), 1665 (1985). Cited on page/s 59.

[128] John P Perdew and Wang Yue. *Accurate and simple density functional for the electronic exchange energy: Generalized gradient approximation*. Physical review B **33** (12), 8800 (1986). Cited on page/s 59.

[129] John P Perdew, Kieron Burke, and Matthias Ernzerhof. *Generalized gradient approximation made simple*. Physical review letters 77 (18), 3865 (1996). Cited on page/s 59.

[130] Viktor N. Staroverov, Gustavo E. Scuseria, Jianmin Tao, and John P. Perdew. *Tests of a ladder of density functionals for bulk solids and surfaces*. Physical Review B **69**, 075102 (2004). Cited on page/s 59.

[131] N. Moll, M. Bockstedte, M. Fuchs, E. Pehlke, and M. Scheffler. *Application of generalized gradient approximations: The diamond–$\beta$-tin phase transition in Si and Ge*. Physical Review B **52**, 2550–2556 (1995). Cited on page/s 59.

[132] S Tinte, MG Stachiotti, CO Rodriguez, DL Novikov, and NE Christensen. *Applications of the generalized gradient approximation to ferroelectric perovskites*. Physical Review B **58** (18), 11959 (1998). Cited on page/s 59.

[133] Stefan Kurth, John P Perdew, and Peter Blaha. *Molecular and solid-state tests of density functional approximations: LSD, GGAs, and meta-GGAs*. International journal of quantum chemistry **75** (4-5), 889–909 (1999). Cited on page/s 59.

[134] Aleš Zupan, Peter Blaha, Karlheinz Schwarz, and John P Perdew. *Pressure-induced phase transitions in solid Si, SiO 2, and Fe: Performance of local-spin-density and generalized-gradient-approximation density functionals*. Physical Review B **58** (17), 11266 (1998). Cited on page/s 59.

[135] M. Asato, A. Settels, T. Hoshino, T. Asada, S. Blügel, R. Zeller, and P. H. Dederichs. *Full-potential KKR calculations for metals and semiconductors*. Physical Review B **60**, 5202–5210 (1999). Cited on page/s 59.

[136] Stefan Blügel and Gustav Bihlmayer. *Full-potential linearized augmented planewave method*. Computational Nanoscience: Do It Yourself! **31**, 85–129 (2006). Cited on page/s 59, 61, 62.

[137] Felix Bloch. *Über die quantenmechanik der elektronen in kristallgittern*. Zeitschrift für

physik **52** (7-8), 555–600 (1929). Cited on page/s 60.

[138] Charles Kittel and Paul McEuen. *Introduction to solid state physics*. John Wiley & Sons (2018). Cited on page/s 60.

[139] *https://upload.wikimedia.org/wikipedia/commons/thumb/0/07/Cupcake-tin.jpg/1280px-Cupcake-tin.jpg* (2010). Cited on page/s 60.

[140] Eva Prinz, Benjamin Stadtmüller, and Martin Aeschlimann. *Twisted light affects ultrafast demagnetization*. arXiv preprint arXiv:2206.07502 (2022). Cited on page/s 62.

[141] F. Freimuth, Y. Mokrousov, D. Wortmann, S. Heinze, and S. Blügel. *Maximally localized Wannier functions within the FLAPW formalism*. Physical Review B **78**, 035120 (2008). Cited on page/s 62, 64, 65, 67, 68, 70, 76.

[142] Xinjie Wang, Jonathan R Yates, Ivo Souza, and David Vanderbilt. *Ab initio calculation of the anomalous Hall conductivity by Wannier interpolation*. Physical Review B **74** (19), 195118 (2006). Cited on page/s 63, 64, 72, 73, 74, 80.

[143] Nicola Marzari and David Vanderbilt. *Maximally localized generalized Wannier functions for composite energy bands*. Physical Review B **56**, 12847–12865 (1997). Cited on page/s 64, 65, 66, 68, 69.

[144] Ivo Souza, Nicola Marzari, and David Vanderbilt. *Maximally localized Wannier functions for entangled energy bands*. Physical Review B **65**, 035109 (2001). Cited on page/s 64, 65, 66, 68, 69, 70, 71.

[145] Gregory H Wannier. *The structure of electronic excitation levels in insulating crystals*. Physical Review **52** (3), 191 (1937). Cited on page/s 64.

[146] E. Anderson, Z. Bai, C. Bischof, S. Blackford, J. Demmel, J. Dongarra, J. Du Croz, A. Greenbaum, S. Hammarling, A. McKenney, and D. Sorensen. *LAPACK Users' Guide*. Society for Industrial and Applied Mathematics Philadelphia, PA third edition (1999). ISBN 0-89871-447-8 (paperback). Cited on page/s 65, A-1.

[147] EI Blount. *Formalisms of band theory*. In *Solid state physics* volume 13 pages 305–373. Elsevier (1962). Cited on page/s 67.

[148] Giovanni Pizzi. *Wannier90 as a community code new features and applications*. Journal of Physics: Condensed Matter **32** (16), 165902 (2020). Cited on page/s 68, 76.

[149] Per-Olov Löwdin. *On the non-orthogonality problem connected with the use of atomic wave functions in the theory of molecules and crystals*. The Journal of Chemical Physics **18** (3), 365–375 (1950). Cited on page/s 70.

[150] Éric Cancès, Antoine Levitt, Gianluca Panati, and Gabriel Stoltz. *Robust determination of maximally localized Wannier functions*. Physical Review B **95** (7), 075114 (2017). Cited on page/s 71.

[151] Hendrik J Monkhorst and James D Pack. *Special points for Brillouin-zone integrations*. Physical review B **13** (12), 5188 (1976). Cited on page/s 76.

[152] Charles R. Harris, *et al. Array programming with NumPy*. Nature **585** (7825), 357–362 (2020). Cited on page/s 78.

[153] *NPY-for-Fortran*. https://github.com/MRedies/NPY-for-Fortran (2017). Cited on page/s 78.

[154] J. D. Hunter. *Matplotlib: A 2D graphics environment*. Computing in Science & Engineering **9** (3), 90–95 (2007). Cited on page/s 78.

[155] Maximilian Daniel Merte. *Microscopic theory of magneto-electric polarization in solids*. *Master's thesis*. RWTH Aachen University (2018). Cited on page/s 78.

[156] Yang Gao, Shengyuan A Yang, and Qian Niu. *Field induced positional shift of Bloch electrons and its dynamical implications*. Physical review letters **112** (16), 166601 (2014). Cited on page/s 78.

[157] Di Xiao, Ming-Che Chang, and Qian Niu. *Berry phase effects on electronic properties*.

Reviews of modern physics **82** (3), 1959 (2010). Cited on page/s 78.

[158] Andrei Kirilyuk, Alexey V. Kimel, and Theo Rasing. *Ultrafast optical manipulation of magnetic order*. Rev. Mod. Phys. **82**, 2731–2784 (2010). Cited on page/s 79.

[159] Wanxiang Feng, Jan-Philipp Hanke, Xiaodong Zhou, Guang-Yu Guo, Stefan Blügel, Yuriy Mokrousov, and Yugui Yao. *Topological magneto-optical effects and their quantization in noncoplanar antiferromagnets*. Nature communications **11** (1), 1–9 (2020). Cited on page/s 79, 158.

[160] D. Côté, N. Laman, and H. M. van Driel. *Rectification and shift currents in GaAs*. Applied Physics Letters **80** (6), 905–907 (2002). ISSN 0003-6951. Cited on page/s 87.

[161] M Bieler, K Pierz, and U Siegner. *Simultaneous generation of shift and injection currents in (110)-grown GaAs/ AlGaAs quantum wells*. Journal of applied physics **100** (8) (2006). Cited on page/s 87.

[162] Reinold Podzimski, Huynh Thanh Duc, and Torsten Meier. *Anisotropic excitons and their contributions to shift current transients in bulk GaAs*. Physical Review B **96**, 205201 (2017). Cited on page/s 87.

[163] F. Nastos and J. E. Sipe. *Optical rectification and shift currents in GaAs and GaP response: Below and above the band gap*. Physical Review B **74**, 035201 (2006). Cited on page/s 87.

[164] Valeriy Yu Verchenko, Alexander A Tsirlin, Alexei V Sobolev, Igor A Presniakov, and Andrei V Shevelkov. *Ferromagnetic order, strong magnetocrystalline anisotropy, and magnetocaloric effect in the layered telluride Fe3- δGeTe2*. Inorganic chemistry **54** (17), 8598–8607 (2015). Cited on page/s 93.

[165] Bei Ding, Zefang Li, Guizhou Xu, Hang Li, Zhipeng Hou, Enke Liu, Xuekui Xi, Feng Xu, Yuan Yao, and Wenhong Wang. *Observation of Magnetic Skyrmion Bubbles in a van der Waals Ferromagnet Fe3GeTe2*. Nano Letters **20** (2), 868–873 (2020). Cited on page/s 93.

[166] Yingying Wu, Senfu Zhang, Junwei Zhang, Wei Wang, Yang Lin Zhu, Jin Hu, Gen Yin, Kin Wong, Chi Fang, Caihua Wan, Xiufeng Han, Qiming Shao, Takashi Taniguchi, Kenji Watanabe, Jiadong Zang, Zhiqiang Mao, Xixiang Zhang, and Kang L. Wang. *Néel-type skyrmion in WTe2/Fe3GeTe2 van der Waals heterostructure*. Nature Communications **11** (1), 3860 (2020). ISSN 2041-1723. Cited on page/s 93.

[167] Tae-Eon Park, *et al. Néel-type skyrmions and their current-induced motion in van der Waals ferromagnet-based heterostructures*. Physical Review B **103**, 104410 (2021). Cited on page/s 93.

[168] Øyvind Johansen, Vetle Risinggård, Asle Sudbø, Jacob Linder, and Arne Brataas. *Current Control of Magnetism in Two-Dimensional* $Fe_3GeTe_2$. Physical Review Letters **122**, 217203 (2019). Cited on page/s 94.

[169] Tom G Saunderson, Dongwook Go, Stefan Blügel, Mathias Kläui, and Yuriy Mokrousov. *Hidden interplay of current-induced spin and orbital torques in bulk Fe 3 GeTe 2*. Physical Review Research **4** (4), L042022 (2022). Cited on page/s 94.

[170] Chong Wang, Xiaoyu Liu, Lei Kang, Bing-Lin Gu, Yong Xu, and Wenhui Duan. *First-principles calculation of nonlinear optical responses by Wannier interpolation*. Physical Review B **96**, 115147 (2017). Cited on page/s 98.

[171] S Abe, M Matsumoto, T Kaneko, H Yoshida, H Morita, and T Kanomata. *Magnetic properties of ordered alloy AuMn2*. Journal of magnetism and magnetic materials **140**, 103–104 (1995). Cited on page/s 103.

[172] Sergii Khmelevskyi and Peter Mohn. *Layered antiferromagnetism with high Neel temperature in the intermetallic compound Mn 2 Au*. Applied Physics Letters **93** (16), 162503 (2008). Cited on page/s 103, 104.

[173] VMTS Barthem, CV Colin, H Mayaffre, M-H Julien, and Dominique Givord. *Revealing the properties of Mn2Au for antiferromagnetic spintronics*. Nature communications **4** (1),

1–7 (2013). Cited on page/s 103.

[174] P Wells and JH Smith. *The structure of Mn2Au and Mn3Au*. Acta Crystallographica Section A: Crystal Physics, Diffraction, Theoretical and General Crystallography **26** (3), 379–381 (1970). Cited on page/s 103, 104.

[175] J. Železný, H. Gao, K. Výborný, J. Zemen, J. Mašek, Aurélien Manchon, J. Wunderlich, Jairo Sinova, and T. Jungwirth. *Relativistic Néel-Order Fields Induced by Electrical Current in Antiferromagnets*. Physical Review Letters **113**, 157201 (2014). Cited on page/s 103.

[176] S Yu Bodnar, Libor Šmejkal, I Turek, T Jungwirth, Olena Gomonay, Jairo Sinova, AA Sapozhnik, H-J Elmers, Mathias Kläui, and Martin Jourdan. *Writing and reading antiferromagnetic Mn2Au by Néel spin-orbit torques and large anisotropic magnetoresistance*. Nature communications **9** (1), 1–7 (2018). Cited on page/s 103, 123.

[177] Markus Meinert, Dominik Graulich, and Tristan Matalla-Wagner. *Electrical Switching of Antiferromagnetic* $Mn_2Au$ *and the Role of Thermal Activation*. Phys. Rev. Applied **9**, 064040 (2018). Cited on page/s 103.

[178] Vladimir Grigorev, Mariia Filianina, Stanislav Yu. Bodnar, Sergei Sobolev, Nilabha Bhattacharjee, Satya Bommanaboyena, Yaryna Lytvynenko, Yurii Skourski, Dirk Fuchs, Mathias Kläui, Martin Jourdan, and Jure Demsar. *Optical Readout of the Néel Vector in the Metallic Antiferromagnet* $Mn_2Au$. Phys. Rev. Appl. **16**, 014037 (2021). Cited on page/s 103.

[179] Vladimir Grigorev, Mariia Filianina, Yaryna Lytvynenko, Sergei Sobolev, Amrit Raj Pokharel, Amon P Lanz, Alexey Sapozhnik, Armin Kleibert, Stanislav Bodnar, Petr Grigorev, *et al. Optically Triggered Néel Vector Manipulation of a Metallic Antiferromagnet Mn2Au under Strain*. ACS nano **16** (12), 20589–20597 (2022). Cited on page/s 103.

[180] John P. Perdew, Kieron Burke, and Matthias Ernzerhof. *Generalized Gradient Approximation Made Simple*. Physical Review Letters 77, 3865–3868 (1996). Cited on page/s 104.

[181] Hendrik Antoon Kramers. *Théorie générale de la rotation paramagnétique dans les cristaux*. Proc. Acad. Amst **33** (6) (1930). Cited on page/s 106.

[182] C Herring. *Magnetism, Vol. IV, edited by GT Rado and H. Suhl* (1966). Cited on page/s 106.

[183] Hua Wang and Xiaofeng Qian. *Electrically and magnetically switchable nonlinear photcurrent in PT-symmetric magnetic topological quantum materials*. NPJ Computational Materials **6** (1), 1–8 (2020). Cited on page/s 106, 117.

[184] Libor Šmejkal, Jakub Železnỳ, Jairo Sinova, and Tomáš Jungwirth. *Electric control of Dirac quasiparticles by spin-orbit torque in an antiferromagnet*. Physical review letters **118** (10), 106402 (2017). Cited on page/s 106.

[185] Vladimir Grigorev, Mariia Filianina, Stanislav Yu Bodnar, Sergei Sobolev, Nilabha Bhattacharjee, Satya Bommanaboyena, Yaryna Lytvynenko, Yurii Skourski, Dirk Fuchs, Mathias Kläui, *et al. Optical Readout of the Néel Vector in the Metallic Antiferromagnet Mn 2 Au*. Physical Review Applied **16** (1), 014037 (2021). Cited on page/s 106.

[186] Vitoria MTS Barthem, Claire V Colin, Richard Haettel, Didier Dufeu, and Dominique Givord. *Easy moment direction and antiferromagnetic domain wall motion in Mn2Au*. Journal of Magnetism and Magnetic Materials **406**, 289–292 (2016). Cited on page/s 109.

[187] Pauli Virtanen, *et al. SciPy 1.0: Fundamental Algorithms for Scientific Computing in Python*. Nature Methods **17**, 261–272 (2020). Cited on page/s 118.

[188] Tobias Dannegger, Marco Berritta, Karel Carva, Severin Selzer, Ulrike Ritzmann, Peter M Oppeneer, and Ulrich Nowak. *Ultrafast coherent all-optical switching of an antiferromagnet with the inverse Faraday effect*. Physical Review B **104** (6), L060413 (2021). Cited on page/s 119.

[189] Frank Freimuth, Stefan Blügel, and Yuriy Mokrousov. *Laser-induced torques in metallic antiferromagnets*. Physical Review B **103** (17), 174429 (2021). Cited on page/s 121.

[190] J. Železný, H. Gao, K. Výborný, J. Zemen, J. Mašek, Aurélien Manchon, J. Wunderlich, Jairo Sinova, and T. Jungwirth. *Relativistic Néel-Order Fields Induced by Electrical Current in Antiferromagnets*. Physical Review Letters **113**, 157201 (2014). Cited on page/s 122, 123.

[191] Peter Wadley, Bryn Howells, Jakub Zelezny, Carl Andrews, Victoria Hills, Richard P. Campion, Vit Novak, Frank Freimuth, Yuriy Mokrousov, Andrew W. Rushforth, Kevin W. Edmonds, Bryan L. Gallagher, and Tomas Jungwirth. *Electrical switching of an antiferromagnet*. (2015). Cited on page/s 123.

[192] Qiming Shao, Peng Li, Luqiao Liu, Hyunsoo Yang, Shunsuke Fukami, Armin Razavi, Hao Wu, Kang Wang, Frank Freimuth, Yuriy Mokrousov, Mark D. Stiles, Satoru Emori, Axel Hoffmann, Johan Åkerman, Kaushik Roy, Jian-Ping Wang, See-Hun Yang, Kevin Garello, and Wei Zhang. *Roadmap of Spin–Orbit Torques*. IEEE Transactions on Magnetics **57** (7), 1–39 (2021). Cited on page/s 123.

[193] Markus Weißenhofer, Francesco Foggetti, Ulrich Nowak, and Peter M. Oppeneer. *Néel-Vector Switching and THz Spin-Wave Excitation in $Mn_2Au$ due to Femtosecond Spin-Transfer Torques* (2023). Cited on page/s 123.

[194] J. Wunderlich, B. Kaestner, J. Sinova, and T. Jungwirth. *Experimental Observation of the Spin-Hall Effect in a Two-Dimensional Spin-Orbit Coupled Semiconductor System*. Physical Review Letters **94**, 047204 (2005). Cited on page/s 125.

[195] V. Sih, W. H. Lau, R. C. Myers, V. R. Horowitz, A. C. Gossard, and D. D. Awschalom. *Generating Spin Currents in Semiconductors with the Spin Hall Effect*. Physical Review Letters **97**, 096605 (2006). Cited on page/s 125.

[196] Jonas Wätzel and Jamal Berakdar. *All-optical generation and ultrafast tuning of non-linear spin Hall current*. Scientific reports **8** (1), 1–11 (2018). Cited on page/s 125.

[197] Frank Freimuth, Stefan Blügel, and Yuriy Mokrousov. *Anisotropic spin Hall effect from first principles*. Physical review letters **105** (24), 246602 (2010). Cited on page/s 130.

[198] Xianzhe Chen, Shuyuan Shi, Guoyi Shi, Xiaolong Fan, Cheng Song, Xiaofeng Zhou, Hua Bai, Liyang Liao, Yongjian Zhou, Hanwen Zhang, *et al. Observation of the antiferromagnetic spin Hall effect*. Nature Materials **20** (6), 800–804 (2021). Cited on page/s 130.

[199] Sergey D Ganichev, EL Ivchenko, VV Bel'Kov, SA Tarasenko, M Sollinger, Dieter Weiss, Werner Wegscheider, and Wilhelm Prettl. *Spin-galvanic effect*. Nature **417** (6885), 153–156 (2002). Cited on page/s 131, 153.

[200] Ka Shen, Giovanni Vignale, and Roberto Raimondi. *Microscopic theory of the inverse Edelstein effect*. Physical review letters **112** (9), 096601 (2014). Cited on page/s 131.

[201] Frank Freimuth, Stefan Blügel, and Yuriy Mokrousov. *Charge pumping driven by the laser-induced dynamics of the exchange splitting*. Physical Review B **95**, 094434 (2017). Cited on page/s 131.

[202] B Andrei Bernevig, Taylor L Hughes, and Shou-Cheng Zhang. *Orbitronics: The intrinsic orbital current in p-doped silicon*. Physical review letters **95** (6), 066601 (2005). Cited on page/s 134.

[203] Dongwook Go, Daegeun Jo, Hyun-Woo Lee, Mathias Kläui, and Yuriy Mokrousov. *Orbitronics: Orbital currents in solids*. Europhysics Letters **135** (3), 37001 (2021). Cited on page/s 134, 157.

[204] T Adamantopoulos, M Merte, D Go, F Freimuth, S Blügel, and Y Mokrousov. *Orbital Rashba effect as a platform for robust orbital photocurrents*. arXiv preprint arXiv:2303.04546 (2023). Cited on page/s 134, 157.

[205] Hiroki Hayashi and Kazuya Ando. *Observation of orbital pumping*. arXiv preprint arXiv:2304.05266 (2023). Cited on page/s 134.

[206] Libor Šmejkal, Rafael González-Hernández, Tomáš Jungwirth, and Jairo Sinova. *Crystal*

*time-reversal symmetry breaking and spontaneous Hall effect in collinear antiferromagnets*. Science advances **6** (23), eaaz8809 (2020). Cited on page/s 141.

[207] A Markou, JM Taylor, A Kalache, P Werner, SSP Parkin, and C Felser. *Noncollinear antiferromagnetic mn 3 sn films*. Physical Review Materials **2** (5), 051001 (2018). Cited on page/s 157.

[208] Seng Huat Lee, Yanglin Zhu, Yu Wang, Leixin Miao, Timothy Pillsbury, Hemian Yi, Susan Kempinger, Jin Hu, Colin A Heikes, Patrick Quarterman, *et al. Spin scattering and noncollinear spin structure-induced intrinsic anomalous Hall effect in antiferromagnetic topological insulator MnB i 2 T e 4*. Physical Review Research **1** (1), 012011 (2019). Cited on page/s 157.

[209] Weifeng Zhang, Wei Han, See-Hun Yang, Yan Sun, Yang Zhang, Binghai Yan, and Stuart S. P. Parkin. *Giant facet-dependent spin-orbit torque and spin Hall conductivity in the triangular antiferromagnet $IrMn_3$*. Science Advances **2** (9), e1600759 (2016). Cited on page/s 157.

[210] Jan-Philipp Hanke, Frank Freimuth, Stefan Blügel, and Yuriy Mokrousov. *Prototypical topological orbital ferromagnet γ-FeMn*. Scientific reports 7 (1), 41078 (2017). Cited on page/s 158.

[211] Nikhil Sivadas, Satoshi Okamoto, and Di Xiao. *Gate-controllable magneto-optic Kerr effect in layered collinear antiferromagnets*. Physical Review Letters **117** (26), 267203 (2016). Cited on page/s 158, 159.

[212] John Nickolls, Ian Buck, Michael Garland, and Kevin Skadron. *Scalable parallel programming with cuda: Is cuda the parallel programming model that application developers have been waiting for?* Queue **6** (2), 40–53 (2008). Cited on page/s 163.

[213] *Intro to GPU Programming with the OpenMP API*. https://www.openmp.org/wp-content/uploads/2021-10-20-Webinar-OpenMP-Offload-Programming-Introduction.pdf (2021). Cited on page/s 163.

[214] *ju_wip gitlab*. Cited on page/s A-1.

[215] L Susan Blackford, Antoine Petitet, Roldan Pozo, Karin Remington, R Clint Whaley, James Demmel, Jack Dongarra, Iain Duff, Sven Hammarling, Greg Henry, *et al. An updated set of basic linear algebra subprograms (BLAS)*. ACM Transactions on Mathematical Software **28** (2), 135–151 (2002). Cited on page/s A-1.

[216] *Intel MKL*. https://www.intel.com/content/www/us/en/developer/articles/release-notes/onemkl-release-notes.html (2003). Cited on page/s A-1.

[217] Dorian Krause and Philipp Thörnig. *JURECA: general-purpose supercomputer at Jülich supercomputing centre*. Journal of large-scale research facilities JLSRF **2**, A62–A62 (2016). Cited on page/s A-1.

[218] *config_fortran*. https://github.com/jannisteunissen/config_fortran.git (2016). Cited on page/s A-2.

[219] *CLAIX-2018-MPI*. https://help.itc.rwth-aachen.de/en/service/rhr4fjjutttf/article/fbd107191cf14c4b8307f44f545cf68a/ (2018). Cited on page/s A-13.

Part VI

# Appendix

# *Dissemination of research*

## Publications in peer reviewed journals

[1] **Maximilian Merte**, Frank Freimuth, Theodoros Adamantopoulos, Dongwook Go, Tom G. Saunderson, Matthias Kläui, Lukasz Plucinski, Olena Gomonay, Stefan Blügel, and Yuriy Mokrousov. Photocurrents of charge and spin in single-layer $Fe_3GeTe_2$. *Physical Review B* **104**, L220405 (2021) [Maximilian Merte: Conceptualization, Software, Investigation, Visualization, Writing - Original Draft].

[2] **Maximilian Merte**, Frank Freimuth, Dongwook Go, Theodoros Adamantopoulos, Fabian R. Lux, Lukasz Plucinski, Olena Gomonay, Stefan Blügel, and Yuriy Mokrousov. Photocurrents, inverse Faraday effect, and photospin Hall effect in $Mn_2Au$. *APL Materials* **11**, 071106 (2023) [Maximilian Merte: Conceptualization, Software, Investigation, Visualization, Writing - Original Draft].

[3] Kartik Samanta, Marjana Ležaić, **Maximilian Merte**, Frank Freimuth, Stefan Blügel, Yuriy Mokrousov. Crystal Hall and crystal magneto-optical effect in thin films of $SrRuO_3$. *Journal of Applied Physics* **127**, 213904 (2020) [Maximilian Merte: Software, Investigation, Visualization].

[4] Jonathan Kipp, Kartik Samanta, Fabian R. Lux, **Maximilian Merte**, Dongwook Go, Jan-Philipp Hanke, Matthias Redies, Frank Freimuth, Stefan Blüegel, Marjana Ležaić, Yuriy Mokrousov. The chiral Hall effect in canted ferromagnets and antiferromagnets. *Communications Physics* **4**, 99 (2021) [Maximilian Merte: Software, Investigation, Visualization].

[5] Theodoros Adamantopoulos, **Maximilian Merte**, Dongwook Go, Frank Freimuth, Stefan Blügel, Yuriy Mokrousov. Laser-induced charge and spin photocurrents at $BiAg_2$ surface: a first principles benchmark. *Physical Review Research* **4**, 043046 (2022) [Maximilian Merte: Software].

### Manuscript under review

[1] Theodoros Adamantopoulos, **Maximilian Merte**, Dongwook Go, Frank Freimuth, Stefan Blügel, and Yuriy Mokrousov. Orbital Rashba effect as a platform for robust orbital photocurrents. arXiv:2303.04578v1 (2023) [Maximilian Merte: Software].

## Conference participation (presentations)

[1] **Maximilian Merte**†, Frank Freimuth, Stefan Blügel, Yuriy Mokrousov. *Magnetoelectric Polarizability in Magnetic Insulators*. Poster presentation at 9th Joint European Magnetic Symposia Conference, Mainz, Germany, September 03-07 2018.

[2] **Maximilian Merte**. workshop participation at Quantum many-body methods in condensed matter systems, Jüelich, Germany, September 24-27 2018.

[3] **Maximilian Merte**. workshop participation at SPICE-Workshop Ultrafast Spintronics: from Fundamentals to Technology, Mainz, Germany, October 23-26 2018.

[4] **Maximilian Merte**†, Frank Freimuth, Stefan Blügel, Yuriy Mokrousov. *Magnetoelectric Polarizability In Magnetic Insulators*. Contributed talk at Deutsche Physikalische Gesellschaft e.V. DGP-Früjahrstagung, Regensburg, Germany, March 31-April 5 2019.

[5] **Maximilian Merte**†. retreat participation at *Scientific Group Retreat.*Quantum Theory of Materials (PGI-1/IAS-1), Marienburg, Germany, August 5 - 9 2019

[6] **Maximilian Merte**†, Jan-Philipp Hanke, Frank Freimuth, Stefan Blügel, Yuriy Mokrousov. *Towards proper non-linear photocurrents in antiferromagnets*. Poster presentation at SPICE-workshop Antiferromagnetic Spintronics: from topology to neuromorphic computing, Mainz, Germany, October 7-10 2019.

[7] **Maximilian Merte**†, Frank Freimuth, Theodoros Adamantopoulos, Dongwook Go, Tom G. Saunderson, Mathias Kläui, Lukasz Plucinski, Olena Gomonay, Stefan Blügel and Yuriy Mokrousov. *Photocurrents in single-layer $Fe_3GeTe_2$ from first principles*. Contributed talk at Deutsche Physikalische Gesellschaft e.V. virtual 84. Annual Meeting of DPG and DPG-Tagung (DPG Meeting) of the Condensed Matter Section (SKM), virtual, September 27 - October 1 2021.

[8] **Maximilian Merte**†, Frank Freimuth, Theodoros Adamantopoulos, Dongwook Go, Tom G. Saunderson, Mathias Kläui, Lukasz Plucinski, Olena Gomonay, Stefan Blügel and Yuriy Mokrousov. *Photocurrents of charge and spin in single-layer Fe3GeTe2.* Poster presentation at 757. WE-Heraeus-Seminar Non-Linear Magnetism, Bad Honnef, Germany, January 5-7 2022.

Name of the author with † indicates the presenter. All posters and talks are available in PDF format upon request.

# Appendix A

# *ju_wip details*

## A.1 Compiling

The *ju_wip* code is available upon invitation on the IFF gitlab[214] and can be compiled on most *nix operating systems, including but not limited to Arch Linux, macOS, CentosOS7 and RockyOS. The code requires a lapack[146] and blas[215] library to be present or alternatively Intels MKL backend of these libraries[216]. The presence of a MPI library is not required but strongly recommended, however, users are encouraged to build the code also on there local machines, ie. for calculating small (model) systems, were a MPI-library might no be available. To download and build a code on the Jureca DC cluster the following steps have to be performed

```
git clone https://iffgit.fz-juelich.de/merte/ju_wip --recurse-submodules
cd ju_wip
mkdir build
cd build
#

module load CMake Intel imkl
module load IntelMPI
# or use module load ParastationMPI
#
export FC=mpiifort
# in case of parastationMPI export mpif90 compiler instead
cmake ..
make
cd bin
ls ju_wip
```

By setting the environment variable *FC* the user can tell `CMake` the desired fortran compiler which will be used during compilation. In case of gfortran and Intel ifort the compilation is then completely automatic thanks to CMake. In case of using $gfortran$ the code requies the presence of Lapack and Blas libraries. For usage on cluster systems such as the Jureca cluster[217] the usage of the Intel fortran compiler $ifort$ or on of its mpi wrappers like $mpiifort$

or *mpif90* is recommended. With the Intel compiler the IntelMKL backend is used for Lapack and Blas calls. The *ju_wip* code uses CMake to allow for an easy, mostly automated, compilation of the code. The code can be compiled without MPI as a pure OpenMP parallel code, which can be usefull on laptops or desktop computer were a MPI implementation might not be available.

## A.2 INPUT FILE

The *ju_wip* requires a input file named input.cfg, formatted in the configuration file format, to be present in the root folder of the calculation. Further the real space basis set exported by Wannier90 has to be provided in a subfolder `./w90files`. A open source library publicly available on github was used to read in the .cfg file[218]. A full input file looks like

```
# input file for TB model from New J Physics 12, 053032 (2010)
# generated on 11:48AM on February 04, 2019

[jobs]
    plot_bands=F
    debug_mode=F
    do_write_velo=F
    do_velo_int=F
    do_mep=False
    do_kubo=False
    do_ahc=f
    do_opt=False
    do_gyro=False
    do_keldysh=t
    do_photoC=f
    do_bcd_photo=f

[unitCell]
    a1= 6.29089827960000 0.0 0.0
    a2= 0.0  6.29089827960000   0.0
    a3= 3.14544913980000 3.14544913980000 8.07102024030000
    a0= 1.0 #0.529177 #1.0




[wannBase]
    seed_name=WF1
    force_hr_file=f
    N_at_centers=3
    N_wf=0
    at_centers_x=.33 -.33 .0
    at_centers_y=.33  .33 .0
    at_centers_z=.33 -.33 .0

[wannInterp]
    use_cart_velo=T
    doGaugeTrafo=T
    do_wip_velo=F
    do_wip_conn=F
    do_wip_pauli=F
    do_wip_anglmom=F
    do_wip_curv=F
    do_wip_sigma=F
    mp_grid= 16 16 16
    do_sciss_shft=F
    sciss_shft=1.15
    num_val_bands=8
    do_adpt_kmesh=F
    adpt_bk_grid= 3 3 3
    adpt_threshold=4.0


```

```
[Keldysh]
    do_kely_resonant=F
    do_kely_epC=F
    do_kely_spC=F
    do_kely_pauliat=F
    do_kely_pauli_pat=T
    do_kely_anglmom=F
    do_kely_resonant=F

[MEP]
    valence_bands= 8
    do_write_mep_bands= True

[Fermi]
    N_eF= 1
    eF_min=  9.3901
    eF_max= 11.3901
    Tkelvin= 00.0
    N_eta_smr=1
    N_eta_smr2=0
    eta_smr_min=0.025
    eta_smr_max=0.400
    eta_smr_max2=1.0
    kuboTol= 1e-15

[Laser]
    N_hw= 6
    hw_min=  0.01
    hw_max=  5.10
```

The input file is divided into 9 sections each containing input parameters controlling a specific part of the calculation. Each section and the input parameters within are briefly discussed here.

### *jobs*

The first section, the *jobs* section, only contains booleans.

```
[jobs]
    plot_bands=False
    debug_mode=F
    do_write_velo=F
    do_velo_int=F
    do_mep=False
    do_ahc=T
    do_keldysh=True
    do_photoC=False
```

`plot_bands` switches on the bandstructure path mode, `debug_mode` makes the codes output more verbose, with `do_write_velo` & `do_velo_int` the Wannier interpolated velocity operator can be written out $k$-point resolved or integrated over all $k$-points respectively. The other variables activate the various response tensors routines, more on the response tensors in Section 6.2.

### *unitCell*

The second section *unitCell* section is used to input the unit cell of the system.

```
[unitCell]
    a1= 6.2 0.0 0.0 # Bohr radii
    a2= 0.0 6.2 0.0 # Bohr radii
    a3= 3.1 3.1 8.1 # Bohr radii
    a0= 0.529177    # universal scaling factor
```

The 3D vectors `a1`, `a2`, `a3` represent the lattice vectors and are expected to be in Bohr radii. `a0` is a scaling factor applied to complete unit cell.

### *wannBase*

The *unitCell* section is used to specify which basis set, written by wannier90 [103], should be read.

```
[wannBase]
    seed_name=WF1
    force_hr_file=f
    N_at_centers=3
    at_centers_x=.33 -.33 .0
    at_centers_y=.33 -.33 .0
    at_centers_z=.33 -.33 .0
```

`seed_name` specifies the name of the real space basis set written out by wannier90 ("$(`seed_name`)_tb.dat", "$(`seed_name`)_hr.dat", "$(`seed_name`)_r.dat", etc.). If "$(`seed_name`)_tb.dat" is present the code will use this file to read Hamiltonian and position operator, however, the Hamiltonian can be overwritten with the Hamiltonian stored in the file "$(`seed_name`)_hr.dat" if the `force_hr_file` flag is set to `True`, allowing the user to manually change the Hamiltonian without changing the position operator. The *ju_wip* code allows to project response tensors onto `N_at_centers` individual atoms, with positions specified by `at_centers_x`, `at_centers_y`, `at_centers_z`.

### *wannInterp*

The second section *unitCell* section is used to input the unit cell of the system.

```
[wannInterp]
    use_cart_velo=True
    doGaugeTrafo=True
    do_wip_velo=False
    do_wip_conn=False
    do_wip_pauli=False
    do_wip_anglmom=False
    do_wip_curv=False
    do_wip_sigma=False
    mp_grid= 272 272 272
```

```
    do_kres_backfold_1stBZ=F
    N_BZ_backfold_levels=2
    do_apply_zeeman=T
    zeeman_field= 0.0 0.0 1.0
    zeeman_strength_eV= 1.0
```

The `do_wip_velo`, `do_wip_conn`, etc. flags allow the user to explicity force the code to interpolate the velocity operator, the connection, etc.. These flags are mostly implemented for debugging purposes and can usually be ignored by the user. The code will automatically interpolate all quantities required to do all tasks defined in the *Jobs* section. `mp_grid` defines the number of Monkhorst Pack mesh points per dimension used in the core mode. Setting `do_kres_backfold_1stBZ` to `True` instructs the code to backfold all Monkhorst Pack grid points and write them into a list which is useful to visualize Brillouin zone resolved quanities. This list can then be read by python plotting script allowing to plot $k$-resolved responses in the 1. Brillouin zone. If `do_kres_backfold_1stBZ` is set `False` the code will simply write out the internal Monkhorst Pack mesh (square box). `N_BZ_backfold_levels` specifies the amount of neighboring cells per dimension to be considered in the backfolding process, the default value is 2 and might have to be increased depending on the geometry of a given system. The final three parameters control the Zeeman field applied to the system as described above in subsection 6.3.4. With `do_apply_zeeman` the application of a Zeeman field is switched on and off, `zeeman_field` is a vector pointing in the direction of the applied field and `zeeman_strength_eV` is the magnetic field strength $B_0$ and for convenience given directly in eV, remembering that with $\mathbf{B} = B_0 \frac{\mathbf{B}}{|\mathbf{B}|}$ one can use

$$\begin{aligned} H_{\text{Zeeman}} &= \mu_0(\mathbf{S}^{(W)} \cdot \mathbf{B}) \\ &= (\mu_0 B_0)(\mathbf{S}^{(W)} \cdot \mathbf{B}/|\mathbf{B}|) \\ &\equiv (\text{zeeman\_strength\_eV})(\mathbf{S}^{(W)} \cdot \mathbf{B}/|\mathbf{B}|). \end{aligned} \tag{1}$$

Note that the code will normalize the field direction `zeeman_field` upon input.

### *MEP*

The section *MEP* is used to control the calculation of the magnetoelectric polarization as described in subsection 6.2.1. With `valence_bands` the number of valence bands assumed for the calculation of the MEP tensor is set by the user.

```
[MEP]
    valence_bands= 8
```

### *Keldysh*

The *Keldysh* section controls the various Kelydsh routines. `do_kely_epC` switches on the charge photocurrent routine, `do_kely_spC` the calculation of spin polarized photocurrents and `do_kely_pauli` the calculation of the nonequilibrium spin density. If at least two of these flags are set to true, the code will enter the "Keldysh God mode" and calculate all 3 responses in one run, preventing the numerical expensive evaluation of the energy integrals within the Keldysh formalism to be evaluated separately for each response tensor, instead in the "Keldysh God mode" the energy integration is performed once and then applied to all tensors.

```
[Keldysh]
    do_kely_resonant=False
    do_kely_epC=True
    do_kely_epC_pat= True
    do_kely_epC_pat_kres=True
    do_kely_epC_kres= False
    do_kely_spC =  True
    do_kely_spC_kres=True
    do_kely_spC_pat=False
    do_kely_spC_pat_kres =True
    do_kely_pauli = True
    do_kely_pauli_kres=True
    do_kely_pauli_pat= True
    do_kely_pauli_pat_kres =True
```

By setting `do_kely_resonant True` the Keldysh routines will calculate only resonant transitions in which the initial and final state are required to be the same, reducing the computational complexity from $\sim O(N_{wf}^3)$ to $\sim O(N_{wf}^2)$, where $N_{wf}$ is the number of Wannier functions. LPGE effects are described by resonant transitions, while CPGE are usually associated with non resonant transitions. In case the user is only interested in calculating LPGE photocurrents setting `do_kely_resonant` might save the user some time. A detailed discussion of resonant transitions can be found in Section 3.8. For each response it also possible to project the response onto individual atomic sites as outlined in subsection 6.3.3. To active the atom-projected routines simply attach `_pat` to the desired input flag, *i.e.* `do_kely_epC_pat`, and specify the number of sites and there position in the *wannInterp* section of the input file (A.2). Attaching `_kres` to a Keldysh input switch will active the $k$-resolved mode as outlined in subsection 6.3.5.

### *Fermi*

The *Fermi* section is used to control the Fermi level and the numerical broadening.

```
[Fermi]
    N_eF= 1
    eF_min=  9.3901 # eV
    eF_max= 11.3901 # eV
    Tkelvin= 00.0   # Kelvin
    N_eta_smr=21
    N_eta_smr2=3
    eta_smr_min=0.010 # eV
    eta_smr_max=0.200 # eV
    eta_smr_max2=0.4  # eV
    kuboTol= 1e-8
```

With `N_eF` the number of Fermi levels can be specified. The code will then set up a evenly spaced (closed) interval of `N_eF` Fermi levels in the interval [`eF_min` ,`eF_max`]. The same can be done for the numerical broadening parameter controlled by `N_eta_smr` which sets up the interval [`eta_smr_min`,`eta_smr_max`]. With `N_eta_smr2` the user can specify a second interval [`eta_smr_max`,`eta_smr_max2` ] of smearing levels which will be automatically knitted together with the first interval by the code, allowing the user to attach a "tail" with larger spacing to reach larger broadening values in the dirty limit. The Fermi levels and the broadening values are given in eV. `Tkelvin` specifies the assumed temperature which enters the AHC tensor, the optical conductivity tensor and the Nagaosa Kubo photocurrent tensor routines via the Fermi distribution. Note that the Keldysh routines assume zero temperature to allow for a analytic evaluation of the energy integrals (see Chapter 3) and are not effected by the `Tkelvin` parameter. However, the effect of finite temperature can still analyzed within the Keldysh routines by considering different broadening values. `kuboTol` is a numerical parameter which should be left untouched.

### *Laser*

Finally in the *Laser* section the user can input the laser frequencies to consider for the calculations of optical conductivity, the Nagaosa Kubo photocurrent routines and the Keldysh routines.

```
[Laser]
    N_hw= 42
    hw_min=  0.10
    hw_max=  4.20
```

`N_hw` specifies the number of frequencies to consider, the code will then setup `N_hw` evenly spaced frequencies in the closed interval [`hw_min`,`hw_max`].

## A.3 SCALING

The chapter is concluded by providing some performance metrics and scaling behavior of the *ju_wip* code. The intend is to highlight the codes ability to perform massively parallel calculations on large cluster systems and guide users in their choice of parallelization scheme to maximize efficiency.

Example jobscript for a job on Jureca DC CPU.

```
#!/bin/bash
#
#
#******** JOB ALLOCATION ************************
#SBATCH -J mn2au_110_spDpat_hw
#SBATCH -A jiff40
#SBATCH -N 1
#SBATCH --ntasks-per-node=4
#SBATCH --cpus-per-task=64
#SBATCH --time=02:00:00
#SBATCH -o log_juWIP-%j.out
#SBATCH -e log_juWIP-%j.err
#SBATCH -p dc-cpu-devel # booster-devel
#SBATCH --mail-user=m.merte@fz-juelich.de
#SBATCH --mail-type=END
################################################
#
#
#EXE_PATH=/p/project/cjiff40/merte1/ju_wip/build_booster/bin
EXE_PATH=/p/project/cjiff40/merte1/ju_wip/dc_cpu_new_pat_build/bin
#
#******** ENV SETUP ****************************8
#module load Architecture/KNL
#wait
#
#module use /usr/local/software/jurecabooster/otherstages/
module load Stages/2022
#wait
#
#ml intel-para imkl
ml Intel  IntelMPI imkl
################################################
#
#
#
#
#**** JOB EXECUTION ***************************
#
# MPI job
export OMP_NUM_THREADS=${SLURM_CPUS_PER_TASK}
srun $EXE_PATH/ju_wip
#
################################################
#
##### FORCE EXIT ################################
wait
exit 0
################################################
```

### A.3.1 *k*-point scaling

Figure A.1 shows the convergence behavior of $Mn_2Au$ spin-photocurrent tensor vs the per dimension $k$-point count. Since the $k$-convergence also heavily dependence on the applied broadening value, convergence curves for multiple broadening values are displayed.

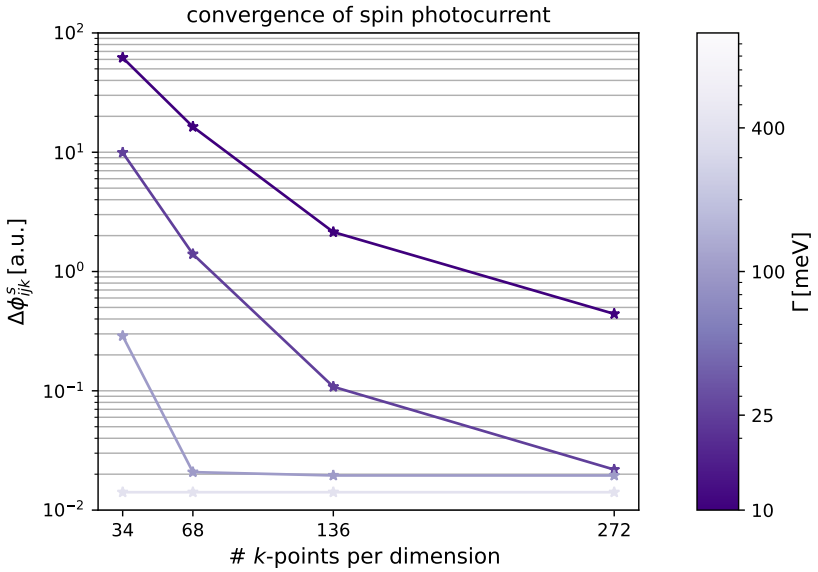


**FIGURE A.1.** Relative change of response tensor with respect to a $N_k = 544$ calculation. 34 up to 272 $k$-points were considered at broadening values 10, 25, 100, 400 meV.

Figure A.1 shows the trade-off between small broadening values Γ and the number of $k$-points required to converge the results at a given broadening level. For a room-temperature like broadening of $\Gamma = 25$ meV well converged results are obtained when using 256 or more $k$-points per dimension.

### A.3.2 Parameter space scaling

Figure A.2 shows the overall walltime plotted versus the parameter space size (here the parameter space is varied by changing the number of laser frequencies `N_hw` in the input file) and compares the scaling of the second order charge photocurrent (blue curve), with the second order spin photocurrent (red curve) and the first order optical conductivity (green curve). Each curve

was fitted (the respective fits are shown by dashed lines) to make a qualitative comparison easier.

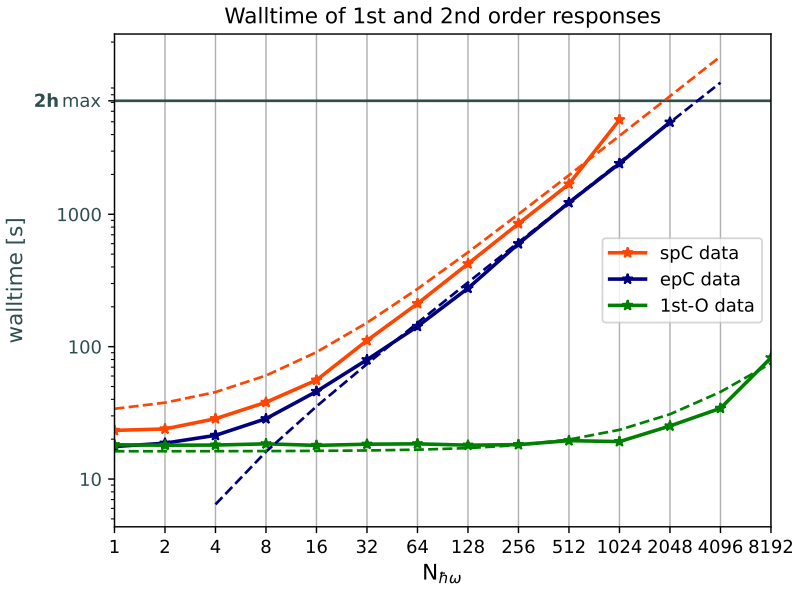


**FIGURE A.2.** Scaling of $Mn_2Au$ job calculating the 2nd order spin-photocurrents (red), the second order photocurrent (blue) and the 1st order optical conductivity tensor (green) for different sizes of the parameter space $N_{\hbar\omega}$ on a $N_k = 16^3$ $k$-mesh. A single JURECA DC-CPU node was used and filled with 128 MPIs and 2 OpenMPs. The maximum walltime for each job was set to 2 hours.

Figure A.2 shows that both second order effects scale similarly, however, the spin photocurrent calculation is a little heavier then the charge photocurrent since the spin tensor has one additional spatial dimension. Interestingly the first order effects walltime is effectively constant up to a parameter space size of roughly 256 parameters. This suggests that the first order calculation spends most of its time in the Wannier interpolation step (which is independent of the parameter space size) and only for very large parameter spaces the tensor routine becomes the most time consuming part of the calculation. For the second order effects however the situation is reversed: the walltime already increases when jumping from a single parameter space point to a two parameterpoint calculation. Suggesting that the Keldysh tensor routines are the most time consuming part of the calculation. Future performance optimizations of the code should thus focus on optimizing the Keldysh routines and users should be aware that parameterpoints are more expensive in a second order calculation when compared to the scaling of the more established

first order effects.

### *A.3.3 MPI-scaling*

Figure A.3 shows the scaling of the MPI parallelization for a typical calculation of spin-photocurrents in $Mn_2Au$. $N_k = 272^3$ were calculated with a single point in parameter space. To analyze the parallel efficiency the walltime was plotted for different number of MPI nodes. On each node 68 MPI threads and 4 OpenMP threads were used. Only jobs with 8 or more nodes finished within the given walltime maximum of JURECA BOOSTER of 24 hours. Therefore, the parallel Figure A.3 efficiency was normalized to the 8 node job (efficiency set to 1.0) and then analyzed for different node counts. Up to 272 nodes in parallel were considered.

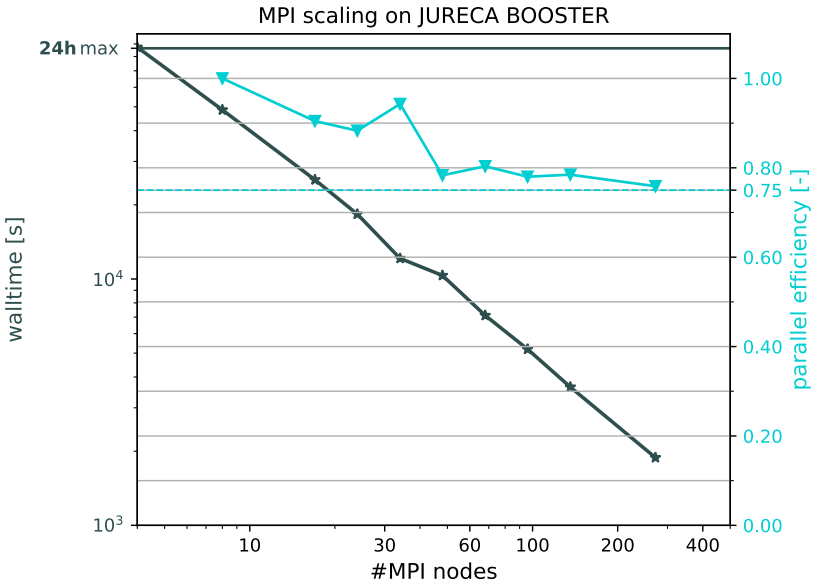


**FIGURE A.3.** MPI scaling of $Mn_2Au$ job calculating spin-photocurrents for a single point in parameter space on a $N_k = 272^3$ $k$-mesh. The $x$-axis shows the number of nodes running in parallel. Each node was filled with 68 MPIs and 4 OpenMPs. Since jobs with less then 8 nodes did not finish within the 24h maximum walltime limit, the parallel efficiency was normalized to 1 at 8 node.

As Figure A.3 shows the *ju_wip* code shows a very efficient MPI parallelization above 75% even for 272 nodes in parallel. Since the MPI parallelism splits up the numerical $k$-point integration, communication between MPI

threads is only required before (broadcasting the real space basis set) and after (MPI reduction of the response tensors) entering the $k$-point loop.

### *A.3.4 OpenMP scaling*

In this section the openMP implementation is tested in terms of its parallel efficiency. The *ju_wip* uses openMP indirectly via the lapack and boost library to speedup the matrix operations required for the wannier interpolation. Further the Keldysh routines use an explicit openMP implementation to speedup the double nested summation over Wannier functions to obtain the response tensor. The OpenMP parallelism should therefore be most efficient for large basis sizes, meaning large number of Wannier functions, and large parameter space sizes. Figure A.4shows the walltime of a typical spin-photocurrent calculation versus the number of OpenMP threads used. Additionally on the right side the $y$-axis shows the parallel efficiency. 4096 $k$-points were calculated on a single node of JURECA BOOSTER and the openMP thread count was varied from 1 up to 272 threads (maximum number of threads per node). $Mn_2Au$ with 54 Wannier functions was used as basis set and a single point in parameter space calculated.

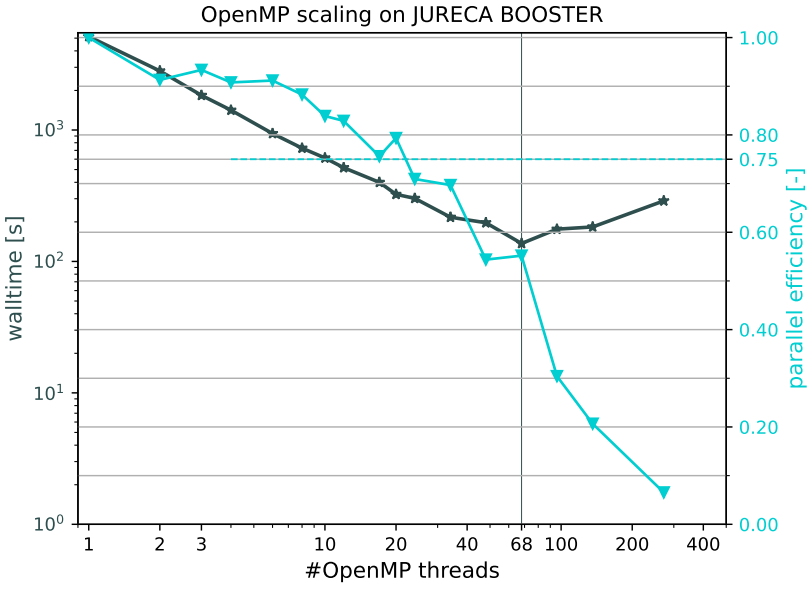


**FIGURE A.4.** OpenMp scaling on a single Jureca Booster node for a $Mn_2Au$ job calculating spin-photocurrents for a single point in parameter space on a $N_k = 16^3$ $k$-mesh. The $x$-axis shows the number of shared memory OpenMP threads running in parallel. A parallel efficiency larger then 75% is maintained up to $\sim 12$ threads. Note that running more then 68 OpenMP threads actually increases the overall walltime.

Figure A.4 shows a good parallel efficiency of more then 75% for up to 20 OpenMP threads in parallel. At 68 threads the parallel efficiency is slightly above 50%. Using more then 68 OpenMP threads lead to an actual increase in the walltime. Using more then 68 threads also means some of the 68 physical cores have to run more then one thread in parallel (hyperthreading). This might explain the catastrophic scaling beyond 68 threads. Similar to Figure A.4, Figure A.5 shows the OpenMP parallel scaling on the CLAIX-2018-MPI cluster[219] for various parameter space sizes.

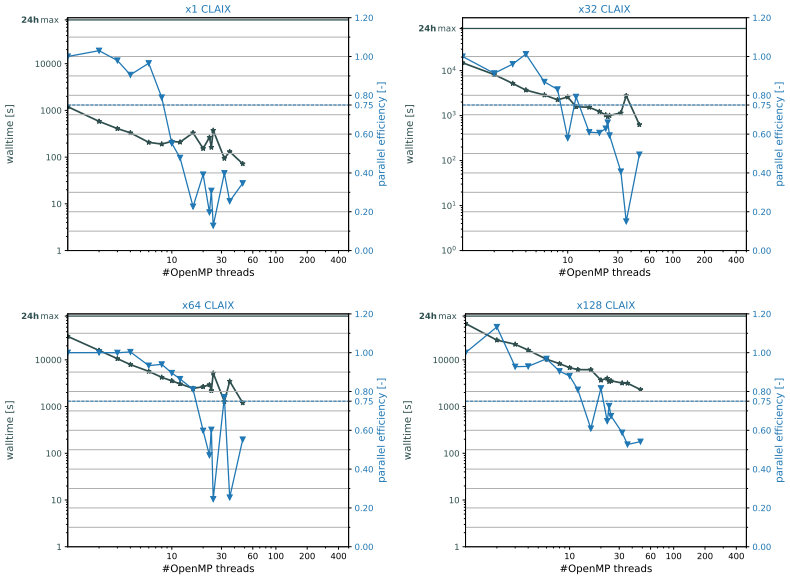


**FIGURE A.5.** OpenMp scaling on a single Claix node for a $Mn_2Au$ job calculating spin-photocurrents for different parameter space sizes on a $N_k = 16^3$ $k$-mesh. The $x$-axis shows the number of shared memory OpenMP threads running in parallel up to the maximum of 48 threads per node. Parameter space sizes of 1,32,64,128 were considered.

Figure A.5 shows that the OpenMP parallel efficiency increases for larger parameter space sizes.

## A.4 CHOOSING OPTIMAL HYBRID PARALLELIZATION SCHEME

In Figure A.6 different hybrid parallelization schemes are compared for a single node job on JURECA BOOSTER calculating photocurrents in GaAs with $N_{WF} = 16$ and $N_k = 16^3$. To save computing time a single node was used and $N_k = 16^3 = 4096$ $k$-points calculated. For a fully converged calculation about $N_k = 256^3$ $k$-points are required, which can be achieved by runing 64 nodes in parallel with each node calculating $N_k = 16^3$ $k$-points. The $x$-axis indicates the choosen hybrid parallelization scheme which is given as (#MPIs × #OpenMPs), on the $y$-axis the size of the parameter space is indicated. parameter space sizes from 1 to 180 points were used. The plot indicates the normalized walltime of a given calculation via the color coding. Red tiles indicate jobs which crashed. To normalize the walltime the walltime of each run for a given parameter space size was divided by the maximum walltime of this parameter space size.

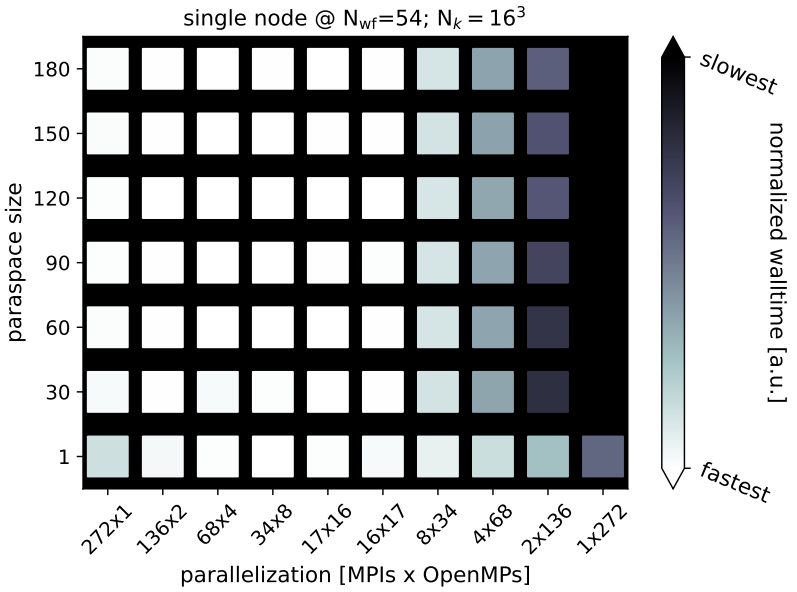


**FIGURE A.6.** Walltime of a photocurrent calculation on a single node of JURECA BOOSTER. GaAs Wannier functions with a basis size of $N_{Wf} = 16$ were used on a $N_k = (16 \times 16 \times 16)$ $k$-point mesh. Each tile represent a calculation, the colorcoding indicates the normalized walltime. The $y$-axis represents different parameter space sizes from 1 up to 180 points and the $x$-axis different hybrid parallelization schemes. One JURECA BOOSTER node has 272 threads available, hence the $x$-axis changes from a pure MPI sheme (272×1) MPIs via various hybrid schemes to a pure OpenMP parallelization (1×272). The same is done for a single DC-CPU node with a maximum of 256 threads.

Figure A.6 suggest to use a high number of MPIs even within the node. The fastest configuration is 68 MPIs paired with 4 OpenMPs for all considered parameter space sizes. Note that JURECA BOOSTERs CPUs have 68 cores which can handle 4 threads simultaneously (Intel Hyperthreading). The optimal parallelization scheme for Booster seems to be to assign as many MPIs as the number of physical cores and use OpenMP to "fill" the Hyperthreads. However for the more relevant runs with multiple points in parameter space (≥30) parallelization schemes with 16 or more MPIs all have similar walltimes. So reducing the number of MPIs might be a good strategy when *e.g.* 68 MPIs can not be spawned due to insufficient main memory. As a example Figure A.7 shows the same walltime analysis as Figure A.6 but now for a larger system, namely $Mn_2Au$ with 54 Wannier functions. As Figure A.7 (left figure) shows parallelization schemes (272x1) and (136x2) crash due to insufficient amount of RAM available. On the right-hand side, Figure A.7 the same analysis is performed on a JURECA DC-CPU node. Since DC-CPU nodes

have 4GB of memory available per core, which is more then twice as much as BOOSTER nodes, enough RAM is available for a pure MPI scheme (256x1). The fastest parallelization scheme on DC-CPU was the (128x2) scheme. This confirms the trend from the BOOSTER node to fill the physical cores with MPIs and use OpenMP to utilize the simultaneous multithreading (DC-CPU has only 2 SMT threads compared to BOOSTERs 4). For very large parameter space sizes, above 128 points, the parallel efficiency of the (4x64) and (2x128) scheme start to become reasonable on DC-CPU.

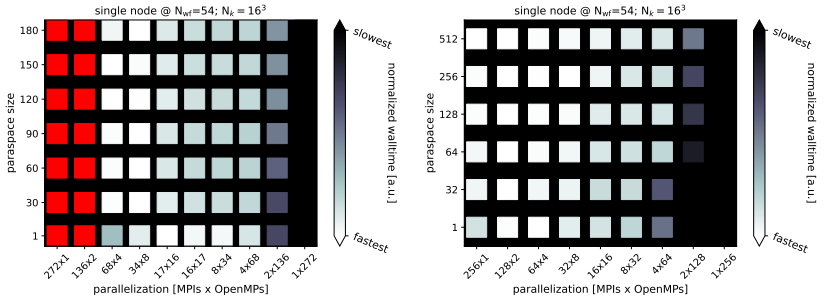


**FIGURE A.7.** Walltime of a photocurrent calculation on a single node of JURECA BOOSTER (left) and JURECA DC-CPU (right). $Mn_2Au$ Wannier functions with a basis size of $N_{Wf} = 54$ were used on a $N_k = (16 \times 16 \times 16)$ $k$-point mesh. Each tile represent a calculation, the colorcoding indicates the normalized walltime. The $y$-axis represents different parameter space sizes from 1 up to 180 points and the $x$-axis different hybrid parallelization schemes. One JURECA BOOSTER node has 272 threads available, hence the $x$-axis changes from a pure MPI sheme (272×1) MPIs via various hybrid schemes to a pure OpenMP parallelization (1×272). Red tiles indicate runs which crashed, here all schemes with 136 or more MPIs crash due to insufficient memory.

With 3 atoms in the unit cell and 54 Wannier functions $Mn_2Au$ is a good representative system for a typical production level calculation performed with the *ju_wip* code. The hybrid parallelization of the *ju_wip* code allows the user to achieve high parallel efficiency on a variety of machines and especially on systems with high core count but low amount of memory such as JURECA BOOSTER and possibly GPUs in the future (see also Chapter 10).

## A.5 SNIPPETS

In this appendix some code snippets from the *ju_wip* code are given to outline crictical design choices of the code.
The first snippet shows the slicing of the $k$-point loop in the core module to allow for MPI parallelization of the $k$-point loop.

```
1 logical pure function mpi_ki_selector(ki_id)
```

```
  !   for $(mpi_nProcs_i8) MPI threads in total
  !   map the kpt "ki_id" to the MPI thread $(mpi_id_i8)
  integer(8),   intent(in)    ::    ki_id
  !
  mpi_ki_selector = ( mod(ki_id-1-mpi_id_i8,mpi_nProcs_i8)==0 )
  !
  return
end function


!-------------------------------------------------------------------------------
! loop  k-space
!-------------------------------------------------------------------------------
do kiz = 1, mp_grid(3)
  do kiy = 1, mp_grid(2)
    do kix = 1, mp_grid(1)
      ki  =    kix  + mp_grid(1) * ( (kiy-1) + mp_grid(2) * (kiz-1))
      !~
      if( mpi_ki_selector(ki) ) then
        kloop_t0  = clock_get_runtime()
        n_ki    =   n_ki + 1
        kpt     = get_rel_kpt(ki, kix,kiy,kiz)
        !-------------------------------------------------------------------
        !-------------------------------------------------------------------
        !-------------------------------------------------------------------
        ! INTERPOLATE K-POINT
        !-------------------------------------------------------------------
```

The Fourier transform in the Wannier interpolation (see Section 5.5) was OpenMP parallelized as shown below in case of the interpolated Hamiltonian

```
!^^^^^^^^^^^^^^^^^^^^^^^^^^^^^|
! HAMILTONIAN INTERP     |
!~~~~~~~~~~~~~~~~~~~~~~~~~~~~~|
!$OMP PARALLEL DEFAULT(none)  &
!$OMP SHARED(   H_k, H_real,ft_phase, n_sc,n_wf) PRIVATE(n,m)
!$OMP DO REDUCTION(+: H_k)
do sc =1, n_sc
  do m =1, n_wf
    do n=1, n_wf
      H_k(n,m)      = H_k(n,m)      + ft_phase(n,m,sc)  * H_real(n,m,sc)
    end do
  end do
end do
!$OMP END DO
!$OMP END PARALLEL
!~~~~~~~~~~~~~~~~~~~~~~~~~~~~~
!~~~~~~~~~~~~~~~~~~~~~~~~~~~~~
```

The gauge transformation from Wannier to Hamiltonian gauge is given by rotating the operators into the eigenbasis, which requires to evaluate multiple matrix products. A wrapper for the BLAS matrix multiplication routines is provided in the *ju_wip* code to allow parallel execution of these matrix products

```
interface blas_matmul
    module procedure     d_blas_matmul
    module procedure     z_blas_matmul
end interface blas_matmul


function z_blas_matmul(A, B)      result(C)
    !   C := alpha*op(A)*op(B) + beta*C
    complex(dp),         intent(in)       ::  A(:,:), B(:,:)
    complex(dp),         allocatable      ::  C(:,:)
    integer                               ::  m, n, k
    !
    m       =   size(A,1)
    k       =   size(A,2)
    n       =   size(B,2)
    if( k /= size(B,1))   stop  '[z_blas_matmul]:   warning matrix size do not match
      correctly (k<->size(B,1))'
    !
```

```
    !
    allocate(    C(m,n)      )
    !dir$ vector aligned
    C       =     cmplx(0.0_dp,0.0_dp,dp)
    !
    call zgemm('N', 'N', m, n, k, 1.0_dp, A(:,:), m,  B(:,:), k, 0.0_dp,     C(:,:), m)
    !
    return
end function
```

Next a source code example of the Keldysh routines, showcasing the OpenMP parallelization, for a generic vector (for example the velocity operator in case of the charge photocurrent, or the pauli operator in case of IFE) is presented.

```
subroutine kely_generic_vector(kpt, en_k,Vec_ka, V_ka, hw_lst, smr_lst, ef_lst, phi_surf,
    phi_sea,kweight)
  !   see  Freimuth et al., PRB 94, 144432 (2016)
  !    EQ.(2)
  real(dp),        intent(in)       ::  kpt(3), en_k(:), hw_lst(:), smr_lst(:), ef_lst(:),
      kweight
  complex(dp),     intent(in)       ::  Vec_ka(:,:,:), V_ka(:,:,:)
  complex(dp),     intent(inout)    ::  phi_surf(:,:,:,:,:,:), phi_sea(:,:,:,:,:,:)
  complex(dp)              ::  v_ijk(3,3,3), v_ikj(3,3,3), en_int_ijk, en_int_ikj
  integer                  ::  a,b,c,i, j,k, hw, smr, ef
  !
  !$OMP PARALLEL DO REDUCTION(+:phi_surf,phi_sea)        collapse(1)          &
  !$OMP DEFAULT(NONE) SHARED(Vec_ka, V_ka, en_k, ef_lst, smr_lst, hw_lst, kpt, kweight,
      do_kely_resonant) &
  !$OMP PRIVATE(c,b,a,i, k,j, v_ijk, v_ikj, ef, smr, hw, en_int_ijk, en_int_ikj)
  do c = 1, size(en_k,1)
    do b = 1, size(en_k,1)
      do a = 1, size(en_k,1)
        if(   do_kely_resonant .and. (a.ne.c)   )cycle
        !
        ! GET VELO NOMINATOR
        do k = 1,3
          do j = 1,3
            do i = 1,3
              v_ijk(i,j,k)  =   Vec_ka(i,c,a) * V_ka(j,a,b) * V_ka(k,b,c)
              v_ikj(i,j,k)  =   Vec_ka(i,c,a) * V_ka(k,a,b) * V_ka(j,b,c)
            end do
          end do
        end do
        !
        !
        ! LOOP PARASPACE
        do ef = 1, size(ef_lst)
          do smr = 1, size(smr_lst)
            do hw = 1, size(hw_lst)
              !^^^^^^^^^^^^^^^^^^^^^^^^^^^^^^^^^^^^^^^^^^^^^^^^^^^^^^^^^^^^^^^^^^^^
              ! FERMI SURFACE CONTRIBUTIONS
              !~~~~~~~~~~~~~
              !   ijk
              en_int_ijk  =  - en_int_RRA(  en_k(a), en_k(b)-hw_lst(hw), en_k(c),   ef_lst
    (ef),     smr_lst(smr))
              en_int_ijk  =   en_int_ijk &
                      + en_int_RRA(   en_k(a), en_k(b)-hw_lst(hw), en_k(c), ef_lst(ef)-
    hw_lst(hw),  smr_lst(smr))
              !~~~~~~~
              ! ikj
              en_int_ikj  =  -  en_int_RRA( en_k(a), en_k(b)+hw_lst(hw), en_k(c),   ef_lst
    (ef),     smr_lst(smr))
              en_int_ikj  = en_int_ikj &
                      + en_int_RRA(   en_k(a), en_k(b)+hw_lst(hw), en_k(c), ef_lst(ef)+
    hw_lst(hw),  smr_lst(smr))
              !~~~~~~~~~~~~~~~~~~~~~~~
              en_int_ijk  = en_int_ijk * kweight
              en_int_ikj  = en_int_ikj  * kweight
              !~
              do k = 1,3
              do j = 1,3
              do i = 1,3
              phi_surf(i,j,k,hw,smr,ef) = phi_surf(i,j,k,hw,smr,ef) + en_int_ijk * v_ijk(i
    ,j,k)
```

```
53                phi_surf(i,j,k,hw,smr,ef) = phi_surf(i,j,k,hw,smr,ef) + en_int_ikj * v_ikj(i
      ,j,k)
54                end do
55                end do
56                end do
57                !
58                !^^^^^^^^^^^^^^^^^^^^^^^^^^^^^^^^^^^^^^^^^^^^^^^^^^^^^^^^^^^^^^^^^^^^^^^^^^^
59                ! FERMI SEA CONTRIBUTIONS
60                !~~~~~~~~~~~~~
61                en_int_ijk  = kweight * en_int_RRR( en_k(a), en_k(b)-hw_lst(hw), en_k(c),
      ef_lst(ef), smr_lst(smr))
62                en_int_ikj  = kweight * en_int_RRR( en_k(a), en_k(b)+hw_lst(hw), en_k(c),
      ef_lst(ef), smr_lst(smr))
63                !~
64                do k = 1,3
65                do j = 1,3
66                do i = 1,3
67                phi_sea(i,j,k,hw,smr,ef)  = phi_sea(i,j,k,hw,smr,ef)  + en_int_ijk * v_ijk(i
      ,j,k)
68                phi_sea(i,j,k,hw,smr,ef)  = phi_sea(i,j,k,hw,smr,ef)  + en_int_ikj * v_ikj(i
      ,j,k)
69                end do
70                end do
71                end do
72              end do
73            end do
74          end do
75        end do
76      end do
77    end do
78    !$OMP END PARALLEL DO
79    return
80  end subroutine
```

The analytic energy integration (see subsection 3.3.4) is hard coded as pure functions to allow inlining into the Keldysh routines (see example above) by the compiler. Below is an example for the scenario of a triple product of retarded Greens functions.

```
complex(dp) pure function en_int_RRR(E1, E2, E3, E4,  smr)
  !   see  Freimuth et al., PRB 94, 144432 (2016)
  !    EQ.(B7)  / EQ.(B9)   / EQ.(B11)
  !   i.e.  I1(E1,E2,E3,E4)
  real(dp),   intent(in)    ::  E1, E2, E3, E4, smr
  real(dp)                  ::  smrsmr
  real(dp)                  ::  denom_1213, denom_2321, denom_3132, dE_14, dE_24, dE_34,&
                            dE_14_smr, dE_24_smr, dE_34_smr,&
                            re_rrr, im_rrr
  !
  dE_14   = E4 -E1
  smrsmr    =   smr**2
  !^^^^^^^^^^^^^^^^^^^^^^^^^^^^^^^^^^^^^^^^^^^^^^^^^^^^^^^^^^^^^^^^^^^^^^^^
  !     BAND DEGENERACY
  !       use EQ.(B9)/(B11)
  ! with identity
  ! ->  EQ.(B9):    I1(E1,E1,E3,E4) = I1(E1,E3,E1,E4) = I1(E3,E1,E1,E4)
  ! ->  EQ.(B11):     I1(E1,E1,E1,E4)
  !
  !^^^^^^^^^^^^^^^^^^^^^^^^^^
  if (        ( abs(E1-E2)  < kubo_tol )      &
        .and. ( abs(E1-E3)  < kubo_tol )      &
        .and. ( abs(E2-E3)  < kubo_tol )      &
  )then
    ! Eq.(B11):
    en_int_RRR  = -0.5_dp / cmplx(dE_14, smr,dp)**2
    !-------------------------
  !^^^^^^^^^^^^^^^^^^^^^^^^^^
  else if(      ( abs(E1-E2)  < kubo_tol )      & ! E1==E2
        .and. ( abs(E1-E3)  > kubo_tol )      & ! E1/=E3
  )then
    ! Eq.(B9):
    en_int_RRR  = en_int_DGN_RRR( E1, E3, E4, smr, smrsmr)
    !-------------------------
  !^^^^^^^^^^^^^^^^^^^^^^^^^^
  else if(      ( abs(E1-E3)  < kubo_tol )      & ! E1==E3
        .and. ( abs(E2-E1)  > kubo_tol )      & ! E1/=E2)then
  )then
    ! Eq.(B9):
    en_int_RRR  = en_int_DGN_RRR( E1, E2, E4, smr, smrsmr)
    !-------------------------
  !^^^^^^^^^^^^^^^^^^^^^^^^^^
  else if(      ( abs(E2-E3)  < kubo_tol )      & ! E2==E3
        .and. ( abs(E1-E2)  > kubo_tol )      & ! E1/=E2)then)then
  )then
    ! Eq.(B9):
    en_int_RRR  = en_int_DGN_RRR(E2, E1, E4, smr, smrsmr)
    !-------------------------
  !^^^^^^^^^^^^^^^^^^^^^^^^^^
  else
    ! EQ.(B7):   I1(E1,E2,E3,E4)
    dE_34   = E4 -E3
    dE_24   = E4 -E2
    !
    dE_14_smr = dE_14 / smr
    dE_24_smr = dE_24 / smr
    dE_34_smr = dE_34 / smr
    !
    denom_1213  = (E1-E2) * (E1-E3)
    denom_2321  = (E2-E3) * (E2-E1)
    denom_3132  = (E3-E1) * (E3-E2)
    !
    re_rrr    =       log(  1.0_dp  + dE_14_smr**2  ) / denom_1213
    re_rrr    = re_rrr  + log(  1.0_dp  + dE_24_smr**2  ) / denom_2321
    re_rrr    = re_rrr  + log(  1.0_dp  + dE_34_smr**2  ) / denom_3132
    re_rrr    = 0.5_dp  *   re_rrr
    !
    im_rrr    =     -   atan( dE_14_smr )       / denom_1213
    im_rrr    = im_rrr  - atan( dE_24_smr )       / denom_2321
    im_rrr    = im_rrr  - atan( dE_34_smr )       / denom_3132
    !
    en_int_RRR  = cmplx(  re_rrr, im_rrr,   dp)
```

```
  end if
  return
end function
```

Example standard output produced by *ju_wip*.

```
[clock_init]:  system_clock rate          1.0 (MHz)
[clock_init]:  system_clock at rel pos  0.0 % ( will cycle in ~  2561581456.498 hours)
[#0000000;main/Fri Mar 10 18:06:27 2023]: welcome to ju_wip
 *
 ^^^^^^^^^^^^^^^^^^^^^^^^^^^^^^^^^^^^^^^^^^^^^^^^^^^^^^^^^^^^^^^^^^^^^^^^^^^^|
 ^^^^^^^^^^^^^^^^^^^^^^^^^^^^^^^^^^^^^^^^^^^^^^^^^^^^^^^^^^^^^^^^^^^^^^^^^^^^|
 ~~~~~~~~~~~~~~~~~~~~~~BUILD INFO~~~~~~~~~~~~~~~~~~~~~~~~~~~~~~~~~~~~~~|
 ^^^^^^^^^^^^^^^^^^^^^^^^^^^^^^^^^^^^^^^^^^^^^^^^^^^^^^^^^^^^^^^^^^^^^^^^^^^^|
 git origin              :
 git branch              :
 git hash                :
 compiled on             : Linux (version: 4.18.0-425.3.1.el8.x86_64 )
 fortran compiler id     : Intel
 fortran compiler version: 2021.4.0.20210910
 fortran compiler flags  :
  -mkl -qopenmp -fpp -g -O3 -march=core-avx2  -qopt-prefetch=5  -qopt-report=5
 compile time            : 12:32:20 06/01/2023
 *
 *
 RUNTIME INFO:
Linux jrc0730 4.18.0-425.13.1.el8_7.x86_64 #1 SMP Tue Feb 21 19:25:54 UTC 2023 x86_64
      x86_64 x86_64 GNU/Linux
model name  : AMD EPYC 7742 64-Core Processor
 ~~~~~~~~~~~~~~~~~~~~~~~~~~~~~~~~~~~~~~~~~~~~~~~~~~~~~~~~~~~~~~~~~~~~~~~~|
 ~~~~~~~~~~~~~~~~~~~~~~~~~~~~~~~~~~~~~~~~~~~~~~~~~~~~~~~~~~~~~~~~~~~~~~~~|
 ~~~~~~~~~~~~~~~~~~~~~~~~~~~~~~~~~~~~~~~~~~~~~~~~~~~~~~~~~~~~~~~~~~~~~~~~|
 *
 *
[#0000000;main]:  #MPI-tasks  =     4
[#0000000;main]:  #OMP-threads=    64
[#0000000;main]:  OMP_proc_bind =  false
 *
 *
 parallelization with #           4  MPI threads
 max_wall_time:     0.000000000000000E+000  (sec.)

 ^^^^^^^^^^^^^^^^^^^^^^^^^^^^^^^^^^^^^^^^^^^^^^^^^^^^^^^^^^^^^^^^^^^^^^^^^^^^^^^^^^^^|
 ^^^^^^^^^^^^^^^^^^^^^^^^^^^^^^^^^^^^^^^^^^^^^^^^^^^^^^^^^^^^^^^^^^^^^^^^^^^^^^^^^^^^|
 ^^^^^^^^^^^^^^^^^^^^^^^^^^^^^^^^^^^^^^^^^^^^^^^^^^^^^^^^^^^^^^^^^^^^^^^^^^^^^^^^^^^^|
 **********************init_parameter interpretation**************************|
 ~
 real space lattice
    a1:     6.29089827960000        0.000000000000000E+000  0.000000000000000E+000
    a2:   0.000000000000000E+000    6.29089827960000        0.000000000000000E+000
    a3:     3.14544913980000        3.14544913980000         8.07102024030000
 mp_grid
          16           16           16
kubo tol= 0.36749324E-16
 # atom  centers
           3
 wannier centers
#  1  |    0.33  0.33  0.33
#  2  |   -0.33  0.33 -0.33
#  3  |    0.00  0.00  0.00
 wann interpolation options
    use_cart_velo:   T
    do_wip_wf_centers F
    do_gauge_trafo:  T
      do_adpt_kmesh:   F
 *
 *
 jobs:
  plot_bands:     F
  debug_mode:     F
  do_write_velo:    F
  do_mep:       F
  do_mep_kubo:      F
  do_ahc:       F
  do_ahc_kBastin:   F
  do_opt:       F
  do_photoC:      F
  do_bcd_photo:   F
  do_keldysh:     T
```

```
 do_kely_epC:      F
 do_kely_epC_kres:     F
 do_kely_epC_pat:      F
 do_kely_epC_pat_kres:  F
 do_kely_spC       F
 do_kely_spC_kres    F
 do_kely_spC_pat_kres F
 do_kely_spCat     F
 do_kely_trq:      F
 do_kely_pauli:      F
 do_kely_pauli_pat:    T
 do_kely_pauli_pat_kres:  F
 do_kely_pauliat:    F
 do_kely_anglmom:    F
 do_gyro:      F
*
full interpolation of:
***k-space matrices to be interpolated****
velocity op:  T
velocity pat:    F
berry conne:  F
berry curva:  F
pauli   op:   T
pauli   pat:  T
pauliat op:   F   (N_at=           0 ).
anglmom op:   F
pauli*velo:     F
torques:        F
2 deriv Ham:  F
conn grad  :  F
do_wip_apply_zeeman: F
*
***expectation values to be calcualted****
op_pauli:       F
op_pauli_kres:  F
op_anglmom:       F
op_anglmom_kres:  F
op_velo:      F
op_velo_kres:   F
*
*
*
*
paraspaces:
 hw   linspace := ( 0.367E-03,  0.187E+00,    6).
 smr1 linspace := ( 0.919E-03,  0.147E-01,    1).
 ef   linspace := ( 0.345E+00,  0.419E+00,    1).
*
*
*
 WARNING , too small temperature value (<1e-2). WARNING Fermi Dirac will assume T=0 (
     stepfunction)
 ********************************************************************************
 ********************************************************************************
 ********************************************************************************
 *
 ----------------------MAKE TARGET DIRECTORIES-------------------------
[#0000000;init_parameters]: start target mkdir...
[#0000000; init_parameters]: (fake) created directory out/
[#0000000; init_parameters]: (fake) created directory raw/
[#0000000;init_parameters]: ...all required directories created
 *
 ----------------------K-SPACE SETUP-------------------------
 [set_recip_latt] b1=  0.998773947363698        0.000000000000000E+000
 -0.389243560300255
 [set_recip_latt] b2=  0.000000000000000E+000  0.998773947363698
 -0.389243560300255
 [set_recip_latt] b3=  0.000000000000000E+000  0.000000000000000E+000
  0.778487120600511
 reciprocal lattice:
  0.998773947363698        0.000000000000000E+000 -0.389243560300255
  0.000000000000000E+000  0.998773947363698       -0.389243560300255
  0.000000000000000E+000  0.000000000000000E+000  0.778487120600511
[#0000000;k_space]: k-space setup done (mp_grid=   16x   16x   16).
[#0000000;k_space]: unit_vol=319.4139,(a0**3) -> bz_vol=  0.7766 (1/a0**3)
 *
 ----------------------GET REAL SPACE BASIS--------------------------
 *
 ----------------------GET REAL SPACE BASIS--------------------------
```

```
[#00000;core]: Basis size: n_wf=  54 n_sc=  1879
[#00000;core]: now try to allocate all arrays (k-space && R-space)...
[#00000;core]: ... allocated; wait for all (mpi) cores to finish allocation...
[#00000;core]: ... all cores allocated! root will attempt reading the TB basis
[#00000;read_tb_ham_binary]: read binary TB Hamiltonian from w90files/ufo_H_tb.dat    (
        0.0174 sec.)
[#00000;read_tb_posOp_binary]: read binary TB pos.Op. from w90files/ufo_r_tb.dat    (
       0.0519 sec.)
[#00000;read_tb_ham_binary]:  read TB R-vector from w90files/ufo_rvec.dat
[#00000;read_tb_pauli_binary]: read binary TB pauli.Op. from w90files/ufo_rspauli1.dat   (
          0.0505 sec.)
[#00000read_tb_basis]: finished reading TB basis (       0.122 sec).
 Start mpi_bcast...
[#00000read_tb_basis]:...bcasted flags...
[#00000read_tb_basis]:...bcasted hmat & rvect...(       0.036 sec.)
[#00000read_tb_basis]:...bcasted rmat ...(       0.107 sec.)
[#00000read_tb_basis]:...bcasted pauli ...(       0.108 sec.)
[#00000read_tb_basis]: ...finished MPI-Bcast of TB-Basis matrices (       0.252 sec.)
 [read_tb_basis]: absmax ham=  0.683027085905403
 [read_tb_basis]: absmin ham=  0.000000000000000E+000
 [read_tb_basis]: absmax pOp=   4.49363077420862
 [read_tb_basis]: absmin pOp=  0.000000000000000E+000
 *
 *
 #at |  rel. center  | wf_per_atom
 ---------------------------------------
  1 |  0.33  0.33  0.33 |  18
  2 | -0.33  0.33 -0.33 |  18
  3 |  0.00  0.00  0.00 |  18
 ---------------------------------------
 *
 *
 #WF |       center     | assoc atom
 ---------------------------------------
  1 |       3.14565       1.79758       2.93933 |   1
  2 |       3.14546       3.14534       1.16630 |   1
  3 |       1.79723       3.14531       2.93924 |   1
  4 |       3.14560       4.49363       2.93815 |   1
  5 |       3.14636       3.14645       3.34745 |   1
  6 |       3.14453       3.15011       2.56931 |   1
  7 |       3.14124       3.14448       2.56926 |   1
  8 |       4.49328       3.14544       2.93824 |   1
  9 |       3.14952       3.14089       2.69508 |   1
 10 |      -3.14745      -3.14362      -1.64928 |   2
 11 |      -3.14374      -3.14703      -3.76966 |   2
 12 |      -1.89632      -3.14556      -2.67262 |   2
 13 |      -3.14567      -4.39458      -2.67275 |   2
 14 |      -4.39444      -3.14530      -2.67584 |   2
 15 |      -3.14522      -3.14544      -2.69521 |   2
 16 |      -3.14545      -3.14565      -2.69521 |   2
 17 |      -3.14527      -1.89646      -2.67570 |   2
 18 |      -3.14543      -3.14547      -2.68977 |   2
 19 |      -0.00004       0.00004       1.28414 |   3
 20 |       0.00002      -0.00002      -1.35251 |   3
 21 |       1.36758       0.00003       0.01862 |   3
 22 |      -0.00003      -1.36758       0.01861 |   3
 23 |      -1.36755      -0.00001       0.01853 |   3
 24 |       0.00001      -0.00005      -0.00837 |   3
 25 |       0.00005      -0.00001      -0.00837 |   3
 26 |       0.00001       1.36755       0.01853 |   3
 27 |      -0.00004       0.00004       0.00156 |   3
 28 |       3.14394       3.14710       1.64810 |   1
 29 |       3.14677       3.14402       3.76875 |   1
 30 |       4.39454       3.14563       2.67364 |   1
 31 |       3.14554       1.89636       2.67354 |   1
 32 |       3.14533       4.39444       2.67620 |   1
 33 |       3.14560       3.14545       2.69492 |   1
 34 |       3.14544       3.14527       2.69492 |   1
 35 |       1.89646       3.14529       2.67610 |   1
 36 |       3.14547       3.14544       2.68978 |   1
 37 |      -1.79766      -3.14564      -2.93885 |   2
 38 |      -3.14533      -3.14547      -1.16696 |   2
 39 |      -4.49355      -3.14560      -2.93775 |   2
 40 |      -3.14531      -1.79731      -2.93880 |   2
 41 |      -3.14638      -3.14635      -3.34849 |   2
 42 |      -3.14455      -3.14133      -2.56939 |   2
 43 |      -3.15002      -3.14454      -2.56943 |   2
 44 |      -3.14543      -4.49320      -2.93780 |   2
 45 |      -3.14098      -3.14942      -2.69507 |   2
```

```
 46 |      -0.00003       0.00003      -1.28429 |   3
 47 |       0.00002      -0.00002       1.35239 |   3
 48 |       1.36757       0.00002      -0.01855 |   3
 49 |      -0.00002      -1.36757      -0.01855 |   3
 50 |       0.00002       1.36756      -0.01848 |   3
 51 |       0.00001      -0.00005       0.00834 |   3
 52 |       0.00005      -0.00001       0.00834 |   3
 53 |      -1.36756      -0.00002      -0.01848 |   3
 54 |      -0.00005       0.00005      -0.00154 |   3
 ----------------------------------------
 ^
 ---------------------------------------------------------------
 ---------------------------------------------------------------
 ---------------------------------------------------------------
 *
 *
 ******^  - FULL INTERPOL MODE (KSPACE MODE)  - ^^^^***
 ******^  -     ~~~ WANNIER FT CONVENTION ~~~     - ^^^^***
 ******^  -  ~~~ found pos operator   ~~~   - ^^^^***
 ******^  -      will interp CONN & CURV       - ^^^^***
 *
 ---------------------------------------------------------------
 ---------------------------------------------------------------
 ---------------------------------------------------------------
 ******^  - BZ INTEGRATION LOOP - ^^^^***
[#0000000; core_worker/Fri Mar 10 18:06:29 2023]:  I start interpolating now (#OMP THREADS
     = 64)....
[#0000003; core_worker/Fri Mar 10 18:06:29 2023]:  I start interpolating now (#OMP THREADS
     = 64)....
[#0000001; core_worker/Fri Mar 10 18:06:29 2023]:  I start interpolating now (#OMP THREADS
     = 64)....
[#0000002; core_worker/Fri Mar 10 18:06:29 2023]:  I start interpolating now (#OMP THREADS
     = 64)....
[#0000000;core_worker/Fri Mar 10 18:06:46 2023]: done with #      10 kpts (progress:~
     1.0%).
[#0000000;clock_check_maxWall/Fri Mar 10 18:06:46 2023]: estimated walltime=0000:32:10 (
     hhh:mm:ss)
[#0000001;core_worker/Fri Mar 10 18:06:46 2023]: done with #      10 kpts (progress:~
     1.0%).
[#0000001;clock_check_maxWall/Fri Mar 10 18:06:46 2023]: estimated walltime=0000:32:19 (
     hhh:mm:ss)
[#0000003;core_worker/Fri Mar 10 18:06:46 2023]: done with #      10 kpts (progress:~
     1.0%).
[#0000003;clock_check_maxWall/Fri Mar 10 18:06:46 2023]: estimated walltime=0000:32:20 (
     hhh:mm:ss)
[#0000002;core_worker/Fri Mar 10 18:06:47 2023]: done with #      10 kpts (progress:~
     1.0%).
[#0000002;clock_check_maxWall/Fri Mar 10 18:06:47 2023]: estimated walltime=0000:32:38 (
     hhh:mm:ss)
[#0000000;core_worker/Fri Mar 10 18:09:17 2023]: done with #     102 kpts (progress:~
     10.0%).
[#0000000;clock_check_maxWall/Fri Mar 10 18:09:17 2023]: estimated walltime=0000:28:22 (
     hhh:mm:ss)
[#0000001;core_worker/Fri Mar 10 18:09:17 2023]: done with #     102 kpts (progress:~
     10.0%).
[#0000001;clock_check_maxWall/Fri Mar 10 18:09:17 2023]: estimated walltime=0000:28:24 (
     hhh:mm:ss)
[#0000003;core_worker/Fri Mar 10 18:09:17 2023]: done with #     102 kpts (progress:~
     10.0%).
[#0000003;clock_check_maxWall/Fri Mar 10 18:09:17 2023]: estimated walltime=0000:28:27 (
     hhh:mm:ss)
[#0000002;core_worker/Fri Mar 10 18:09:19 2023]: done with #     102 kpts (progress:~
     10.0%).
[#0000002;clock_check_maxWall/Fri Mar 10 18:09:19 2023]: estimated walltime=0000:28:40 (
     hhh:mm:ss)
[#0000000;core_worker/Fri Mar 10 18:12:06 2023]: done with #     205 kpts (progress:~
     20.0%).
[#0000001;core_worker/Fri Mar 10 18:12:06 2023]: done with #     205 kpts (progress:~
     20.0%).
[#0000003;core_worker/Fri Mar 10 18:12:07 2023]: done with #     205 kpts (progress:~
     20.0%).
[#0000002;core_worker/Fri Mar 10 18:12:09 2023]: done with #     205 kpts (progress:~
     20.0%).
[#0000000;core_worker/Fri Mar 10 18:14:53 2023]: done with #     307 kpts (progress:~
     30.0%).
[#0000001;core_worker/Fri Mar 10 18:14:53 2023]: done with #     307 kpts (progress:~
     30.0%).
[#0000003;core_worker/Fri Mar 10 18:14:54 2023]: done with #     307 kpts (progress:~
     30.0%).
```

```
279 [#0000002;core_worker/Fri Mar 10 18:14:58 2023]: done with #     307 kpts (progress:~
        30.0%).
280 [#0000000;core_worker/Fri Mar 10 18:17:42 2023]: done with #     410 kpts (progress:~
        40.0%).
281 [#0000001;core_worker/Fri Mar 10 18:17:42 2023]: done with #     410 kpts (progress:~
        40.0%).
282 [#0000003;core_worker/Fri Mar 10 18:17:43 2023]: done with #     410 kpts (progress:~
        40.0%).
283 [#0000002;core_worker/Fri Mar 10 18:17:49 2023]: done with #     410 kpts (progress:~
        40.0%).
284 [#0000000;core_worker/Fri Mar 10 18:20:28 2023]: done with #     512 kpts (progress:~
        50.0%).
285 [#0000000;clock_check_maxWall/Fri Mar 10 18:20:28 2023]: estimated walltime=0000:28:02 (
        hhh:mm:ss)
286 [#0000001;core_worker/Fri Mar 10 18:20:28 2023]: done with #     512 kpts (progress:~
        50.0%).
287 [#0000001;clock_check_maxWall/Fri Mar 10 18:20:28 2023]: estimated walltime=0000:28:02 (
        hhh:mm:ss)
288 [#0000003;core_worker/Fri Mar 10 18:20:31 2023]: done with #     512 kpts (progress:~
        50.0%).
289 [#0000003;clock_check_maxWall/Fri Mar 10 18:20:31 2023]: estimated walltime=0000:28:06 (
        hhh:mm:ss)
290 [#0000002;core_worker/Fri Mar 10 18:20:38 2023]: done with #     512 kpts (progress:~
        50.0%).
291 [#0000002;clock_check_maxWall/Fri Mar 10 18:20:38 2023]: estimated walltime=0000:28:20 (
        hhh:mm:ss)
292 [#0000000;core_worker/Fri Mar 10 18:21:39 2023]: done with #     555 kpts (progress:~
        54.2%).
293 [#0000000;clock_check_maxWall/Fri Mar 10 18:21:39 2023]: estimated walltime=0000:28:01 (
        hhh:mm:ss)
294 [#0000001;core_worker/Fri Mar 10 18:21:39 2023]: done with #     555 kpts (progress:~
        54.2%).
295 [#0000001;clock_check_maxWall/Fri Mar 10 18:21:39 2023]: estimated walltime=0000:28:01 (
        hhh:mm:ss)
296 [#0000003;core_worker/Fri Mar 10 18:21:41 2023]: done with #     555 kpts (progress:~
        54.2%).
297 [#0000003;clock_check_maxWall/Fri Mar 10 18:21:41 2023]: estimated walltime=0000:28:05 (
        hhh:mm:ss)
298 [#0000002;core_worker/Fri Mar 10 18:21:49 2023]: done with #     555 kpts (progress:~
        54.2%).
299 [#0000002;clock_check_maxWall/Fri Mar 10 18:21:49 2023]: estimated walltime=0000:28:19 (
        hhh:mm:ss)
300 [#0000000;core_worker/Fri Mar 10 18:23:15 2023]: done with #     614 kpts (progress:~
        60.0%).
301 [#0000001;core_worker/Fri Mar 10 18:23:16 2023]: done with #     614 kpts (progress:~
        60.0%).
302 [#0000003;core_worker/Fri Mar 10 18:23:18 2023]: done with #     614 kpts (progress:~
        60.0%).
303 [#0000002;core_worker/Fri Mar 10 18:23:26 2023]: done with #     614 kpts (progress:~
        60.0%).
304 [#0000000;core_worker/Fri Mar 10 18:26:04 2023]: done with #     717 kpts (progress:~
        70.0%).
305 [#0000000;clock_check_maxWall/Fri Mar 10 18:26:04 2023]: estimated walltime=0000:28:00 (
        hhh:mm:ss)
306 [#0000001;core_worker/Fri Mar 10 18:26:05 2023]: done with #     717 kpts (progress:~
        70.0%).
307 [#0000001;clock_check_maxWall/Fri Mar 10 18:26:05 2023]: estimated walltime=0000:28:01 (
        hhh:mm:ss)
308 [#0000003;core_worker/Fri Mar 10 18:26:07 2023]: done with #     717 kpts (progress:~
        70.0%).
309 [#0000003;clock_check_maxWall/Fri Mar 10 18:26:07 2023]: estimated walltime=0000:28:04 (
        hhh:mm:ss)
310 [#0000002;core_worker/Fri Mar 10 18:26:17 2023]: done with #     717 kpts (progress:~
        70.0%).
311 [#0000002;clock_check_maxWall/Fri Mar 10 18:26:17 2023]: estimated walltime=0000:28:18 (
        hhh:mm:ss)
312 [#0000000;core_worker/Fri Mar 10 18:28:52 2023]: done with #     819 kpts (progress:~
        80.0%).
313 [#0000001;core_worker/Fri Mar 10 18:28:53 2023]: done with #     819 kpts (progress:~
        80.0%).
314 [#0000003;core_worker/Fri Mar 10 18:28:54 2023]: done with #     819 kpts (progress:~
        80.0%).
315 [#0000002;core_worker/Fri Mar 10 18:29:06 2023]: done with #     819 kpts (progress:~
        80.0%).
316 [#0000000;core_worker/Fri Mar 10 18:31:41 2023]: done with #     922 kpts (progress:~
        90.0%).
317 [#0000001;core_worker/Fri Mar 10 18:31:42 2023]: done with #     922 kpts (progress:~
        90.0%).
318 [#0000003;core_worker/Fri Mar 10 18:31:44 2023]: done with #     922 kpts (progress:~
```

```
      90.0%).
[#0000002;core_worker/Fri Mar 10 18:31:56 2023]: done with #     922 kpts (progress:~
      90.0%).
~
~
~
~
[#0000000;fermi_selector]:^^^^^^^ FERMI SELECTOR   ^^^^^^^^^^^^^^^^^^^^^^
[#0000000;fermi_selector]:  select eF s.t.  N_el(eF)= N_el
 [#           0 ;fermi_selector]: n_ki_glob=                  4096
[#0000000;fermi_selector]:~~~~~~~~~~~~~~~~~~~~~~~~~~~~~~~~~~~~~~~~~~~~~~~~~~~~~~
[#0000000;fermi_selector]: the system is expected to have N_el,sys :=     8 electron(s)
[#0000000;fermi_selector]: now try to find a optimal Fermi energy value s.t. N_el( e_fermi
      ) == N_el,sys ..
 ...
 ...
[#0000000;fermi_selector]:  #eF   | eF (eV)  |  N_el(#eF) |  abs_err( N_el(#eF) - N_el )
[#0000000;fermi_selector]:
      ------------------------------------------------------------------------
[#0000000;fermi_selector]:      0 |  -       |    8       |    (electron(s) in system)
[#0000000;fermi_selector]:
      ------------------------------------------------------------
[#0000000;fermi_selector]:      1 |        9.390100  |    25.004883  |    0.17004883E+02

[#0000000;write_occ_lst]:   SUCCESS wrote occ_lst to out/occ_lst.npy
[#0000000;fermi_selector]:
      ------------------------------------------------------------------------
[#0000000;fermi_selector]:
      ------------------------------------------------------------------------
 ...
[#0000000;fermi_selector]: determined optimal fermi energy eF_optimal=    9.390100 eV with
       abs( N_el(eF_optimal) - N_el )=  0.17004883E+02
[#0000000;fermi_selector]:~~~~~~~~~~~~~~~~~~~~~~~~~~~~~~~~~~~~~~~~~~~~~~~~~~~~~~
 \n
[#00000;z7_int_kspace]: wrote tensor to file
out/kely_spD_pat_surf.npy
[#00000;z7_int_kspace]: wrote tensor to file
out/kely_spD_pat_sea.npy
[#00000;z7_int_kspace]: wrote tensor to file
out/kely_spD_pat_SUM.npy
 ^
 ^
 ^
 ^^^^^^^^^^^^^^^^^^^^^^^^^^^^^^^^^^
 *****  CORE WORKER LOAD INFO ******
 ^^^^^^^^^^^^^^^^^^^^^^^^^^^^^^^^^^
 -> MEMORY ESTIMATE(per MPI):
VmPeak= 6855036 kB
VmSize= 6150508 kB
VmHWM = 998740 kB
VmData= 601432 kB
VmStk = 264 kB
VmExe = 2452 kB
VmSwap= 0 kB
 -> TIMING INFO:
 wann_interp:  13.1362 %     (         88.474 sec.)
   ->wi fourier:  58.3890 %   (         51.659 sec.)
   ->wi_solver :  14.8130 %   (         13.106 sec.)
   ->wi_gauge  :  16.5674 %   (         14.658 sec.)
 fermi_level:   0.0530 %     (          0.357 sec.)
 tens_calcul:  86.8106 %     (        584.684 sec.)
   other     :   0.0002 %     (          0.001 sec.)
--------------
   total     : 100.0000 %     (        673.516 sec.)
 ~~~~~~~~
 k_integrate:         16.60753 sec.
 write___npy:          0.00359 sec.
 ~~~~~~~~~~~~~~~~~~~~~~~~~~~~~~~~~~
 ~~~~~~~~~~~~~~~~~~~~~~~~~~~~~~~~~~
 ^
 ^
 ^
 ^
^^^^^^^^^^^^^^^^^^^^^^^^^^^^^^^^^^^^^^^^^^^^^^^^^^^^^^^^^^^^^^^^^^^^^^^^^^^^^^^
^^^^^^^^^^^^^^^^^^^^^^^^^^^^^^^^^^^^^^^^^^^^^^^^^^^^^^^^^^^^^^^^^^^^^^^^^^^^^^^^
^^^^^^^^^^^^^^^^^ TIMING INFO ^^^^^^^^^^^^^^^^^^^^^^^^^^^^^^^^^^^^^^^^^^^^^^^^^
 submodule      |   walltime (sec)   | walltime(hhh:mm:ss)
-------------------------------------------------------------------------------
 input i/o      |       0.065   | 0000:00:00
```

```
band_worker    |      0.000  | 0000:00:00
core_worker    |   1697.294  | 0000:28:17
-----------------
tot            |   1697.494  | 0000:28:17
   ~~~~~~~~~~~~~~~~~~~~~~~~~~~~~~~~~~~~~~~~~~~~~~~~~~~~~~~~~~~~
#MPI PROCS     |          4  |   ---
#OMP THREADS   |         64  | pinning:  false
est cHour(sec)|     434558.51  |   ---
est cHours (h)|        120.71  |   ---
~~~~~~~~~~~~~~~~~~~~~~~~~~~~~~~~~~~~~~~~~~~~~~~~~~~~~~~~~~~~~~~~~~~~
~~~~~~~~~~~~~~~~~~~~~~~~~~~~~~~~~~~~~~~~~~~~~~~~~~~~~~~~~~~~~~~~~~~~
[#0000000;main/Fri Mar 10 18:34:45 2023]: all done, by by
```

Band / Volume 113
**Development of Superparamagnetic Based Biological Sensor for the Detection of Brucella DNA Using Frequency Mixing Magnetic Detection**
A. Abuawad (2025), X, 129 pp
ISBN: 978-3-95806-836-0

Band / Volume 114
**A System for the Cryogenic Power Management of Quantum Computing Electronics: Development, Integration, and Test**
A. R. Cabrera Galicia (2025), xxv, 110, lviii pp
ISBN: 978-3-95806-844-5

Band / Volume 115
**Investigation of 2D Materials using Low Energy Electron Microscopy (LEEM)**
H. Yin (2025) viii, 137 pp
ISBN: 978-3-95806-848-3

Band / Volume 116
**Topotactic phase transition in $La_{0.6}Sr_{0.4}CoO_{3-\delta}$ thin films: oxygen content, dynamics and reversibility**
S. He (2025) ix, 137 pp
ISBN: 978-3-95806-868-1

Band / Volume 117
**Electrical anisotropy and shear-resistant topology in the quasi one-dimensional van-der-Waals material α-$Bi_4Br_4$**
J.K. Hofmann (2025) xv, 129 pp
ISBN: 978-3-95806-869-8

Band / Volume 118
**Spin-orbital mixing in the topological ladder of the two-dimensional metal $PtTe_2$**
M. Qahosh (2025), ix, 170 pp
ISBN: 978-3-95806-872-8

Band / Volume 119
**Functions of SNNs constrained by biology**
A. Korcsak-Gorzo (2025), xvi, 145 pp
ISBN: 978-3-95806-876-6

Band / Volume 120
**On Scalable Integrated Charge State Tuning for Semiconductor Quantum Dot Devices**
F. A. Hader (2026), xx, 145 pp
ISBN: 978-3-95806-884-1

Band / Volume 121
**Efficient Massively Space-Time-Parallel Simulations with Adaptive Spectral Deferred Correction**
T. Saupe (2026), v, 149 pp
ISBN: 978-3-95806-886-5

Band / Volume 122
**Controlled single-molecule manipulation**
P. Kopp (2026), viii, 136 pp
ISBN: 978-3-95806-887-2

Band / Volume 123
**Growth and Excitation Dynamics of Epitaxial 2D Materials and Molecular Layers Studied by Electron and Momentum Microscopy**
M. E. Raths (2026), xvi, 161, XXIX pp
ISBN: 978-3-95806-892-6

Band / Volume 124
**Ferroelectric and Resistive Switching in Epitaxial $Hf_{0.5}Zr_{0.5}O_2$**
J. R. Knabe (2026), 145 pp
ISBN: 978-3-95806-895-7

Band / Volume 125
**Temperature Influences on Frequency Mixing Magnetic Detection for mobile Drinking Water Analysis in Crisis Areas**
M. Jessing (2026), xx, 113 pp
ISBN: 978-3-95806-902-2

Band / Volume 126
**Light-matter interaction from ab-initio Keldysh formalism**
M. D. Merte (2026), xvi, 184, A-27 pp
ISBN: 978-3-95806-906-0

Weitere ***Schriften des Verlags im Forschungszentrum Jülich*** unter
http://wwwzb1.fz-juelich.de/verlagextern1/index.asp

Information
Band / Volume 126
ISBN 978-3-95806-906-0

Mitglied der Helmholtz-Gemeinschaft

JÜLICH
Forschungszentrum